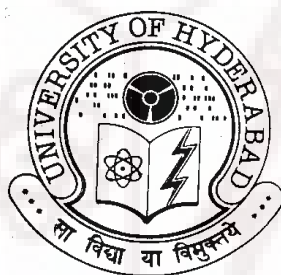


**SUPERCONTINUUM GENERATION, SURFACE FOUR-WAVE  
MIXING AND MULTIPHOTON ABSORPTION IN  
NONLINEAR OPTICAL TRANSPARENT MEDIA STUDIED  
WITH FEMTOSECOND LASER PULSES**

**A Thesis Submitted for the Degree of  
DOCTOR OF PHILOSOPHY**

**By**

**R. SAI SANTOSH KUMAR**



**School of Physics  
University of Hyderabad  
Hyderabad - 500 046  
India**

**February 2009**

The background of the page features a large, faint watermark of the University of Hyderabad logo. The logo is circular, with the text "UNIVERSITY OF HYDERABAD" around the top and "सा विद्या या विमुक्तये" in Devanagari script around the bottom. In the center of the logo is a shield containing a book and a lamp.

***To my Parents  
and  
Grandmother***

## DECLARATION

I here by declare that the matter embodied in the thesis entitled **“Supercontinuum generation, surface four-wave mixing and multiphoton absorption in nonlinear optical transparent media studied with femtosecond laser pulses”** is the result of investigation carried out by me in the School of Physics, University of Hyderabad, India, under direct supervision of Prof. D. Narayana Rao.

Place: Hyderabad

Date:

(R. Sai Santosh Kumar)



## CERTIFICATE

This is to certify that the work described in this thesis entitled “**Supercontinuum generation, surface four-wave mixing and multiphoton absorption in nonlinear optical transparent media studied with femtosecond laser pulses**” has been carried out by **R. Sai Santosh Kumar**, under my direct supervision and this has not been submitted for any degree or diploma at this or any other University.

Place: Hyderabad

Date:

(Prof. D. Narayana Rao)

Dean  
School of Physics

## ACKNOWLEDGEMENTS

I express my deep sense of gratitude and profound thanks to my thesis supervisor, Prof. D. Narayana Rao, for his inspiring guidance and constant encouragement throughout the course of this research work. I have been able to learn a great deal in this fascinating field of research through his inspiring and thought provoking discussions, and I consider my association with him a rewarding experience. His guidance to me goes even beyond science and he has helped me to grow as a strong individual.

I thank Prof. V. Srivastava, Dean, School of Physics, former Dean Prof. V. S. S. Sastry, and faculty for their co-operation in providing facilities in the School. I should also express my sincere thanks to Dr. Suneel Singh for his constant support in the development of the theoretical results during the course of my dissertation work. The encouragement and support provided by the Non-teaching staff in the school is highly appreciable.

My association with Dr. S. Venugopal Rao, ACRHEM has been very rewarding and sincere thanks to him. I have learnt the art of literature search from him. Special thanks to Prof. H. L. Bhatt and his research student Mr. Babu, for providing the KDP crystals used in my studies and extending their crystal polishing facility to me. I would like to thank Dr. L. Giribabu (IICT, Hyd.), for providing me the phthalocyanine molecules for the multiphoton studies.

A special word of thanks and appreciation to all my lab seniors, Prem, Naga Srinivas, Manoj. Sree Harsha, Bhakta, Chaitanya and Venkatram, for constantly encouraging and supporting me throughout my time here and directly helping me in getting into suitable research problems. Thanks to my present lab members Maruthi Manoj, Deepak, Ali, Kurumurthy, Reddeppa, Balamurali, Shekhar, Praveen, Sriram for creating friendly and pleasant lab atmosphere. Without the support of these guys this thesis work wouldn't have been successful.

At this juncture, I should extend my sincere thanks and deep appreciation to my friend Dr. Jaggu for being my strength right through the course of my PhD days. My heartfelt thanks to Shalu for being there for me always through out all the ups and downs during this journey of four and a half years.

My gratitude to Dr. Basavoju for providing the accommodation at the very beginning of my days in university and for his inspiring words of wisdom. My stay on this campus has been pleasant with the association of many other students whose list cannot be mentioned due to lack of space. I would like to thank my SSSU classmates in Hyderabad. Special thanks to Sarat and Sampy for constantly supporting and encouraging me.

The unconditional love of my Amma, Nanna and ammomma (granny) and their blessings made me what I am today and I owe everything to them. Special word of thanks to my little sister Sowmya. I would like to thank all my family members and relatives for their support and guidance throughout my life.

As a final note, I would like to express my love and gratitude to Bhagawan Sri Sathya Sai Baba, who is my source of inspiration, and who taught me the basic principles of life. I thank him for giving me patience and perseverance to endure challenges in my life. I dedicate this thesis at his lotus feet.

R. Sai Santosh Kumar

## Table of Contents

Declaration	i
Certificate	ii
Acknowledgments	iii
<b>Chapter 1: Introduction</b>	<b>1-33</b>
	3
1.1 Introductory remarks on femtosecond laser technology	8
1.2 Fundamentals of femtosecond laser pulses	9
1.2.1 Relationship between pulse Duration and Spectral width	
1.3 Nonlinear optics review	
1.3.1 Interaction of light with a medium:	11
1.3.2 Interaction of light with nonlinear media	12
1.3.3 Second order nonlinear optical process	14
1.3.4 Third order nonlinear optical process	16
1.3.4.1 Techniques for measuring $\chi^{(3)}$ nonlinearity	17
1.3.4.2 Self focusing	17
1.3.4.3 Self-phase modulation	19
1.3.4.4 Multiphoton absorption	20
1.4 Pulse propagation equation through nonlinear media	21
1.4.1 Interpretation of the simplified NLSE	22
1.4.1.1 Group velocity dispersion	23
1.4.1.2 Self-phase modulation	25
1.4.2 Self-steepening	26
1.4.3 Space-time coupling	27
1.5 Organization of the thesis	28
1.6 Conclusions	29
1.7 References	30
<b>Chapter 2: Experimental details and techniques</b>	<b>35-54</b>
2.1 Laser system used	35
2.2 Pulse-width measurement: The autocorrelation technique	41
2.2.1 Experimental details	42
2.2.2 Signal interpretation	43
2.3 Calculating pulse broadening due to GVD	45
2.4 Details of the experiments presented in the dissertation	
2.4.1 Supercontinuum generation	46
2.4.2 Degenerate Four wave mixing	48
2.4.3 Z-scan technique	53
2.5 References	54
<b>Chapter 3: Supercontinuum generation in transparent media</b>	<b>55-83</b>
3.1 Introduction and literature review	57
3.1.1 The critical power for self-focusing ( $P_{cr}$ )	59
3.2 SCG in different media	
3.2.1 SCG spectra in different media	60
3.2.2 SCG spectra with input peak power	63
3.2.3 Basic observations on SCG in transparent media	64

3.3	Mechanisms leading to SCG in bulk media	
3.3.1	Spectral broadening due to SPM	64
3.3.2	Limitations of 1-D wave equation model	
3.3.2.1	Assumptions considered for the 1-D modeling	67
3.3.2.2	Material dependence of SCG	68
3.3.3	Generalized theoretical formalism for SCG	69
3.3.4	Role of multiphoton ionization (MPI)	71
3.3.5	Role of spatio-temporal effects (conical emission of SCG)	72
3.3.6	Concluding remarks on SCG in bulk transparent media	73
3.4	Issues on SCG addressed in this dissertation work	75
3.5	Summary	76
3.6	References	77
<b>Chapter 4: Broadband supercontinuum generation in a Potassium Di-hydrogen Phosphate (KDP) crystal</b>		<b>85-118</b>
4.1	Choice of KDP as SCG media	87
4.1.1	Anisotropy of $\chi^{(3)}$ in KDP crystal	88
4.2	Supercontinuum generation (SCG) studies in a KDP crystal	
4.2.1	SCG in z-cut KDP media	91
4.2.1.1	SCG studies with linearly polarized input pulses	91
4.2.1.2	Studies on the role of input polarization	95
4.2.1.3	Formation of the filaments	98
4.2.1.4	Coherence properties of SCG	98
4.2.1.5	Polarization properties of SCG	100
4.2.2	SCG studies with orientation of KDP and its applications	
4.3	Broadband supercontinuum generation in a KDP crystal	
4.3.1	Second harmonic generation (SHG) in tandem with SCG	101
4.3.2	Sum frequency generation (SFG) in tandem with SCG	104
4.3.2.1	Theoretical studies	109
4.3.2.2	On polarization of the broadband SCG	112
4.3.2.3	Generation of spectrally flat broadband SCG	113
4.4	Conclusions	114
4.5	References	116
<b>Chapter 5: Depolarization properties of the supercontinuum generated in condensed media and its control</b>		<b>119-146</b>
5.1	Introduction	121
5.2	Experimental Details	124
5.3	Results and discussion	
5.3.1	Depolarization properties of SCG from BK-7, BaF <sub>2</sub> and KDP crystal	126
5.3.2	Reduction of depolarization in KDP crystal	134
5.4	Conclusions	143
5.5	References	144
<b>Chapter 6: Femtosecond four wave mixing (FWM) at air-dielectric interfaces</b>		<b>147-175</b>
6.1	Introduction	149



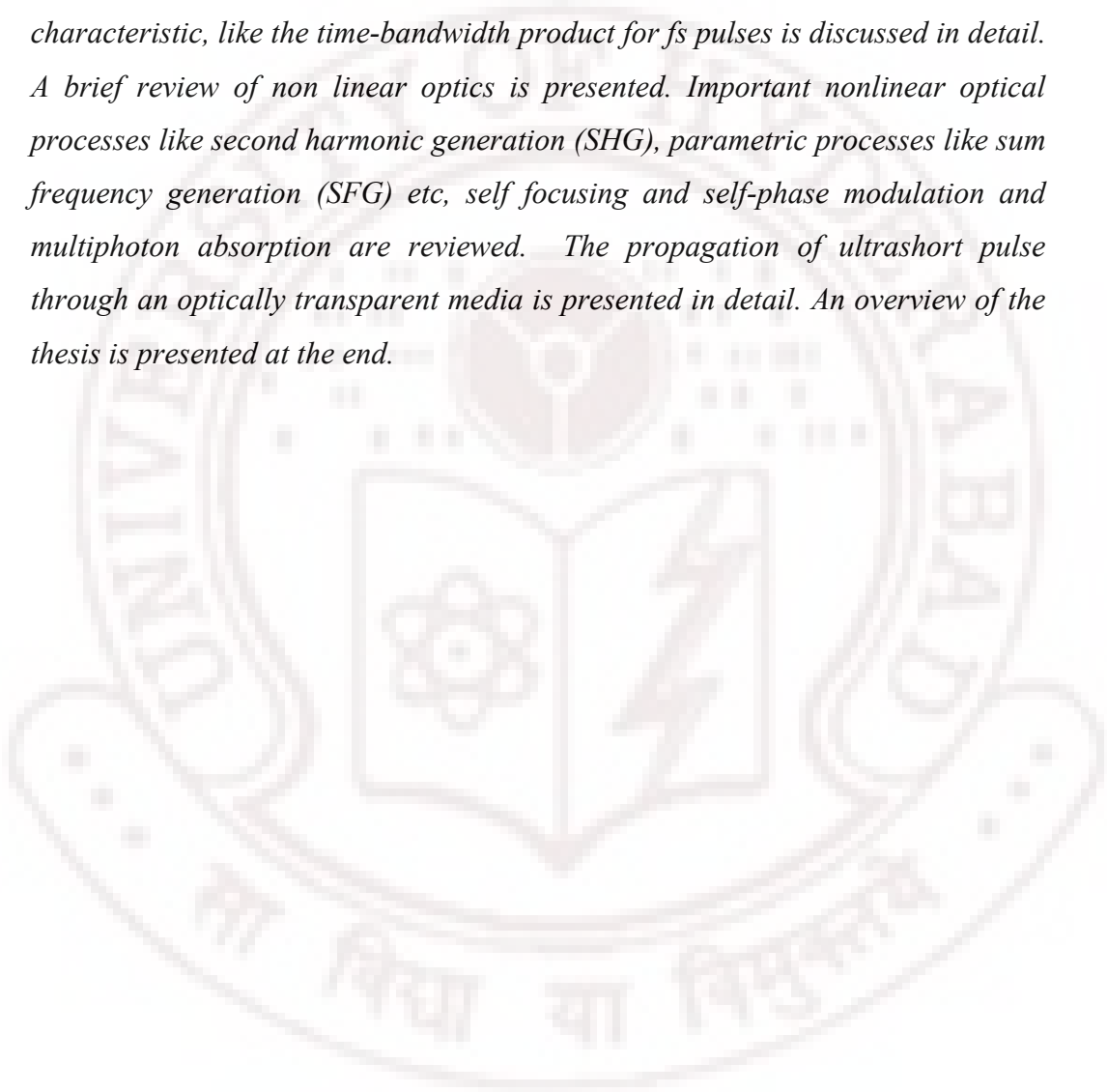
6.2	Theoretical formulation of $\chi^{(3)}$ at surfaces	151
6.3	Experimental details	157
6.4	Studies on FWM at interfaces	
6.4.1	Preliminary observations	158
6.4.2	Spectral studies with position of the slide	161
6.4.3	Intensity studies of FWM signal	162
6.4.4	Delay studies of FWM signal	164
6.5	Analysis of the experimental observations	
6.5.1	Enhancement of $\chi^{(3)}$ at interfaces	165
6.5.2	Analysis for observation of no FWM from bulk	166
6.5.3	Analysis for observation of peak shift in FWM	167
6.5.4	On the nomenclature of usage of FWM and not THG	172
6.5	Conclusions	173
6.6	References	174
<b>Chapter 7: Multiphoton absorption and ultrafast nonlinear optical properties of alkyl phthalocyanines</b>		<b>177-212</b>
7.1	Introduction	179
7.2	Molecular structure and spectroscopic characterization	182
7.3	Multiphoton absorption studies by Z-scan technique	
7.3.1	Theoretical considerations for multiphoton absorption processes	184
7.3.2	Experimental Details	187
7.3.3	Three photon absorption with 800 nm, 100 fs pulses	188
7.3.4	Two photon absorption with 532 nm, 6 ns pulses	192
7.4	Nonlinear refraction properties with closed aperture Z- scans	195
7.5	Optical limiting properties with ns pulses	196
7.6	Investigation of ultrafast nonlinear optical properties by degenerate four-wave mixing studies	
7.6.1	Experimental details	198
7.6.2	Third order nonlinear optical properties by DFWM measurements	199
7.6.3	Figures of merit (FOM) for photonic switching applications	203
7.7	Conclusions	207
7.8	References	208
<b>Chapter 8: Conclusions &amp; Future perspectives</b>		<b>213-220</b>
8.1	Conclusions	
8.1.1	Supercontinuum generation in KDP	215
8.1.2	Enhanced third order nonlinearities at air-dielectric interfaces	217
8.1.3	Multi-photon absorption studies in organic molecules	218
8.2	Future perspectives	219
<b>Appendix-I: Propagation of ultrashort pulses through nonlinear media</b>		<b>iii</b>
<b>Appendix-II: About the author</b>		<b>ix</b>
<b>Appendix-III: List of publications</b>		<b>xi</b>

The logo of the University of Hyderabad is a circular emblem. The outer ring contains the text "UNIVERSITY OF HYDERABAD" in English at the top and "ता विद्या या विमुक्तये" in Sanskrit at the bottom. The inner circle features a central sun-like symbol with rays, flanked by a book and a lightning bolt, and a molecular structure below the book.

# CHAPTER 1

## Abstract

*In this chapter important issues related to femtosecond (fs) pulses and its relevance to this dissertation work are introduced and discussed. A fundamental characteristic, like the time-bandwidth product for fs pulses is discussed in detail. A brief review of non linear optics is presented. Important nonlinear optical processes like second harmonic generation (SHG), parametric processes like sum frequency generation (SFG) etc, self focusing and self-phase modulation and multiphoton absorption are reviewed. The propagation of ultrashort pulse through an optically transparent media is presented in detail. An overview of the thesis is presented at the end.*



# Introduction

## 1.1 Introductory remarks on femtosecond laser technology:

*Timing is everything*, as the old adage goes, and this is a pivotal time for femtosecond laser pulse technology. Within a few decades of invention of the lasers, scientists have quickly moved into the regime of femtosecond (fs) optics, building lasers with pulses that last for only a few fs, or millionths of billionths of a second ( $10^{-15}$  sec). This is a remarkable achievement, as on this time scale even the movement of light seems insignificant: in one femtosecond, light travels only 300 nm, which is smaller than the diameter of most of the biological cells!

Femtosecond lasers have opened up a large variety of engineering and industrial applications [1-3]. These “real world” applications range from high-tech, such as high-speed circuit testing and biological imaging, to more everyday applications such as inspection of packaged food. Significant advances were made in developing compact, rugged, turnkey ultrafast lasers for use in many such applications [4]. From a scientific standpoint, femtosecond optics has therefore become a field of tremendous significance, spawning research groups around the world. Chemists and physicists developed these lasers for measuring extremely fast physical processes such as molecular vibrations, chemical reactions, charge transfer processes, and molecular conformational changes. All these processes take place on time scales of femtoseconds to picoseconds. In the realm of condensed matter physics, carrier relaxation and thermalization, wavepacket evolution, electron-hole scattering, and countless other processes also occur on these incredibly fast time scales.

The evolution of ultrashort laser pulse technology and applications has its roots in the necessity of shorter time pulses to measure a short-time event. Perhaps nothing better illustrates the remarkable capabilities of very short light pulses than the ability to capture on film the flight of a bullet as it tears through a playing card, as shown in the famous pictures produced by Harold Edgerton, who

pioneered fast strobe photography. The high speed and short duration of light pulses can “freeze” the action of just about any processes that one can think of. But the speed—or more accurately, the brevity of pulse duration—of light sources has increased dramatically since the days of high-speed strobe photography, which used light flashes on the order of microseconds. Today’s ultrafast lasers produce pulses that are millions of times faster than the strobe flashes used for strobe photography. Immediately following the first demonstration of the laser by Maiman in 1960 [5], efforts were underway to produce shorter and shorter optical pulses. Maiman’s flashlamp-pumped ruby laser produced a burst of spikes, each several hundred nanoseconds [6]. The application of Q-switching to lasers in 1961-62 allowed the production of single pulses of just tens of nanoseconds [7]. The introduction of mode-locking in 1964 dropped the available pulsewidth to 100 picoseconds [8] and by 1981; pulsewidths has been reduced down to 100 fs with the colliding-pulse mode-locking technique [9]. With successive improvements in passive mode-locking and dispersion compensation, few-cycle (sub-6 fs) pulses have been obtained [10].

Figure 1.1 gives a graphical representation of the improvements in ultrashort pulse generation since the first demonstration of a laser in 1960. The filled symbols indicate results directly achieved from a laser; open symbols indicate results achieved with additional external pulse compression. Until the end of the 1980s, ultrashort pulse generation was dominated by dye lasers, and pulses as short as 27 fs with an average power of ~10 mW were achieved at a centre wavelength of 630 nm [11]. External pulse compression ultimately resulted in pulses as short as 6 fs—a world record result by C. V. Shank’s group that was not surpassed for about 10 years [12]. This situation changed with the discovery of the Ti:sapphire laser. Pulses with only two optical cycles at FWHM (full-width half-maximum) at a centre wavelength of 800 nm have been generated with Ti:sapphire lasers with more than 100 mW average output power [13]. External compression resulted in pulses as short as 3.8 fs [14]. By the year 2003 a new record of obtaining the shortest pulse-width of just 3.4 fs was achieved by Yamane *et al* [15]. Though at present much shorter pulses in the

attosecond regime are accomplished, the current record in the femtosecond regime is now held by Matsubara *et al.* for obtaining 2.6 fs [16].

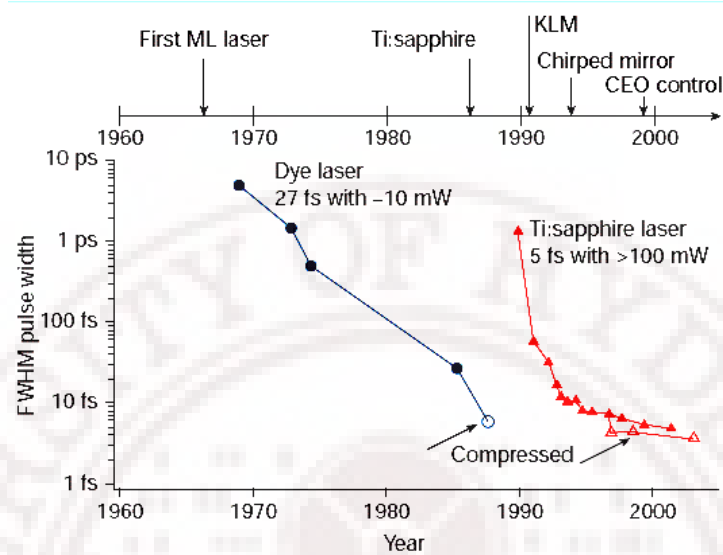


**Fig. 1.1:** Year-wise improvements in ultrashort pulse generation since the first demonstration of a laser [figure adapted from ref. 4]

As the period of one optical cycle in the near-infrared is just  $\sim 2.6$  fs, lasers with pulse-widths in this range up to about 100 fs are generally termed as “ultrafast” laser (a misnomer, since the light doesn’t go any faster-ultrashort is more appropriate). Most of the research with fs lasers relies on three unique characteristics of these ultrashort laser pulses.

- (i) The geometrical path length of a fs pulse amounts only to several micrometers (10 fs corresponds to  $3 \mu\text{m}$  in vacuum). Such a coherence length is usually associated with incoherent light. Therefore a short pulse can be used to measure very fast processes affording a high time resolution in pump-probe measurements, allowing a wealth of physical process to be studied including scattering times, carrier recombinations, coherent lattice oscillations, plasma dynamics, and chemical bond-breaking. (In this context “ultrafast” is not such a misnomer: *ultrashort* laser pulses enable the study of *ultrafast* process)

- (ii) Energy can be concentrated in a temporal interval as short as several  $10^{-15}$  sec, which corresponds to only a few optical cycles in the visible range implying a short pulse can create very non-equilibrium conditions. For example, ionic cores respond much more slowly than valence electrons and a femtosecond pulse can excite electrons to a very high temperature while the ions are still cold.
- (iii) The pulse peak power can be extremely large even at moderate pulse energies. For instance, a 50 fsec pulse with energy of 1mJ exhibits an average power of 20 GW. Focusing this pulse to a  $100\text{ }\mu\text{m}^2$  spot yields an intensity of 20 petawatts/cm<sup>2</sup> which means electric field strength of  $\sim 3\text{GV/cm}$ . This value is larger than a typical inner atomic field of 1 GV/cm. As the electric field of the laser becomes comparable to or exceeds the binding fields that hold the material together, the familiar linear approximations used to describe the interactions between light and materials break down.

Broadly one can envisage two powerful applications of femtosecond pulses in optics - in probing processes on a femtosecond time scale and creating high intensity photons. The latter has generated further interest in studying the interaction of femtosecond pulses with optically transparent materials because at such high peak intensities even these materials absorb laser radiation through multi-photon processes. Manifestation of such mechanism is the observation of numerous novel nonlinear optical (NLO) phenomena. Several processes such as second- and third harmonic generation, optical parametric down-conversion, self-phase modulation, self-focusing, multiphoton absorption, optical breakdown are now routinely studied. Exotic phenomena including above threshold ionization (ATI), high-harmonic generation (HHG), attosecond pulse generation (1 atto =  $10^{-18}$  sec), and relativistic nonlinear optics are now demonstrated in the laboratory [17]. On the other hand, the very property that is unique of fs pulses (short pulse widths, high peak intensities), make working with ultrafast lasers a challenging task. Typical unfocused emission intensities of these lasers are on the order of tens to hundreds of GW/cm<sup>2</sup> (assuming single-stage amplifier). At this level of



intensity, normal coated mirrors generally ablate and lead to laser damage of the optical components.

In the linear optics regime, that is associated with very low intensities, the interaction of light with transparent materials is straightforward. Light gets refracted and is reflected at interfaces, and polychromatic light is dispersed with propagation through a material [18]. However at the high intensities available from fs laser pulses, the subject becomes much richer, as the pulse itself affects and is affected by the material it propagates through in dramatic ways. Interactions representative of both of these classes form the subject of this thesis. As mentioned earlier though one can observe myriads of nonlinear optical phenomenon with fs pulses, in this thesis we limit our studies to third order nonlinear phenomenon associated with the interaction of fs pulses with transparent media that are observed at high input intensities namely:

1. Supercontinuum Generation in which the fs pulse gets spectrally broadened into white light after propagating in transparent media due to the complex interplay of various nonlinear optical processes. This serves as an example of a fs pulse getting affected by itself after interaction with media
2. Enhanced four-wave mixing at interfaces in which the enhancement of the third order nonlinear susceptibility ( $\chi^{(3)}$ ) at air-dielectric-air interfaces is demonstrated easily owing to the high peak intensity achievable with fs pulses.
3. Multiphoton absorption in which the high intensities associated with fs pulses can induce profound changes in the optical properties of a material leading to the enhanced probability of the material absorbing more than one photon before relaxing to the ground state. This serves as an example of a fs pulse affecting the material.

SCG is a universal phenomenon observed when amplified fs pulses are focused into most of the transparent media. As will be discussed in chapter 3, the main mechanism contributing to SCG is self-focusing phenomenon followed by



multiphoton absorption induced ionization (MPI) resulting in the appearance of free electrons that enhances SPM and gives rise to the spectra broadening of the input pulses. The large bandgap of transparent media enables  $n$ -photon absorption (usually  $n > 6$ ). The self focusing, mainly due to third-order susceptibility ( $\chi^{(3)}$ ) of the media, manifests strongly at high intensities available with fs pulses. As a topic of immense interest we have attempted the SCG studies in nonlinear crystals such as potassium di-hydrogen phosphate (KDP) that has a large band gap of  $\sim 7.4$  eV. Assuming a gaussian input pulse the focusing of fs pulses leads to a certain Rayleigh range ( $2z_0$ ) that has same intensities available throughout the length  $2z_0$ . Often the Rayleigh range extends beyond the interface of the media bringing into picture the interface effects on the  $\chi^{(3)}$ . Our studies established that a simple interface between two non absorbing dielectric media has enhanced third order nonlinearities owing to the symmetry breaking at the interface in normal directions resulting in a large field gradient. Thus, it becomes essential to consider the interface effects too. Furthermore, multiphoton absorption, being purely intensity dependent, also manifests in the interaction of fs pulses with materials possessing small bandgap. Organic molecules are one such example of materials that exhibit strong multiphoton absorption. In the context of multiphoton absorption we chose phthalocyanines as a particular organic molecule of our interest that has received lots of attention because of their large  $\pi$  electron delocalization.

## 1.2 Fundamentals of femtosecond laser pulses:

Femtosecond laser pulses are electromagnetic wave packets and as such are fully described by the time and space dependent electric field. In the frame of a semi-classical treatment the propagation of such fields and the interaction with matter are governed by Maxwell's equation with the material response given by the macroscopic polarization. The real electric field corresponding to an ultrashort pulse oscillates at an angular frequency  $\omega_0$  corresponding to the central wavelength of the pulse. To facilitate calculations, a complex field  $\tilde{E}(t)$  is

defined. It is defined as the analytic signal corresponding to the real field. The central angular frequency  $\omega_0$  is explicitly written in the complex field, which may be separated as an intensity function  $I(t)$  and a phase function  $\psi(t)$ :

$$\tilde{E}(t) = \sqrt{I(t)} \exp(i\omega_0 t) \exp[i\psi(t)] \quad (1.1)$$

The expression of the complex electric field in the frequency domain is obtained from the Fourier transform of  $\tilde{E}(t)$ :

$$\tilde{E}(\omega) = F(\tilde{E}(t)) \quad (1.2)$$

Because of the presence of the  $\exp(i\omega_0 t)$  term,  $\tilde{E}(\omega)$  is centered around  $\omega_0$ , and it is a common practice to refer to  $\tilde{E}(\omega - \omega_0)$  by writing just  $\tilde{E}(\omega)$ . Just as in the time domain, intensity and a phase function can be defined in the frequency domain:

$$\tilde{E}(\omega) = \sqrt{S(\omega)} \exp[i\phi(\omega)] \quad (1.3)$$

The quantity  $S(\omega)$  is the *spectral density* (or simply, the *spectrum*) of the pulse, and  $\phi(\omega)$  is the *spectral phase*. The intensity functions  $I(t)$  and  $S(\omega)$  determines the time duration and spectral bandwidth of the pulse.

### 1.2.1 Relationship between pulse Duration and Spectral width

We define the pulse duration  $\tau_p$  as the full width at half maximum (FWHM) of the intensity profile  $|\tilde{E}(t)|^2$ , and the spectral width  $\Delta\omega_p$  as the FWHM of the spectral intensity  $|\tilde{E}(\omega)|^2$ . Because the temporal and spectral characteristics of the field are related to each other through Fourier transforms, the bandwidth  $\Delta\omega_p$  and the pulse duration  $\tau_p$  cannot vary independently of each other.

There is a minimum *duration-bandwidth product* given by:

$$\Delta\omega_p \tau_p = 2\pi\Delta\nu_p \tau_p \geq 2\pi c_B \quad (1.4)$$

where  $c_B$  is a numerical constant on the order of 1, depending on the actual pulse shape. Some examples are shown in Table 1.1.

**Table 1.1:** Examples of standard pulse profiles. The spectral values are given for unmodulated pulses (table adapted from ref. [3])

Shape	Intensity profile [ $I(t)$ ]	Spectral profile [ $S(\omega)$ ]	$c_B$
Gauss	$e^{-2(t/\tau_G)^2}$	$e^{-\left(\frac{\omega\tau_G}{2}\right)^2}$	0.441
Sech	$\text{sech}^2(t/\tau_s)$	$\text{sech}^2 \frac{\pi\omega\tau_s}{2}$	0.315
Lorentz	$\left[1 + (t/\tau_L)^2\right]^{-2}$	$e^{-2 \omega \tau_L}$	0.142
Asym. sech	$\left[e^{t/\tau_a} + e^{-3t/\tau_a}\right]^{-2}$	$\text{sech} \frac{\pi\omega\tau_s}{2}$	0.278
Square	1 for $ t/\tau_r  \leq 1$ 0 elsewhere	$\text{sinc}^2(\omega\tau_r)$	0.443

The classical physical relationship eq. (1.4), which leads to the quantum-mechanical time-energy uncertainty principle, has several important consequences in the field of ultrashort light pulses:

- i. In order to produce a light pulse with a given duration it is necessary to use a broad enough spectral bandwidth. A Gaussian-shaped pulse lasting for one picosecond ( $10^{-12}$  sec) has a minimum spectral bandwidth of 441 MHz ( $\Delta\omega_p = 4.41 \times 10^{11}$  Hz). If the central frequency  $\nu_0$  of the pulse lies in the visible part of the electromagnetic spectrum, say  $\nu_0 = 4.84 \times 10^{14}$  Hz (i.e.  $\lambda_0 = 620\text{nm}$ ), then the relative frequency bandwidth is  $\Delta\nu/\nu_0 \approx 10^{-3}$ . But for a 100 times shorter pulse ( $\Delta t = 10$  fs),  $\Delta\nu/\nu_0 \approx 0.1$ . As  $|\Delta\lambda/\lambda| = \Delta\nu/\nu_0$ , the wavelength extension of this pulse is 62 nm, covering 15% of the visible window of the electromagnetic spectrum. Taking into account the wings of the spectrum, a 10 fs pulse covers most of the visible window.

- ii. The equality in eq. (1.4) holds for pulses without frequency modulation (unchirped) which are called “bandwidth limited” or “Fourier transform limited” pulses. Such pulses exhibit the shortest possible duration at a given spectral width and pulse shape.
- iii. For a given spectrum, one pulse envelope can be constructed that has the shortest possible duration. The shortest constructed pulse can only be *transform-limited* if its spectrum is symmetrical.

### 1.3 Nonlinear optics review:

In this section we briefly review the basics of nonlinear optics [19-21]. The NLO effects due to second order and third order nonlinear susceptibilities are discussed before we move the propagation of ultrashort pulse in a nonlinear transparent medium in the next section.

#### 1.3.1 Interaction of light with a medium:

A molecular medium, such as an organic crystalline or polymeric solid, is generally non-conducting and non-magnetic and the electrons are regarded as being tightly bound to the nuclei. The charge distribution induced in the molecule by the field is approximated by that of an induced dipole. The applied field polarizes the molecules in the medium, displacing them from their equilibrium positions and induces a dipole moment  $\mu_{ind} = -er$ ,  $e$  is the electronic charge and  $r$  is the field induced displacement. The bulk polarization resulting from this induced dipole is given by  $P = -Ner$ , where  $N$  is the electron density in the medium. The electric field inside the material is lowered by the polarization that opposes the externally applied field. The reduction in field intensity in the volume element containing the molecule of interest is by the factor  $1 + \varepsilon$ , where  $\varepsilon$  is defined as the dielectric constant of the medium. If the field strength is relatively low, the polarization of the medium is linear in the applied field.  $P = \chi^{(1)}E$ . The proportionality constant is related to the dielectric constant by  $\varepsilon = 1 + 4\pi\chi^{(1)}$ .  $\chi^{(1)}$  is susceptibility, a second rank tensor, because it relates

all of the components of the polarization vector to all of the components of the electric field vector.

Another quantity that is related to the polarization is the dielectric displacement,  $\bar{D} = \bar{E} + 4\pi\bar{P}$ .  $\bar{E}$  gives the contribution to the electric flux density emanating from a distribution of charges, if those charges were in free space. The effect on the medium is usually to reduce the forces between charges by an amount proportional to the polarization of the medium. In vacuum,  $\bar{D}$  and  $\bar{E}$  are equal. In an isotropic medium,  $\bar{D}$  and  $\bar{E}$  are parallel vectors and the polarization response is equal in all directions. In anisotropic media, the vectors  $\bar{D}$  and  $\bar{E}$  are no longer parallel and  $\epsilon$  is therefore a second rank tensor with properties similar to the susceptibility tensor. The optical response of the medium can equivalently be represented by its refractive index. For an isotropic medium  $n_c = \epsilon(\omega) = 1 + 4\pi\chi^{(\omega)}$ . Because of resonances in molecules and solids associated with electronic and nuclear motions, the refractive index and, hence the dielectric constant are complex quantities. Near a resonance corresponding to an electronic absorption, the complex refractive index is given by  $n_c = n + ik$ , the real part of  $\epsilon(\omega)$  and, hence  $n$  accounts for refraction while the imaginary part  $ik$  describes the absorption of light in the dielectric medium.

### 1.3.2 Interaction of light with nonlinear media:

When a medium is subject to an intense electric field such as that due to an intense laser pulse, the polarization response of the material is not adequately described by equation 1.5. Assuming that the polarization of the medium is still weak compared to the binding forces between the electrons and nuclei, polarization can be expressed in a power series of the field strength  $\bar{E}$

$$\bar{P} = \chi^{(1)} \cdot \bar{E} + \chi^{(2)} : \bar{E}\bar{E} + \chi^{(3)} : \bar{E}\bar{E}\bar{E} \dots \quad (1.5)$$

- The term that is quadratic in the field strength  $\bar{E}$  describes the first nonlinear effect. The coefficient  $\chi^{(2)}$  relating the polarization to the square

of the field strength  $\bar{E}$  is called the second-order nonlinear susceptibility of the medium. Its magnitude describes the strength of second-order process.

- The term  $\chi^{(3)}$  describes the third order processes. For most materials, the higher-order effects are extremely difficult to observe. For this reason we limit here our discussion up to and third-order effects.

Equation 1.5 can be recast as  $\bar{P} = \chi_{\text{eff}} \cdot \bar{E}$ , where  $\chi_{\text{eff}}$  depends on the field strength. All the nonlinear effects can be thought of as arising from field induced modulation of the nonlinear index of refraction. And this nonlinear index of refraction is related to the applied modulating electric field,  $\bar{E}$ , through the electric field dependent susceptibility,  $\chi_{\text{eff}}$ , of a material, through  $n^2 = \epsilon = 1 + 4\pi \chi_{\text{eff}}$ , where  $\epsilon$  is the dielectric constant of the material at optical frequencies. The induced polarization therefore results in a **modulation of the refractive index**. The manifestation of the optical behavior can be clearly seen by considering a sinusoidal field equation

$$E(z, t) = E_0 \cos(\omega t - kz), \text{ with } k^2 = \epsilon \omega^2 / c^2 \quad (1.6)$$

where,  $E_0$  defining the amplitude of the field,  $k$  is the propagation vector, characterizing the phase of the optical wave with respect to a reference point,  $kz$  describes the relative phase of the wave. Substituting 1.6 in eqn. 1.5 we have:

$$\begin{aligned} P &= \chi^{(1)} E_0 \cos(\omega t - kz) + \chi^{(2)} E_0^2 \cos^2(\omega t - kz) + \chi^{(3)} E_0^3 \cos^3(\omega t - kz) \dots \\ \Rightarrow P &= \chi^{(1)} E_0 \cos(\omega t - kz) + \left(\frac{1}{2}\right) \chi^{(2)} E_0^2 [1 + \cos(2\omega t - 2kz)] \\ &\quad + \chi^{(3)} E_0^3 \left[ \left(\frac{3}{4}\right) \cos(\omega t - kz) + \left(\frac{1}{4}\right) \cos(3\omega t - 3kz) \right] \dots \end{aligned} \quad (1.7)$$

The above equation clearly shows the presence of new frequency components due to the nonlinear polarization.



### 1.3.3 Second order nonlinear optical process:

The second term gives of eq. 1.13 describes the processes due to second order nonlinear susceptibility  $\chi^{(2)}$ :

- i. a frequency independent contribution suggests that a dc polarization should appear in a second order nonlinear material when it is appropriately irradiated, termed as optical rectification.
- ii. The presence of  $2\omega$  indicates the possibility of second-harmonic generation (SHG).
- iii. One can also envisage parametric processes involving  $\chi^{(2)}$  like sum-frequency generation (SFG) and difference frequency generation (DFG).

There is an important symmetry constraint for observing second harmonic generation or other quadratic (and in general any even order) NLO effects. In systems having a center of symmetry, reversal of the electric field should exactly reverse the polarization, *i.e.*,  $\bar{P}(\bar{E}) = -\bar{P}(E)$ . In order for Equation 1.9 to satisfy this condition, all coefficients of even powers of  $E$  have to be equal to zero. In noncentrosymmetric systems no such equality exists and  $\bar{P}(\bar{E}) \neq -\bar{P}(E)$ . This implies that quadratic and other even order effects are possible if and only if the system is noncentrosymmetric (*i.e.*, if it lacks the center of inversion).

#### 1.3.3.1 Second harmonic generation (SHG)

When a noncentrosymmetric crystal is illuminated with photons with angular frequency  $\omega$  some pairs of these photons disappear, replaced by single photons with angular frequency  $2\omega$ . This effect is called **second-harmonic generation**. The SHG process is illustrated schematically in figure 1.2. The most common way to do this is to use birefringent crystals for which the ordinary ( $n_o$ ) and extraordinary index ( $n_e$ ) surfaces for the fundamental and doubled frequencies cross one another as shown in figure 1.3. Calculation of the phase-matching angle  $\theta_c$  between the propagation direction, taken orthogonal to the

surface of the crystal, and the  $c$  axis of the crystal can be made using the equation:

$$\left( \frac{1}{n_e^{2\omega}(\theta)} \right)^2 = \frac{\cos^2(\theta)}{(n_e^{2\omega})^2} + \frac{\sin^2(\theta)}{(n_e^{2\omega})^2} = \left( \frac{1}{n_o^\omega(\theta)} \right)^2 \quad (1.8)$$

Various situations can be encountered depending on the birefringent crystal: in positive crystals, like quartz,  $n_e > n_o$ , while in negative crystals, like calcite,  $n_e < n_o$ . For type I phase-matching crystals the two mixing photons have the same polarization direction, while in type II crystals they are orthogonally polarized.

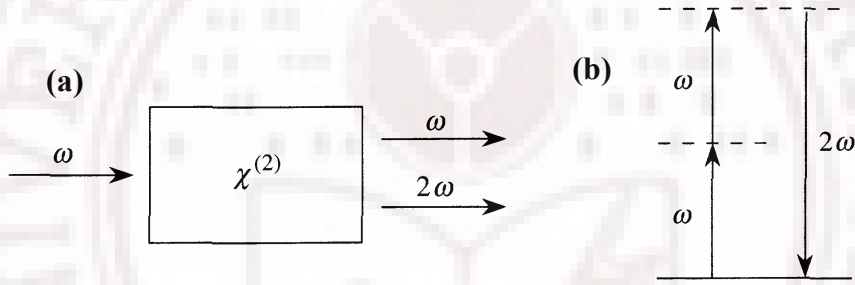


**Fig. 1.2:** (a) Geometry of SHG, (b) Energy-level diagram describing SHG. (figure adapted from ref.[19])

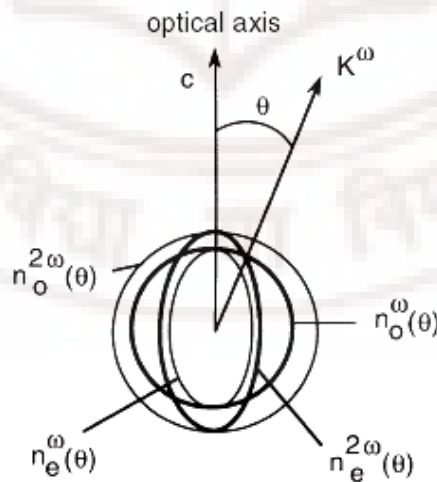


**Fig. 1.3:** Thin lines: intersection of the plane containing the  $c$  axis of a birefringent crystal with its ordinary index surfaces. Thick lines: intersection with the extraordinary surfaces (figure adapted from ref.[3])



### 1.3.3.2 Parametric interactions:

Apart from SHG, the second-order susceptibility  $\chi^{(2)}$  is responsible for a variety of other effects involving three photons and generating new frequencies. These effects are called parametric effects. A classification of these parametric effects can be based on energy and momentum conservation for the three photons involved in the process. A nonlinear crystal with second-order susceptibility  $\chi^{(2)}$  is illuminated with an intense pump pulse containing  $n_2$  photons at angular frequency  $\omega_2$  and a weak signal pulse containing  $n_1$  photons at angular frequency  $\omega_1$ ;  $n_3$  photons are emitted with angular frequency  $\omega_3$ . Such a classification is given in Table 1.2.

**Table 1.2:** Optical parametric interactions ordered according to energy and momentum conservation (table adapted from ref. [3])

Photon number variation	$\omega_1 > \omega_2$	$\omega_1 < \omega_2$	Photon number variation
$n_1 - 1$	Frequency difference	Frequency sum	$n_1 - 1$
$n_2 + 1$	$\omega_3 = \omega_1 - \omega_2$	$\omega_3 = \omega_1 + \omega_2$	$n_2 + 1$
$n_3 + 1$	$k_1 = k_2 + k_3$	$k_3 = k_1 + k_2$	$n_3 + 1$
$n_1 - 1$	Frequency sum	Parametric amplification	$n_1 + 1$
$n_2 - 1$	$\omega_3 = \omega_1 + \omega_2$	$\omega_3 = \omega_2 - \omega_1$	$n_2 - 1$
$n_3 + 1$	$k_3 = k_1 + k_2$	$k_2 = k_1 + k_3$	$n_3 + 1$

### 1.3.4 Third order nonlinear optical process:

The third term in Equation 1.13 describes two terms (a) a frequency response at the frequency of the optical field at  $3\omega$  that leads to third harmonic generation (THG), and (b) the a nonlinear contribution to the polarization at the frequency of the incident field: this term hence leads to nonlinear contribution to the refractive index experienced by a wave at frequency  $\omega$ . The refractive index in the presence of this type of nonlinearity can be represented as

$$n = n_0 + n_2 I \quad (1.9)$$

where  $n_0$  is the usual refractive index, and  $n_2 = \frac{12\pi^2}{n_0^2 c} \chi^{(3)}$  (1.10)

is an optical constant that characterizes the strength of the optical nonlinearity. Some of the processes that can occur as a result of the intensity-dependent refractive index of our interest are self-focusing, and self-phase modulation.

#### 1.3.4.4 Techniques for measuring $\chi^{(3)}$ nonlinearity:

The magnitude and response of third-order nonlinear susceptibility are important parameters in characterizing and determining the applicability of any material as a nonlinear optical device. There are several techniques [19-21, 28] for measuring these parameters that include

1. Degenerate Four Wave Mixing (DFWM): For measurement of both magnitude and response time of the third-order nonlinearity.
2. Third Harmonic Generation: For measurement of magnitude of third-order nonlinearity only.
3. Z-scan: For measurement of sign, magnitude of third-order nonlinearity.
4. Time-resolved Optical Kerr Effect and Transient Absorption techniques: For the study of photo-physical processes determining the nonlinearity.
5. Time Correlated Single Photon Counting (TCSPS) technique to measure the radiative (fluorescence) lifetimes

Among which DFWM and Z-scan are widely used techniques for measuring both absorptive and non-absorptive nonlinearities and we employed these techniques in the studies presented in this work. The details of each technique would be presented in chapter 2.

#### 1.3.4.2 Self-focusing:

The change in the refractive index or spatial distribution of the refractive index of a medium due to the presence of intense optical field called nonlinear refractive index ( $n_2$ ). The refractive index of air  $n$  in the presence of an intense

electromagnetic field does not only depend on its frequency, but also on the space and time dependent intensity  $I(r,t)$  of the laser according to the law:

$$n = n_0 + n_2 I(r,t) \quad (1.11)$$

The coefficient  $n_2$  is usually positive, leading to an increase of the refractive index in the presence of intense radiation. Assuming monochromatic incident laser beam with a Gaussian-beam intensity profile given:

$$I(r,t) = I_0 \exp\left(\frac{-2r^2}{\omega_0^2}\right), \text{ implying } n = n_0 + n_2 I_0 \exp\left(\frac{-2r^2}{\omega_0^2}\right), \text{ can be expanded into}$$

infinite series; Considering only first order term of the infinite series, the

intensity of the beam, at the center of the beam is given by  $\approx n_0 + n_2 I_0 \left(1 - \frac{2r^2}{\omega_0^2}\right)$

In such scenario the phase delay relative to the radial coordinate of the wavefront is given by

$$\begin{aligned} \varphi(r) &= nk_0 L = n_0 k_0 L - n_2 k_0 L I_0 \left(\frac{2r^2}{\omega_0^2}\right) \\ \Rightarrow \varphi(r) &\approx \text{const.} - 2n_2 k_0 L I_0 \left(\frac{r^2}{\omega_0^2}\right) \end{aligned} \quad (1.12)$$

which is very similar to that of a lens is involved, with the difference that here the effect is cumulative and can lead, in the absence of other saturating effects, to a catastrophic collapse of the beam on itself. This effect is represented in a diagrammatic way in figure. 1.4.

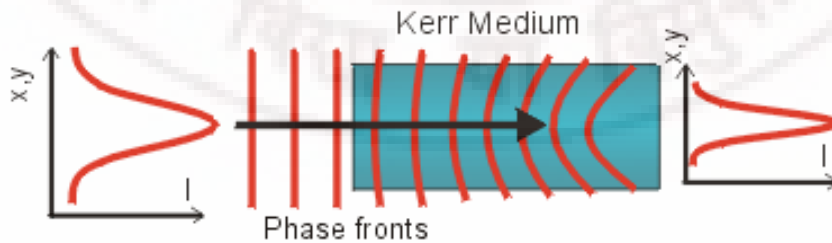


**Fig. 1.4.** Distortion of the wavefront of laser beam leading to self-focusing in a nonlinear medium for  $n_2 > 0$

### 1.3.4.3. Self-phase modulation:

Self-phase modulation (SPM) is a nonlinear optical effect of light-matter interaction. An ultrashort pulse of light, when traveling in a medium, will induce a varying refractive index of the medium due to the optical Kerr effect. This variation in refractive index will produce a phase shift in the pulse, leading to a change of the pulse's frequency spectrum. The nonlinear index of material depends on the time dependence of a light pulse intensity envelope, which can be expressed as:

$$n = n_0 + n_2 I(r, t), \quad I(t) = e^{-\Gamma t^2}$$

To examine the influence of this time varying index on the frequency of the light, we simplify our analysis by considering a plane wave propagating in a nonlinear medium:  $E(z, t) = E_0 \cos(\omega_0 t - kz)$ , where  $k = (\omega_0/c)n(t)$

The instantaneous frequency, being the time derivative of the phase, can be written as

$$\omega(t) = \frac{\partial}{\partial t} \Phi(t) = \omega_0 - \frac{\omega_0}{c} \frac{\partial n(t)}{\partial t} z \quad (1.13)$$

and the frequency variation can be written as

$$\delta\omega(t) = \omega(t) - \omega_0 = -\frac{\omega_0 n_2}{2c} z \frac{\partial I(t)}{\partial t} \quad (1.14)$$

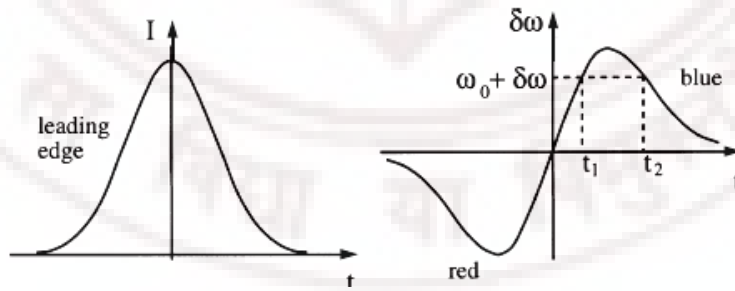


**Fig. 1.5.** (Left) intensity dynamics of a Gaussian light pulse; the earlier times, i.e. the leading edge of the pulse, lie on the left side of the graph. (Right), time variation of the central pulsation, which is proportional to the negative of the pulse envelope derivative when the nonlinear index of refraction is positive (figure adapted from ref.[3])

Figure 1.5 shows a graphical elucidation of the above relation in case of the considered pulse of Gaussian phase variation. As a consequence of the Fourier duality between time and frequency, an application of periodic amplitude or phase modulation to a periodic signal results in creation of new components in its frequency spectrum. In the self-phase-modulation process, with  $n_2$  positive, new low frequencies are created in the leading edge of the pulse envelope and new high frequencies are created in the trailing edge. These new frequencies are not synchronized, but are still created inside the original pulse envelope. Self-phase-modulation is not a dispersive effect in itself, but a pulse does not remain transform-limited when it crosses a transparent material.

### 1.3.4.3 Multiphoton absorption

Nonlinear absorption refers to the change of transmittance of a material as a function of intensity or fluence. The high intensities associated with fs pulses can induce profound changes in the optical properties of a material leading to a nonlinear response of the real and imaginary parts of polarization. The imaginary part of the nonlinear polarization is associated for instance with multiphoton transitions and will exhibit a  $n$ -photon resonance when two level of an atomic or molecular system can be connected by  $n$  optical quanta as shown in figure 1.6.

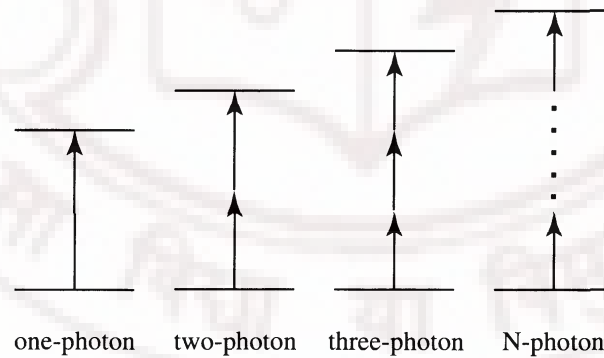


**Fig. 1.6.** Examples of multiphoton processes (figure adapted from ref. [21])

At sufficiently high intensities, the probability of a material absorbing more than one photon before relaxing to the ground state can be greatly enhanced. As early as 1931 Göppert-Mayer derived the two-photon transition

probability in a system using the second order quantum perturbation theory [23]. With the availability of high intensities with fs pulses, in addition to numerous investigations into this phenomenon of the simultaneous absorption of two photons, multiphoton ( $>2$ ) absorption has also been widely studied. Multiphoton absorption processes are highly promising for a number of processes including optical limiting [24], 3D microfabrication [25], optical data storage [26], and biomedical applications [27]. More on this is discussed in chapter 7.

### 1.4 Pulse propagation equation through nonlinear media

In the present section we discuss the fate of an ultrashort pulse propagating through a nonlinear media. We begin our discussion starting from the **generalized nonlinear Schrödinger equation (NLSE)** as derived in Appendix I. The discussion in this section is along the notation followed by Boyd [21]. The generalized NLSE for the slowly varying field amplitude  $\tilde{A}(\bar{r}, t)$  is as follows:

$$\left[ \left( 1 + \frac{i}{\omega_0} \frac{\partial}{\partial \tau} \right)^{-1} \nabla_{\perp}^2 + 2ik_0 \frac{\partial}{\partial z} + 2k_0 \tilde{D} \right] \tilde{A}(\bar{r}, t) = - \frac{4\pi\omega_0^2}{c^2} \left( 1 + \frac{i}{\omega_0} \frac{\partial}{\partial t} \right)^2 \tilde{p} \quad (1.15)$$

where the nonlinear polarization is expressed in terms of its slowly varying amplitude approximation  $\tilde{p}(\bar{r}, t)$ . The above equation includes the effects of higher-order dispersion (presence of  $\tilde{D}$ ), space-time coupling [presence of factor  $\left( 1 + \frac{i}{\omega_0} \frac{\partial}{\partial t} \right)$  in the left hand side of the Eq.] and self-steepening [influence of factor  $\left( 1 + \frac{i}{\omega_0} \frac{\partial}{\partial t} \right)$  in the right hand side of the Eq. on the nonlinear source term  $\tilde{p}(\bar{r}, t)$ ]. The higher-order dispersion term  $D$  is defined

$$\text{as } \tilde{D} = \sum_{n=2}^{\infty} \frac{1}{n} k_n \left( i \frac{\partial}{\partial t} \right)^n.$$

### 1.4.1 Interpretation of the simplified NLSE:

For simplifying the generalize NLSE, we make the following approximations and assumptions:

- We consider only the second-order dispersion term  $D = \frac{1}{2}k_2 \left( i \frac{\partial}{\partial t} \right)$  and ignoring the correction terms  $\frac{i}{\omega_0} \frac{\partial}{\partial t}$  by replacing  $\left( 1 + \frac{i}{\omega_0} \frac{\partial}{\partial t} \right)$  by unity.
- For the case of material with an instantaneous third-order nonlinear response, the polarization is given by:  $\tilde{p}(\bar{r}, t) = 3\chi^{(3)} |\tilde{A}(\bar{r}, t)|^2 \tilde{A}(\bar{r}, t)$

Making use of the above mentioned approximations the generalized NLSE can be simplified into:

$$\left[ \nabla_{\perp}^2 + 2ik_0 \frac{\partial}{\partial z} + 2k_0 \left( \frac{1}{2}k_2 \left( i \frac{\partial}{\partial t} \right) \right) \right] \tilde{A}(\bar{r}, t) = -\frac{4\pi\omega_0^2}{c^2} 3\chi^{(3)} |\tilde{A}(\bar{r}, t)|^2 \tilde{A}(\bar{r}, t) \quad (1.16)$$

Rearranging the above Eq. we obtain:

$$\frac{\partial \tilde{A}(\bar{r}, t)}{\partial z} = \left[ \underbrace{\frac{i}{2k_0} \nabla_{\perp}^2}_{(i)} - \underbrace{\frac{i}{2}k_2 \frac{\partial^2}{\partial t^2}}_{(ii)} + \underbrace{\frac{6\pi i \omega_0}{n_0 c} \chi^{(3)}(\omega_0) |\tilde{A}|^2}_{(iii)} \right] \tilde{A} \quad (1.17)$$

Equation 1.17 lead to the interpretation that the field amplitude  $\tilde{A}$  varies with the propagation distance  $z$  because of three physical effects indicated below:

- (i) describes the spreading of the beam due to diffraction
- (ii) describes temporal spreading of the pulse due to group velocity dispersion, and
- (iii) describes the non-linear acquisition of phase

We now define the distance scales where each of the three effects becomes appreciable:

$$L_{dif} = \frac{1}{2}k_0\omega_0^2 \quad (\text{Diffraction length}) \quad (1.18a)$$

$$L_{dis} = \frac{\tau_p^2}{|k_2|} \quad (\text{Dispersion length}) \quad (1.18b)$$

$$L_{NL} = \frac{n_0 c}{6\pi\omega_0 \chi^{(3)} |A|^2} = \frac{1}{(\omega/c) n_2 I} \quad (\text{Nonlinear length}) \quad (1.18c)$$

Here  $\omega_0$  is the measure of the characteristic beam radius, and  $\tau_p$  is a measure of the characteristic pulse duration. The significance of these distance scales is that for a given physical situation the process with the shortest distance scales is expected to be dominant.

#### 1.4.1.1 Group velocity dispersion

The first case of interest is for materials in which the nonlinearities are small resulting in the pulse propagation dominated by group velocity dispersion. The group velocity dispersion (GVD) describes the variation of group velocity through a material as a function of wavelength. In normal dispersion, the red wavelengths travel faster than the blue wavelengths. The reverse is true with anomalous dispersion. An fs pulse necessarily has a large spectral width. As a consequence, GVD can affect the propagation of an fs pulse by introducing a phase delay as a function of wavelength (or chirp), and by changing the pulse-width. In the case of GVD dominated propagation, Eq. (1.17) reduces to

$$\frac{\partial A(z,t)}{\partial z} + \frac{i}{2} k_2 \frac{\partial^2 A(z,t)}{\partial t^2} = 0 \quad (1.19)$$

The solution of (1.19) can be obtained analytically in the frequency domain and is of the form:

$$\tilde{A}(z, \Omega) = A(0, \Omega) \exp\left(-i \frac{k_2}{2} \Omega^2 z\right) \quad (1.20)$$

where  $A(z,t)$  can be obtained by the Fourier transform of (1.20). To illustrate the concepts of chirp and pulse broadening, consider a Gaussian input field having a



pulse envelope given by  $A(z, t) = A(z) \exp\left[-\left(\tau/\sqrt{2}\tau_0\right)^2\right]$  with a pulse width  $\tau_0$ .

To solve (1.20), we first find  $\tilde{A}(z=0, \Omega)$  to be

$$\tilde{A}(0, \Omega) = \sqrt{2\pi}\tau_0 A(0) \exp\left[-\left(\Omega\tau_0/\sqrt{2}\right)^2\right] \quad (1.21)$$

Substituting (1.21) in (1.20) and taking the inverse Fourier transform, we find

$$A(z, \tau) = \frac{\tau_0}{\sqrt{2\xi}} A(0) \exp\left[-(\tau/2\xi)^2\right] \quad (1.22)$$

where  $\xi^2 = (\tau_0^2 + ik_2 z)/2$ . By rewriting  $\xi = |\xi| \exp[-i\varphi(z)]$ , substituting into (1.28) and simplifying, one can write the field amplitude as

$$A(z, \tau) = A(0) \left[1 + \left(\frac{z}{L_{dis}}\right)^2\right]^{-1/4} \exp\left[i\varphi(z) + i\psi(z, \tau) - \left(\frac{\tau}{\sqrt{2}\tau_{eff}}\right)^2\right] \quad (1.23)$$

where  $\varphi(z) = \frac{1}{2} \tan^{-1}\left(\frac{z}{L_{dis}}\right)$ ,  $\psi(z, \tau) = z\tau^2 / 2\tau_{eff}^2 L_{dis}$ , and  $\tau_{eff}^2 = \tau_0^2 \left[1 + \left(\frac{z}{L_{dis}}\right)^2\right]$

$L_{dis}$  is the dispersion length as define in [1.18(b)]. We see now that the temporal pulse width has now changed to  $\tau_{eff}$ , as a function of the propagation distance through the material. This pulse width spreading is proportional to the GVD coefficient though  $L_{dis}$ . Rewriting (1.23) in the form

$$A(z, \tau) = A(0) \left[1 + \left(\frac{z}{L_{dis}}\right)^2\right]^{-1/4} \exp\left[i\varphi(z) + iC\tau^2 - \left(\frac{\tau}{\sqrt{2}\tau_{eff}}\right)^2\right] \quad (1.24)$$

(1.24) shows that the propagating Gaussian pulse now has a linear chirp

coefficient  $C$  given by  $C = \frac{z}{2\tau_{eff}^2 L_{dis}}$ . The chirp coefficient defines how the phase

of each frequency component develops as it propagates a given length, and is dependent on  $k_2$  and inversely proportional to initial pulse width. Shorter pulses have stronger chirp due to GVD. Figure 1.7 is a pictorial illustration of the effect

of GVD on the temporal profile of an ultrashort pulse. The pulse broadens with time but, from energy conservation, its time-integrated intensity remains constant.

In all practical applications while a making intensity calculation which depends on the pulse-width it is important to estimate the pulse broadening due to the GVD as it propagates through various optical components before actually reaching the sample. Further discussion on this issue is addressed in the next chapter.

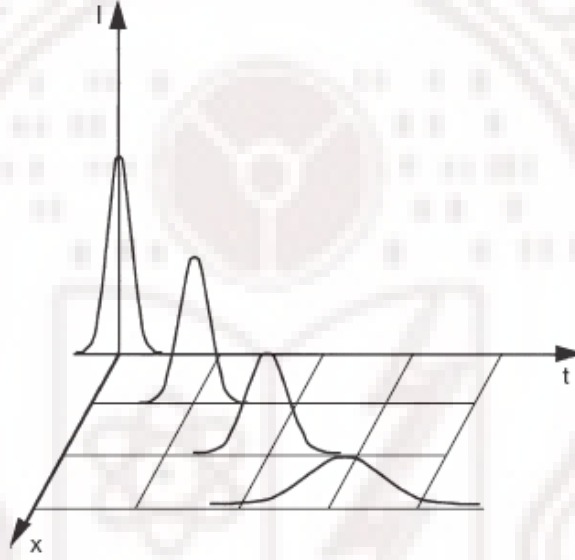


**Fig. 1.7.** Figure showing the effect of GVD on the pulse propagating in a lossless, transparent medium along x-direction (figure adapted from ref. [3])

#### 1.4.1.2 Self-phase modulation

We next consider the case where GVD is negligible and only the nonlinearity on the right hand side of (1.17) exists. This is the case where self-phase modulation is expected to dominate. As discussed in the earlier section, the effect of SPM considering  $n_2$  to be positive, new low frequencies are created in the leading edge of the pulse envelope and new high frequencies are created in the trailing edge. In regions of normal dispersion, the "redder" portions of the pulse have a higher velocity than the "blue" portions, and thus the front of the

pulse moves faster than the back, broadening the pulse in time. In regions of anomalous dispersion, the opposite is true, and the pulse is compressed temporally and becomes shorter. If the pulse is of sufficient intensity, the spectral broadening process of SPM can balance with the temporal compression due to anomalous dispersion and reach an equilibrium state. The resulting pulse is called an *optical soliton*. Another important consequence of SPM in the fs regime is that due to the availability of high peak intensities there is enormous amount of phase modulation taking place that results in super-broadening of the initial pulse spectrally leading to a phenomenon called the ***Supercontinuum generation*** [22]. More discussion regarding SPM induced SCG is presented in chapter 3.

#### 1.4.2 Self-Steepening

As mentioned in the beginning of this section, influence of the factor  $\left(1 + \frac{i}{\omega_0} \frac{\partial}{\partial t}\right)$  in the right hand side of (1) on the nonlinear source term  $\tilde{p}(\bar{r}, t)$  leads to phenomenon termed as *self-steepening*. To study the effect of self-steepening alone the standard procedure is to drop the correction factor  $\frac{i}{\omega_0} \frac{\partial}{\partial t}$  in other parts of the equation. Self-steepening has been first described by De Martini *et al.* [29] for gaussian pulses in a dispersive medium and its effects on the ultrashort pulse propagation were shown by Yang and Shen [30]. Briefly, the factor  $\left(1 + \frac{i}{\omega_0} \frac{\partial}{\partial t}\right)$  in the RHS of (1.23) results in a intensity dependant group index  $n_2^g$ . The intensity dependence of  $n_2^g$  leads to the phenomena of self-steepening as described pictorially below in figure 1.8.

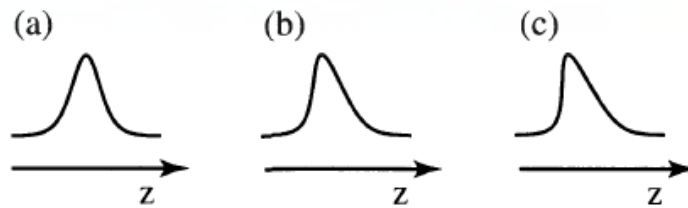


**Fig.1 8:** Self-steepening and optical shock formation (figure adapted from ref. [21])

The incident optical pulse is assumed to have a Gaussian time evolution. After propagation through a nonlinear medium, the pulse displays self-steepening, typically of the trailing edge as shown in figure 1.8(b). If the self-steepening becomes sufficiently pronounced that the intensity changes instantaneously, an optical shock wave is formed as depicted in figure 1.8(c).

### 1.4.3 Space-time coupling:

To study the effect of space-time coupling, we start with an assumption that the pulse is propagating through a dispersionless, linear media. In this scenario the wave equation (3) becomes

$$\left(1 + \frac{i}{\omega_0} \frac{\partial}{\partial \tau}\right)^{-1} \nabla_{\perp}^2 \tilde{A}(\vec{r}, t) + 2ik_0 \frac{\partial}{\partial z'} \tilde{A}(\vec{r}, t) = 0 \quad (1.25)$$

The first term is said to represent space-time coupling because it involves both temporal and spatial derivatives of the field amplitude. For deeper understanding we rewrite (5) as

$$\nabla_{\perp}^2 \tilde{A}(\vec{r}, t) + \left(1 + \frac{i}{\omega_0} \frac{\partial}{\partial \tau}\right) 2ik_0 \frac{\partial}{\partial z'} \tilde{A}(\vec{r}, t) = 0 \quad (1.26)$$

Consider an artificial medium of the form  $\tilde{A}(\vec{r}, t) = a(\vec{r})e^{-i\delta\omega t}$ ; such that the field is monochromatic at frequency  $\omega_0 + \delta\omega$ . Substituting we obtain

$$\nabla_{\perp}^2 a(\vec{r}) + \left(1 + \frac{\delta\omega}{\omega_0}\right) 2ik_0 \frac{\partial}{\partial z'} a(\vec{r}) = 0 \quad (1.27)$$

which can be rewritten as

$$\nabla_{\perp}^2 a(\vec{r}) + 2i(k_0 + \delta k) \frac{\partial}{\partial z'} a(\vec{r}) = 0 \quad (1.28)$$

where  $\delta k = k_0(\delta\omega/\omega_0)$ . This wave thus diffracts as a wave frequency  $\omega_0 + \delta\omega$  rather than a wave of frequency  $\omega_0$ . In general in the case of ultrashort pulse, the

operator  $\left(1 + \frac{i}{\omega_0} \frac{\partial}{\partial t}\right)$  describes the fact that different frequency components of the pulse diffract into different cone angles. Thus, after propagation different frequency components will have different radial dependences [31].

## 1.5 Organization of the thesis

**Chapter 2** is devoted for the discussion on the experimental details of various experiments carried out during the period of the dissertation work. The details of the laser system and its pulse-width characterization are also presented here.

Although all the work described in this dissertation involves the interaction of short laser pulses with transparent materials, several different nonlinear phenomena were studied and many different experimental techniques were used. For this reason, I have tried to make each of the experimental chapters (3 – 7) as “stand alone” as possible, so that they may be read independently.

**Chapter 3** serves as an introductory material to the complex phenomenon of supercontinuum generation (SCG). This was important considering the voluminous literature already available describing this broad area of research. We conclude this chapter discussing various key issues yet to be addressed and our contribution to this exciting field.

**Chapter 4** is dedicated to the investigation of potassium di-hydrogen phosphate (KDP) crystal as a novel and potential candidate for supercontinuum generation. We demonstrate the relevance of the combined effect of second order nonlinearity and intrinsic optical anisotropy of KDP in enhancing the overall bandwidth of the SCG and controlling its overall spectral content.

**Chapter 5** involves the study of depolarization properties of SCG that sets in at high input intensities. We present a systematic study of depolarization of supercontinuum across its spectral range as a function of the femtosecond laser pump intensity for an anisotropic crystalline condensed medium, KDP crystal, and compare our results with commonly used supercontinuum generation

materials namely BK-7 glass (representing isotropic amorphous condensed media) and BaF<sub>2</sub> (isotropic crystalline condensed media).

**Chapter 6** we present experimental results on non collinear four-wave mixing (FWM) at air-dielectric interfaces. We generated FWM signal from the two interfaces of a 1mm thick fused silica slide with air using two 800 nm, 100 fs pump pulses in non-collinear pump-probe type geometry. We attribute the signals observed at the surfaces to the enhanced surface nonlinearities arising from the structural discontinuity and local fields caused by the field discontinuity at the interface. We elaborate on this observation with systematic study of FWM with fused silica slide.

**Chapter 7** discusses our results on the nonlinear optical properties of tetra *tert*-butyl phthalocyanines using the z-scan and degenerate four-wave mixing technique. To the best of our knowledge, ours is the first report on the three photon absorption behavior of phthalocyanines. We observed large off-resonant second hyperpolarizability ( $\gamma$ ) for these molecules with ultrafast nonlinear optical response in the femtosecond domain. Our studies on their figures of merit indicate these molecules possess enormous potential for photonic switching applications.

**Chapter 8** summarizes the results obtained in this dissertation work. Future implications and directions are discussed in brief.

## 1.6 Conclusions

- In this chapter we have discussed in brief some of the important issues related to fs pulses and its relevance to this dissertation work
- Important fundamental characteristics like the Time-Bandwidth product for fs pulses was discussed in detail.
- The field of nonlinear optics is reviewed with more attention given to the second order- and third order nonlinearities and their affects on the ultrashort pulses were discussed. Important NLO phenomenon like second harmonic generation (SHG), parametric processes like sum frequency

generation (SFG) etc, self focusing and self-phase modulation and multiphoton absorption were introduced.

- Starting from the *generalized nonlinear Schrödinger equation* (NLSE) the fate of an ultrashort pulse propagating on an optically transparent media is discussed in detail. Concepts of group velocity dispersion (GVD), self-steepening and space-time focusing is introduced and discussed.

## 1.7 References:

1. M. E. Fermann, A. Galvanauskas, and G. Sucha, *Ultrafast Lasers-Technology and Applications*, Marcel Dekker, Inc., New York (2001) and references therein.
2. J-C. Diels, and W. Rudolf, *Ultrafast laser pulse phenomenon*, 2<sup>nd</sup> Ed. Academic Press, Elsevier (2006).
3. C. Rullière (ed.), *Femtosecond Laser Pulses*, 2<sup>nd</sup> Ed. Springer (2005).
4. U. Keller, *Nature* **424**, 813 (2003) and references therein.
5. T. H. Maiman, *Nature* **187**, 493 (1960)
6. A. E. Seigman, *Lasers*, University Science Books, California (1986).
7. R.W. Hellwarth, “Control of fluorescent pulsations” in *Advances in Quantum Electronics*, J.R. ed., New york: Columbia University Press, 1961, p.334; J. McClung and R.W. Hellwarth, *J. Appl. Phys.* **33**, 828 (1968).
8. M. DiDomenica, *J.Appl. Phys.* **35**, 2870 (1964); L.E. Hanrgrove, R.L. Fork, and M.A. Pollack, *Appl.Phys.Lett.* **5**, 4 (1964), A. Yariv, *J. Appl. Phys.* **36**, 388 (1965).
9. R.L. Fork, B.I. Green and C.V. Shank, *Appl. Phys. Lett.* **38**, 71 (1981); R.L. Fork, C.V. Shank, R. Yen, and C.A. Hirlimann, *IEEE J. Quantum. Electron.* **QE-19**, 500 (1983).
10. U. Morgner, F.X. Kärtner, S.H. Cho, Y. Chen, H.A. Haus, J.G. Fujimoto, and E.P. Ippen, *Opt. Lett.* **24**, 411 (1999); U. Mornger, R. Ell, G. Metzler, T.R. Schibili, F.X. Kärtner, J.G. Fujimoto, H.A. Haus, and E.P. Ippen, *Phys. Rev. Lett.* **86**, 546 (2001); L. Gallman, D.H. Sutter, N. Matuschek, G. Steinmeyer, U. Keller, C. Iaconis, and I.A. Walmsley, *Opt. Lett.* **24**, 1314



11. J. A. Valdmanis, and R. L. Fork, IEEE J. Quantum Electron. **22**, 112 (1986).
12. R. L. Fork, C. H. B. Cruz, P. C. Becker, and C. V. Shank, Opt. Lett. **12**, 483 (1987)
13. D. H. Sutter, G. Steinmeyer, L. Gallmann, N. Matuschek, F. Morier-Genoud, U. Keller, V. Scheuer, G. Angelow, and T. Tschudi, Opt. Lett. **24**, 631 (1999); R. Ell, U. Morgner, F. X. Kärtner, J. G. Fujimoto, E. P. Ippen, V. Scheuer, G. Angelow, T. Tschudi, M. J. Lederer, A. Boiko, and B. Luther-Davies, Opt. Lett. **26**, 373 (2001).
14. B. Schenkel, J. Biegert, U. Keller, C. Vozzi, M. Nisoli, G. Sansone, S. Stagira, S. De Silvestri, and O. Svelto, Opt. Lett. **28**, 1987 (2003).
15. K. Yamane, Z. Zhang, K. Oka, R. Morita, and M. Yamashita, and A. Suguro, Opt. Lett. **28**, 2258 (2003).
16. E. Matsubara, K. Yamane, T. Sekikawa, and M. Yamashita, J. Opt. Soc. Am. B, **24**, 985 (2007).
17. T. Brabec and F. Krausz, Rev. Mod. Phys. **72**, 545 (2000) and references therein; G. Steinmeyer, D. H. Sutter, L. Gallmann, N. Matuschek, U. Keller, Science **286**, 1507 (1999) and references therein; M. Wegener, *Extreme Nonlinear Optics-An Introduction*, Springer (2005); T. Brabec and H. Kapteyn (eds.), *Strong laser field physics*, Springer (2007); G. A. Mourou, C. P. J. Baity, and M. D. Perry, Phys. Today, January, 22 (1998); M. Schnurer, Ch. Spielmann, P. Wobrauschek, C. Streli, N. H. Burnett, C. Kan, K. Ferencz, R. Koppitsch, Z. Cheng, T. Brabec, and F. Krausz, Phys. Rev. Lett. **80**, 3236 (1998); R. Wagner, S.-Y. Chen, A. Maksemchak, and D. Umstadter, Phys. Rev. Lett. **78**, 3125 (1997).
18. M. Born, and E. Wolf, *Principles of Optics*, 7<sup>th</sup> Ed., Cambridge University Press, (reprint, 2003); E. Hecht, *Optics*, 4<sup>th</sup> Ed, Addison Wesley (2001)
19. Y. R. Shen, *The principles of Nonlinear Optics*, Wiley, New York (2002); A. Yariv, *Quantum Electronics*, John Wiley & Sons, New York, USA,



- 1988; P. N. Butcher and D. Cotter, *The Elements of Nonlinear Optics*, Cambridge University Press, Cambridge, 1990;
20. R. L. Sutherland, *Handbook of Nonlinear Optics*, Second Edition, Revised and expanded, New York, NY: Marcel Dekker (2003).
  21. R. W. Boyd, *Nonlinear Optics*, 2<sup>nd</sup> Ed. Academic Press, New York (2003)
  22. R. R. Alfano, *The Supercontinuum laser source*, Springer, Berlin (1989); J. M. Dudley, G. Genty, and S. Coen, , *Rev. Mod. Phys.* **78**, 1135 - 1184 (2006); R. R. Alfano, and S. L. Shapiro, *Phys. Rev. Lett.* **24**, 584–587 (1970); *Phys. Rev. Lett.* **24**, 592-594 (1970); *Phys. Rev. Lett.* **24**, 1219-1222 (1970); P. B. Corkum, C. Rolland, and T. Srinivasan-Rao, *Phys. Rev. Lett.* **57**, 2268 (1986); R. L. Fork, C. V. Shank, C. Hirlimann, R. Yen, and W. J. Tomlinson, *Opt. Lett* **8**, 1 (1983).
  23. M. Göppert-Meyer, *Ann. Phys.* **9**:273 (1931).
  24. G. S. He, L-S. Tan, Q. Zheng, and P. N. Prasad, *Chem. Rev.* **108**, 1245 (2008) and references there in; N. Venkatram L. Giribabu , S. Venugopal Rao and D. N. Rao, *Appl. Phys. B*, **91**, 149 (2008); P. P. Kiran, D. R. Reddy, B. G. Maiya, A. K. Dharmadhikari, G. R. Kumar, and D. N. Rao *Appl. Opt.*, **41** , 7631 (2002); G. S. He, G. C. Xu, P. N. Prasad, B.A. Reinhardt; J.C. Bhatt, R. McKellar, and A.G. Dillard, *Opt. Lett.* **20**, 435 (1995), **20**, 435.
  25. S. Maruo, O. Nakamura, and S. Kawata, *Opt. Lett.* **22**, 132 (1997); B.H. Cumpston, S.P. Ananthavel, S. Barlow, D.L. Dyer, J.E. Ehrlich, L.L. Erskine, A.A. Heikal, S. M. Kuebler, I.-Y. S. Lee, D. McCord-Maughon, J. Qin, H. Röckel, M. Rumi, X.-L. Wu, S.R. Marder, and J. W. Perry, *Nature* **398**, 51(1999); S. Kawata, H.-B. Sun, T. Tanaka, K. Takada, *Nature* **412** , 697 (2001); W. H. Zhou, S. M. Kuebler, K.L. Braun, T.Y. Yu, J.K. Cammack, C.K. Ober, J.W. Perry, and S.R. Marder, *Science* **296**, 1106 (2002).
  26. D. A. Parthenopoulos, P.M. Rentzepis, *Science* **245**, 843 (1989); J. H. Strickler, and W. W. Webb, *Opt. Lett.* **16**, 1780 (1991); A.S. Dvornikov, and P.M. Rentzepis, *Opt. Commun.* **119**, 341 (1995); K.D. Belfield, and K.J. Schafer, *Chem. Mater.* **14**, 3656 (2002).

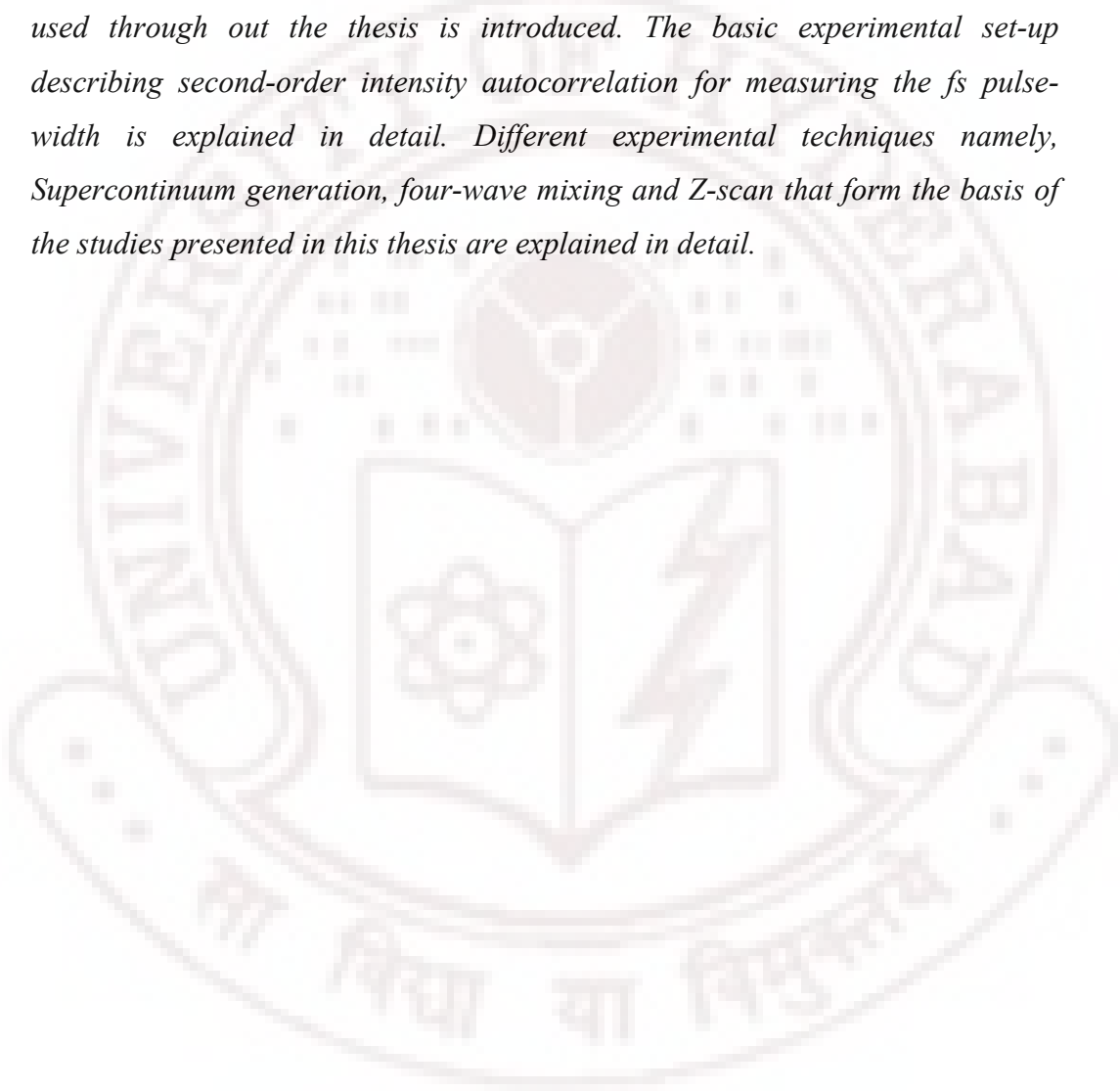
27. M.F. Yanik, H. Cinar, H. N. Cinar, A. Gibby, A. D. Chisholm, Y. Jin, and A. Ben-Yakar, *IEEE Journ. Quantum Electron.*, **12**, 1283 (2006); P.N. Prasad, *Introduction to Biophotonics*, Chapter-12, Wiley-Interscience, New Jersey (2003); A. Karotki, M. Khurana, J. R. Lepock and B. C. Wilson, *Photochem. and Photobio.* **82**, 443 (2006); I.G. Meerovich, V. M. Derkacheva, G.A. Meerovich, N.A. Oborotova, Z.S. Smirnova, A.P. Polozkova, I.Y. Kubasova, E.A. Lukyanets, and A.Y. Baryshnikov, *Proc. of SPIE*, **6427**, 64270X (2007).
28. M.D. Levenson, *Introduction to Nonlinear Laser Spectroscopy*, New York: Academic (1982); R.A. Fischer, *Optical Phase Conjugation*, New York: Academic, USA (1983); H.J. Eichler, P. Gunter, and D.W. Pohl, *Laser-Induced Dynamic Gratings*, Springer-Verlag, Berlin, Heidelberg, Germany (1986); D.M. Pepper, Ed. *Opt. Engg.* **21**, 2 (1982); M. Sheik-Bahae, A.A. Said, T.H. Wei, D.J. Hagan, and E.W. Van Stryland, *IEEE J. Quant. Electron.* **QE-26**, 760 (1990).
29. F.DeMartini, C. H. Townes, T. K. Gustafson, and P. L. Kelley, *Phys. Rev.* **164**, 312 A967).
30. G. Yang, Y. R. Shen: *Opt. Lett.* **9**, 510-512 (1984)
31. J. E. Rothenberg, *Opt. Lett.* **17**, 1340 (1992).

The logo of the University of Hyderabad is a circular emblem. The outer ring contains the text "UNIVERSITY OF HYDERABAD" at the top and the Sanskrit motto "सा विद्या या विमुक्तये" at the bottom. The inner circle features a central sun-like symbol with rays, flanked by a book on the left and a lightning bolt on the right, with a gear-like shape below the book.

## CHAPTER 2

### **Abstract**

*This chapter deals with the important aspects of the different experimental techniques presented in this thesis. The amplified fs laser system used through out the thesis is introduced. The basic experimental set-up describing second-order intensity autocorrelation for measuring the fs pulse-width is explained in detail. Different experimental techniques namely, Supercontinuum generation, four-wave mixing and Z-scan that form the basis of the studies presented in this thesis are explained in detail.*



## Experimental details and techniques

### 2.1 Laser system used:

The laser system used in this dissertation is a commercially available diode-pumped mode-locked Ti:Sapphire Laser purchased from *Spectra Physics Inc.* The laser system consists of (i) oscillator unit producing high repetition rate, nJ, fs pulses, *Mai-Tai* and (ii) regenerative amplifier producing amplified fs pulse, *Spitfire* [1]. The pictorial overview of the fs laser facility present at the laser lab of University of Hyderabad is as shown in figure 2.1.

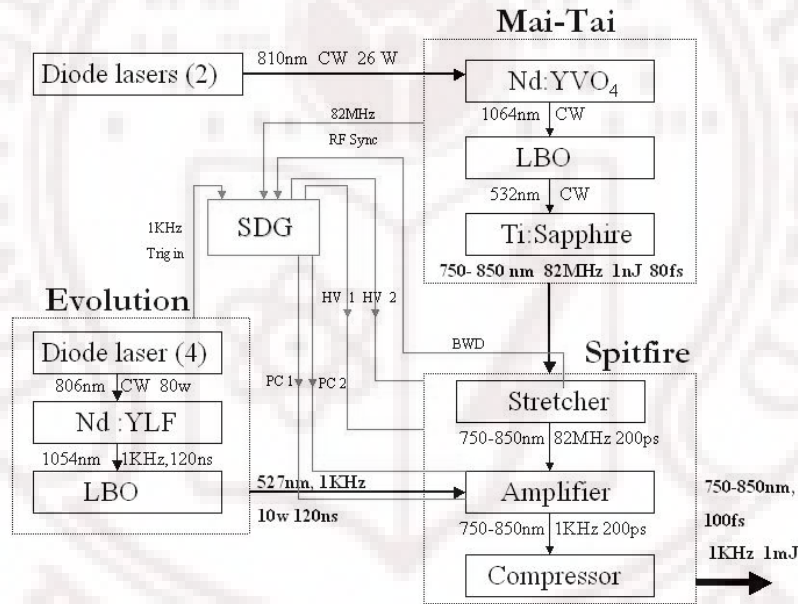


Fig. 2.1: Overview of the fs laser facility

#### 2.1.1 The fs oscillator [Mai-Tai™ System]

The *Mai Tai* comprises of two lasers: a cw diode-pumped laser and a mode-locked Ti: Sapphire pulsed laser. As seen in figure 2.1, the laser head has two chambers, a cw pump chamber and a pulsed output chamber. The cw pump chamber contains a diode-pumped, intracavity, frequency doubled, solid-state Nd: YVO<sub>4</sub> laser giving 532 nm laser output. The pulsed output chamber contains a mode-locked Ti: Sapphire cavity. Because of Ti: Sapphire's broad absorption

band in the blue and green, the 532 nm output of the cw laser is an ideal pump source for the Ti: Sapphire laser. The fluorescence band of Ti: Sapphire medium extends from 600 nm to wavelength greater than 1000 nm making it possible for wide broadband tunable laser. The mode locking is achieved by an acousto-optic modulator (AOM) to ensure reliable mode-locked operation when the laser starts up and provides smooth wavelength tunings. It also allows the laser to operate for extended periods without dropouts or shut-downs associated with pure kerr-lens mode locking. The fs pulse laser can be wavelength tuned using a prism sequence and a slit. The prism sequence provides a region in the cavity where the wavelengths are spatially spread, and the slit is placed in the dispersed beam. By changing the position of the slit in the dispersed beam, the output wavelength is tuned.

The pulse-width tunings characteristics of a Ti: Sapphire laser are generally influenced by three factors: those inherent in the Ti: Sapphire material itself, those from cavity parameters, and to a degree, from the wavelength selection. While we cannot readily modify the Ti: Sapphire material to change pulse width, we can modify the net group velocity dispersion (GVD) of the cavity. The optical components in the laser cavity introduce positive GVD and cause temporal pulse spreading. Further pulse spreading is caused by self-phase modulation (SPM) in the Ti: Sapphire rod, which results from the interaction of the short optical pulse with the nonlinear refractive index. In order to obtain stable, short optical pulses, these effects must be compensated with negative GVD. Because positive GVD in the cavity changes with wavelength, the amount of compensating negative GVD must be varied with wavelength. In *Mai Tai*, prism pairs are used to produce a net variable negative GVD in the cavity. This compensation scheme is fully automated and results in an optimized pulse at any chosen wavelength.

*Mai Tai* delivers a  $\sim 80$  fs, 82 MHz pulse train with pulse energy of 1 nJ. The output spectrum with its peak at 800 nm is as shown in figure 2.2.

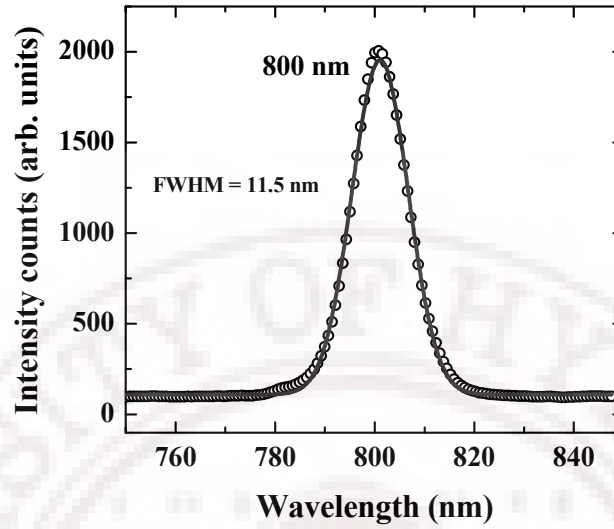
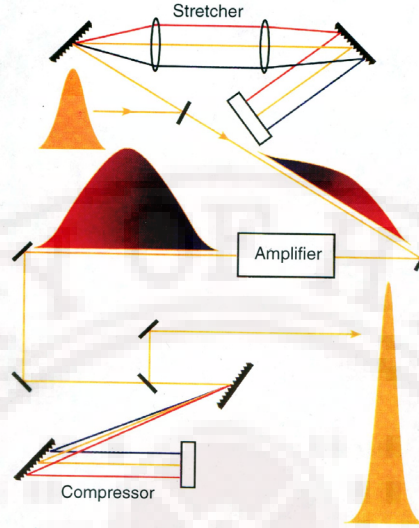


Fig. 2.2: *Mai Tai* output spectrum

### 2.1.2 The fs amplifier [*Spitfire*]

As the output energy of the oscillator is of the order of nJ, we make use of an amplifying unit, *Spitfire*, to amplify the energy without introducing much temporal broadening. *Spitfire* is a regenerative amplifier (RGA) system that employs the conventional chirped pulse amplification (CPA) technique. The general principle of RGA is as follows: (a) Trap seed pulse in optical resonator, (b) Multipass pulse through the active medium (in our case Ti: Sapphire rod) until amplified to desired energy level, and (c) Switch pulse out. But with such short high energy pulses there is always risk of laser induced damage of optics used for the amplification and other effects like self-focusing. To overcome this difficulty *Spitfire* employs Chirped Pulse Amplification (CPA) technique. The general principle of CPA is as follows: (a) pass the fs seed pulses from the output of the oscillator through a stretching mechanism that broadens the pulse to an order to  $10^3$  by introducing chirp using a grating (in most cases); (b) amplify the temporally broadened pulse; and (c) recompress the amplified pulse to its original pulse-width by pass it though a pulse compressor mechanism. The amplification

is done by the RGA cavity described above. Figure 2.3 shows the figurative explanation of the CPA technique used in *Spitfire*



**Fig. 2.3:** CPA technique basic principle

As shown in figure 2.1, the regenerative amplifier consisting of a Ti: Sapphire rod is pumped by the output of *Evolution* which is a 125 ns, 1 kHz rep. rate Nd: YLF laser delivering high power laser pulses of 532 nm. The amplification of the seed pulse from *Mai Tai* is obtained as follows:

1. The seed pulse from *Mai Tai* having a pulse-width of  $\sim 82$  fs is stretched using a combination of grating and mirror to about 250 ps as shown in the top half of the figure 2.1.
2. The temporally stretched pulse is then made to oscillate in the regenerative cavity pumped by the laser pulses of *Evolution* laser head to attain maximum desired energy amplification. The entry and the exit of the seed pulse is achieved by the use of two high-voltage Pockel cells whose delay is adjustable by a Signal Delay generator (SDG) as shown in figure 2.1.
3. The amplified seed pulse exited from the regenerative cavity is then recompressed following the reverse mechanism of stretching procedure to obtain amplified pulses of  $\sim 100$  fs of a maximum of 1mJ average energy at



a repetition rate of 1kHz.. The output of *Spitfire* is of 9 mm diameter with a spectral bandwidth of 9.4 nm at the peak wavelength operation at 800 nm as shown in figure 2.4.

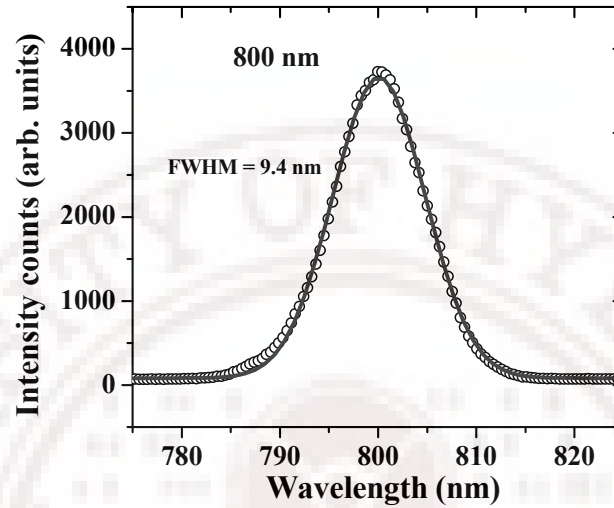


Fig. 2.4: *Spitfire* output spectrum

Table 2.1 summarizes the general and most important characteristics of the fs laser system used through out the present studies in this thesis.

**Table- 2.1:** Summary of laser output characteristics of fs laser system used.

	<i>Mai Tai</i>	<i>Spitfire</i>
Pulse-width	~82 fs	~100 fs
Max output energy	1 nJ	1 mJ
Rep. rate	80 MHz	1kHz
Beam diameter	3 mm	9 mm
Polarization	Horizontal	horizontal

## 2.2 Pulse-width measurement- The autocorrelation technique

An autocorrelator is the most common set-up used for measuring an femtosecond (fs) or picosecond (ps) optical pulse [2]. By using the speed of light to convert optical path lengths into temporal differences, we use the pulse to measure itself. The basic optical configuration is similar to that of a Michelson interferometer. An incoming pulse is split into two pulses of equal intensity and an adjustable optical delay is imparted to one. The two beams are then

recombined within a nonlinear crystal for second harmonic generation (SHG). The efficiency of the SHG resulting from the interaction of the two beams is proportional to the degree of pulse overlap within the crystal. Monitoring the intensity of SHG as a function of delay between the two pulses produces the autocorrelation function directly related to pulse width. Two types of autocorrelation configurations are possible. The first type, known as interferometric collinear autocorrelation as shown in figure 2.5(a), recombines the two beams in a collinear fashion. This configuration results in a autocorrelation signal on top of a constant dc background, since the SH generated by each beam independently is added to the autocorrelation signal. Alternatively, if the beams are displaced from a common optical axis and then recombined in a noncollinear fashion as shown in figure 2.5(b) the background is eliminated because the SHG from the individual beams is separated spatially from the autocorrelation signal. This configuration is called “background-free” and is employed in the pulse-diagnostics of the amplified fs pulses from *Spitfire* used for all the experiments presented in this dissertation. In the subsequent section we explain the details of the autocorrelation in the non-collinear geometry.

### 2.2.1 Experimental details:

While performing the retro-reflection in longer-pulse regime, retro-prisms are usually employed but in the case of fs pulse regime, the retro-prisms are replaced by a pair of mirrors as shown in figure 2.5(b). This is to come over dispersion-effects created within the fs pulses owing to the propagation in the prism-material medium that leads to temporal broadening of the pulses resulting in wrong results. As shown in the figure the incoming beam is first split into two arms and passed through the retro-reflecting arrangement such that the two separated beams follow a parallel path before focusing into a 1mm BBO crystal used for SHG. The retro-reflector on the delay stage is moved with a resolution of 6  $\mu\text{m}$  that corresponds to a minimum temporal resolution of  $\sim 20$  fs. From the experimental configuration the autocorrelation signal (SHG) which is generated as a resultant of temporal and spatial overlap of the two fundamental input beams

is collected into a fast photodiode (FND100) after passing through a SHG filter to cut-off the residual input pulses. Different neutral density filters are used for attenuation to ensure that the photodiode does not get saturated. The photodiode output is fed to a lock-in amplifier (SRS 830) and is finally recorded. The averaged signal is then sent to an interfaced ADC card and then to a computer. The autocorrelation trace is obtained by recording the SHG signal as a function of delay obtained by translation of the stage on which the retro-reflector arrangement is mounted.

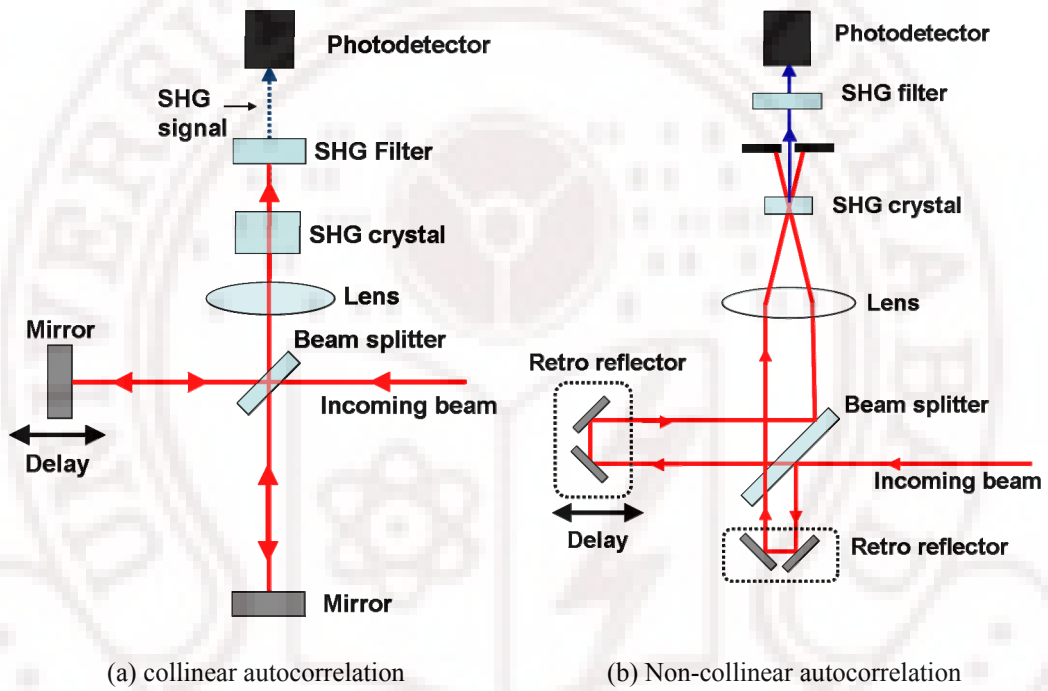


Fig. 2.5: Interferometer autocorrelation set-up

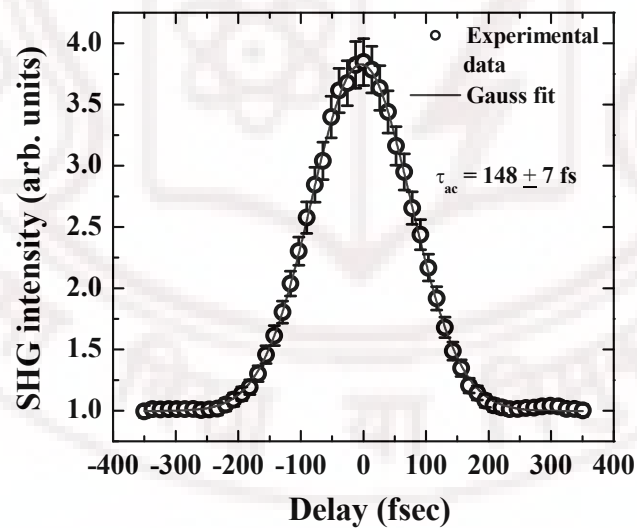
### 2.2.2 Signal interpretation:

In order to determine the actual pulse width from the obtained experimental autocorrelation data, it is necessary to make an assumption about the pulse shape. Table 2.2 shows the relationship between the FWHM of the intensity envelope of the pulse ( $\tau_p$ ) and the FWHM of autocorrelation function of the pulse ( $\tau_{ac}$ ), for several pulse shapes. It also shows the time-bandwidth, for transform-limited pulses as discussed in chapter 1.

**Table 2.2:** Second-order autocorrelation functions and time-bandwidth products for various pulse shape models

Function	$I(\tau)$	$\frac{\tau_p}{\tau_{ac}}$	$\tau_p \Delta\nu$
Gaussian	$I(\tau) = \frac{\exp[-(4 \ln 2)\tau^2]}{\tau_p^2}$	0.707	0.44
Hyperbolic Secant	$I(\tau) = \text{sech}^2 \left( \frac{1.76 \tau}{\Delta\tau_p} \right)$	0.648	0.315
Lorentzian	$I(\tau) = \frac{1}{1 + (4\tau^2 / \Delta\tau_p^2)}$	0.5	0.221

The autocorrelation trace obtained for the amplified fs pulse generated from *Spitfire* is as shown in figure 2.6. The error bars shown corresponds to an experimental error of ~5% which is within the acceptable limits. Similarly we considered a maximum error of ~5% in the x-axis where the source of error is mainly in the movement of the translational stage.

**Fig. 2.6:** Autocorrelation trace obtained for the *Spitfire* amplified fs pulses fitted with Gaussian pulse shape

By performing Gaussian fit to the experimental autocorrelation trace we obtained the FWHM,  $\tau_{ac}$ , to be  $(148 \pm 7)$  fs. From Table-2.2 we have the relation for Gaussian pulse:

$$\frac{\tau_p}{\tau_{ac}} = 0.707 \Rightarrow \tau_p = 0.707\tau_{ac} \Rightarrow \tau_p = (104 \pm 7)$$

Thus the pulse-width obtained from the second-order intensity correlation is  $(104 \pm 7)$  fs. Since the FWHM of the spectral envelope of *Spitfire* as shown in the previous section is  $\Delta\lambda \sim 9.4$  nm with its peak at  $\lambda_0 = 800$  nm.

$$\therefore \tau_p \Delta\nu = \tau_p \frac{c\Delta\lambda}{\lambda_0^2} = 0.458.$$

Thus we have *nearly-transformed limited* pulses assuming Gaussian pulse shape.

### 2.3 Calculating pulse broadening due to GVD:

Because the pulses produced by the Spitfire are  $\sim 100$  fs, as it propagates through optical materials, the pulse get temporally broadened due to the group-velocity dispersion (GVD) discussed in the previous chapter. Thus while a making intensity calculation which depends on the pulse-width it is important to estimate the pulse broadening due to the GVD as it propagates through various optical components before actually reaching the sample. Below is some simple formulae for calculating the effects of GVD and compensation.  $B$  (broadening) is defined as the ratio defined as the ratio of the output pulse-width to the input pulse-width (in terms of fs) i.e.,

$$B = \tau_{out} / \tau_{in} \Rightarrow \tau_{out} = B \times \tau_{in}$$

For a transform-limited gaussian pulse:  $B = \left\{ 1 + \left[ 7.68 \left( k_2 \times \frac{L}{\tau_{in}^2} \right)^2 \right] \right\}^{\frac{1}{2}}$ , where

$k_2$  (in terms of  $\text{fs}^2/\text{cm}$ ) is the second order dispersion coefficient. Table 2.3 gives the values of  $k_2$  for different standard materials at 800 nm.

**Table 2.3:** Dispersion values of different materials at 800 nm

Material	$k_2$ ( fs <sup>2</sup> /cm)
Fused silica	300
BK-7 glass	450
Ti: Sapphire	580
KDP crystal	25 ( <i>o</i> – ray); 38 ( <i>e</i> – ray)
SF-10	1590

## 2.4 Details of the Experiments presented in the dissertation:

### 2.4.1 Supercontinuum generation:

In a typical SCG experiment [3], the beam is focused into the transparent media under consideration and the generated continuum is detected using a fiber coupled CCD spectrometer (Ocean Optics - SD2000). As shown in figure 2.7, the output of the amplified laser pulses is first passed through a variable aperture to control the input beam diameter. Various neutral density filters are made use to attenuate the input power. It should be noted here that the control over the input power of the incident laser beam is important as from the definition of the critical power of self-focusing ( $P_{cr}$ ) depends only on the input peak power and not on the overall input peak intensity. Upon focusing the incident laser beam of suitable input power into the transparent media supercontinuum is generated as a conical emission. With increase in input power the emission becomes brighter until the media experiences laser induced damage. The laser beam depicted as red line focusing into the media and the supercontinuum output is depicted as yellowish-white conical emission to depict broadband output. The use of a large aperture lens is dual-purpose: (a) to collect all the conical emission and (b) either

collimate the output for further study of SCG properties or focus it onto a screen to record the spectrum with a spectrometer.

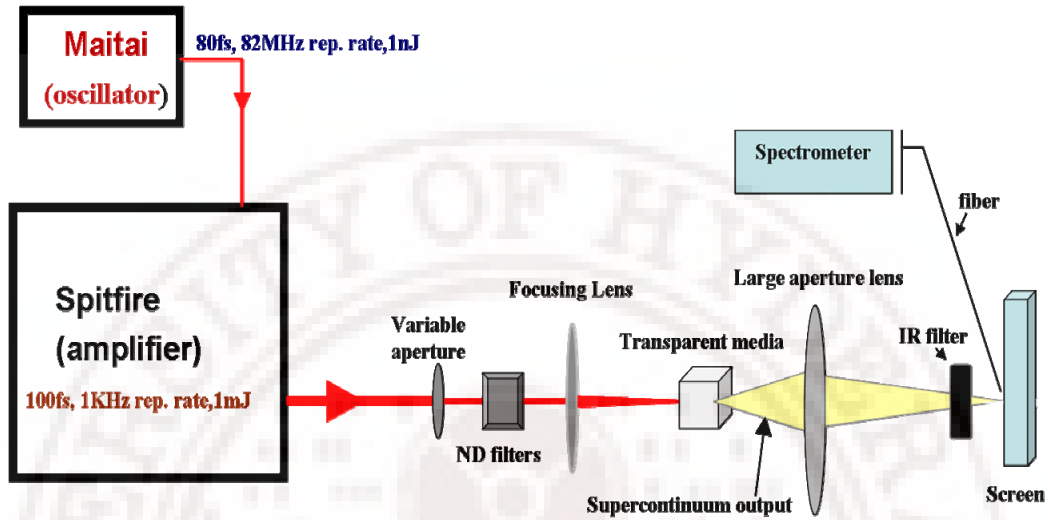


Fig. 2.7. Experimental schematic for supercontinuum generation in transparent bulk media

The spectra of continuum are recorded using a fiber coupled spectrometer (Ocean Optics USB2000) after collimation and suppressing fundamental by an IR filter thus limiting our study of SC to the visible region (400 – 780 nm). To avoid saturation of the detector used in the spectrometer the continuum was focused onto a white board and the scattered light was collected by placing the fiber tip very close to the board. The choice of the screen is crucial as the material of the screen used (for example, white paper) can absorb a part of broadband SCG emission and produce its own fluorescence emission that gets eventually added to the actual SCG spectrum while recording the spectrum with the spectrometer. The detector used in the spectrometer was a silicon charge coupled device that has a range from 350-800 nm with maximum sensitivity at 500 nm. Beyond 750 nm there is a monotonic decrease in the detector sensitivity. The fiber used for collection has excellent transmission for the range 300-900 nm. Neutral density filters with known absorbance spectra in the region was used to collect the continuum spectra obtained at high intensities. Taking into account the absorbance spectra of the filters used, the resultant spectra thus obtained was



corrected. The integrated intensity measurements of the SC are measured by focusing onto a photodetector (FND100). The laser power that was incident on the material under study was measured using a power meter (OPHIR) with a nearly flat and wide spectral response. The same power meter was also used to measure the power of the entire white light continuum after attenuation of the fundamental through an IR filter.

### 2.4.3 Degenerate Four Wave Mixing (DFWM)

A Four Wave Mixing experiment [4] can be considered as an interaction of three optical fields in a medium leading to the generation of fourth field, via third order polarization. The presence of a third-order optical nonlinear susceptibility  $\chi^{(3)}$  leads to the creation of various components of material polarization, giving rise to new optical fields. If the phase-matching condition is fulfilled (i.e. the phase relation between the waves emitted by different parts of the nonlinear medium leads to constructive build up of the resulting wave), new beams of light are created. If the fields are of identical frequencies, the process is called Degenerate Four Wave Mixing and the output beam will have the same frequency. The time resolution of the FWM measurements depends on two parameters. The first is related to the time duration of the laser pulses and the second is related to the coherence time of the laser pulses. DFWM provides information about the magnitude and response of the third-order nonlinearity. In this process, three coherent beams incident on a nonlinear medium generate a fourth beam due to the third order nonlinearity. The strength of this fourth beam is dependent on a coupling constant that is proportional to effective  $\chi^{(3)}$  and hence measurements on observed signal will yield information about the  $\chi^{(3)}$  tensor components of the medium. DFWM can be employed in backward (or generally called the Phase Conjugate), forward or boxcar configurations, with the choice on the experimental conditions and the requirements. Using different polarizations of the three beams it is possible to measure all the independent  $\chi^{(3)}$  tensor components of a material. Though the backward geometry is the most popular



for DFWM measurements, in the case of femtosecond pulses the box-car geometry is preferred.

#### Box-car geometry:

The basic principle of the method is as follows: Two synchronized pulses (called the  $k_1$  and  $k_2$  pulse) propagating in two slightly different directions ( $\mathbf{k}_1, \mathbf{k}_2$ ) interfere in the sample to form a grating by spatially modulating its optical properties. Depending on the experimental conditions, the absorption (amplitude grating), or the refractive index (phase grating) can be modulated. After the laser pulse interaction, the amplitude of the modulation decreases: the dynamics of the modulation (i.e. the grating) will depend on the population lifetime (for amplitude grating) and/or the dynamics of the changes in the refractive index (for phase grating). A third beam,  $k_3$ , propagating in direction  $\mathbf{k}_3$ , is sent into the sample and is diffracted by the grating in directions  $\mathbf{k}_4$ , which satisfies the conservation of momentum:  $\mathbf{k}_4 = \mathbf{k}_3 - \mathbf{k}_2 + \mathbf{k}_1$ .

The experimental schematic of the DFWM set-up used in our studies is as shown in the figure 2.8. Since all the pumps are in same plane, the three beam form three corners of the square and the signal is seen at the fourth corner of the square. The delays of beams 2 and 3 could be varied using the stepper motor. Observing and optimizing the diffracted signals, in both horizontal and vertical directions, ensured the zero delay of different beams. The signal(s) obtained are spatially filtered before being fed to the fast PD to lock-in amplifier and to ADC which finally gets recorded in the computer. In the set-up a lens of focal length 400mm ( $\phi=50\text{mm}$ ) is used to focus the three beams into the sample. For the relative measurements of  $\chi^{(3)}$  of the samples under study we used pure  $\text{CCl}_4$  solvent in case of samples in solution and an optically polished fused silica slide for solid samples. Other details related to the specific experiments carried out in the thesis work are explained in the subsequent chapters appropriately.

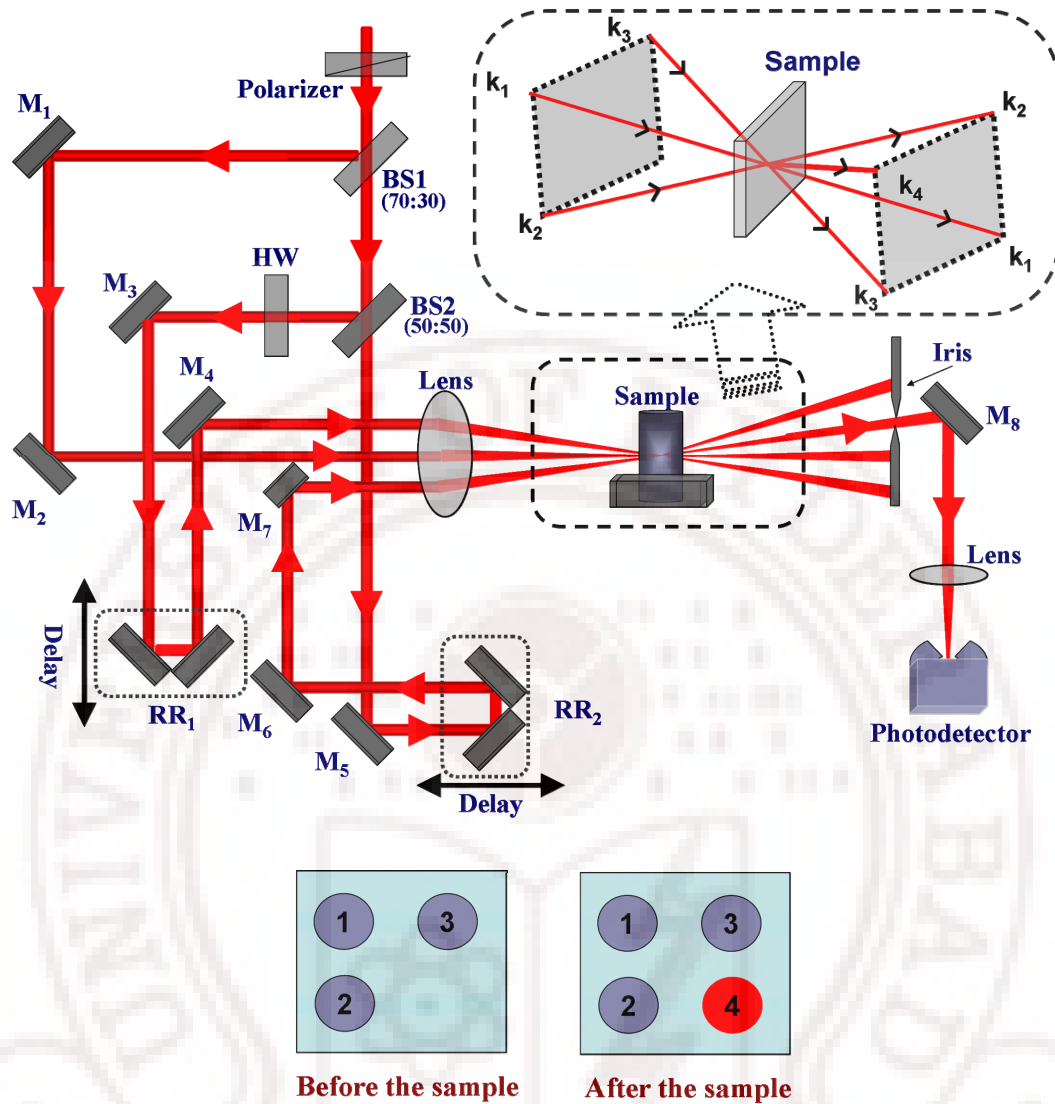


**Fig. 2.8.** Experimental schematic for femtosecond Degenerate Four wave mixing set-up in box-car configuration. The inset shows the wave-vector representation of the geometry of the DFWM experiment. Beams 1-3 are coincident on the sample. The resultant fourth beam is the DFWM signal that occurs because of the interaction  $\mathbf{k}_4 = \mathbf{k}_3 - \mathbf{k}_2 + \mathbf{k}_1$ . The lower panel of the figure shows formation of the fourth beam at the vacant corner of the box formed by the interacting three waves.

The time-resolved DFWM profiles were obtained by delaying beam 3 with respect to the other two beams with a time resolution of  $\sim 33$  fs. Since we used 100 fs input pulses we used  $\text{CCl}_4$  solvent taken in a 1 mm cuvette as a standard sample for relative studies.  $\text{CCl}_4$  is known to show only the electronic response ( $\sim$  few fs) and thus the time-resolved signal obtained can be treated as an autocorrelation trace of the input fundamental pulses. Autocorrelation trace for

$\text{CCl}_4$  is shown in figure 2.9. Open circles are the experimental data and the solid line is the fit assuming the Gaussian profile of the pulse and has the FWHM  $\sim 145$  fs similar to the FWHM of the autocorrelation trace obtained earlier with second order intensity correlation.

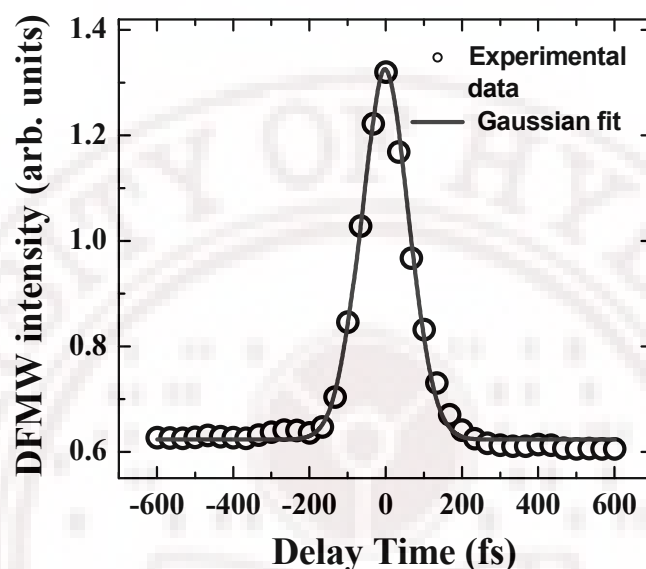


Fig. 2.9: Autocorrelation trace of  $\text{CCl}_4$

#### Non-collinear two beam geometry:

The schematic of a non-collinear two beam four-wave mixing (FWM) is as shown in figure 2.10. As shown in the figure the fundamental beam is split into two beams of almost equal intensity and they are brought back to form parallel beams before focusing into the sample. The FWM geometry is such that if the pump beams are represented by the wave vectors  $\mathbf{k}_1$  and  $\mathbf{k}_2$ , the generated phase matched FWM signals are at  $2\mathbf{k}_1 + \mathbf{k}_2$  and  $\mathbf{k}_1 + 2\mathbf{k}_2$  respectively, and appear well separated from the fundamentals  $\mathbf{k}_1$  and  $\mathbf{k}_2$ . As denoted in the figure the FWM signals do not have the same frequency as that of the fundamental and hence this geometry is called non-degenerate four-wave mixing. A more detailed analysis and the utility of this geometry is presented in the studies presented in chapter-6.

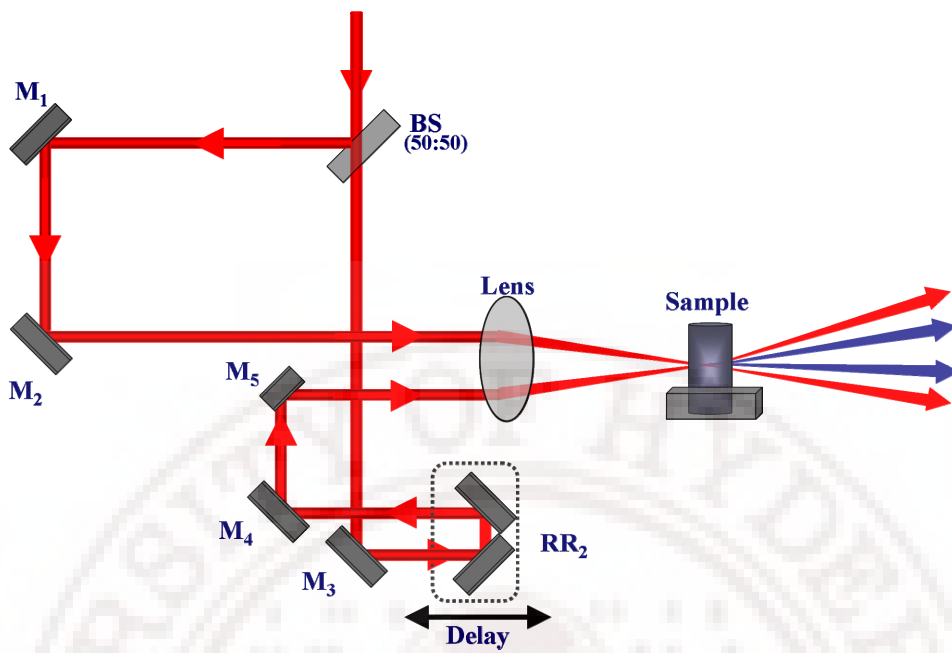


Fig.2.10: Schematic of a femtosecond non-collinear two beam four wave mixing set-up

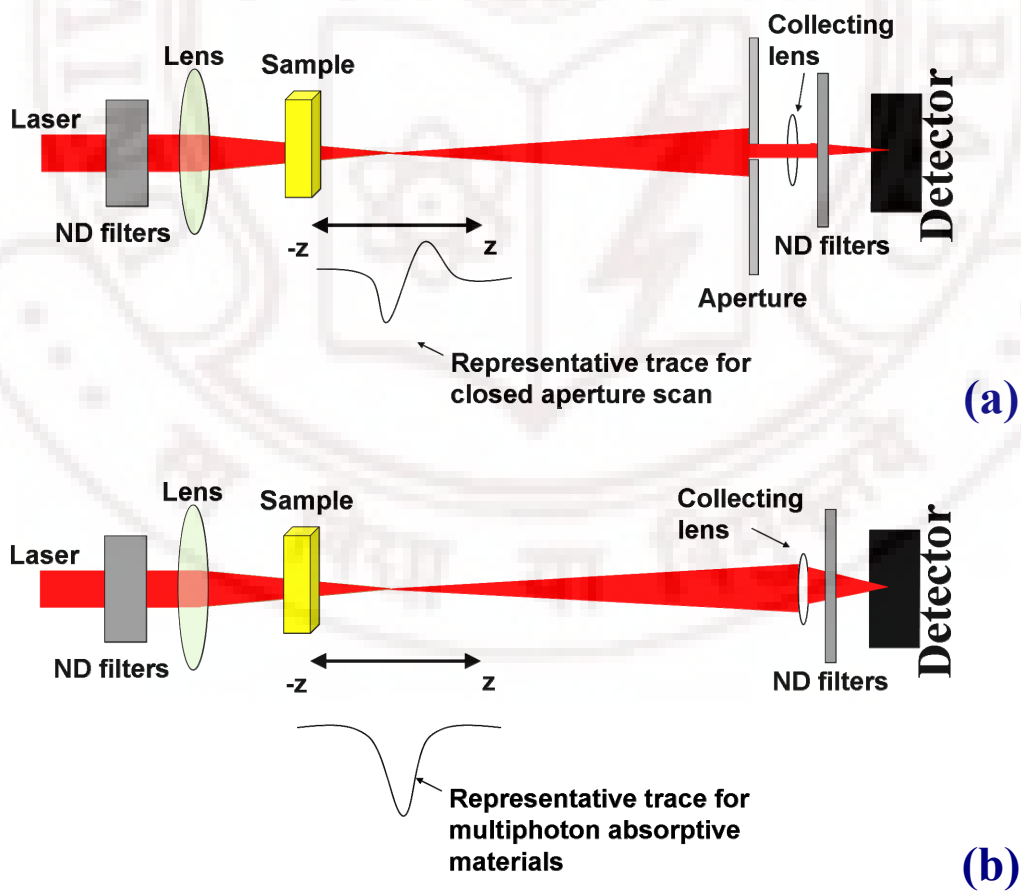


Fig.2.11: Schematic of a femtosecond z-scan set. (a) closed aperture; (b) open aperture

#### 2.4.4 Z-scan

The Z-scan technique is a single beam technique, which allows the determination of the real and imaginary parts of the third order susceptibility [5]. This technique is a simple, sensitive, single beam method that uses the principle of spatial beam distortion to measure both the sign and the magnitude of refractive nonlinearities of optical materials. The experiment uses a Gaussian beam from a laser in tight focus geometry to measure the transmittance of a nonlinear medium through a finite aperture in the far field as a function of the sample position  $Z$ , from the focal plane. In addition to this, the sample transmittance without an aperture is also measured to extract complementary information about the absorptive nonlinearities of the sample.

##### Closed-aperture Z-scan for sign and refractive nonlinearity

Consider, for instance, a material with a negative nonlinear refraction and of thickness smaller than the diffraction length ( $\pi\omega_0^2/\lambda$ ) of the focused beam being positioned at various positions along the  $Z$ -axis as shown in figure 2.11(a). This situation can be regarded as treating the sample as a thin lens of variable focal length due to the change in the refractive index at each position ( $n = n_0 + n_2 I$ ). When the sample is far from the focus and closer to the lens, the irradiance is low and the transmittance characteristics are linear. Hence the transmittance through the aperture is fairly constant in this region. As the sample is moved closer to the focus, the irradiance increases inducing a negative lensing effect. A negative lens before the focus tends to collimate the beam. This causes the beam narrowing leading to an increase in the measured transmittance at the aperture. A negative lens after the focus tends to diverge the beam resulting in the decrease of transmittance. As the sample is moved far away from the focus, the transmittance becomes linear in  $Z$  as the irradiance becomes low again. Thus the curve for  $Z$  versus transmittance has a peak followed by a valley for a negative refractive nonlinearity. The curve for a positive refractive nonlinearity will give rise to the opposite effect, i.e. a valley followed by a peak.

### Open-aperture Z-scan for absorptive nonlinearity

In the above discussion a purely refractive nonlinearity was considered assuming that absorptive nonlinearities are absent. The presence of multi-photon (two or more) absorption suppresses the peak and enhances the valley, while saturation of absorption produces the opposite effect. The sensitivity of the experiment to refractive nonlinearities is entirely due to the aperture. The removal of the aperture will make the Z-scan sensitive to absorptive nonlinearities alone. Thus by doing the Z-scan with and without aperture both the refractive and absorptive nonlinearities of the sample can be studied. The schematic of an open aperture Z-scan is as shown in figure 2.11(b). Spatially filtered input beam is focused using a lens. In the case of fs pulse excitation we used an achromatic doublet of focal length 120 mm. Usage of achromatic doublet for focusing the fs pulses is essential to overcome the chromatic aberration at the focus owing to the large bandwidth of the input spectrum when compared to ns or ps pulses. The sample is scanned across the focus using a stepper motor controlled by PC. The transmitted light is then collected using another lens (large area) of  $f \sim 100$  mm and fast photodiode (FND100). Different neutral density filters are used for attenuation to ensure that the photodiode does not get saturated. The photodiode output is fed to a lock-in amplifier or a boxcar averager/gated integrator and is finally recorded. The averaged signal is then sent to an interfaced ADC card and then to a computer.

## 2.5 References

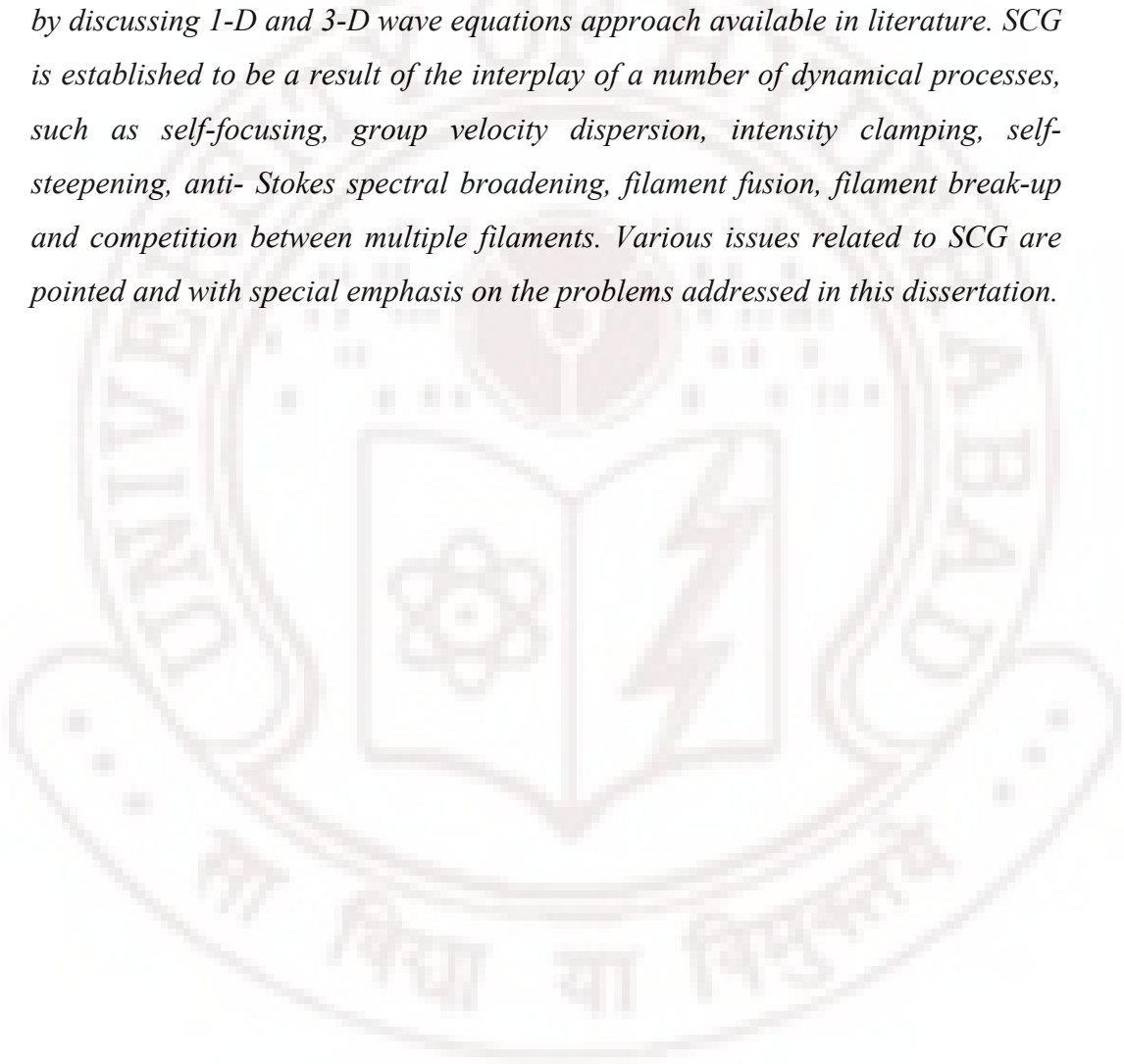
1. Spectra-Physics Inc. operation manuals for *Mai-Tai<sup>TM</sup>* and *Spitfire<sup>TM</sup>*.
2. J-C. Diels, and W. Rudolf, *Ultrafast laser pulse phenomenon*, 2<sup>nd</sup> Ed. Academic Press, Elsevier (2006).
3. R. R. Alfano, *The Supercontinuum laser source*, Springer, Berlin (1989)
4. R. L. Sutherland, *Handbook of Nonlinear Optics*, Second Edition, Revised and expanded, New York, NY: Marcel Dekker (2003).
5. M. Sheik-Bahae, A.A. Said, T.H. Wei, D.J. Hagan, and E.W. Van Stryland, *IEEE J. Quant. Electron.* **QE-26**, 760 (1990).

The logo of the University of Hyderabad is a circular emblem. The outer ring contains the text "UNIVERSITY OF HYDERABAD" at the top and the Sanskrit motto "सा विद्या या विमुक्तये" at the bottom. The inner circle features a central sun-like symbol with rays, flanked by a stylized atom on the left and a lightning bolt on the right, all set against a background of a grid of dots.

# CHAPTER 3

### Abstract

*In this chapter, the phenomenon of supercontinuum generation (SCG) is introduced. SCG in different transparent media at high input intensity is shown. Various mechanisms leading to SCG is discussed from a theoretical perspective by discussing 1-D and 3-D wave equations approach available in literature. SCG is established to be a result of the interplay of a number of dynamical processes, such as self-focusing, group velocity dispersion, intensity clamping, self-steepening, anti-Stokes spectral broadening, filament fusion, filament break-up and competition between multiple filaments. Various issues related to SCG are pointed and with special emphasis on the problems addressed in this dissertation.*





# Supercontinuum generation in transparent media

## 3.1. Introduction and literature review:

The propagation of short pulses of intense laser light through an optical medium can lead to considerable temporal and spatial broadening that becomes mapped, in the frequency domain, into spectral broadening [1]. When the incident laser pulse is ultrashort, of femtosecond duration, the spectral broadening manifests itself in light that emerges out of the medium as a white disk surrounded by a distinct, concentric, rainbow-like pattern that is referred to as the conical emission; the central, low-divergence part of the output beam is referred to as the “white-light continuum” or “supercontinuum”. This self-transformation of the pulse-shape and spectral broadening are the result of strong nonlinear-optical interaction of the light field with the medium, which takes place in the conditions of high localization of the radiation both in space and time. In bulk media the localization of the light field is achieved due to geometrical focusing, self-focusing, or temporal compression of the radiation. Thus, when a high-intensity ultrashort pulse is focused into a transparent medium, a white-light continuum ranging from ultraviolet to infrared is generated.

In the first observation of SC generation, Alfano and Shapiro [2] reported the generation of a white light spectrum covering the entire visible range from 400 to 700 nm after propagating 5 mJ picosecond pulses at 530 nm in bulk BK7 glass. Shortly afterward, similar results were reported independently by Bondarenko et al. [3]. It is important to note that the nonlinear spectral broadening of laser light was not completely new at the time, having been observed earlier by Stoicheff [4]. Indeed, Jones and Stoicheff [5] had even applied a relatively narrow “continuum” of light in what was the first inverse Raman spectroscopy measurement. Spectral broadening had also been reported in CS<sub>2</sub> [6] and correctly interpreted in terms of the nonlinear process of self-phase

modulation (SPM) [7]. What made the experiment of Alfano and Shapiro [2] so exciting was the sheer extent of the spectral width of the generated light, more than 10 times wider than anything previously reported. Interestingly, the authors do not particularly emphasize this aspect in their publication. Their work is actually dedicated to the first identification of nonresonant four-photon coupling, i.e., four-wave mixing. The term “supercontinuum” was introduced later by Manassah *et al.*, [8, 9]. In the meantime, the phenomenon of SC generation was referred to as superbroadening [3, 10], anomalous frequency broadening [10, 11] or white-light continuum [12].

Various nonlinear processes were established to be responsible for continuum generation. Most important ones are self-, induced- and cross-phase modulation and four-photon parametric generation. Whenever an intense laser pulse propagates through a medium, it changes the refractive index, which in turn changes the phase, amplitude, and frequency of the incident laser pulse. A phase change can cause a frequency sweep within the pulse envelope. This process has been called *self-phase modulation (SPM)* [2]. Nondegenerate *four-photon parametric generation (FPPG)* usually occurs simultaneously with the SPM process [2]. Photons at the laser frequency parametrically generate photons to be emitted at Stokes and anti-Stokes frequencies in an angular pattern due to the required phase-matching condition. When a coherent vibrational mode is excited by a laser, stimulated Raman scattering (SRS) occurs. SRS is an important process that competes and couples with SPM. The interference between SRS and XPM causes a change in the emission spectrum resulting in *stimulated Raman scattering cross-phase modulation (SPR-XPM)* [14]. Spectral broadening of ultrashort-pulse propagation in a nonlinear medium was calculated more exactly by solving three coupled nonlinear wave equation by Yang *et. al* [15] that included the effects of four-wave mixing and pulse deformation on phase modulation. The results yielded asymmetric Stokes-anti-stokes broadening in the fair agreement with the experimental observation. A process similar to SRS-XPM occurs when an intense laser pulse propagates through a medium possessing a large second-order  $\chi^{(2)}$  and third-order  $\chi^{(3)}$  susceptibility. Both second harmonic

generation (SHG) and SPM alters the emission spectrum and is called *second harmonic generation cross-phase modulation (SHG-XPM)* [16]. A process closely related to XPM, called *induced phase modulation (IPM)* [17], occurs when a weak pulse at a different frequency propagates through a dispersive medium whose index of refraction is changed by an intense laser pulse. The phase of the weak optical field can be modulated by the time variation of the index of refraction originating from the primary intense pulse. Apart from this the ionization-enhanced SPM also contributes to the overall spectral bandwidth [18, 19]. However, the primary process responsible for these changes is self-focusing, which plays the role of the initiator of the sequence of processes that lead to white light generation.

### 3.1.1. The critical power for self-focusing ( $P_{cr}$ ):

Experiments have shown that the power threshold for continuum generation coincides with the calculated critical power for self-focusing, in line, with the proposal made by Bloembergen [12] to explain white light generation obtained using picosecond pulses. The critical power for self-focusing given by [20]:

$$P_{cr} = 3.77 \lambda_o^2 / 8 \pi n_o n_2 \quad (3.1)$$

When the laser power incident on a medium exceeds  $P_{cr}$  a catastrophic collapse of laser energy occurs at a finite distance. The linear and nonlinear refractive indices of the medium are denoted by  $n_o$  and  $n_2$  respectively, and  $\lambda_o$  is the wavelength of the laser in vacuum. In this model, self-focusing is topped by avalanche ionization; the appearance of free electrons that enhances SPM and gives rise to the continuum. For femtosecond continuum generation, a similar mechanism can be envisaged in condensed media. In this case the important mechanism for free-electron generation (in other words plasma generation) is multiphoton ionization (MPI) [21, 22].

Self-focusing overcomes diffraction and leads to collapse only if the input peak power  $P_{in}$  exceeds a critical threshold [20]. While, the nonlinear refractive

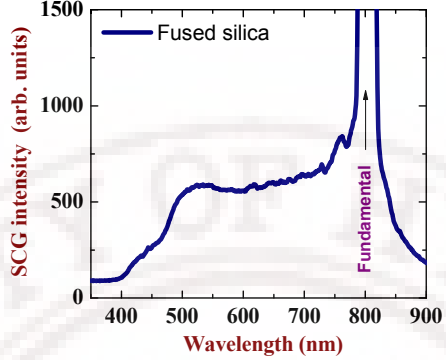
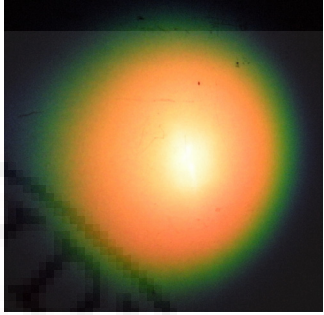
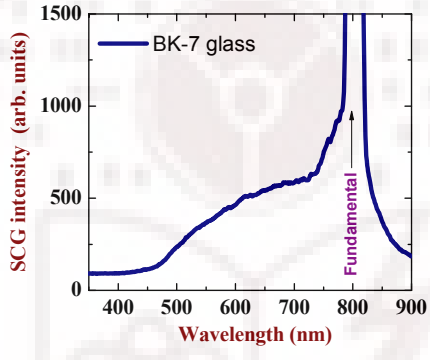
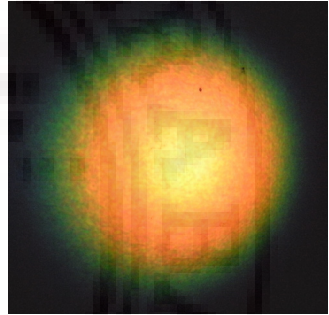
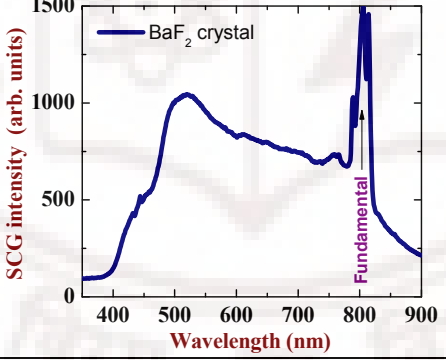
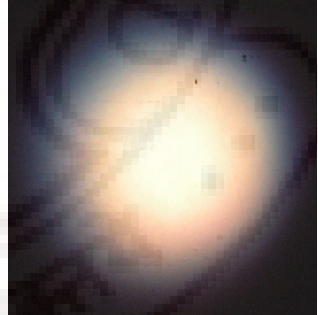
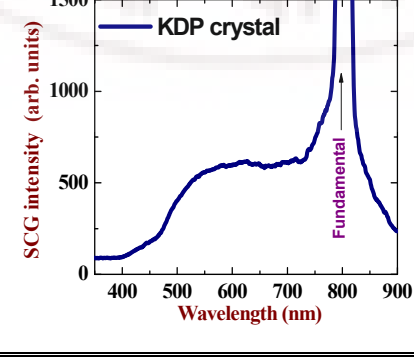
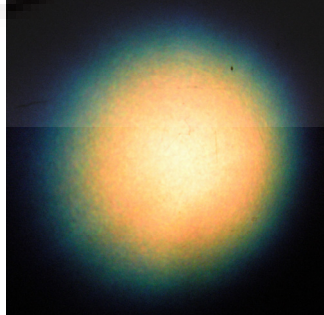
index ( $n_2$ ) acts against diffraction and tends to focus the beam on itself the multiphoton absorption limits the intensity. The ensuing ionization of the atmosphere reduces the local refraction index of the medium and leads to beam defocusing. For a given medium, the focusing and defocusing of the beam counter-balance each other when the input intensity  $P_{in} \sim 10 P_{cr}$  which results in the formation of the well known phenomenon termed as **filamentation**. At pulse powers well above the threshold the beam is observed to fragment and form multiple self-focused whitelight filaments. These filaments form as a result of aberrations on the beam's spatial profile therefore the spatial distribution is inherently random; the temporal distribution however exhibits a cone-shaped distribution for a Gaussian input beam. This cone-shaped pattern is due to the center of the pulse having a higher local intensity than the periphery and since self-focusing is an intensity dependent effect this means that the filaments originating from the center of the beam will form at shorter distances.

### 3.2 SCG in different media

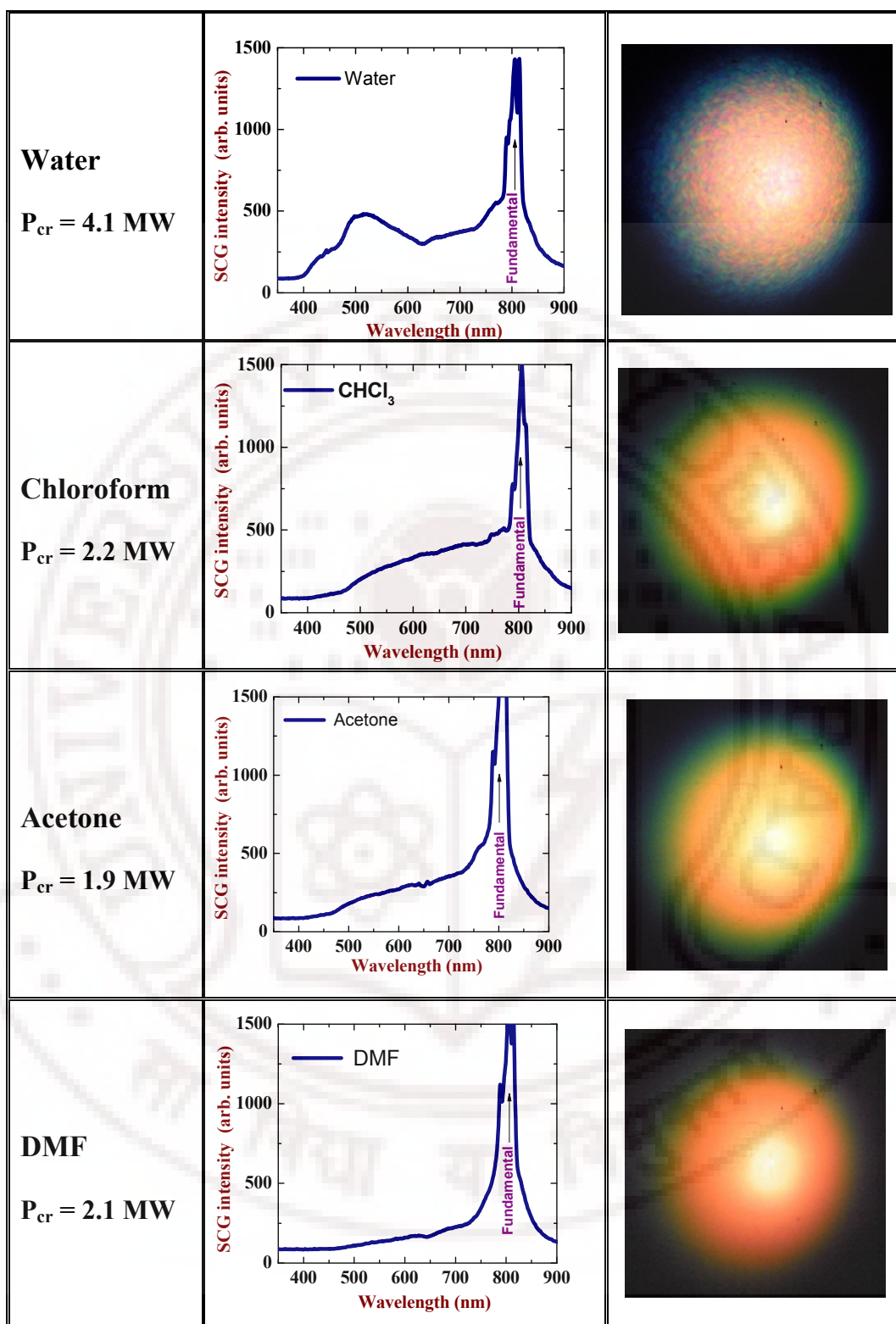
#### 3.2.1. SCG spectra in different media

The SCG spectra of different media were recorded by following procedure explained in the previous chapter. Table 3.1 shows the SCG spectrum and the corresponding snapshot of the SCG for both condensed solids and liquid media showing the universal nature of SC formation in transparent media. All the SCG studies showed in this section were done at an input peak power of 2.1 GW ( $P_{average} = 210$  mW) that corresponds to  $800 P_{cr}$  for BK-7 glass. The peak intensity incident on the front face of the sample is  $\sim 5.2 \times 10^{12}$  W/cm<sup>2</sup>. In the next section we show the input power dependence of SCG in the case of BK-7 glass.

Table: 3.1 SCG spectra in different media

Sample	Spectra	Snapshot of SCG
<b>Fused silica</b> $P_{cr} = 2.2\text{MW}$	 <p>SCG intensity (arb. units)</p> <p>Wavelength (nm)</p> <p>Fundamental</p>	
<b>BK-7 glass</b> $P_{cr} = 2.5\text{ MW}$	 <p>SCG intensity (arb. units)</p> <p>Wavelength (nm)</p> <p>Fundamental</p>	
<b>BaF<sub>2</sub> crystal</b> $P_{cr} = 3.4\text{ MW}$	 <p>SCG intensity (arb. units)</p> <p>Wavelength (nm)</p> <p>Fundamental</p>	
<b>KDP crystal along z-axis</b> $P_{cr} = 2.8\text{ MW}$	 <p>SCG intensity (arb. units)</p> <p>Wavelength (nm)</p> <p>Fundamental</p>	





## 3.2.2. Dependence of SCG spectra with input peak power (eg. BK-7 glass)

Peak power ( $P_{in}$ )	Spectra	Snap shot of SCG
$P_{in} = 27 \text{ MW}$ $\sim 10P_{cr}$		
$P_{in} = 120 \text{ MW}$ $\sim 50 P_{cr}$		
$P_{in} = 250 \text{ MW}$ $\sim 100 P_{cr}$		
$P_{in} = 1.2 \text{ GW}$ $\sim 500 P_{cr}$		

### 3.2.3. Basic observations on SCG in transparent media

1. All the samples considered in the section 3.2.1 exhibited good SCG at high input power.
2. Though pumped with high input peak power the SCG spectra for all the media considered showed no spectral content below 420 nm.
3. Section 3.2.2 shows the intensity power dependence of SCG in a popular SCG media namely, BK-7 glass. The data shows that with increase in input power the SCG spectrum gets broadened.
4. SCG starts from  $P_{in} = 10P_{cr}$
5. At lower input powers there is a interference-sort of pattern observed across the SCG spectra snap-shot in the third column. We attribute this to the interference between the filaments generated as described in the earlier section [23].
6. With increase in input power the central part of the generated SCG became whiter.
7. We observed a conical emission of SCG. The blue-shifted components of the frequency spectrum are formed at the off-axis position in the transverse distribution of the radiation.

In the next section, we discuss briefly the theoretical basis of the observed phenomenon available in the literature.

## 3.3 Mechanisms leading to SCG in bulk media

### 3.3.1. Spectral broadening due to SPM (1-D wave equation model [1]):

In its early days of investigations [1,2] the theoretical basis of spectral broadening was widely understood to be due to the phenomenon of self-phase modulation (SPM). In this section we briefly elaborate on this phenomenon by examining the nonlinear wave equation to describe the self-phase modulation mechanism. We start from the simplified NLSE (Eq. 1.23) described as below:



$$\frac{\partial A(\bar{r}, t)}{\partial z} = \left[ \frac{i}{2k_0} \nabla_{\perp}^2 - 2ik_0 \tilde{D} + \frac{6\pi i \omega_0}{n_0 c} \chi^{(3)}(\omega_0) |\tilde{A}|^2 \right] \tilde{A} \quad (3.2)$$

where  $\tilde{D} = \sum_{n=2}^{\infty} \frac{1}{n} k_n \left( i \frac{\partial}{\partial t} \right)^n$  are dispersion terms.

We define the nonlinear refractive index ( $n_2$ ) related to the third order nonlinear optical susceptibility  $\chi^{(3)}$  as

$$n_2 = \frac{12\pi^2}{n_0^2 c} \chi^{(3)}. \quad (3.3)$$

Replacing the  $\chi^{(3)}$  with  $n_2$  in (2.2) we have

$$\frac{\partial A(\bar{r}, t)}{\partial z} = \left[ \frac{i}{2k_0} \nabla_{\perp}^2 - \frac{i}{2k_0} \tilde{D} + i \frac{\omega_0 n_2}{2c} (\omega_0) |\tilde{A}|^2 \right] \tilde{A} \quad (3.4)$$

The above differential equation can be solved analytically by neglecting the radial dependent and higher order GVD terms ( $n \geq 2$ ) for examining the SPM effect and spectral broadening and defining group velocity as,  $v_g = \frac{1}{k_0^{(1)}}$  to

obtain the electric field envelope solution of given by

$$A(z, \tau) = a(\tau) \exp \left[ i \frac{\omega_0 n_2}{2c} a_0^2 F^2(\tau) z \right]. \quad (3.5)$$

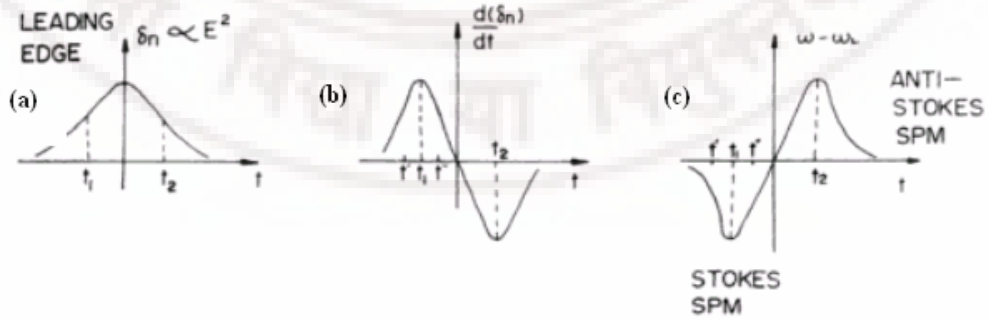


**Fig.3.1:** A simple mechanism for SPM for a non-linear index following the envelope of a symmetrical laser pulse: (a) time-dependent nonlinear index change; (b) time rate of change of index change; (c) time distribution of SPM-shifted frequencies  $\omega(t) - \omega_0$  (figure adapted from [1])

The main physics behind the supercontinuum generation by SPM is contained in Eq. (3.5) and is presented in figure 3.1. As shown in figure 3.1a, the index change becomes time dependent and, therefore, the phase of a pulse propagating in a distorted medium becomes time dependent, resulting in SPM. The electric field is continuously shifting in time (figure 3.1c). From the slowly varying envelope approximation consideration, the pulse duration is much larger than the optical period  $2\pi/\omega_0$ , the electric field at each position  $\tau$  within the pulse has a specific *local* and *instantaneous frequency* at given time given by

$$\omega(\tau) = \omega_0 + \delta\omega(\tau), \quad \text{where} \quad \delta\omega(\tau) = -\frac{\partial\alpha}{\partial\tau} = -\frac{\omega_0}{2c}n_2a_0^2z\frac{\partial F^2(\tau)}{\partial\tau} \quad (3.6)$$

$\delta\omega(\tau)$  is the frequency shift generated at a particular time location  $\tau$  within the pulse shape. This frequency shift is proportional to the derivative of the pulse envelope, which corresponds to the generation of new frequencies resulting in wider spectra. Figure 3.1 shows the frequency distribution within the pulse shape. The leading edge, the pulse peak, and the trailing edge are red-shifted, non-shifted and blue-shifted, respectively. In most cases, the phase of  $A(z, \tau)$  is large compare with  $\pi$ , and the stationary phase method leads to

$$\Delta\omega(z)_{\max} = \frac{\omega_0}{2c}n_2a_0^2\left[\frac{\partial F^2}{\partial\tau}\Big|_{\tau_1} - \frac{\partial F^2}{\partial\tau}\Big|_{\tau_2}\right]z \quad (3.7)$$

where  $\Delta\omega(z)_{\max}$  is the maximum frequency spread,  $\tau_1$  and  $\tau_2$  are the pulse envelope inflections points. An estimate of the modulation frequency  $\Delta\omega(z)_{\max}$  was made by Alfano *et al.* [24] for gaussian pulses of 5 ps pulse duration and obtained an analytical estimation of  $\Delta\omega_{\max} = \frac{\omega_0 n_2 a_0^2 z}{c\tau_0}$ .

The maximum frequency shift indicates the following salient features:

- The frequency extent is inversely proportional to the pumping pulse duration. The shorter the incoming pulse, the greater the frequency extent.

- The spectral broadening is proportional to  $n_2$ . The SCG can be enhanced by increasing the nonlinear refractive index.
- The spectral broadening is linearly proportional to amplitude  $a_0^2$ . Therefore, multiple-excitation laser beams of different wavelengths may be used to increase SCG. This leads to the basic principle of IPM and XPM.

### 3.3.2. Limitations of 1-D wave equation model:

#### 3.3.2.1 General assumptions considered for the 1-D modeling:

Despite the logical explanation for creation of new frequencies in SCG there are a few other important issues that the SPM theory failed to explain. In particular, the observed experimental SCG spectra were asymmetric and the SPM predicts symmetric broadening. Also the 1-D modeling assumes, (a) linearly polarized electric field, (b) homogeneous radial fields, (c) slowly varying envelope, (d) isotropic and nonmagnetic medium, (e) negative Raman Effect, (f) frequency-independent  $\chi^{(3)}$  and (g) neglect of GVD, absorption, self-steepening, and self-frequency shift. In most of the practical cases encountered in experimental conditions the above assumptions fail and this forms a serious limitation to the theoretical modeling. To take this modeling a step further Yang *et al.* [15] calculated more exactly by solving three 1-D nonlinear wave equation that included the effects of four-wave mixing, self-steepening and pulse deformation on phase modulation into the modeling and could explain the asymmetric Stokes-anti-Stokes broadening in fair agreement with the experimental observation. Moreover, GVD always exists in any medium and the effects of GVD should also be considered in the modeling. Apart from all these factors, the properties of the media generating SCG was never considered which also plays an important role in the generation of SC. In the next section we discuss some important issues that deal with the material dependence of SCG.

### 3.3.2.2 Material dependence of SCG:

From the investigations of SCG and self-focusing in transparent condensed media by Brodier *et. al.*, [25], an intimate connection was established between the two phenomena, as their threshold powers coincide  $P_{th}$  (defined as the peak power at the entrance of the medium) corresponds to the critical power for self-focusing  $P_{cr}$ . The investigation revealed four features of the continuum:

- i. Continuum generation depends on the band gap  $E_{gap}$  of the material. The most striking observation was that continuum generation required  $E_{gap}$  larger than the threshold value  $E_{th}$  gap of 4.7 eV,
- ii. continuum width increased with increasing bandgap (i.e., decreasing Kerr nonlinearity)
- iii. the anti-Stokes wing of the SCG is much larger than Stokes wing

Medium	$E_{gap}$ (eV)	$\Delta\omega_+$ (cm <sup>-1</sup> )	$d_{min}$ (μm)	$F_{max}$ (J/cm <sup>2</sup> )	$E_{loss}$ (%)	$P_{th}$ (MW)
LiF	11.8	19 800	10.8	1.3	13	8.8
CaF <sub>2</sub>	10.2	18 300	10.4	1.0	11	7.4
Water	7.5	14 600	9.8	0.62	4	4.4
D <sub>2</sub> O	7.5	14 600	10.6	0.46	4	3.6
Fused silica	7.5	13 500	10.4	0.57	3	4.3
Propanol	6.2	14 200	9.1	0.57	3	3.3
Methanol	6.2	14 500	10.2	0.54	4	3.9
NaCl	6.2	9000	9.9	0.29	3	2.0
1,4-Dioxane	6.0	10 200	9.3	0.44	3	2.7
Chloroform	5.2	11 200	10.0	0.29	1	2.2
CCl <sub>4</sub>	4.8	10 400	8.7	0.44	2	2.5
C <sub>2</sub> HCl <sub>3</sub>	4.7	950	14.6	0.08	<1	1.2
Benzene	4.5	600	14.0	0.07	<1	0.90
CS <sub>2</sub>	3.3	400	15.6	0.01	<1	0.23
SF-11 Glass	3.3	340	15.6	0.03	3	0.52

TABLE I. Anti-Stokes broadening  $\Delta\omega_+$  and self-focal characteristics measured at  $P = 1.1P_{th}$ : minimum beam diameter  $d_{min}$  (FWHM) ( $\pm 0.5$  mm), maximum fluence  $F_{max}$  ( $\pm 10\%$ ), and energy loss  $E_{loss}$  ( $\pm 1\%$ ).  $P_{th}$  is accurate within  $\pm 20\%$ .  $E_{gap}$  is obtained from the medium's absorption spectrum, which generally exhibits a sharp absorption edge in the UV corresponding to  $E_{gap}$ . (adapted from the results of [25])

SPM theory, which is generally thought to explain the continuum, is not consistent with these features. Thus, a mechanism was proposed that involves free-electron generation in the self-focus by multiphoton excitation; the free

electrons would be responsible for enhancing anti-Stokes broadening and for limiting the beam collapse that is due to self-focusing. The low beam divergence of the continuum was explained in terms of a Kerr-lens effect in the beam periphery. It was shown that this low divergence does not imply the absence of strong self-focusing in continuum generation. Based on simulations of femtosecond pulse propagation in water the numerical results of Kolesik *et al.*, [26] showed that linear chromatic dispersion also played a major role in imposing a limit to supercontinuum broadening.

### 3.3.3. Generalized theoretical formalism for SCG:

Most of the theoretical formalisms to explain SCG before year 2000 were based on the 1-D wave equation modeling with the inclusion of many NLO processes like SPM, self-steepening terms, GVD terms etc. in the wave equation to describe the combined interplay of all the effects. However, a consistent theoretical explanation emerged based on the simulations of full three-dimensional simulations of light propagation by A. L. Gaeta [27] as shown below (from the derivation of Appendix-I [28])

$$\left[ \left( 1 + \frac{i}{\omega_0} \frac{\partial}{\partial \tau} \right)^{-1} \nabla_{\perp}^2 + 2ik_0 \frac{\partial}{\partial z'} + 2k_0 \tilde{D} \right] \tilde{A}(\bar{r}, t) = -\frac{4\pi\omega_0^2}{c^2} \left( 1 + \frac{i}{\omega_0} \frac{\partial}{\partial t} \right)^2 \tilde{p} \quad (3.13)$$

In the simulations the input pulse was considered to be Gaussian in space and time  $A(\bar{r}, z=0, t) = A_0 \exp[-r^2/2\omega_0^2 - t^2/2\tau_p^2]$ . Using the definitions of diffraction length ( $L_{dif}$ ), dispersion length ( $L_{dis}$ ), and nonlinear length ( $L_{NL}$ ) as described earlier in chapter-1, we can rewrite Eq. (3.13) into a more meaningful relation in terms of the normalized amplitude  $u(r, z, t) = A(r, z, t)/A_0$ , as

$$\boxed{\frac{\partial u}{\partial z} = \frac{i}{4} \left( 1 + \frac{i}{\omega_0} \frac{\partial}{\partial \tau} \right)^{-1} \nabla_{\perp}^2 u - i \frac{L_{dif}}{L_{dis}} \frac{\partial^2 u}{\partial \tau^2} + i \left( 1 + \frac{i}{\omega_0} \frac{\partial}{\partial \tau} \right) p_{nl}} \quad (3.14)$$

In the expression for the nonlinear polarization ( $p_{nl}$ ) the effects of the nonlinear refractive index change, multiphoton absorption, and formation of an electron plasma density ( $\rho_e$ ) were included such that

$$p_{nl} = \frac{L_{dif}}{L_{NL}} |u|^2 u - \frac{L_{dif}}{L_{pl}} \left( 1 - \frac{i}{\omega \tau_c} \right) \rho u + i \frac{L_{dif}}{L_{mp}} |u|^{2(m-1)} u \quad (3.15)$$

where  $\tau_c$  is the electron collision time,  $L_{mp} = 1/\beta^{(m)} I_0^{m-1}$  is the  $m$ -photon absorption length,  $\beta^{(m)}$  is the  $m$ -photon absorption coefficient,  $L_{pl} = 2\rho_0/\sigma\omega\tau_c$  is the plasma length,  $\sigma$  is the cross section for inverse bremsstrahlung, and  $\rho = \rho_e/\rho_0$  is the electron density normalized to the total density  $\rho_0 = \beta^{(m)} I_0^m \tau_p / n\hbar\omega$  of electrons that would be produced by the input pulse through multiphoton absorption. The following were the important conclusions from the calculations of Gaeta:

- i. It provides a theoretical model that allows us to investigate the dynamics of self-focusing of femtosecond laser pulses both near and above the point at which the pulse effectively undergoes catastrophic collapse.
- ii. It is shown that, as the pulse approaches the collapse point, a steep edge is formed at the back of the pulse (i.e., an optical “shock wave”) and is accompanied by a large phase jump. The resulting pulse spectrum exhibits a broad blue-shifted pedestal with a sharp cutoff.
- iii. The results show that shock formation due to space-time focusing and self-steepening dictates the collapse dynamics and that the role of multiphoton absorption and plasma formation is simply to halt the collapse at the powers significantly above the threshold for collapse.
- iv. Also the temporal and spectral behavior that produces SCG occurs over a wide range of parameters as long as the input focusing conditions of the beam are such that shock formation can occur before MPA and plasma formation dominates the interaction.
- v. In addition, if the initial focusing conditions are such that the beam is tightly focused into the material such that the linear focusing is



responsible for creating sufficiently high intensities to create a plasma then SCG is also not observed.

After similar numerical (with addition of more NLO effects) and experimental results by other research groups [29] it is now understood that SCG in bulk material is due to the formation of an optical shock at the back of the pump pulses due to space-time focusing and self-steepening, confirming the early ideas of Werncke *et al.* [11]. The role of multiphoton absorption and plasma formation is simply to arrest the collapse of the beam and to prevent the optical breakdown of the material. Self-trapped filaments may or may not form in the process depending on the pulse duration and on the relative strength of chromatic dispersion, self-focusing, and plasma defocusing. This scenario is in agreement with all known observations, including the dependence of SC generation on the band gap of the material [25]. In material with a small band gap, self-focusing is stopped at lower intensities by free-electron defocusing, preventing the formation of a shock.

#### 3.3.4. Role of multiphoton ionization (MPI):

The high laser intensities that are the necessary starting point for supercontinuum generation are initiated by self-focusing collapse of the incident optical pulse within the medium. Such collapse has to be accompanied by a mechanism like multiphoton ionization (MPI) that arrests an intensity catastrophe within the medium. MPI accounts for two arresting mechanisms: (i) a direct energy loss is provided for the collapsing field, and (ii) plasma formation occurs within the medium; the plasma serves to defocus and absorb the increasing intensity. Plasma formation acts as a balance against the self-focusing effect: it limits the beam diameter at the self-focus region and, hence, limits the peak intensity that can be attained within the medium. In air, this “intensity clamping” [30] occurs along a filament at a peak intensity of about  $5 \times 10^{13} \text{ W/cm}^2$  [31]. In general terms, MPI effects, along with plasma defocusing, clamp the maximum value of intensity,  $I_{\text{max}}$  that may be reached by a collapsing pulse. If  $\rho$  denotes the plasma density, it is clear that  $\partial_t \rho$  will be proportional to  $I_{\text{max}}^n$ , where  $n$

denotes the order of the multiphoton process; the value of  $I_{\max}^n$  limits the maximum rate of plasma generation. Prevailing wisdom maintains that the major contribution to the blue side of the supercontinuum is made by plasma-induced effects [25, 32], with the maximum blue-side frequency being directly proportional to  $\partial_r \rho$ . Thus, it is the arrest of the maximum self-focusing intensity by MPI and plasma defocusing effects that largely governs the spectral extent of the supercontinuum that is generated.

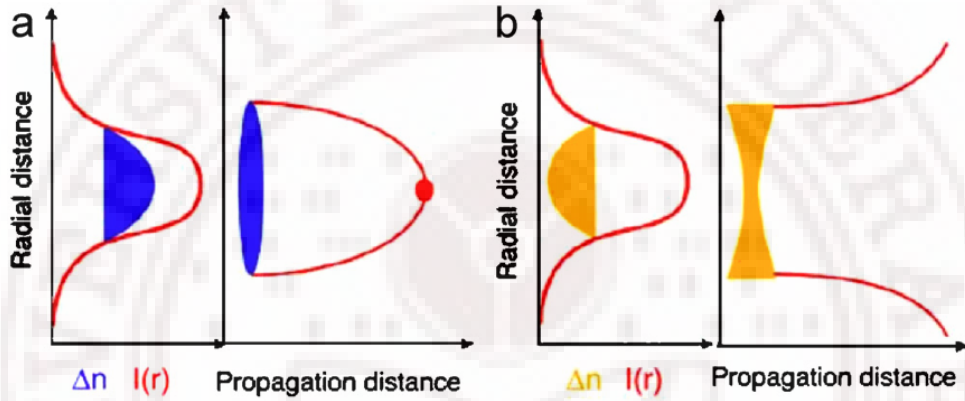


**Fig. 3.** (a) Self-focusing of a beam by optical Kerr effect. The refractive index of the medium depends on the intensity of the laser and acts as a lens by making convergent an initially collimated beam. Self-focusing prevails over diffraction when the power of the beam exceeds a critical power  $P_{\text{cr}}$  ( $P_{\text{cr}} = 3.2\text{GW}$  for air at the wavelength of 800 nm) and leads, in the absence of other nonlinear effects, to the collapse of the beam on itself. (b) Defocusing of the beam by the presence of a plasma. The ionization of the medium initially takes place in the center of the beam, where the intensity is most significant. The creation of under-dense plasma decreases the local index of the medium, which causes beam defocusing. (Figure adapted from [33])

### 3.3.5 Role of spatio-temporal effects (conical emission of SCG):

In the conditions of tight focusing of fs laser pulses into the medium, where  $\chi^{(3)}$  is comparatively low (e.g. in the noble gases), the major contribution to the spectral transformation comes from the free electrons. This phenomenon was studied experimentally in ref [34] and numerically in references [35, 36]. The extension of the blue wing formed after the tight focusing of a 100-fs pulse with the central wavelength of 620 nm into the noble gases varied from  $\approx 15$  nm in 1-atm argon, krypton, and xenon to  $\approx 50$  nm when these gases were at 5-atm pressure. Spectral blue shifting was accompanied by the spatial defocusing of



laser beam and the formation of rings in the trailing part of the pulse [37]. It was found as the result of numerical simulations [36, 38] and registered experimentally [39] that the blue-shifted components of the frequency spectrum are formed at the off-axis position in the transverse distribution of the radiation. A larger frequency shift is generated at positions farther from the propagation axis. Thus, the spectrum of the pulse is transformed not only in the frequency domain but also in the domain of the spatial wave numbers. Numerical simulations of pulse propagation in the conditions of self-focusing and normal group-velocity dispersion [40] also propose that the short-pulse supercontinuum conical emission is the result of four-wave mixing in the medium. According to results of several groups [41] the conical emission is the result of spatio-temporal self-phase modulation of a femtosecond pulse propagating in the conditions of self-focusing and plasma production. The temporal phase gradient  $\partial\varphi/\partial\tau$ , which defines the frequency deviation  $\delta\omega(\tau)$ , is proportional to the time derivative of the electron density:  $\delta\omega(\tau) = \partial\varphi/\partial\tau \approx \partial N_e(\tau)/\partial\tau$ . At the same time, the spatial phase gradient,  $\partial\varphi/\partial r$ , which defines the transverse component of the wave vector  $\delta k_r$ , is proportional to the radial derivative of the electron density:  $\delta k_r = \partial\varphi/\partial r \sim |\partial N_e(r)/\partial r|$ . In the course of nonlinear interaction high spatio-temporal gradients of free-electron density arise simultaneously in space and time. As a result, high-frequency spectral components propagate at a larger angle to the propagation direction.

### 3.3.6 Concluding remarks on SCG in bulk transparent media

- In bulk material, SCG is a highly complex process involving an intricate coupling between spatial and temporal effects.
- The interplay between various NLO processes inside the transparent bulk media gets seemingly random with competition between the various processes.
- The material-bandgap dependence apart from the chromatic dispersion limits the spectral extent in the blue pedestal of the SCG. In case of

800nm amplified input pulses the spectra extent in the high frequency region has a cut off  $\sim 420$  nm for most of the media (see Table-3.1)

- At high input peak powers the interplay results in uncontrollable spectral broadening.
- Overall, the media acts like a black box where the final spectral transformations are mainly due to the various self-action effects of the input fundamental pulse itself and thus the media itself does not offer any control over the spectral modification of the input pulse.

In contrast, SC generation in optical fibers involves purely temporal dynamical processes, with the transverse mode characteristics determined only by linear waveguide properties. This results in a sudden outburst of research interest in the last decade with the most of the current success in envisaging controlled SC generation in core-modified fibers and birefringent fibers, in particular Photonics crystal Fiber (PCFs) [42-44]. The confinement of input pulses inside a fiber core of few microns diameter over long lengths coupled aids long nonlinear interactions resulting in broad spectral broadening even with moderate input energies of few nJ [45]. Broadband SCG which was always associated with femtosecond pulses in bulk media is now envisaged with ps and ns pumping. The recent progress has been tremendous with the demonstration of SCG in PCFs with CW pumping [46]. The use of PCF's as SCG media was first exploited by Ranka *et al.* [42] where they demonstrated broadband SCG spanning from 400 nm to 1600 nm with excitation of unamplified 800 nm, 100fs pulses. Subsequently, several research groups devoted their efforts both theoretical and experimental in understanding the SCG in PCFs [44]. The characteristics of PCFs that have led to such interest relate to their guidance properties that yield single-mode propagation over broad wavelength ranges, their enhanced modal confinement and therefore elevated nonlinearity, and the ability to engineer their group velocity dispersion [47]. The design freedom of PCFs has allowed SC generation to be observed over a much wider range of source parameters than has been possible with bulk media or conventional fibers. SCG in PCFs has subsequently been widely applied in interdisciplinary fields such as optical

coherence tomography, spectroscopy, and, particularly, in optical frequency metrology, leading to the development of a new generation of optical clocks, and has opened up new perspectives to study limits on the drift of fundamental physical constants [48]. The award of one-half of the 2005 Nobel Prize in Physics to Hall and Hänsch, is of course a measure of the tremendous significance and impact this work in precision frequency metrology. The current progress in technology offers turn-key solution to a white-light laser that adapts the SCG from PCF's [49].

### 3.4 Issues on SCG addressed in this dissertation work

With much progress in SCG in both bulk and fiber media; the SCG in PCFs emerges to be useful in most applications simply because it control over the spectral and temporal properties of SCG spectra. With its spectral brightness and high peak intensities SC has found myriads of applications as an ideal broadband ultrafast source. Major applications demonstrated using SCG include femtosecond time resolved spectroscopy, optical pulse compression, optical parametric amplification, optical frequency metrology, two-photon absorption spectroscopy, and biomedical imaging [50]. In spite of voluminous literature available on the generation, understanding and application of SCG in various media, a more detailed scrutiny in this exciting field of research lead us to investigate in more detail the following aspects of SCG:

1. Several experimental studies revealed [25,26] that for a particular medium there is a limit to the spectral extent of the attainable SCG with a high-frequency cutoff insensitive to pulse energy. For condensed media, physical factor such as material band gap and linear chromatic dispersion were found to play a major role in determining the extent of high-frequency cutoff. Strategies to overcome this limitation would be of very great scientific importance.
2. With the general assumption that polarization of the generated SC follows the incident pulse [1], it has been shown that at high input powers the SCG gets depolarized due to the formation of low density plasma [51]. However,

no report till date has ever dealt with the control of polarization properties of the SCG and hence research in this direction is relevant.

3. Neshev *et al.* [52] demonstrated the spatio-spectral control and localization of SCG through nonlinear interaction of spectral components in extended periodic structures. However, there are no other reports that discuss the role of media in exercising any control over SCG. Such a control is essential for fundamental understanding and improved SCG source generation.

In the subsequent two chapters we present our efforts to tackle the above mentioned problems in SCG in transparent bulk media. Since material with material bandgap possesses serious limitation on the high frequency cut-off of the SCG spectra, searching for materials with higher bandgap might not be the only feasible solution. On the other hand it is well known that using nonlinear crystals with high  $\chi^{(2)}$  coefficients, new frequencies can be easily produced by using the second harmonic generation (SHG) and sum frequency generation (SFG). Moreover, the intrinsic anisotropy of these nonlinear quadratic crystals offers intrinsic anisotropy of the nonlinear refractive index  $n_2$  facilitating different  $P_{cr}$  in different directions for the same input power. Recent reports envisage good pulse compression in  $\chi^{(2)}$  media [53]. Thus, all these features could offer control over various media-dependent parameters allowing better control over the spectral and temporal characteristics of SCG. We proceed in this direction and performed studies in a very popular quadratic nonlinear crystal Potassium Dihydrogen Phosphate (KDP) crystal. The obtained results are presented in the next two chapters.

### 3.5 Summary

- The temporal, spatial, and spectral properties of an ultrashort pulse experience modification when it propagates through such media resulting in the generation of a spectrally broad white light termed as Supercontinuum generation (SCG).

- SCG is a consequence of the interplay of several dynamical processes such as self-focusing, group velocity dispersion, intensity clamping, self-steepening, anti-Stokes spectral broadening, filament fusion, filament breakup and competition between multiple filaments.
- Basic theoretical model describing the self-phase modulation as the basic important mechanism for the spectral broadening of input fundamental pulse was presented in brief based on 1-D wave equation.
- A general formalism based on 3-D wave equation based on the theoretical calculations by Gaeta was explained in brief. Theoretical simulations show that (1) as the pulse approaches the collapse point; a steep edge is formed at the back of the pulse (i.e., an optical “shock wave”) and is accompanied by a large phase jump. The resulting pulse spectrum exhibits a broad blue-shifted pedestal with a sharp cutoff; and (2) that shock formation due to space-time focusing and self-steepening dictate the collapse dynamics and the role of multiphoton absorption and plasma formation is simply to halt the collapse at the powers significantly above the threshold for collapse.
- A minimum of 4.7 eV bandgap is essential for obtaining SCG.
- Various issues addressed in this dissertation were discussed.

### 3.6 References

1. R. R. Alfano, *The Supercontinuum laser source*, Springer-Verlag, Berlin (1989).
2. R. R. Alfano, and S. L. Shapiro, Phys. Rev. Lett. **24**, 584–587 (1970); Phys. Rev. Lett. **24**, 592-594 (1970); Phys. Rev. Lett. **24**, 1219-1222 (1970);
3. N. G. Bondarenko, I. V. Eremina, and V. I. Talanov, Pis'ma Zh. Eksp. Teor. Fiz. **12**, 125–128 (1970) [JETP Lett. **12**, 85–87 (1970)].
4. B. P. Stoicheff, Phys. Lett. **7**, 186–188 (1963).
5. W. J. Jones, and B. P. Stoicheff, Phys. Rev. Lett. **13**, 657–659 (1964).
6. R. G. Brewer, Phys. Rev. Lett. **19**, 8–10 (1967).
7. F. Shimizu, Phys. Rev. Lett. **19**, 1097–1100 (1967).

8. J. T. Manassah, P. P. Ho, A. Katz, and R. R. Alfano, *Photonics Spectra* **18**, 53–59. (1984).
9. J. T. Manassah, R. R. Alfano, and M. Mustafa, *Phys. Lett.* **107A**, 305–309 (1985).
10. N. N. Il'ichev, V. V. Korobkin, V. A. Korshunov, A. A. Malyutin, T. G. Okroashvili, and P. P. Pashinin, , *Pis'ma Zh. Eksp. Teor. Fiz.* **15**, 191–194 (1972) [*JETP Lett.* **15**, 133–135 (1972)]
11. W. Werncke, A. Lau, M. Pfeiffer, K. Lenz, H.-J. Weigmann, and C. D. Thuy, *Opt. Commun.* **4**, 413–415 (1972).
12. N. Bloembergen, *Opt. Commun.* **8**, 285–288 (1973).
13. R. L. Fork, C. V. Shank, C. Hirlimann, R. Yen, and W. J. Tomlinson, *Opt. Lett.* **8**, 1–3 (1983).
14. J. Gersten, R. Alfano, and M. Belic, *Phys. Rev. A* **21**, 1222-1224 (1980)
15. G. Yang, Y. R. Shen: *Opt. Lett.* **9**, 510-512 (1984)
16. R. R. Alfano, Q. Z. Wang, T. Jimbo, and P. P. Ho, *Phys. Rev. A* **32**, 459-462 (1987)
17. R. R. Alfano, Q. Li, T. Jimbo, J. Manassah, and P. Ho, *Opt. Lett.* **11**, 626-628 (1986)
18. R.L. Fork, C.V. Shank, C. Hirlimann, R. Yen, W.J. Tomlinson: *Opt. Lett.* **8**, 1-3 (1983)
19. P.B. Corkum, C. Rolland, T. Srinivasan-Rao: *Phys. Rev. Lett.* **57**, 2268-2271 (1986)
20. J. H. Marburger: *Prog. Quant. Electr.*, **4**, 35 (1975)
21. S. L. Chin, A. Brodeur, S. Petit, O. G. Kosareva, V. P. Kandidov: *J. Nonlinear Opt. Phys. Mater.* **8**, 121 (1999)
22. T. A. Birks, W. J. Wadsworth, and P. S. J. Russell: *Opt. Lett.* **25**, 1415 (2000)
23. R.R. Alfano, L. Hope, and S. Shapiro, *Phys. Rev. A* **6**, 433 (1972)
24. N. K. Viswanathan, M. M. Brundavanam and D. N. Rao, proceedings of CLEO (May, 2009), Yang and G. Mu, *Opt. Express* **15**, 4943 (2007); S.L. Chin, N. Akozbek, A. Proulx, S. Petit and C.M. Bowden, *Opt. Commun.* **188**, 181 (2001).



25. A. Brodeur, S.L. Chin, J. Opt. Soc. Am. B **16**, 637 (1999); A. Brodeur, and S. L. Chin, Phys. Rev. Lett. **80**, 4406 (1998)
26. M. Kolesik, G. Katona, J. V. Moloney, E. M. Wright: Phy. Rev. Lett., **91**, 043905 (2003)
27. A.L. Gaeta: Phy. Rev. Lett. **84**, 3582 (2000)
28. T. Brabec, and F. Krausz, Phys. Rev. Lett., **78**, 3282 (1997); R. W. Boyd, *Nonlinear optics*, 2<sup>nd</sup> Ed., Academic Press, New York (2003).
29. N. Aközec, M. Scalora, C. M. Bowden, S. L. Chin; Opt. Commun. **191**, 353 (2001); V.P. Kandidov, O.G. Kosareva, I.S. Golubtsov, W. Liu, A. Becker, N. Akozbek, C.M. Bowden and S.L. Chin, Appl. Phys. B **77**, 149 (2003); H. Kumagai, S-H Cho, K. Ishikawa, K. Midorikawa, M. Fujimoto, S-I Aoshima, and Y. Tsuchiya, J. Opt. Soc. Am B **20**, 597 (2003); R. Gopal, V. Deepak and S. Sivaramkrishnan, Pramana **68**, 547 (2007); X-J Fang, T. Kobayashi, Appl. Phys B **77**, 167 (2003); J Liu, H. Schroeder, S.L. Chin, R. Li, and Z. Xu, Opt. Express **13**, 10248 (2005); M. Trippenbach, and Y.B. Band, Phys. Rev. A **57**, 4791 (1998); M. Kolesik, G. Katona, J.V. Moloney, and E.M. Wright, Appl. Phys. B **77**, 185 (2003)
30. W. Liu, S. Petit, A. Becker, N. Akozbek, C.M. Bowden, S.L. Chin, Opt. Commun. **202**, 189 (2002)
31. H. Yang, J. Zhang, L.Z. Zhao, Y.J. Li, H. Teng, Y.T. Li, Z.H. Wang, Z.L. Chen, Z.Y. Wei, J.X. Ma, W. Yu, Z.M. Sheng, Phys. Rev. E **67**, 015401 (2003)
32. Y.-D. Qin, D.-L. Wang, S.-F. Wang, Q.-H. Gong, Chin. Phys. Lett. **18**, 390 (2001)
33. A. Couairon, and A. Mysyrowicz , Physics Reports **441**, 47 (2007)
34. W.M.Wood, C.W. Siders, and M.C. Downer, IEEE Trans. Plasma Sci. **21**, 20(1993); S.P. Le Blanc, R. Sauerbrey, S.C. Rae, and K. Burnett, J. Opt. Soc. Am. B **10**, 801 (1993)
35. V.P. Kandidov, O.G. Kosareva, and S.A. Shlyonov, J. Nonlinear Opt. Phys. Mater. **12**, 119 (1994)
36. S.C. Rae: Opt. Commun. **104**, 330 (1994)

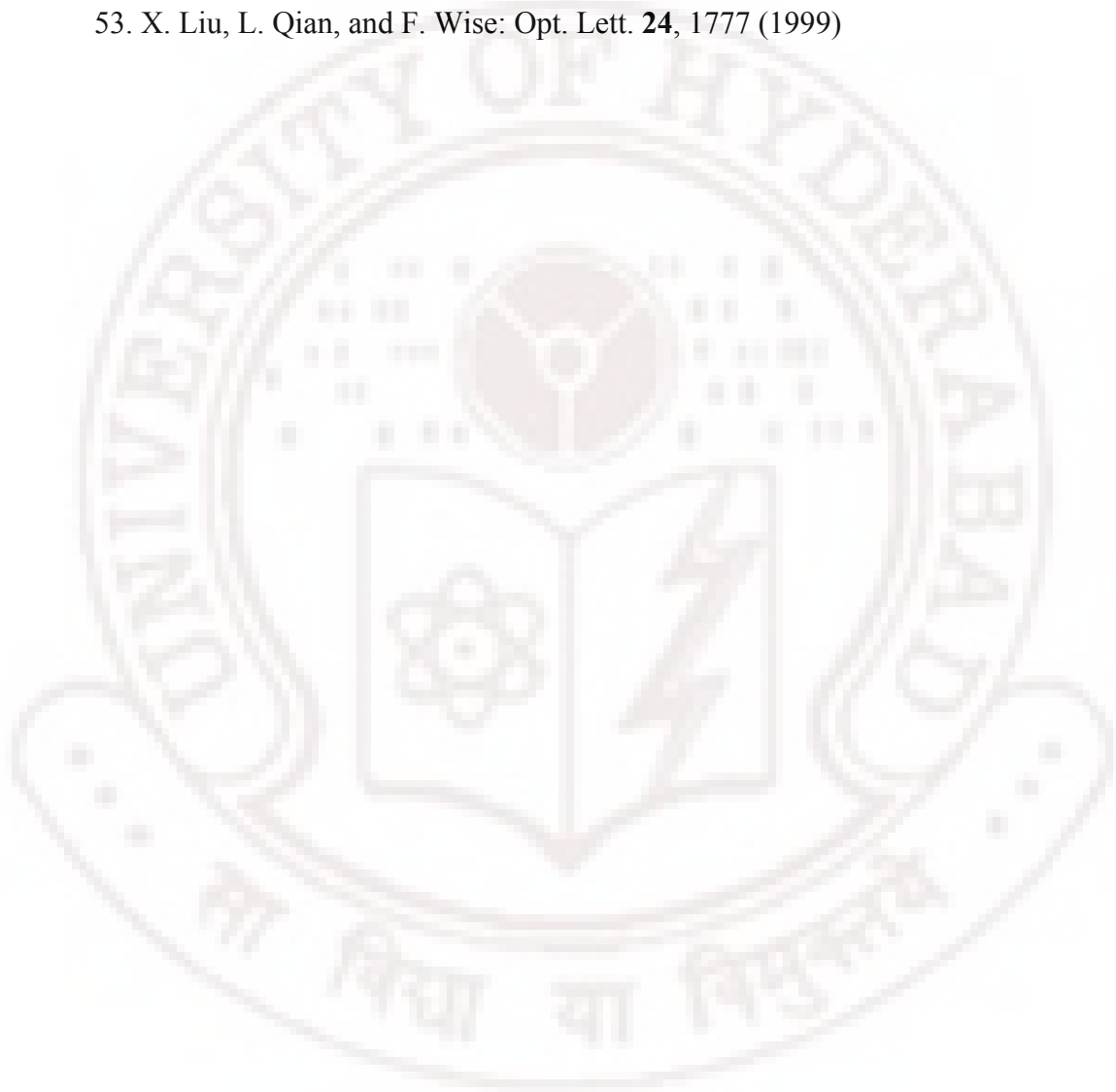
37. P.B. Corkum, C. Rolland: In *Atomic and Molecular Processes with Short Intense Laser Pulses*, ed. by A.D. Bandrauk (NATO ASI Ser. Phys. B 171) (Plenum, New York 1987) p. 157
38. O.G. Kosareva, V.P. Kandidov, S.A. Shlenov: In *Superintense Laser-Atom Physics IV*, ed. by H.G. Muller, M.V. Fedorov (NATO ASI Ser.) (Kluwer, Dordrecht 1996) pp. 489–502
39. C.W. Siders, N.C. Turner III, M.C. Downer, A. Babin, and A. Stepanov, J. Opt. Soc. Am. B **13**, 330 (1996); A.B. Fedotov, N.I. Koroteev, M.M.T. Loy, X. Xiao, and A.M. Zheltikov: Opt. Commun. **133**, 587 (1997).
40. G.G. Luther, A.C. Newell, J.V. Moloney, and E.M. Wright, Opt. Lett. **19**, 789 (1994)
41. D. Faccio, P. Di Trapani, S. Minardi, A. Bramati, F. Bragheri, C. Liberale, V. Degiorgio, A. Dubietis, and A. Matijosius, J. Opt. Soc. Am. B **22**, 862 (2005); S.L. Chin, A. Brodeur, S. Petit, O.G. Kosareva, V.P. Kandidov: J. Nonlinear Opt. Phys. Mater. **8**, 121 (1999); O.G. Kosareva, V.P. Kandidov, A. Brodeur, C.Y. Chien, and S.L. Chin, Opt. Lett. **22**, 1332 (1997); I.S. Golubtsov, V.P. Kandidov, and O.G. Kosareva, Atmos. Ocean. Opt. **14**, 966 (2001)
42. J. K. Ranka, R. S. Windeler, and A. J. Stentz, Opt. Lett. **25**, 25 (2000).
43. T. A. Birks, W. J. Wadsworth, and P. S. J. Russell, Opt. Lett. **25**, 1415 (2000); E. T. J. Nibbering, O. Dühr, G. Korn: Opt. Lett. **22**, 1335 (1997); A. L. Gaeta, Opt. Lett. **27**, 924 (2002); A. K. Abeeluck, C. Headley, and C. G. Jørgensen, Opt. Lett. **29**, 2163 (2004); P.-A. Champert, V. Couderc, P. Leproux, S. Février, V. Tombelaine, L. Labonté, P. Roy, C. Froehly, and P. Nérin, Opt. Express **12**, 4366 (2004); P.-A. Champert, S. V. Popov, M. A. Solodyankin, and J. R. Taylor, Appl. Phys. Lett. **81**, 2157 (2002); P.-A. Champert, S. V. Popov, and J. R. Taylor, Opt. Lett. **27**, 122 (2002); P. Dumais, F. Gonthier, S. Lacroix, J. Bures, A. Villeneuve, P. G. J. Wigley, and G. I. Stegeman, Opt. Lett. **18**, 1996 (1993); González-Herráez, M., S. Martín-López, P. Corredera, M. L. Hernanz, and P. R. Horche, Opt. Commun. **226**, 323 (2003); Hundertmark, H., D. Kracht, D. Wandt, C. Fallnich, V. V. R. K. Kumar, A. K. George, J. C. Knight, and P. St. J.



- Russell, *Opt. Express* **11**, 3196 (2003); Lu, F., and W. H. Knox, *Opt. Express* **12**, 347 (2004); Nicholson, J. W., P. S. Westbrook, K. S. Feder, and A. D. Yablon, *Opt. Lett.* **29**, 2363 (2004).
44. J. M. Stone and J. C. Knight, *Opt. Express* **16**, 2670 (2008); J. M. Dudley, G. Genty, S. Coen, *Rev. Mod. Phys.*, **78**, 1135 - 1184 (2006) and references therein; I. Zeylikovich, V. Kartazayev, and R. R. Alfano, 2005 *J. Opt. Soc. Am. B* **22**, 1453 (2005); S. Coen, A. H. L. Chau, R. Leonhardt, J. D. Harvey, J. C. Knight, W. J. Wadsworth, and P. St. J. Russell, *Opt. Lett.* **26**, 1356 (2001); S. Coen, A. H. L. Chau, R. Leonhardt, J. D. Harvey, J. C. Knight, W. J. Wadsworth, and P. S. J. Russell, *J. Opt. Soc. Am. B*, **19**, 753 (2002); J. M. Dudley, L. Provino, N. Grossard, H. Maillotte, R. S. Windeler, B. J. Eggleton, and S. Coen, *J. Opt. Soc. Am. B* **19**, 765 (2002); P. Falk, M. H. Frosz, and O. Bang, *Opt. Express* **13**, 7535 (2005); A. B. Fedotov, A. N. Naumov, A. M. Zheltikov, I. Bugar, D. Chorvat, Jr., D. Chorvat, A. P. Tarasevitch, and D. von der Linde, *J. Opt. Soc. Am. B* **19**, 2156 (2002); X. Fu, L. Qian, S. Wen, and D. Fan, *J. Opt. A, Pure Appl. Opt.* **6**, 1012 (2002); G. Genty, M. Lehtonen, H. Ludvigsen, J. Broeng, and M. Kaivola, *Opt. Express* **10**, 1083 (2002); G. Genty, M. Lehtonen, H. Ludvigsen, and M. Kaivola, *Opt. Express* **12**, 3471 (2004); Husakou, A. V., and J. Herrmann, *Phys. Rev. Lett.* **87**, 203901 (2001); Sakamaki, K., M. Nakao, M. Naganuma, and M. Izutsu, *IEEE J. Sel. Top. Quantum Electron.* **10**, 876 (2004).
45. J.M. Dudley, L. Provino, N. Grossard, H. Maillotte, R. S. Windeler, B.J. Eggleton, and S. Coen, *J. Opt. Soc. Am. B* **19**, 765 (2002); G. E. Town, T. Funaba, T. Ryan, and K. Lyytikainen, *Appl. Phys. B* **77**, 235 (2003);
46. B. A. Cumberland, J. C. Travers, S. V. Popov, and J. R. Taylor, *Opt. Lett.* **33**, 2122 (2008); J. C. Travers, A. B. Rulkov, B. A. Cumberland, S. V. Popov and J. R. Taylor, *Opt. Express* **16**, 14435 (2008); S. M. Kobtsev and S. V. Smirnov, *Laser Physics* **17**, 1303 (2007); S. M. Kobtsev and S. V. Smirnov, *Laser Physics* **18**, 1260 (2008).
47. W.H. Reeves, D. V. Skryabin, F. Biancalana, J. C. Knight, P. St. J. Russell, F. G. Omenetto, A. Efimov, and A. J. Taylor, *Nature* **424**, 511 (2003)

48. D.J Jones, S. A. Diddams, J. K. Ranka, A. J. Stentz, R. S. Windeler, J. L. Hall, and S. T. Cundiff, *Science* **288**, 635 (2000); R. Holzwarth, J. Reichert, Th. Udem, and T. W. Hänsch, in *Atomic Physics 17*, edited by E. Arimondo, P. DeNatale, and M. Inguscio, AIP, Conf. Proc. No. 551 (AIP, New York), pp. 58–72.(2001); Th. Udem, J. Reichert, R. Holzwarth, M. Niering, M. Weitz, and T. W. Hänsch in *Frequency Measurement and Control: Advanced Techniques and Future Trends*, edited by A. N. Luiten, Topics in Applied Physics Vol. 79 (Springer,Berlin), pp. 275–294 (2002).
49. J. Clowes and J. Knight, Supercontinuum Sources: New white-light supercontinuum sources have no blue deficiency, *Laser Focus World*, November Issue (2008); *White Light Continuum source*, (<http://www.photonics.com/Content/ReadArticle.aspx?ArticleID=34116>)
50. V. I. Klimov, D. W. McBranch: *Opt. Lett.* **23**, 277 (1998); R.A. Negres, J.M. Hales: *IEEE Journal of Quantum Electronics*, **38**, 1205 (2002); R. L. Fork, C. H. Brito Cruz, P. C. Becker, and C. V. Shank, *Opt. Lett.* **12**, 483 (1987); E. T. J. Nibbering, O. Dühr, and G. Korn, *Opt. Lett.* **22** 1335 (1997); G Cerullo and Sandro de Silvestri, *Rev. Sci. Instrum.* **74**, 1 (2003); V. V. Yakovlev, B. Kohler, and K. R. Wilson, *Opt. Lett.* **19**, 2000 (1994); M. K. Reed, M. K. Steiner- Shephard, and D. K. Negus, *Opt. Lett.* **19**, 1885 (1994); P. Rairoux, H. Schillinger, S. Neidermeier, M. Rodriguez, F. Ronneberger, R. Sauerbrey, B. Stein, D. Waite, C. Wedekind, H. Wille, L.Wöste, and C. Zeiner, *Appl. Phys. B.* **71**, 573 (2000); G. S. He, T. C. Lin, P. N. Prasad, R. Kannan, Richard A. Vaia, and L. S. Tan, *Opt. Express*, **10**, 566 (2002); L. De Boni, A. A. Andrade, L. Misoguti, C. R. Mendonca, and S. C. Zillo, *Opt. Express*, **12**, 3921 (2004); L. De Boni, L. Gaffo, L. Misoguti, C.R. Mendonca, *Chem. Phys. Lett.* **419**, 417 (2006); M. Balu, J. Hales, D. J. Hagan, and E. W. Van Stryland, *Opt. Express* **13**, 3594 (2005); T. Udem, R. Holzwarth, and T.W. Hansch, *Nature*, **416**, 233 (2002); J. H. Frank, A. D. Elder, J. Swartling, A. R. Venkitaraman, A. D. Jeyasekharan, and C. F. Kaminski, *J. Microsc.* **227**, 203 (2007); H. Kano, and H. Hamaguchi, *Opt. Lett.* **28**, 2360 (2003).

51. A. K. Dharmadhikari, F. A. Rajgara, D. Mathur, *Opt. Lett.* **31**, 2184 (2006);  
I. Buchvarov, A. Trifonov, T. Fiebig, *Opt. Lett.* **32**, 1539 (2007); V.  
Kartazhev, R. R. Alfano, *Opt. Commun.* **281**, 463 (2008)
52. D. N. Neshev, A. A. Sukhorukov, A. Dreischuh, R. Fischer, S. Ha, J.  
Bolger, L. Bui, W. Krolikowski, B. J. Eggleton, A. Mitchell, M. W. Austin,  
Y. S. Kivshar, *Phys. Rev. Lett.*, **99**, 123901 (2007)
53. X. Liu, L. Qian, and F. Wise: *Opt. Lett.* **24**, 1777 (1999)



The logo of the University of Hyderabad is a circular emblem. The outer ring contains the text "UNIVERSITY OF HYDERABAD" in English at the top and "सा विद्या या विमुक्तये" in Sanskrit at the bottom. The inner circle features a central sun-like symbol with rays, flanked by a book and a lightning bolt, and a molecular structure below the book.

# CHAPTER 4

### Abstract

*In this chapter, Potassium Di-hydrogen Phosphate (KDP) crystal is studied as a potential supercontinuum generation (SCG) media. The intrinsic  $\chi^{(3)}$  anisotropy of KDP is discussed with a goal to study SCG in KDP at different crystal orientations. Initial SCG studies were performed in a z-cut KDP crystal generated along its c-axis and all the general characteristics of SCG were observed. As an effort to study the SCG at other orientations of KDP we tried to generate SCG along the phase matching direction to achieve sum frequency generation and observed an enhancement in the bandwidth of the generated SC. The tunability in the blue region of the spectrum with angle due to wave-mixing between various frequencies present in the SCG and the residual fundamental is demonstrated. The bandwidth of supercontinuum achieved spans from 350 nm to 1300 nm. In addition, by employing arrangement of differently oriented crystals we demonstrate the generation of a spectrally flat SC.*

# Broadband supercontinuum generation in a Potassium Di-hydrogen Phosphate (KDP) crystal

## 4.1 Choice of KDP as SCG media:

Over the past few years many research groups have investigated SCG in various materials. Several efficient and practical methods of SCG and broadband emission have been demonstrated using microstructured fibers, photonic bandgap crystal fiber (PCF), birefringent fibers, new materials like BaF<sub>2</sub> both with single wavelength pumping and dual-wavelength pumping [1]. Of late, much attention and interest are shown in the propagation of ultrashort light pulses in quadratic ( $\chi^{(2)}$ ) media and the effective third-order ( $\chi^{(3)}$ ) nonlinearity that arises from the cascading of second-order ( $\chi^{(2)}$ ) processes [2]. In this regard the reports include pulse compression [3], compensation of self focusing [4], efficient temporal shaping of ultrafast pulse [5], formation of spatiotemporal solitons and X –waves [6], and control of group velocity [7]. J. Moses *et al.* [8] reported the possibility of controlling the sign and magnitude of self-steepening through the wave vector mismatch in a quadratic media, giving vital clues that the SCG could be essentially controllable in a quadratic media. Furthermore, no work has been reported on the generation of supercontinuum in a medium that has high second order susceptibility ( $\chi^{(2)}$ ) and our efforts are concentrated on the usage of the second order nonlinear materials for the SCG. Besides, we know that the higher harmonic generation takes the fundamental easily into UV and far UV regions making use quadratic nonlinear crystals. In this scenario, research on materials with good  $\chi^{(2)}$  suitable for frequency conversion as well as continuum generation at high intensities would be of great relevance.

In consideration of the above discussion, we have chosen potassium di-hydrogen phosphate (KDP), which is a well-known nonlinear crystal possessing high damage threshold [9] as a media to generate SC. KDP belongs to the family

of crystals that exhibit excellent quadratic nonlinearity  $\chi^{(2)}$ . Some of the features of this crystal that make it indispensable for frequency conversion and wave mixing are: (a) Good ultraviolet transmission; (b) High optical damage threshold; (c) High birefringence, and (d) High nonlinear coefficient ( $\chi^{(2)}$ ). The direct band gap of KDP is found to be 7.12 eV (174 nm) [10], which is quite high compared to the minimum requirement of 4.7 eV. This combination of high band gap and presence of high nonlinearity propelled us to investigate the SCG in KDP. With its large bandgap, high damage threshold, and strong nonlinear behavior, KDP shows great promise as a versatile candidate for SCG.

#### 4.1.1 Anisotropy of $\chi^{(3)}$ in KDP crystal:

SCG being essentially a third order process, it is intrinsically dependent on the  $\chi^{(3)}$  of the material. The anisotropic property of the crystals results in dependence of  $\chi^{(3)}$  on the rotation angle. It is found that in case of a KDP crystal, the nonlinearity drops as the angle between the incident light and the principal optic axis increases [11].  $\chi^{(3)}(\theta)$  is a function of the independent non-vanishing  $\chi^{(3)}$  components determined by the symmetry. Isotropic cubic crystals like  $\text{BaF}_2$  and  $\text{CaF}_2$  having a space-group symmetry 43m have a well defined expression for effective  $\chi^{(3)}$  [12]. For uniaxial crystals, like sapphire and KDP, the relation for effective  $\chi^{(3)}$  becomes more complicated as there is direction dependence for e-rays but not for o-rays [13]. Furthermore, KDP being non-centrosymmetric having a tetragonal structure and  $\bar{4}2m$  symmetry, the expression for effective  $\chi^{(3)}$  is more complex [14].

In order to observe the dependence of effective  $\chi^{(3)}$  with simple orientation of the crystal we carried out degenerate four-wave mixing studies in forward box-car geometry [15] on a thin slice of the z-cut crystal by rotating the plane of polarization of the input laser beam with respect to the  $0^\circ$  position (i.e horizontal polarization) rotated by a HW plate as shown in Fig 4.1(a). As explained in chapter 2, in a box-car arrangement the fundamental beam is divided

into three nearly equal intensity beams in such a way that the three form three corners of a square box and are focused into the nonlinear medium (sample) both spatially and temporally. The DFWM signal that comes as the fourth corner of the box generated as a result of the phase-matched interaction  $\mathbf{k}_4 = \mathbf{k}_3 - \mathbf{k}_2 + \mathbf{k}_1$  of the three incident beams as shown in the Fig 4.1(b).

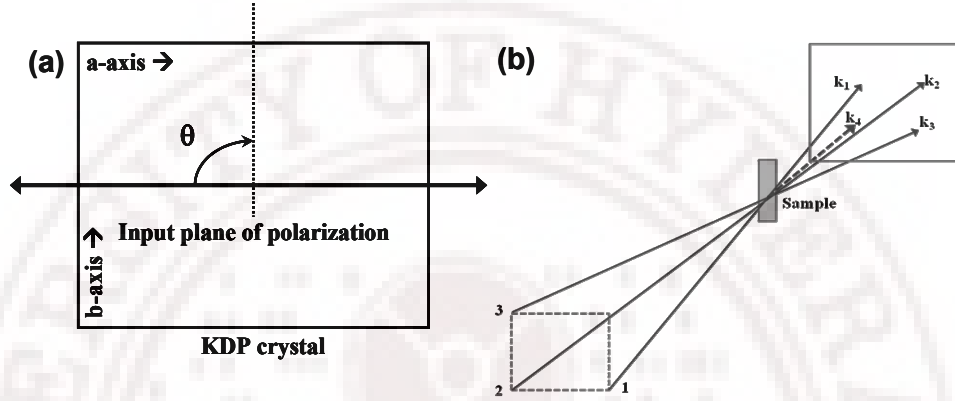


**Fig. 4.1:** (a) Position of the crystal used for the DFWM study the effect of orientation of plane of polarization relative to the horizontal polarization denoted by  $\theta$ ; (b) Geometry of the box-car DFWM set-up.

The third order nonlinear susceptibility  $\chi^{(3)}$  is obtained by comparing the measured DFWM signal for the sample with that of fused silica as reference ( $\chi^{(3)} = 1.4 \times 10^{-14}$  esu at 800 nm) under the same experimental conditions. The following relationship is used [15]:

$$\chi_{sample}^{(3)}(esu) = \left( \frac{n_{sample}}{n_{ref}} \right)^2 \left( \frac{I_{sample}}{I_{ref}} \right)^{1/2} \left( \frac{L_{ref}}{L_{sample}} \right) \alpha L_{sample} \left( \frac{e^{\frac{\alpha L_{sample}}{2}}}{1 - e^{-\alpha L_{sample}}} \right) \chi_{ref}^{(3)}(esu) \quad (4.1)$$

where  $I$  is the DFWM signal intensity,  $\alpha$  is the linear absorption coefficient,  $L$  is sample path length, and  $n$  is the refractive index taken as 1.48 and 1.45 for KDP crystal and fused silica respectively at 800 nm. From the obtained  $\chi^{(3)}$  we estimated the value of nonlinear refractive index ( $n_2$ ) which is related to  $\chi^{(3)}$  by the relation [15]:

$$n_2(cm^2/W) = \frac{0.0395}{n_0^2} \chi^{(3)}(esu) \quad (4.2)$$



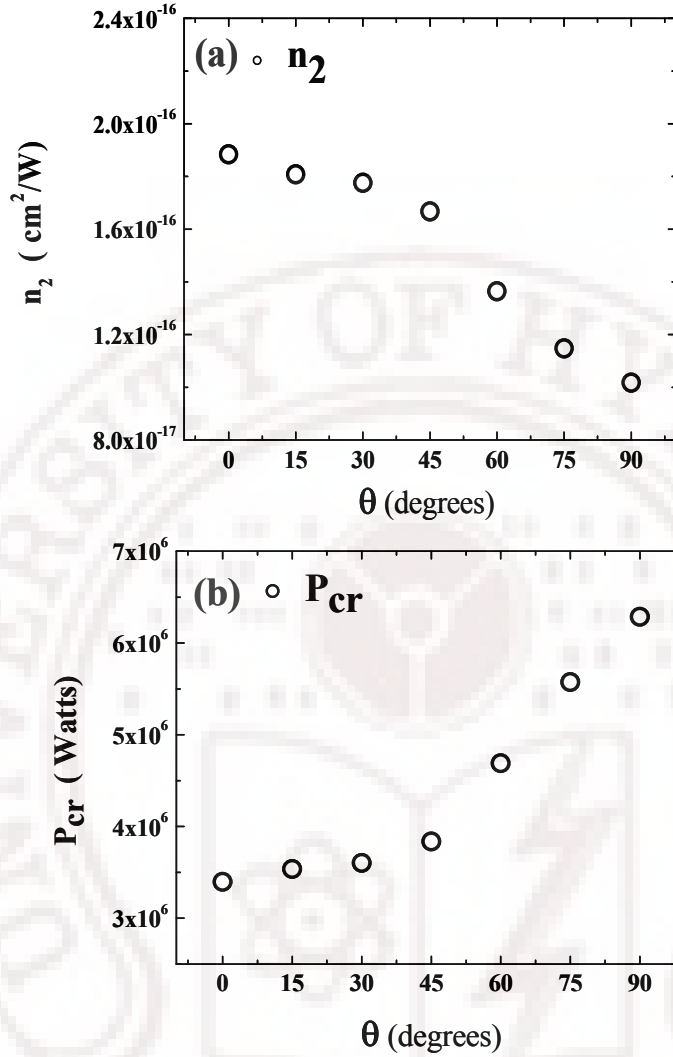


**Fig. 4.2:** (a) Variation of  $n_2$  with orientation of plane of input polarization relative to the horizontal polarization denoted by  $\theta$ . (b) Variation of  $P_{cr}$  with  $\theta$

Fig 4.2(a) shows the variation of  $n_2$  with respect to the rotation of the plane of polarization of the input beam clearly indicating the intrinsic anisotropic nonlinearity in the KDP crystal. Correspondingly, the critical power for self-focusing ( $P_{cr}$ ) that is inversely proportional to  $n_2$  [16] as discussed in chapter 3 increases with increase in the angle of rotation as seen in Fig 4.2(b). From this study we estimated the  $P_{cr}$  for the KDP crystal along the c-axis to be  **$\sim 2.8$  MW**. Conclusively, the anisotropy of  $\chi^{(3)}$  leads to anisotropy of  $n_2$  that in turn results in dependence of  $P_{cr}$  with orientation of the crystal. The immediate application of

the anisotropy of  $\chi^{(3)}$  one can envisage of is that it provides a handle in the control of  $P_{cr}$  which in turn allows control of SCG with orientation of the KDP crystal. We therefore carried out systematic study of SCG in KDP in order to exploit the intrinsic anisotropic nature of the crystal and generate broadband SCG as discussed in the subsequent sections.

## 4.2 Supercontinuum generation (SCG) studies in a KDP crystal:

In this section we discuss our results of SCG in KDP where we achieved generation of broadband white light in a KDP crystal. Initially we generate SCG in a z-cut KDP crystal by focusing the fs pulses along its c-axis. It should be noted that KDP, being an uniaxial crystal, behaves as an optically isotropic medium when the light is passed through its c-axis (i.e., optic axis). Then by using the various orientations of the crystal calculated to make use of the various  $\chi^{(2)}$  nonlinear optical processes like second harmonic generation and sum frequency generation in tandem with SCG in the KDP crystal we achieved enhanced spectral content along with the tunability of SCG in the shorter wavelength regime of SCG.

### 4.2.1 SCG in z-cut KDP media:

#### 4.2.1.1: SCG spectral studies with linearly polarized fundamental pulses:

A z-cut KDP crystal with dimensions  $10 \times 8 \times 5 \text{ mm}^3$  are used for the study. The SC is generated by focusing the 800 nm amplified femtosecond pulses pulse into the crystal using a focusing lens of focal length  $f = 300 \text{ mm}$ . The input beam is considered to be linearly polarized parallel to (100) axis of the crystal and propagating along the (001) axis of the KDP as shown in figure 4.3. The calculated beam waist, taking gaussian beam approximation, at the focal point in vacuum was  $\sim 50 \text{ }\mu\text{m}$ . The face of the sample was always placed 2 cm away before the focus point to avoid any laser induced damage. The incident average power used for the study was varied from 10 - 600 mW corresponding to a maximum peak power variation of  $\sim 0.01 - 6.0 \text{ GW}$  ( $\sim 3 - 2000 P_{cr}$ ) This accounts

for peak intensity of a maximum  $\sim 15 \times 10^{12} \text{ W/cm}^2$  on the front face of the sample. The calculations of the peak powers and peak intensities were performed assuming the gaussian beam profile for the incident pulse and neglecting the Fresnel reflection losses from the surfaces. The spectra of continuum are recorded using a fiber coupled spectrometer (Ocean Optics USB2000) after collimation and suppressing fundamental by an IR filter thus limiting our study of SC to the visible region (400 – 750 nm). The integrated intensity measurements of the SC are measured by focusing onto a photodiode (FND100). The laser power that was incident on the material under study was measured using a power meter (OPHIR) with a nearly flat and wide spectral response.

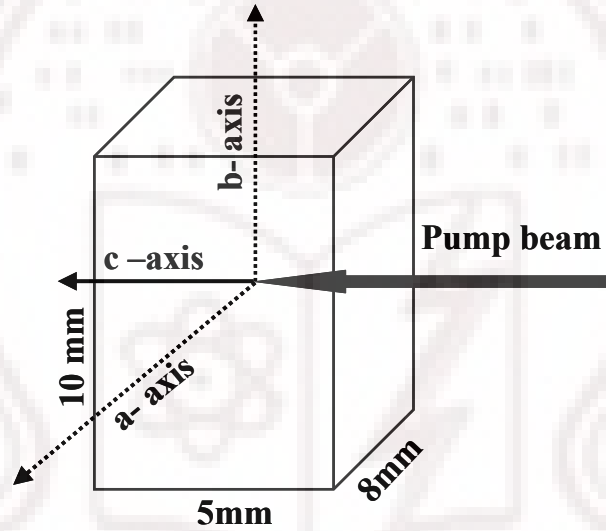


**Fig. 4.3:** Position of the z-cut crystal used in the study

We observed continuum generation at a threshold power of  $\sim 16 \text{ mW}$  ( $\sim 16 \mu\text{J/pulse}$ ) by keeping the crystal at the focus of the lens,. Figure 4.4 shows the SCG data obtained for the z-cut KDP crystal for the incident average power of  $350 \text{ mW}$  (i.e  $350 \mu\text{J}$  per pulse) that corresponds to a peak power of  $\sim 3.5 \text{ GW}$  ( $> 1400 P_{\text{cr}}$  for KDP) and peak intensity of  $\sim 8 \times 10^{12} \text{ W/cm}^2$  on the front face of the crystal. Figure 4.4(a) shows the spectra of the SCG and the snapshot showing the dispersion of the spectra and figure 4.4(b) shows the snapshot of the KDP crystal generating the SC at a far field on the screen. When an input energy of

$\sim 100 \mu\text{J}$  is focused at the center of the crystal, a conversion efficiency of  $\sim 23\%$  was observed.

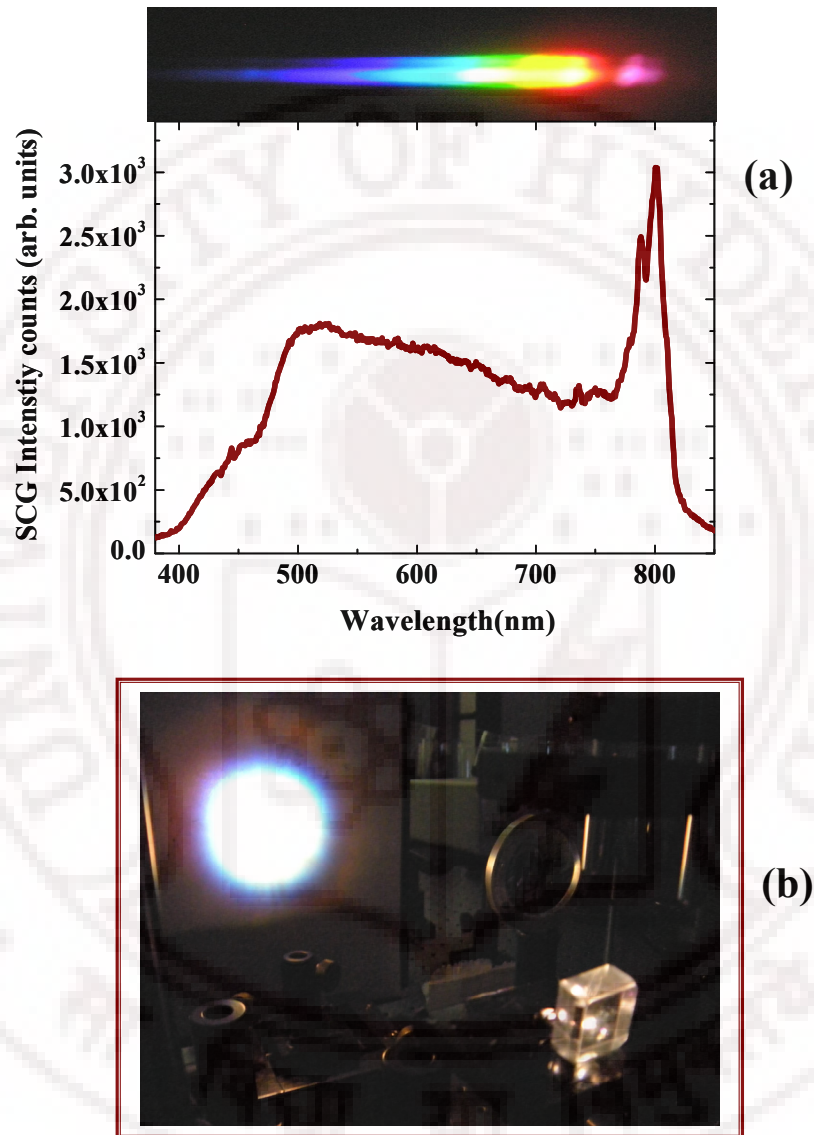


**Fig. 4.4:** (a) Spectra of the SCG at  $\sim 1400P_{cr}$  and the snapshot showing the dispersion of the spectra; (b) snapshot showing the crystal generating the SC at a far field on the screen

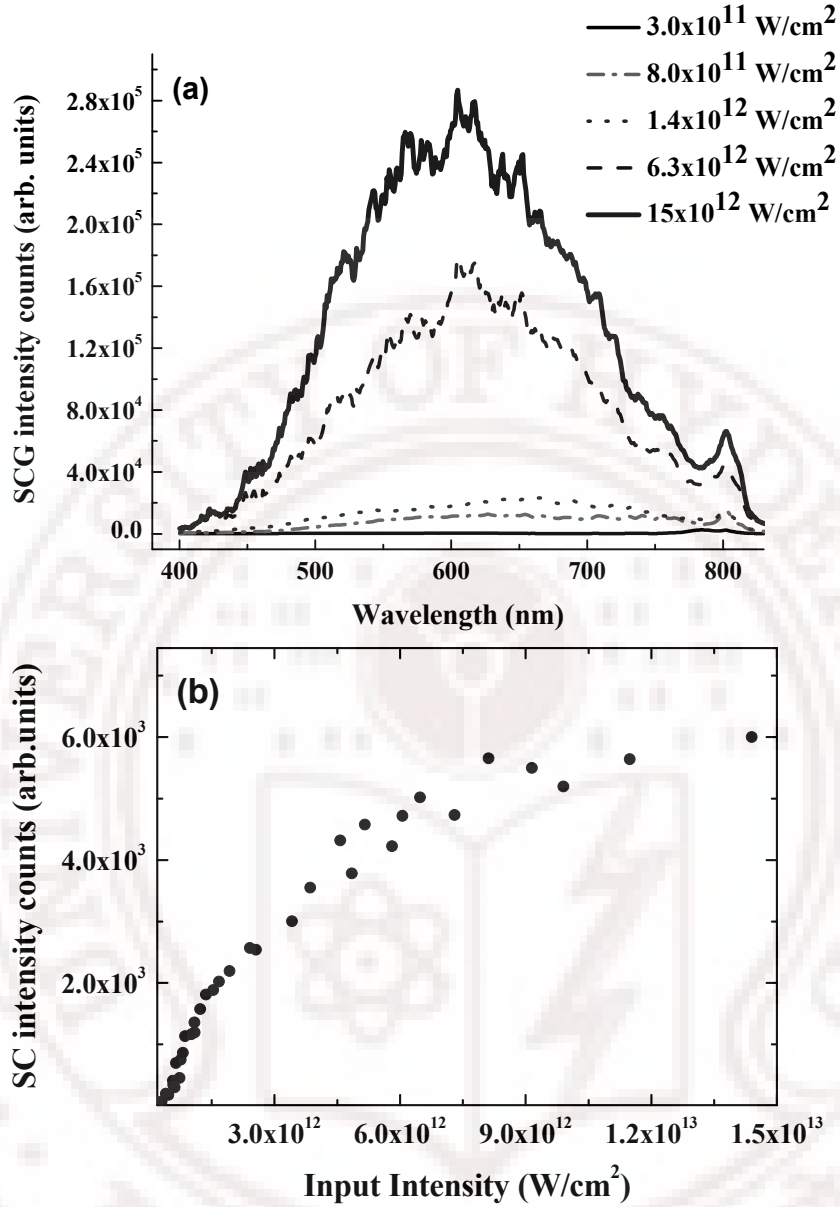


Fig. 4.5: (a) SCG in a z-cut KDP with increase in input intensity;  
(b) Plot of the integrated SCG intensity with input intensity

Figure 4.5 shows the variation of the SCG spectra with increase in the input intensity. Expectedly the blue pedestal of the SCG gets stronger with increase in the input intensity from  $0.3 \times 10^{12}$  to  $15 \times 10^{12} \text{ W/cm}^2$  with more input fundamental pulse getting converted into SCG. Above a threshold intensity of  $1.4 \times 10^{12} \text{ W/cm}^2$  we observe that the maximum positive frequency shift (on the blue side of the central input wavelength of 800 nm) of the spectrum is constant.

We elucidated this observation as mainly due to the clamping of the peak intensity inside the filaments generated due to the propagation of the intense femtosecond pulse in the medium [17]. Also a point of interest is the variation of the integrated SCG intensity with input intensity. We observe that the overall the SC output gets clamped after the input intensity of  $6 \times 10^{12} \text{ W/cm}^2$  and does not increase a great deal with further increase in the input intensity. This is because SCG is mostly efficient till certain input threshold intensity beyond which the media slowly undergoes optical breakdown with increase in the avalanche-ionization effects and the onset of high dense plasma [18].

#### 4.2.1.2: Studies on the role of input polarization on the SCG:

In this section we discuss our results using linearly and circularly polarized laser beams. We generated SCG for different ellipticity of the input laser pulse by making use of a quarter wave plate (QW). Figure 4.6 depicts some typical spectra obtained for the rotation of the QW by  $0^\circ$ ,  $15^\circ$  and  $45^\circ$  i.e., changing the polarization of the laser pulse from linear to circular polarization. Under conditions where the same energy ( $350 \mu\text{J}$ ) is employed, the signal intensity of white light was found to be higher for linearly polarized light compared to that obtained when circular polarization was used. This observation is rationalized on the basis of both MPE-enhanced SPM and SPM processes. In the case of femtosecond pulses, free electrons produced due to MPE enhance SPM, and contribute towards SCG. Moreover, multiphoton effects are known to be dependent on the state of polarization of the incident light. Lambropoulos [20] pointed out that the effect of light polarization on the multiphoton ionization of atoms is related, in a general sense, to the effect of field correlations of multiphoton processes. Both effects arise from the fact that the vectors of the radiation field affect, in nonlinear fashion, the transition amplitudes for multiphoton processes. The nonlinearity in the amplitude of the radiation field leads to ionization rates that depend on the correlation functions of the field, and not just on the absolute value of the field amplitude. When the circular polarization vector  $E_x + iE_y$  is inserted in the expression for the transition

amplitude, cross products of matrix elements involving the orthogonal components  $E_x$  and  $E_y$  occur, and these lead to the dependence of the ionization rate on the polarization state of the incident light field. Sandhu *et al.* [21] have shown that supercontinuum generation in water, using 100 fs pulses, is reduced for circularly polarized light. Petit *et al.* [22] have also shown that multiphoton ionization is less efficient when a circularly polarized laser beam is used. Other reports have theoretically shown that the effective ionization energy for circularly polarized beams is higher than for linearly polarized beam [23]. Recently, Fibich *et al.* have theoretically shown that multiple filamentation caused by self-focusing is suppressed for circularly polarized laser beam in a Kerr medium [24].

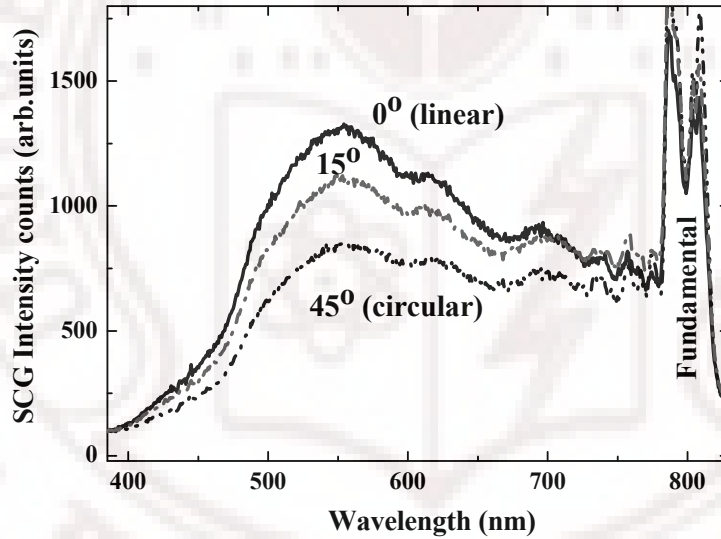


**Fig. 4.6:** SC spectra from z-cut KDP using linearly and circularly polarized light, keeping the incident energy constant at 350  $\mu\text{J}$

The integrated spectral intensity plot with variation in the ellipticity of the input laser pulse by rotation of the QW plate as shown in figure 4.7 which supports the discussion presented above. Clearly the spectral intensity falls at multiples of  $45^\circ$  (i.e.,  $\pi/4$ ) of QW rotation generating circularly polarized fundamental before focusing into the crystal.



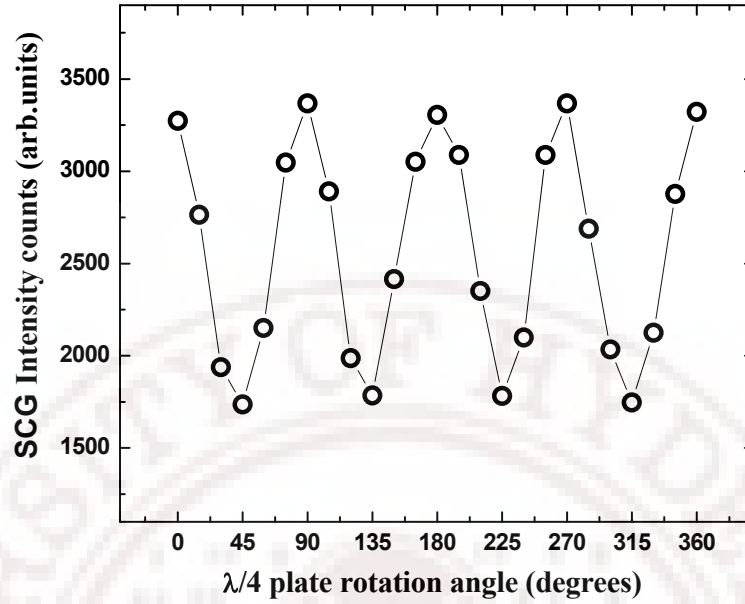


Fig. 4.7: SC intensity with Elliptical polarized input, open circles are the experimental data while the line joining the scatter is to just guide the eye)

We now discuss how SPM processes contribute towards the polarization dependence of white light generation. A z-cut KDP crystal behaves like an optically isotropic when the laser pulse propagates along c-axis and does not show linear birefringence with optical field. However, when the crystal is subjected to a sufficiently intense optical field, SPM and cross phase modulation (XPM) [25] may give rise to the field-induced change in the nonlinear refractive index, whose magnitude is intensity dependent. The presence of XPM gives rise to a nonlinear coupling between orthogonal field components. The nonlinear refractive index change, in general, is unequal for two orthogonal crystal axes since it depends both on the laser intensity and its polarization. Spectra in figure 4.6 show that the blue side is broad and intense for the linearly polarized beam compared to that obtained with a circularly polarized beam. This might be rationalized by considering the difference of interaction intensities at which those spectral components were generated. Generation of the blue spectrum requires higher intensity than that of light in the central part of the overall output spectrum. Therefore, the variation of the white light intensity with laser polarization becomes most significant in the blue region of the spectrum.

#### 4.2.1.3 Formation of the filaments

The estimated peak power for the formation of stable single filament is  $\sim 26\text{MW}$  (i.e.,  $\sim 10P_{\text{cr}}$ ). As we increase the input power to  $\sim 100P_{\text{cr}}$  we start observing multiple filament formation where the number of filaments sharply increases. Each of the individual filaments can generate white light continuum [26]. We start observing coherent interaction between the filaments leading to the fluctuating interference patterns in the far field image of the output on a screen. At still higher powers ( $>270\text{ MW}$ ,  $\sim 100P_{\text{cr}}$ ), the number of filaments become very large with the effect that the intensity fluctuations within the profile of the beam almost diminishes. When the filaments are more than one but are finite in number, the interference due to the filaments leads to colored fringe-like pattern within the beam profile. With large number of filaments, these patterns merge leading to a uniform white continuum at every position of the beam cross-section similar to what was observed for SCG in BK-7 glass as shown in Table 3.2.

#### 4.2.1.4 Coherence properties of SCG:

The supercontinuum that is generated from each of these filaments possesses a high degree of spatial coherence, which has been demonstrated using a simple Young's double slit configuration [27]. High degree of spatial coherence from the white light generated from multiple filaments has been reported in literature [28]. In these experiments, a stable interference is obtained in the far field that indicates that for the white light generated in these filaments, each spectral component has the same coherence as the initial pump pulse. We demonstrated the coherence properties of SCG by using Young's double slit experiment and a Michelson interferometer. A Young's double slit geometry is used to determine the spatial coherence. We have done this by placing two slits of width  $\sim 80\text{ }\mu\text{m}$  and separated by  $\sim 0.25\text{ mm}$  normal to the direction of propagation of white light, and by measuring the fringe visibility of the interference pattern that is obtained in the far field. The fringe pattern is depicted in figure 4.8(a). Fringes are observed until the separation between the slits is increased to  $4\text{ mm}$ , for an input beam diameter of  $12\text{ mm}$ . Part of the laser beam was directed to

Michelson interferometer with a spectrometer at its output end to confirm the temporal coherence of the supercontinuum generated by observing the fringes on a screen as shown in figure 4.8(b). The inset in the figure 4.8(b) showing the spectra considered for the study.

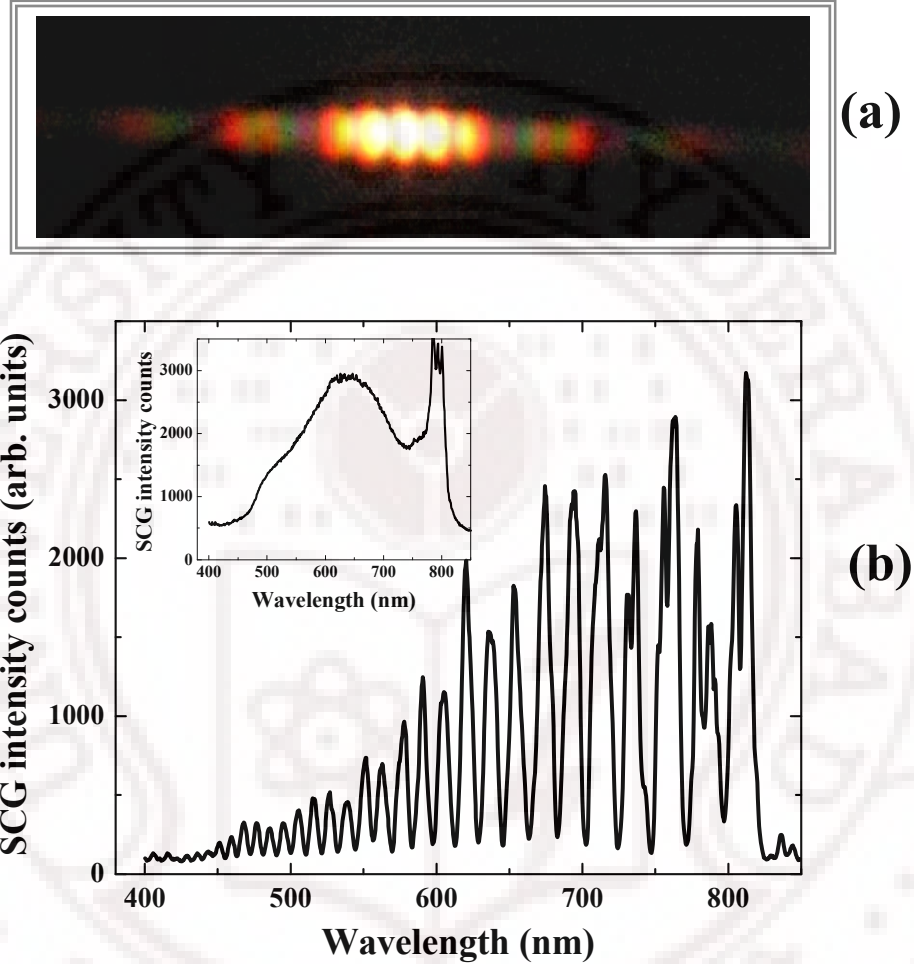


**Fig. 4.8:** (a) Young's double slit fringes with a slit separation of  $\sim 0.25$  mm and  $\sim 80$   $\mu$ m slit width (b) Spectral interference of the SCG showing the temporal coherence (inset) the spectra of the SCG considered for the temporal study

There is a certain difficulty in obtaining the spectral interference using the Michelson set. This is mainly due to the fluctuations associated with the SCG spectrum. The origin of the fluctuations could be due to several reasons to name a few: (i) Pulse to pulse fluctuations of the fundamental pulse, (ii) Instability of the pulse duration with time, (iii) small coherence length of the femtosecond pulse. Nevertheless, this method is the easiest way of estimating the temporal characteristics of SCG. In our case we tried to estimate the temporal

characteristics of the SCG; however the data obtained was insufficient to be able to obtain any useful information other than the proof of temporal coherence of the SCG. In practice, a full-intensity and- phase measurement of the continuum pulses can be made using cross-correlation frequency-resolved optical gating (XFROG) [29]. Many numerical simulations have been used in studies of the temporal and spectral features of supercontinuum generation [30]. In particular, an ensemble average over multiple simulations performed with random quantum noise on the input pulse allows the coherence of the supercontinuum to be quantified in terms of the dependence of the degree of first-order coherence on the wavelength. The coherence was ascertained to depend strongly on the input pulse's duration and wavelength.

#### **4.2.1.5 Polarization properties of SCG:**

A prior knowledge of the polarization properties of SCG is of utmost importance as continuum with stable polarization properties plays an important role in many applications that include femtosecond time resolved spectroscopy, optical pulse compression for generation of ultrashort pulses, a seed pulse of an optical parametric amplifier, optical frequency metrology, two-photon absorption spectroscopy, biomedical applications demand a better control over the production and properties of SC [31]. It is generally assumed that the generated SC follows the state of polarization of the input pump pulse. However we obtained very interesting results with this aspect of the SCG and we discuss more this issue in the chapter 5 where we go on to show that KDP is a better media in provide SCG with better polarization properties.

#### **4.2.2 SCG studies with different orientation of KDP and its applications:**

To summarize the results discussed in the previous section the supercontinuum (SC) generated in a z-cut KDP crystal has all the general characteristics of SCG discussed in chapter 3. As discussed in the section 4.1 we expect the SC to be different in different orientation of the crystal owing to its property of intrinsic anisotropy of nonlinearity. Moreover KDP being an good

$\chi^{(2)}$  opens up many possibility of having the  $\chi^{(3)}$  and  $\chi^{(2)}$  being exploited simultaneously to obtain interesting overall phenomena and the much needed control over the overall SCG output even at high input power of the fundamental laser pulses. In the subsequent sections of this chapter we discuss our most interesting observations of generating SC at different orientations of the KDP crystal obtaining the generation of tunable broadband white light in a KDP crystal employing SCG in tandem with second harmonic generation and sum frequency generation (SFG) with SCG in the KDP crystal. We further go on to demonstrate a novel strategy in obtaining a spectrally flat SCG.

### 4.3 Broadband supercontinuum generation in a KDP crystal:

#### 4.3.1 Second harmonic generation (SHG) in tandem with SCG:

The most important feature of crystalline KDP that make it indispensable in nonlinear optical application is its high nonlinear coefficients allowing efficient frequency conversion and wave mixing. Initial results from our group in this regard were from exploiting the harmonic generation ability of KDP when pumped along its phase matching direction. Most interesting observation when the amplified pulses were focused into the KDP crystal along its phase-matching direction there was tandem generation of SCG along with the second harmonic generation which was never observed before [32].

The phase matching angle of the KDP crystal for SHG of 800 nm is  $45^\circ$  and Type I critical phase matching has been used. The SCG is investigated at phase matching angle (indicated by  $0^\circ$ ) and also away from the phase matching angle. The visual appearance of the generated supercontinuum, away from and at the phase matching angle is shown in figure 4.9 (a) and (b).



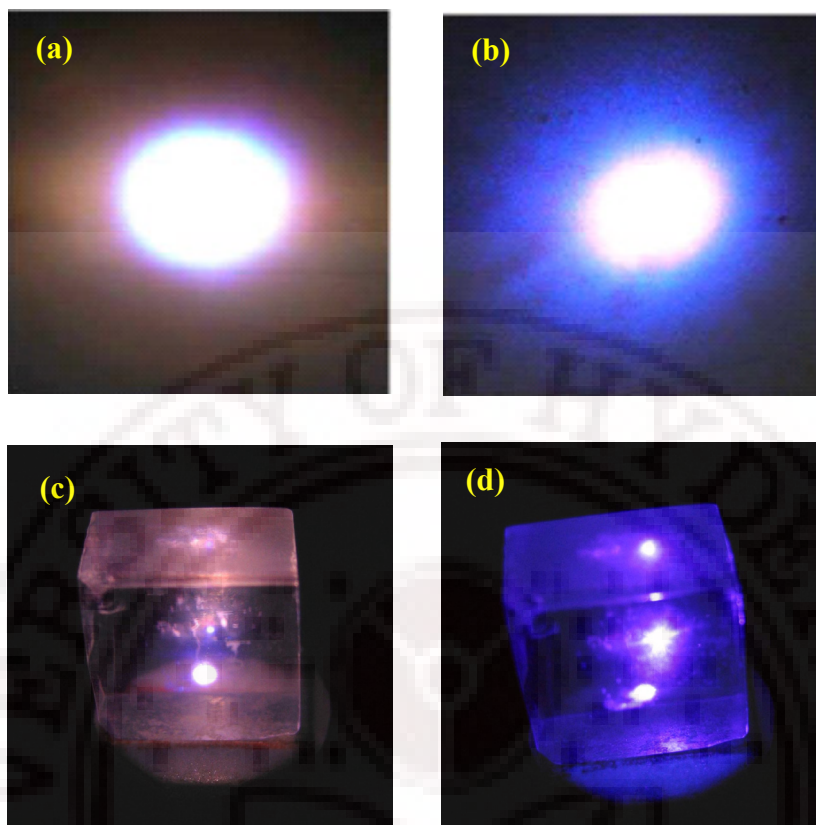


**Fig. 4.9:** (The right panel) (a) shows the supercontinuum generated at the phase matching angle of KDP as seen on a white screen and (c) the appearance of the KDP crystal during the SCG. (The left panel) SCG at an angle far away from phase matching angle, and (d) the appearance of the KDP crystal. The blue color in the right panel is due to the emission from the screen due to SHG

The snapshot in the right panel of figure 4.9 clearly shows the tandem generation of SHG as well as SCG at phase matching angle. It may be noted that blue color seen in the right panel of figure 4.9(a) is the emission from the screen due to SHG. The left panel of figure 4.9(b) shows the SCG generated away from the phase matching angle. The faint blue ring seen on the right panel has its origin in the conical emission, which generally accompanies SCG. The colored emission seen the snapshots of the crystals as shown in figure 4.9(c) and (d) both at and away from the phase matching angle supplements the observation of the SCG in figure 4.9(a), (b). The dispersion and spectral content of the continuum generated away from the phase matching angle is depicted in figure 4.10(a). The observed bandwidth is from 420 - 960 nm (after attenuating the pump beam with an IR filter). As the crystal was rotated towards the phase matching angle, SHG

starts showing up. The dispersion and spectrum measured at phase matching angle of the generated supercontinuum (after attenuating the pump beam with an IR filter) is as shown in figure 4.10(b). The observed bandwidth is from 380 - 960 nm. The spectrum was thus pushed by almost 40 nm more into the ultraviolet, thereby extending the spectral width of the SCG towards the shorter wavelength region.

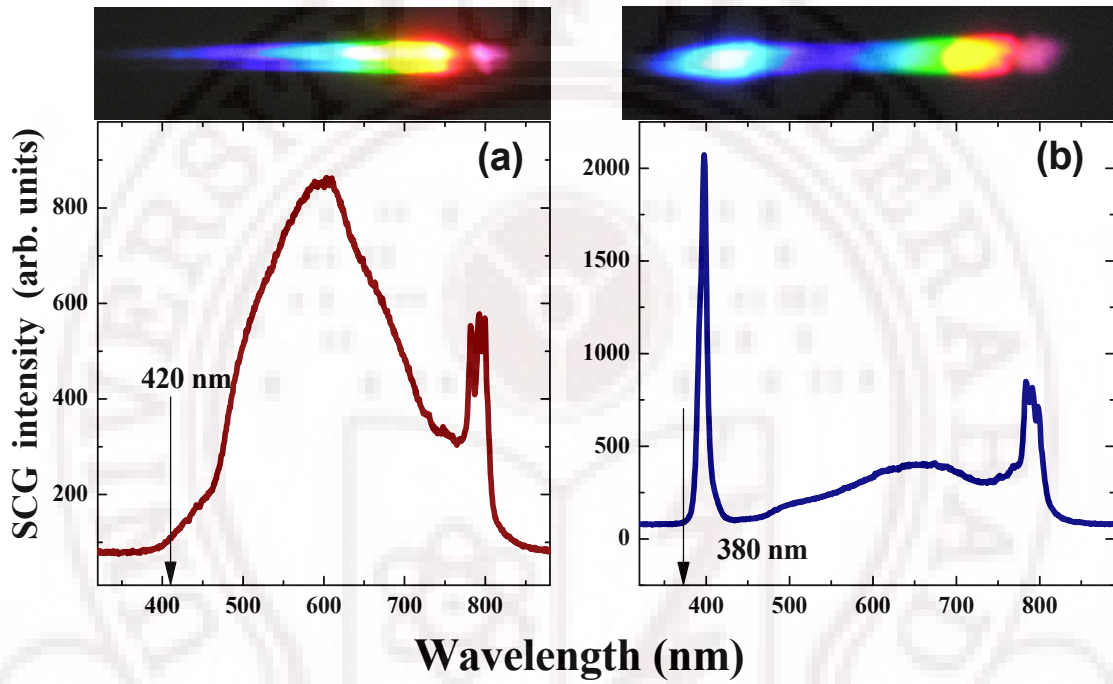


**Fig. 4.10:** (a) left panel showing the spectrum of SCG away from phase matching angle and the snapshot of the dispersion of SCG; (b) right panel showing the spectrum and dispersion of SCG at the phase matching angle. The cut-off wavelength of SCG on the blue side for at and way from the phase matching angle is 380 nm and 420 nm respectively.

One important observation to be made here is that at the phase matching angle the intensity of the second harmonic is dominant compared to the intensity of the SCG. This could be because of the depletion of the input field by the SHG conversion before the onset of self-focusing initiating continuum generation. The evolution of the spectral content of SCG as well as the SHG, as we rotate the crystal away from the phase matching angle, is as shown in figure 4.11. For angles away from the phase matching direction for SHG, we observe an increase in the intensity of the continuum while the SHG intensity reduces.



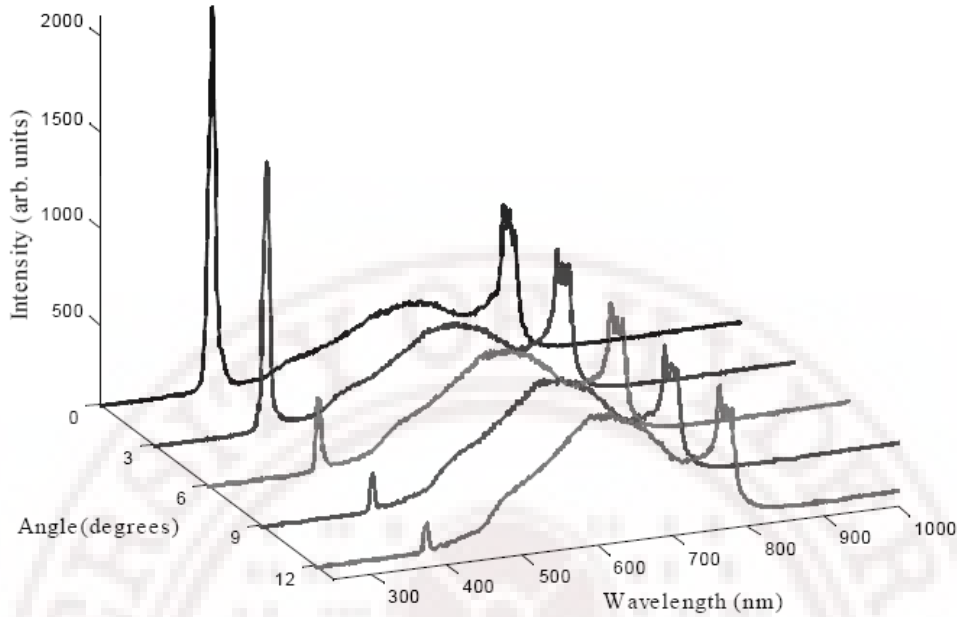


**Fig. 4.11:** Evolution of the SHG and SCG as we rotate the crystal towards the phase matching angle (Here  $0^\circ$  refers to phase-matching angle and the angular variation is measured with respect to it). (Figure adapted from [32])

#### 4.3.2 Sum frequency generation (SFG) in tandem with SCG:

In this section we discuss our results on enhanced supercontinuum generation (SCG) with KDP crystal that was cut at the phase matching angle with respect to the c-axis. This phase-matching condition facilitates the possibility of achieving sum frequency generation (SFG) in tandem with the SCG along the lines of enriching the UV-blue content of the spectral bandwidth of SCG in tandem with SHG as discussed in the previous section. The crystal when oriented at the phase matching angle for SHG as shown in figure 4.12, we obtain SHG in addition to the SC in the spectrum. The spectrum was thus pushed by almost 25 nm more into the ultraviolet, thereby extending the spectral width of the SCG towards the shorter wavelength region. The disadvantage in this scheme is evidently the reduction in SCG intensity in the presence of SHG. This is because of the depletion of the input field by the SHG conversion before the onset of self-focusing of the fundamental, which initiates continuum generation. As an effort to get over this disadvantage of the scheme of SHG and SCG in tandem we

extended our studies to use SFG in tandem with SCG in the KDP crystal. The key idea of achieving SFG and SCG in tandem is that we expect the input fundamental pulse (800 nm) to parametrically mix with any of the wavelengths present in the continuum satisfying the phase matching condition for the sum frequency generation.

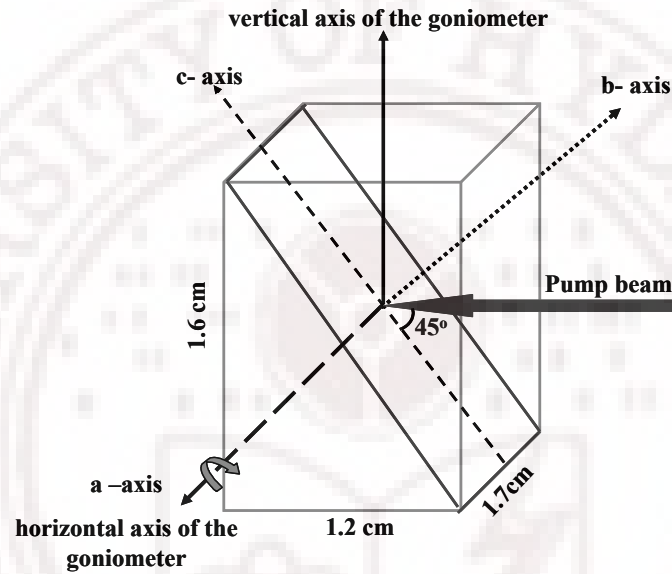


**Fig. 4.12:** The orientation of the KDP crystal axes with respect to the pump. The crystal was cut such that the input beam is incident at  $45^\circ$  with respect to the c – axis.

In a typical optical parametric amplifier (OPA), the continuum was generated in a transparent medium like sapphire and was made to undergo wave mixing in a different nonlinear crystal like beta barium borate (BBO) to generate sum or difference frequencies. Here, we could generate continuum and achieve wave mixing in a single KDP crystal where the mixing crystal itself was used as a source of continuum, which then acts as the seed for the wave mixing process. For this study, the KDP crystal was mounted on a goniometer such that the a-axis of the crystal coincides with the horizontal axis of the goniometer and the c-axis makes an angle of  $45^\circ$  with respect to the vertical axis of the goniometer as shown in figure 4.12. We have observed that the optimum wave mixing and continuum signal output was obtained when the crystal was rotated by  $24^\circ$  around

the vertical axis of the goniometer. It may be pointed here that this  $24^\circ$  rotation was to achieve optimum SHG and continuum and may not represent the exact rotation angles with respect to the three crystal axes as there could be some error in the orientation of crystal while cutting and polishing with hand.

The sum frequency radiation generated at this position was 399 nm that corresponds to the  $0^\circ$  spectra in the figure 4.13(a) and was due to the wave mixing of input pump frequency at 800 nm and frequency at 796 nm in the continuum. From this position the crystal was rotated from  $-7^\circ$  to  $10^\circ$  around the a-axis of the crystal (horizontal axis of the goniometer) to get SFG at each orientation of the crystal. Figure 4.13(a) shows the series of spectra obtained for different orientations of the crystal, where the peaks in the blue region were the sum frequency signals obtained due to the mixing of the fundamental at 800 nm with different components of the continuum generated in the KDP crystal. We can clearly see the peak in the blue region shifting with each rotation of the crystal. Figure 4.13(b) shows two typical spectra obtained at  $-7^\circ$  and  $-5^\circ$  positions which yielded the SFG peaks at 352 nm and 360 nm clearly proving our assertion of stretching the bandwidth till 350 nm as compared to 420 nm obtained in figure 4.10(a).

Figure 4.14 that shows the SFG+SCG spectra obtained for the crystal positions of  $+7^\circ$  and  $+9^\circ$  positions showing SFG peaks at 440 nm and 490 nm, respectively demonstrates the usefulness of KDP in the tunability of SCG with SFG peaks at different orientations of KDP. Figure 4.15 shows the spectra obtained by the SFG in tandem with SCG that has good spectral content starting from 350 nm overcoming the disadvantage in generating SCG with tandem with SHG as was discussed at the beginning of this section. The snapshot in figure 4.15 shows the dispersion of the SCG spectrum with rich content in blue as well as in the green spectral region.

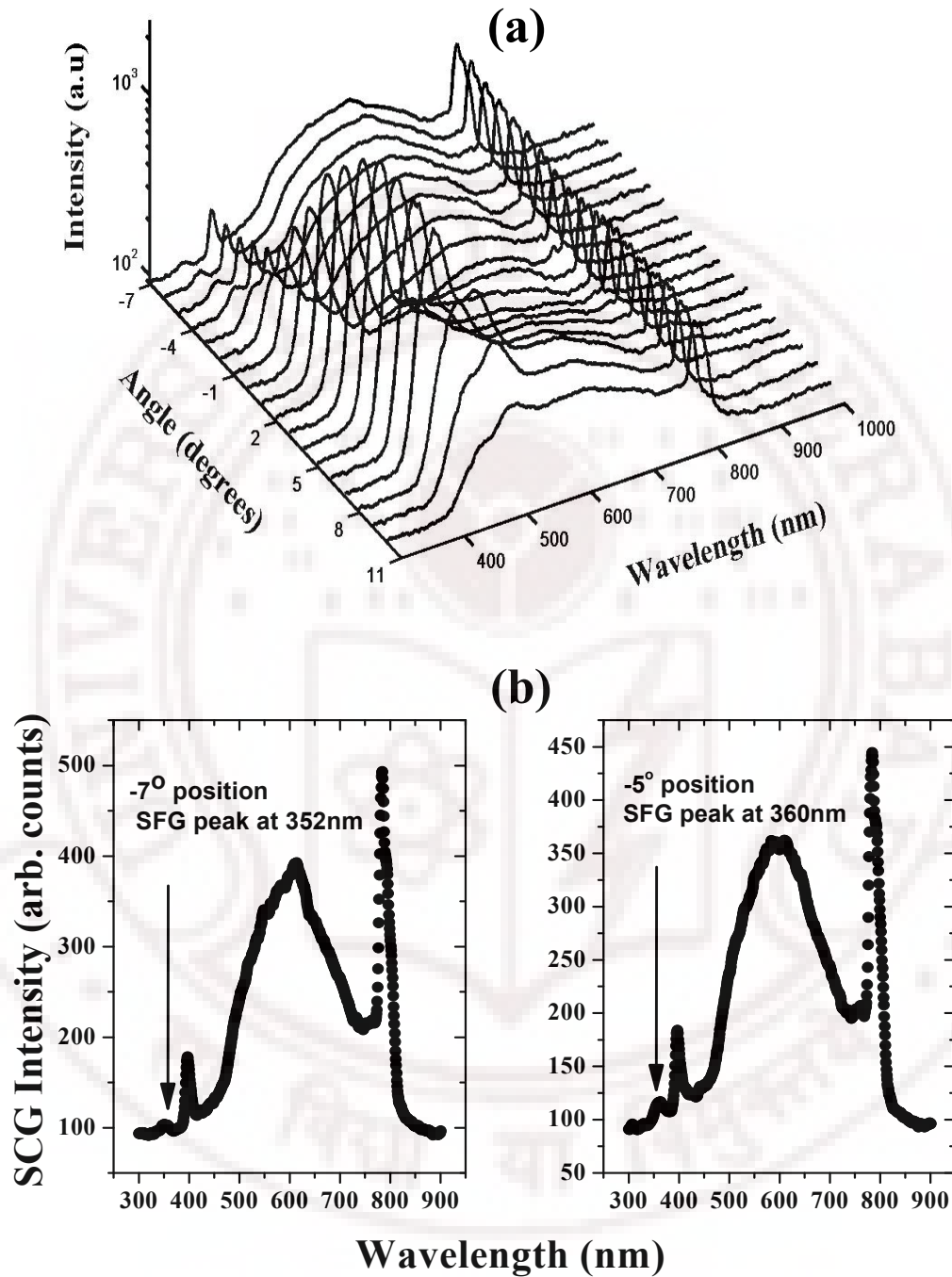


**Fig. 4.13:** (a) A plot showing the tunability of the blue part of the spectrum with change in angle of orientation of the KDP crystal; (b) SFG+SCG spectra obtained for the crystal positions of  $-7^\circ$  and  $-5^\circ$  positions showing SFG peaks at 352 nm and 360 nm, respectively.

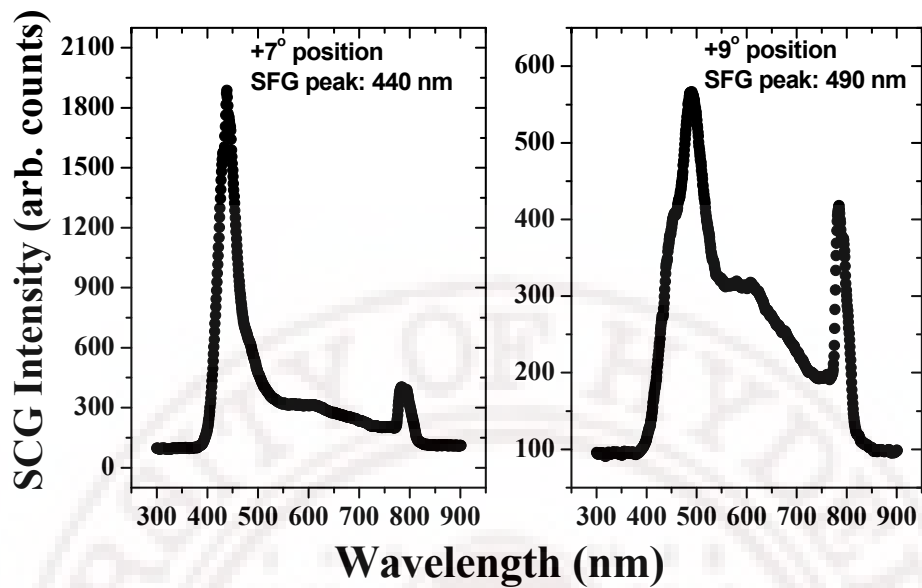


**Fig. 4.14:** SFG+SCG spectra obtained for the crystal positions of  $+7^\circ$  and  $+9^\circ$  positions showing SFG peaks at 440 nm and 490 nm, respectively to show the tunability of SCG with SFG peaks at different orientations of KDP

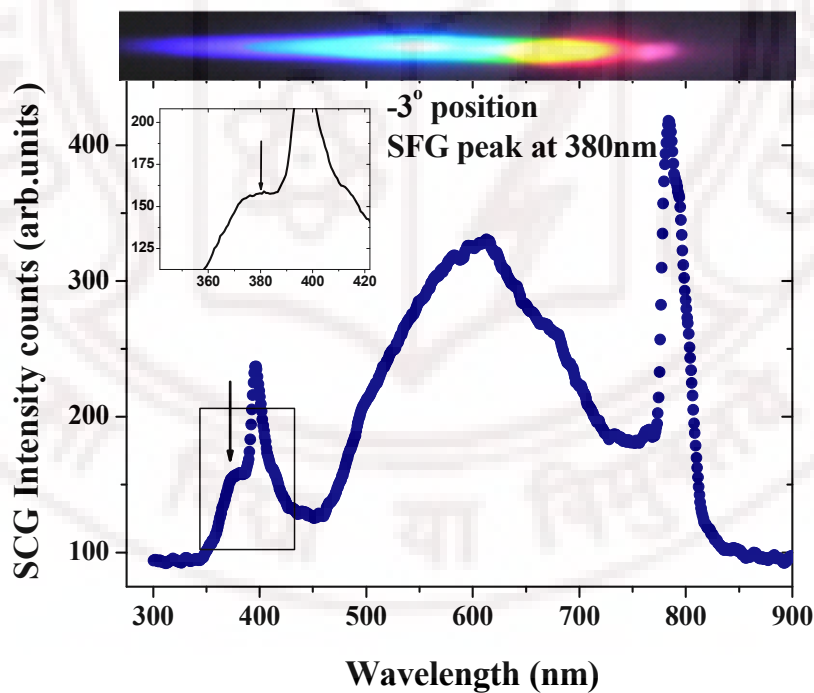


**Fig. 4.15:** Spectrum of SCG with a representative SFG peak to show the enhancement of the spectral content in continuum spectra by combining SFG and SCG in tandem in KDP crystal. The inset shows the SFG peak at 380 nm. The snapshot shows the dispersion of the SCG spectrum with rich content in blue as well as in the green spectral region.

### 4.3.2.1 Theoretical studies

The phase matching angles (Type I) were calculated for the sum frequency generation using the relation:

$$n_{1o}\omega_1 + n_{2o}\omega_2 = n_{3e}\omega_3 \quad (4.1)$$

where  $\omega_1$ ,  $\omega_2$ , and  $\omega_3$  are the frequencies of the fundamental, frequency present in the continuum and the sum frequency generated, respectively and  $n_{1o}$ ,  $n_{2o}$ , and  $n_{3e}$  are the corresponding refractive indices. In this case  $\omega_1$  and  $\omega_2$  were ordinary rays (s-polarized) and  $\omega_3$  is extraordinary ray (p-polarized). The refractive index of the e - ray ( $\omega_3$ ) at different angles was calculated using the relation:

$$\frac{1}{n_e^2(\theta)} = \frac{\cos^2(\theta)}{n_o^2} + \frac{\sin^2(\theta)}{n_e^2} \quad (4.2)$$

We have obtained reasonably good agreement between the calculated phase matching angles and the experimental orientation of the crystal, within the limits of experimental error. The calculated and obtained angles of few representative peaks are presented in the Table-4.1. The tunability achieved in the blue region of the spectrum extends from 352 nm to 489 nm by appropriate rotation of the crystal.

**Table-4.1:** The table showing the few representative wavelength peak shifts with calculated angle of rotation difference ( $\theta_{\text{cal dif}}$ ) and experimental angle of rotation difference ( $\theta_{\text{expt dif}}$ ) to reach from one SFG peak to the next by the rotation of the KDP crystal on the goniometer.

SFG peak wavelength	$\theta_{\text{cal dif}}$	$\theta_{\text{expt dif}}$
425nm to 420nm	0.32°	0.4°
420nm to 415nm	0.29°	0.4°
415nm to 410nm	0.39°	0.5°

Table 4.2 shows the summary of the SCG obtained at different orientations of the crystals ( $\theta_{\text{observed}}$ ). Keeping the input wavelength ( $\lambda_1$ ) as 800

nm, we calculated the mixing wavelength ( $\lambda_2$ ) from the SCG spectrum required to undergo wave-mixing to obtain the corresponding SFG peak ( $\lambda_3$ ) observed experimentally. Using the relation 4.2 we theoretically estimated the required angle of orientation of the crystal ( $\theta_{theory}$ ) with respect to the original position of the crystal (i.e.,  $45^\circ$  relative to c-axis) as shown in figure 4.10. Conclusively we obtained close agreement between the theoretical and observed angle of crystal orientations.

**Table- 4.2:** Summary of experimental and theoretical observations of generation of SFG peaks in SCG

$\lambda_1$ fundamental peak	$\lambda_2$ (theory) mixing wavelength	$\lambda_3$ (observed) SFG peak in SCG	$\theta_{theory}$ wrt $45^\circ$	$\theta_{observed}$ wrt $45^\circ$
800 nm	632 nm	352 nm	$5.8^\circ$	$7^\circ$
800 nm	648 nm	357 nm	$5.2^\circ$	$6^\circ$
800 nm	661 nm	361 nm	$4.8^\circ$	$5^\circ$
800 nm	681 nm	367 nm	$3.6^\circ$	$4^\circ$
800 nm	727 nm	380 nm	$2.7^\circ$	$3^\circ$
800 nm	739 nm	384 nm	$1.8^\circ$	$2^\circ$
800 nm	788 nm	393 nm	$0.7^\circ$	$1^\circ$
800 nm	796 nm	399 nm	$0^\circ$	$0^\circ$
800 nm	819 nm	404 nm	$-0.5^\circ$	$-1^\circ$
800 nm	841 nm	409 nm	$-1.5^\circ$	$-2^\circ$
800 nm	867 nm	415 nm	$-2.4^\circ$	$-3^\circ$
800 nm	890 nm	420 nm	$-3.3^\circ$	$-4^\circ$
800 nm	911 nm	426 nm	$-4.4^\circ$	$-5^\circ$
800 nm	943 nm	432 nm	$-5.2^\circ$	$-6^\circ$
800 nm	980 nm	440 nm	$-6.5^\circ$	$-7^\circ$
800 nm	1199 nm	478 nm	$-7.2^\circ$	$-8^\circ$
800 nm	1270 nm	490 nm	$-7.6^\circ$	$-9^\circ$



From the Table 4.2 we could conclude that the fundamental pump (800 nm) effectively mixes with different frequencies of the continuum starting from 632 nm to 1300 nm, though we cannot detect the wavelengths beyond 960 nm owing to the limitations of the spectrometer. Figure 4.11 (a) does not show much of the IR region of the continuum as we have used an IR filter for suppressing the fundamental going to the spectrometer. The existence of this part of the spectrum (from 850 to 960 nm – within the range of the spectrometer) was confirmed by using a grating to disperse the continuum and by recording the spectrum in the IR region by spatially filtering out the fundamental at 800 nm. Tunability of this blue peak, however, confirms the presence of the spectrum until 1300 nm. Another point to note is that the sum frequency signal broadens towards the longer wavelength as the SFG shifts towards wavelengths more than 430 nm. This is mainly because the refractive index variation with wavelength is slow in the IR region. Thus, we effectively achieve the enhanced continuum extending all the way from 350 nm to 1300 nm. Table 4.3 summarizes the preliminary results from ref. 32 and the improved results obtained with SFG in tandem with SCG in our efforts in enriching the blue spectral content of SCG in KDP crystal

**Table-4.3:** The table shows the lower cut off wavelength achieved

Experimental conditions	$\lambda_{lower\ cutoff}$
Away from phase matching angle	420 nm
At Phase matching angle for SHG	385 nm
At Phase matching angle for Sum frequency generation	350 nm
Lower cut-off wavelength tunable from:	350-500nm

### 4.3.2.2 On polarization of the broadband SCG

The continuum generated retains the polarization of the fundamental excitation pulse and exits the crystal with s-polarization, whereas, the wave-mixing signal generated exits with p-polarization. The output beam, therefore, comprises of wavelengths having orthogonal polarizations. In order to obtain a constant polarization across the entire spectrum a Mach-Zehnder type of arrangement was employed using a prism polarizer to separate the two polarizations and recombining them after the blue region goes through a half-wave plate. One of the mirrors was mounted on the translation stage to achieve equal path difference for both the arms. The schematic experimental arrangement described above is as shown in figure 4.16. The only disadvantage of this scheme is that there is some loss of overall SCG output when it passes the broadband beam-splitter used for remixing beams from the two arms. The disadvantage of having two polarizations can however be an advantage, where one can separate blue and continuum easily with a prism polarizer and use it for pump-probe experiment where the continuum can act like a probe and the SFG emission can be considered as tunable pump source.

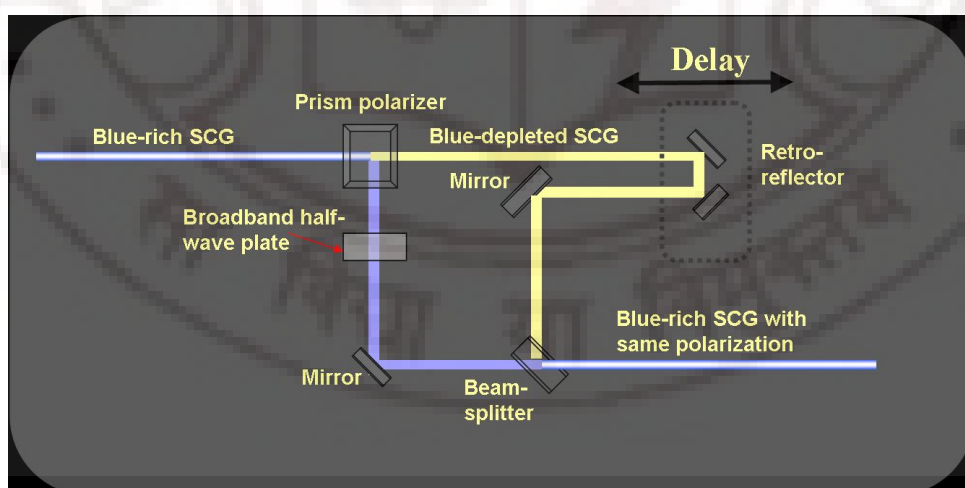


**Fig. 4.16:** Experimental schematic for recombining the orthogonal polarizations generated in SCG in tandem with SFG.

#### 4.3.2.3 Generation of spectrally flat broadband SCG

Various applications requiring a broadband white light source demand that the source is not just, broad band, but also possess constant intensity throughout the emission bandwidth. Of late much interest is shown in the generation of the spectrally broadband SCG [33]. An interesting solution could be to try SCG and wave mixing in a tandem arrangement of differently oriented KDP crystals as shown in figure 4.17(a). Extending our experiments in order to achieve a flat continuum through out the visible range, we employed two slices of KDP, the first one being a cube of 1.2 cm and the second one being a slice of 5 mm thickness, both cut at an angle of  $45^\circ$  with respect to the c-axis. These two crystals were arranged next to each other in tandem as follows [see Fig. 4.15(a)]: The cube was placed at an angle where the peak in the blue region was at 399 nm and the slice was oriented such that its peak was at 423 nm, when each was pumped individually in the absence of the other. The continuum generated by the individual crystals and when both were placed in tandem are as shown in figure 4.17(b). We observe that the tandem generation of white light has almost a very flat spectral output throughout the wavelength range. At the experiment this result gives an indication that the resultant SCG after the two crystals is just addition of the two individual spectra. To negate this we added the spectra of the two individual crystals and averaged as shown in the dotted line of figure 4.17(b). So the most likely phenomenon happening could be that in this tandem arrangement SCG is first generated in the first crystal and the residual fundamental is responsible for SCG in the second crystal with some nonlinear process being contributed by the SCG of the first crystal resulting in spectrally flat-SCG. This was achieved by using just two crystals to form the system. If more crystals were used, it may yield flattened blue and enhanced UV spectrum through wave-mixing. However the usage of this particular arrangement has a straightforward application in the ability to enriching the spectral content of SCG in the spectral region of our choice by choosing appropriately cut crystals.

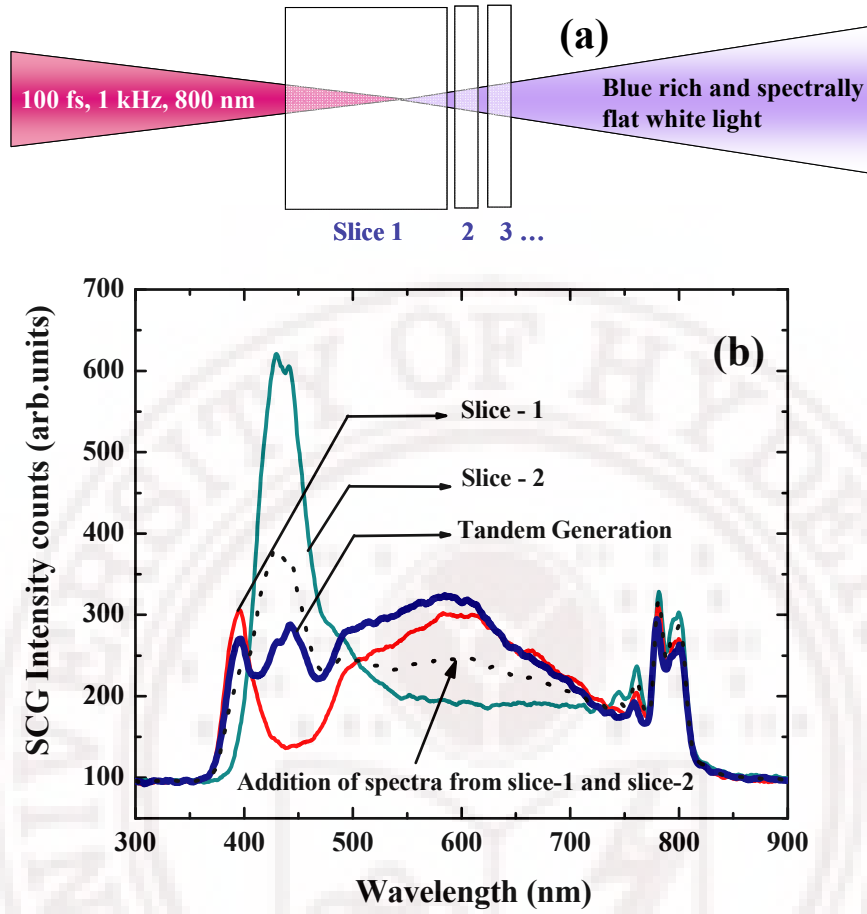


**Fig. 4.17:** (a) Crystal arrangement for tandem generation of spectrally flat SCG; (b) Enhancement of the bandwidth of the continuum generated by using a system of two differently oriented KDP slices that result in the production of a nearly flat spectral output.

#### 4.4 Conclusions:

- In this chapter, Potassium Di-hydrogen Phosphate (KDP) crystal is studied as a potential SCG media.
- The intrinsic  $\chi^{(3)}$  anisotropy of KDP was discussed by performing the degenerate four-wave mixing studies with a goal to study SCG in KDP with different orientations. We estimate the  $P_{cr}$  for the KDP crystal along the c-axis to be **~2.8 MW**.

- Initial SCG studies were performed in a z-cut KDP crystal generated along its c-axis and all the general characteristics of SCG were observed. An efficiency of ~23 % over the visible spectral range was achieved. The coherent nature of the white light is confirmed using Young's double slit and Michelson interferometer experiments.
- From an earlier work [32] when the crystal oriented at the phase matching angle for second harmonic generation (SHG), we obtain SHG in addition to the supercontinuum in the spectrum. The reduction in SCG intensity in the presence of SHG is a major disadvantage in this scheme because of the depletion of the input field by the SHG conversion before the onset of self-focusing of the fundamental, which initiates continuum generation. As an effort to get over this disadvantage of the scheme of SHG and SCG in tandem a new method of achieving broadband femtosecond white light in a KDP was employed where we make use of SFG in tandem with SCG in the KDP crystal.
- Without any phase matching for SHG or sum frequency generation, we observe continuum from 410 nm to 960 nm. However, as we rotate the crystal to a position where the phase matching condition for parametric wave mixing is satisfied we obtain new frequencies in the blue region, tunable with angle. Thus KDP can be effectively used for generation of sum frequency signals along with continuum generation to produce broadband white light generation from 350 nm to 1300 nm. Presence of signal in the region from 960 nm to 1300 nm was confirmed through the appearance of wave mixing signal.
- Further, we have also demonstrated a novel way of achieving white light having a broadband and spectrally flat SC by employing tandem arrangement of differently oriented crystals.

#### 4.5 References:

1. J. K. Ranka, R. S. Windeler, A. J. Stentz: Opt. Lett. **25**, 25 (2000); T. A. Birks, W. J. Wadsworth, and P. S. J. Russell: Opt. Lett. **25**, 1415 (2000); S. Coen, A. H. L. Chau, R. Leonhardt, J. D. Harvey, J. C. Knight, W. J. Wadsworth, P. S. J. Russell: J. Opt. Soc. Am. B, **19**, 753 (2002); A.K. Dharamdhikari, F. A. Rajgara, D. Mathur: Appl. Phys. B, **80**, 61 (2005); K. Wang, L. Qian, H. Luo, P. Yuan, H. Zhu: Opt. Express, **14**, 6366 (2006)
2. H. J. Bakker, P. C. M. Planken, L. Kuipers, and A. Lagendijk: Phys. Rev. A **42**, 4085 (1990); F. Wise, L. Qian, and X. Liu: J. Nonlinear Opt. Phys. Mater. **11**, 317 (2002).
3. X. Liu, L. Qian, and F. Wise: Opt. Lett. **24**, 1777 (1999)
4. K. Beckwitt, F. W. Wise, L. Qian, L. A. Walker II, E. C.-Said: Opt. Lett. **26**, 1696 (2001)
5. S. Zhou, D. G. Ouzounov, F. W. Wise, I. Bazarov, and C. Sinclair, Appl. Opt. **46**, 8488, 2007
6. X. Liu, L. J. Qian, F. W. Wise: Phys. Rev. Lett. **82**, 4631 (1999); I. N. Towers, B. A. Malomed, and F. W. Wise, Phys. Rev. Lett. **90**, 123902 (2003)
7. M. Marangoni, C. Manzoni, R. Ramponi, G. Cerullo, F. Boronio, C. D. Angelis, and K. Kitamura, Opt. Lett., **31**, 534 (2006)
8. J. Moses, and F. W. Wise, Phys. Rev. Lett., **97**, 073903 (2006)
9. M. Aoyama, T. Harimoto, J. Ma, Y. Akahane, and K. Yamakawa, Opt. Express **9**, 579 (2001)
10. V. G. Dimitriev, G. G. Gurzadyan, and D. N. Nikogosyan, *Handbook of Nonlinear Optical Crystals*, 2<sup>nd</sup> revised ed. (Springer, Berlin, 1977).
11. R. A. Ganeev, I. A. Kulagin, A. I. Rysanyanski, R. I. Tugushev, and T. Usmanov, Opt. and Spect., **94**, 561 (2003); R. A. Ganeev, I. A. Kulagin, A. I. Rysanyansky, R. I. Tugushev, and T. Usmanov, Opt. Commun., **229**, 403 (2004)
12. R. Adair, L. L. Chase, and S. A. Payne, Phys. Rev. B **39**, 3337 (1989).
13. Q. Guo and S. Chi, J. Opt. A: Pure Appl. Opt. **2**, 5 (2000)



14. I. A. Kulagin, R. A. Ganeev, R. I. Tugushev, A. I. Ryasnyansky, and T. Usmanov, *J. Opt. Soc. Am. B* **23**, 75 (2006)
15. R. L. Sutherland, *Handbook of Nonlinear Optics* (Dekker, New York, 1996).
16. J. H. Marburger, *Prog. Quant. Electr.*, **4**, 35 (1975)
17. N. Bloembergen, *Opt. Commun.* **8**, 285–288 (1973).
18. W. Liu, S. Petit, A. Becker, N. Akozbek, C.M. Bowden, S.L. Chin, *Opt. Commun.* **202**, 189 (2002)
19. A.K. Dharmadhikari, F. A.Rajgara, and D. Mathur, *Appl. Phys. B* **82**, 575–583 (2006)
20. P. Lambropoulos, *Phys. Rev. Lett.* **29**, 453 (1972)
21. A.S. Sandhu, S Banerjee, and D Goswami, *Opt. Commun.* **181**, 101 (2000)
22. S. Petit, A. Talebpour, A. Proulx, and S.L. Chin, *Opt. Commun.* **175**, 301 (2000)
23. A. M. Perelomov, V.S. Popov, and M.V. Terent'ev, *Sov. Phys. JETP* **23**, 924 (1966)
24. G. Fibich, and B. Ilan, *Phys. Rev. Lett.* **89**, 013 901 (2004)
25. G.P. Agarwal, *Nonlinear Fiber Optics* (Academic, New York 2001); K. Midorikawa, H. Kawano, A. Suda, C. Nagura, and M. Obara, *Appl. Phys.Lett.* **80**, 923 (2004)
26. R. G. Brewer, J. R. Lifshitz, E. Garmire, R. Y. Chiao, and C. H. Townes, *Phys. Rev.* **166**, 326–331 (1968).
27. K. Cook, A. K. Kar, and R. A. Lamb, *Appl. Phys. Lett.* **83**, 3861-3863 (2003).
28. W. Watanabe and K. Itoh, *Jpn. J. Appl. Phys.* **40**, 592-595 (2001).
29. X. Gu, L. Xu, M. Kimmel, E. Zeek, P. O'Shea, A.P. Shreenath, R. Trebino, and R.S. Windeler, *Opt. Lett.* **27**, 1174 (2002); X. Gu, “*Measuring Ultracomplex Supercontinuum Pulses and Spatio-Temporal Distortions*,” Ph.D. thesis, Georgia Institute of Technology (2004).
30. J. M. Dudley and S. Coen, *Opt. Lett.* **27**, 1180-1182 (2002); R. R. Alfano, *The Supercontinuum laser source*, Springer–Verlag, Berlin (1989).



31. R.A. Negres, and J.M. Hales, *IEEE Journal of Quantum Electronics*, **38**, 1205-1216 (2002); B. Schenkel, R. Paschotta, and U. Keller, *J. Opt. Soc. Am. B*, **22**, 687-693 (2005); G. Cerullo and Sandro de Silvestri, *Rev. Sci. Instrum.* **74**, 1- 18(2003); T. Udem, R. Holzwarth, and T.W. Hansch, *Nature*, **416**, 233 – 237 (2002); M. Balu, J. Hales, D. Hagan, and E. Van Stryland, *Opt. Express* **13**, 3594-3599 (2005); J. H. Frank, A. D. Elder, J. Swartling, A. R. Venkitaraman, A. D. Jeyasekharan, C. F. Kaminski, *J. Microsc.* **227**, 203–215 (2007).
32. N. K. M. Naga Srinivas, S. Sree Harsha, and D. Narayana Rao, *Opt Express*, **13**, 3224 (2005)
33. C. Kakkar and K. Thyagarajan, *Opt. Express* **14**, 10292 (2006); S. Martin-Lopez, M. Gonzalez-Herraez, A. Carrasco-Sanz<sup>1</sup>, F. Vanholsbeeck, S. Coen, H. Fernandez, J. Solis, P. Corredera, and M. L Hernanz, *Meas. Sci. Technol.* **17**, 1014–1019 (2006).

The logo of the University of Hyderabad is a circular emblem. The outer ring contains the text "UNIVERSITY OF HYDERABAD" at the top and the Sanskrit motto "सा विद्या या विमुक्तये" at the bottom. The inner circle features a central sun-like symbol with rays, flanked by a stylized atom on the left and a lightning bolt on the right, all set against a background of a grid of dots.

# CHAPTER 5

### Abstract

*In this chapter, a systematic study of depolarization of supercontinuum across its spectral range as a function of the femtosecond laser pump intensity for an anisotropic crystalline condensed medium, KDP crystal, and compare our results with commonly used supercontinuum generation materials namely BK-7 glass (representing isotropic amorphous condensed media) and BaF<sub>2</sub> (isotropic crystalline condensed media) is presented. Our results show that at higher input power depolarization in the continuum increases for BK-7, BaF<sub>2</sub> and along the direction of the optic axis KDP crystal. However in case of KDP crystal we observe that the depolarization properties are strongly dependent on (i) the plane of polarization of incident light and (ii) the orientation of the crystal with respect to the incident light. Our studies also confirm that one can achieve SCG in a KDP crystal that maintains the same state of input polarization even at high input intensities when proper orientation of the crystal is used.*

# **Depolarization properties of the supercontinuum generated in condensed media and its control**

## **5.1 Introduction**

With its high spatial coherence, good polarization properties, spectral brightness and high peak intensities enabling strong light-matter interaction in the nonlinear regime [1], supercontinuum (SC) has found myriads of applications as an ideal broadband ultrafast light source. In the last two decades much research has gone into the generation of SC in various materials like microstructured fibers, photonic bandgap crystal fiber (PCF), birefringent fibers, BaF<sub>2</sub> crystal, sapphire [2]. As discussed in chapter-4, we reported the generation of broadband white light KDP crystal, where we have made use of the second harmonic generation in tandem with SCG in the KDP crystal [3]. By employing SCG and sum frequency generation (SFG) in tandem, the tunability of SCG in the shorter wavelength regime (i.e., < 400nm) was achieved along with the generation of ultra-broadband SCG with suitable orientation of the crystal [4].

Apart from generating spectrally broad SC, a prior knowledge of the polarization properties of SCG is of utmost importance as continuum with stable polarization properties plays an important role in many of the spectroscopic applications. Major applications of SCG that include femtosecond time resolved spectroscopy [5], optical pulse compression for generation of ultrashort pulses [6], a seed pulse of an optical parametric amplifier [7], the broadband spectrum LIDAR [5], and two-photon absorption spectroscopy [9], optical frequency metrology [10], and biomedical applications[11]. With the advent of SCG in microstructured and birefringent photonic crystal fibers the systematic study of polarization properties of obtained SCG have become even more critical as the resultant polarization of SCG suffers from polarization fluctuations because of noise in the input pump pulse and lot of efforts have gone in understanding the SCG phenomenon in fibers [12]. Thus, in this scenario, research in materials for

generating SCG with stable polarization properties has gained precedence over generating SCG with ultra-broad spectral width.

The general assumption is that the generated supercontinuum (SC) follows the state of polarization of the input pump pulse [1]. However, a distinct degree of the degradation of polarization (depolarization) of SC generated in isotropic materials is known to set in with increase in the input intensities owing to the onset of multiphoton-induced free electron generation which also corresponds to the onset of asymmetry in white light spectra [13]. For linear input polarization, the SC spectrum was found to show strong depolarization around the input wavelength, while the preservation of the input polarization is pronounced towards the blue spectral region [14]. As many nonlinear optical experiments require higher intensities for the continuum, it becomes a necessity to pump at higher intensities. While doing so the medium generating the continuum gets damaged and to avoid such damages, it is commonly practiced to rotate / translate the medium. Such rotations /translations were assumed to produce stable intensity and do not affect the continuum properties [15]. However, the polarization of SC is ascertained to depend strongly on the orientation of crystalline media (like sapphire) with respect to the plane of polarization of the pump light [16] thus contradicting the earlier assumption.

From the available literature pertaining to the study of polarization properties of SCG, most of the studies are carried out in either of the following ways: (a) an integrated fashion, i.e., over the entire spectrum [1,17]; (b) in a very narrow spectral range but covering the entire SC spectra [13,16]. Recently, interest in the study of the spectral dependence of the polarization properties has gained precedence over the integrated measurements. In this regard extensive work on the polarization properties of SCG in cubic materials like  $\text{CaF}_2$  and sapphire crystal were reported [14, 18]. Polarization of SC generated in  $\text{CaF}_2$  plate was shown to strongly depend on the orientation of the crystal with respect to the plane of polarization of the pump light. The intensity modulation of the broad blue-shifted wing of SC against crystal rotation for both the polarizations

parallel and orthogonal to the polarization of the pump beam was observed with both  $\text{CaF}_2$  and Sapphire [18]. This study [18] was performed with input power that corresponds to a maximum of  $10P_{\text{cr}}$  for  $\text{CaF}_2$  ( $P_{\text{cr}} = 2\text{MW}$ ) where a stable single filament could be obtained. As with increase in input power results in the increase of input peak intensities one would expect an increase in the degree of depolarization. This demands the study of polarization properties of the SC at high input powers.

From another point of view, much research has been concentrated on the manipulation of temporal and spectral characteristics of the SCG. The photonic crystal fibers (PCFs) were investigated primarily because PCFs allow engineering of the spectral dispersion and confinement of light through the underlying periodicity of their structure [2]. The spatio-spectral control and localization of SC was demonstrated through the nonlinear interaction of spectral components in extended periodic structures [19]. The control of the onset of filamentation had been achieved by rotating the plane of polarization of incident light [20]. The control of the spectral content of SCG was achieved by manipulation of the polarization of input laser pulses [21]. However, no report, till date, has ever dealt with the control of polarization properties of the generated SC and hence any research towards this purpose would be of great relevance.

In the light of the prevailing knowledge of the above mentioned studies on polarization properties of SCG we performed studies of depolarization (defined as loss of input polarization) of SC at a very high input intensity in KDP crystal. In this chapter, we present our detailed systematic study of depolarization of SCG across its spectral range with respect to increase in input powers from  $\sim 50 P_{\text{cr}}$  to  $2500P_{\text{cr}}$  for three classes of popular SCG materials: (a) BK-7 glass ( $P_{\text{cr}} \sim 2.5\text{ MW}$ ) representing isotropic amorphous condensed media, (b)  $\text{BaF}_2$  ( $P_{\text{cr}} \sim 3.4\text{ MW}$ ) isotropic crystalline condensed media and (c) KDP crystal ( $P_{\text{cr}} \sim 2.8\text{ MW}$  for a z-cut crystal) anisotropic crystalline condensed media. Our results at high input peak powers show that there is complete depolarization of SCG in all media. However in case of KDP crystal we observe that the depolarization

properties are dependent on (i) the plane of polarization of incident light, and (ii) the incident orientation of the crystal. Our study also confirms that one can achieve SCG that maintains the same state of input polarization even at high input intensities with appropriate orientation of the crystal. We also performed the integrated spectral intensities measurements to supplement our spectral dependant data.

Our results show, for the first time to the best of our knowledge, that the depolarization (polarization degradation) of SCG is controllable when generated in a quadratic nonlinear media like KDP crystal. The polarization of the generated SC could be maintained similar to that of the incident pulses even at high input powers.

## 5.2 Experimental Details

The experiments were performed with a Ti: Sapphire system (MaiTai + Spitfire, Spectra Physics Inc.), delivering 1 mJ, 100 fs duration laser pulses at 800 nm and 1 kHz repetition rate. The input polarization is p-polarized (extinction ratio  $<10^{-3}$ ). The SC is generated by focusing the 800 nm pulse into three different media using a focusing lens of focal length  $f = 300$  mm. The media considered for the study are (i) a z-cut KDP crystal with dimensions  $10 \times 8 \times 5$  mm<sup>3</sup>, (ii) 1.5 cm thick BK-7 glass, and (iii) 10 mm BaF<sub>2</sub> crystal (EKSLPA, Lithuania) cut for (001) orientation. While comparing the SCG in these three media, input beam is considered to be polarized parallel to (100) axis of the crystal and propagating along the (001) axis of the KDP and BaF<sub>2</sub> crystals as shown in figure 5.1. The calculated beam waist, taking Gaussian beam approximation, at the focal point in vacuum was  $\sim 50$   $\mu$ m. The face of the sample was always placed 2 cm away before the focus point to avoid any laser induced damage. The incident average power used for the study was varied from 10 - 600 mW corresponding to a maximum peak power variation of  $\sim 0.1 - 6.0$  GW. This accounts for peak intensity of a maximum  $\sim 15 \times 10^{12}$  W/cm<sup>2</sup> on the front face of



the sample. The calculations of the peak powers and peak intensities were performed assuming the Gaussian beam profile for the incident pulse.

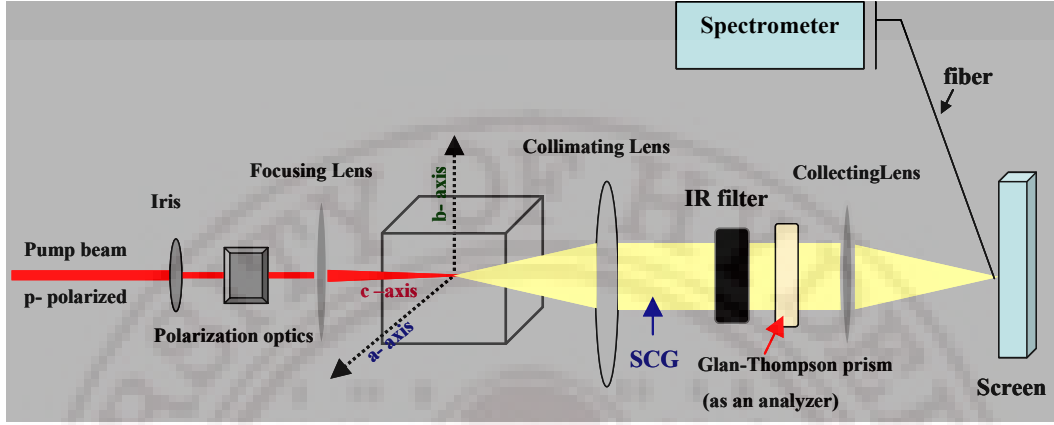


**Fig. 5.1:** Experimental schematic used for the study on polarization properties of SCG

The spectra of continuum are recorded using a fiber coupled spectrometer (Ocean Optics USB2000) after collimation and suppressing fundamental by an IR filter thus limiting our study of SC to the visible region (400 – 750 nm). The polarization of the SC is analyzed with Glan-Thomson polarizer (extinction ratio  $\sim 10^5$ , Thorlabs). Care has been taken to see that the SC entering the Glan polarizer is well collimated. Neutral density filters with known absorption spectra in the region were used to collect the continuum spectra obtained at high input powers. Taking into account the absorption spectra of the filters used, the resultant spectra thus obtained are corrected and presented. For the integrated intensity measurements the SC in both parallel ( $I_{\text{par}}$ ) and perpendicular position ( $I_{\text{orth}}$ ) are performed by focusing onto a photodetector (FND100) after suppressing the fundamental using a 750nm low pass filter (Thorlabs). Different orientations of the crystal presented in the study were confirmed by X-ray peizogoniometer (Rigaku, Japan).

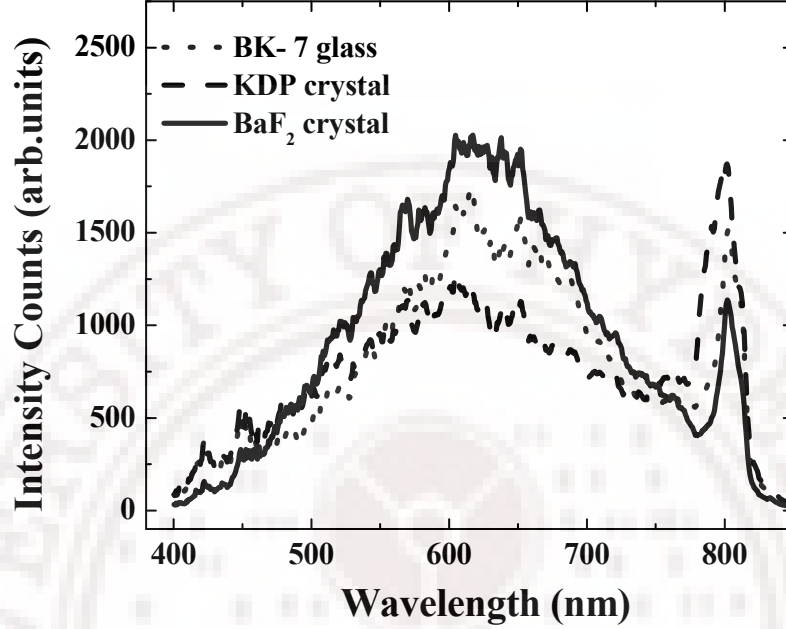
### 5.3 Results and discussion:

#### 5.3.1 Depolarization properties of SCG from BK-7, BaF<sub>2</sub> and KDP crystal

In this section we discuss our results on the degree of depolarization that sets in the supercontinuum generated at high input powers in BK-7, BaF<sub>2</sub> and KDP. To compare the continuum generated in these media, we followed the following methodology [14]. The polarization of the SC was examined by the transmitted SC spectra through the analyzer at perpendicular [ $I_{orth}(\lambda)$ ] and at parallel orientations [ $I_{par}(\lambda)$ ] of the Glan polarizer with respect to the input polarization as a function of the wavelength ( $\lambda$ ). We define the ratio of  $I_{par}(\lambda)$  to  $I_{orth}(\lambda)$  as the polarization ratio [ $\rho(\lambda)$ ]. Thus, larger the observed changes of the SC polarization (depolarization) the smaller the resulting values of  $\rho$ , and hence the input polarization retained in the process of continuum generation can be presented by the polarization ratio. We define the integrated polarization ratio ( $\rho_{int}$ ) as the ratio of integrated spectral intensity (over the entire continuum)  $I_{par}^{int}$  to  $I_{orth}^{int}$ . While comparing the SC in the three media, we mention the different peak powers in multiples of critical power for self-focusing ( $P_{cr}$ ) for BK-7 glass.

Figure 5.2 shows the typical SC spectra of the different media under consideration for an input power of 350mW, corresponding to  $\sim 1400P_{cr}$  and a peak intensity of  $8 \times 10^{12} \text{ W/cm}^2$ . The broad blue pedestal at such a high input power is mainly because, with increase of the incident power, apart from the Kerr effect, free electrons that are generated due to multi-photon ionization (MPI) also begin to contribute to spectral broadening of the fundamental input pulse. In the high power regime, the time variation of the refractive index due to these free electrons leads to asymmetric spectral broadening that is blue shifted while the space variation of the refractive index gives rise to defocusing [22]. The free electrons generated due to MPI give rise to plasma that induces a spectral shift. This onset of plasma induced free-electron generation has been suggested as the reason for the polarization degradation [13]. Thus, one would expect the

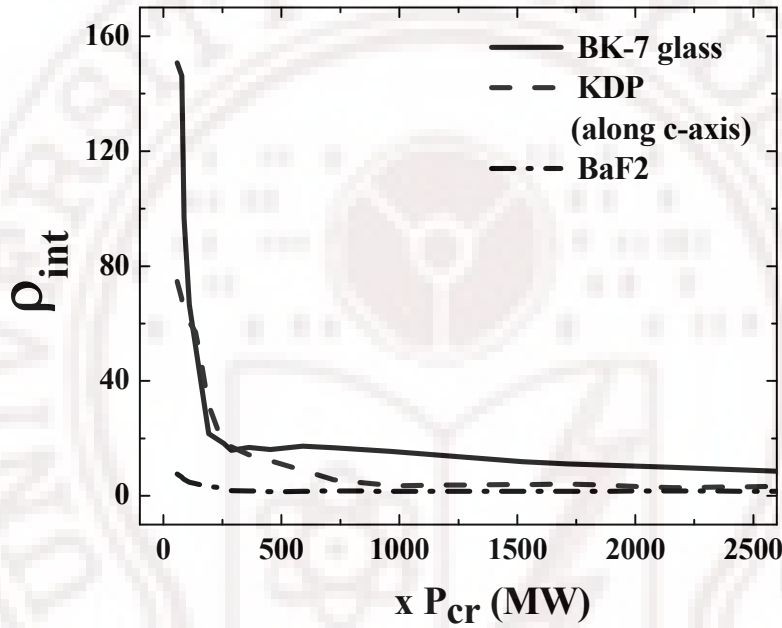
polarization of the SCG to get degraded to a large extent at these higher intensities.



**Fig. 5.2:** Supercontinuum spectra of transparent media under study: BK-7 glass, a z-cut KDP crystal positioned as in Fig.1, BaF<sub>2</sub> crystal

The above discussion is very apparent in Fig. 3 that shows the variation of  $\rho_{\text{int}}$  with increase in input power, where for the input power corresponding to  $1400P_{\text{cr}}$ , the integrated polarization ratio is very low indicating maximum depolarization. From Fig.3, we observe that as the input powers go beyond  $250P_{\text{cr}}$  there is a dramatic reduction in the  $\rho_{\text{int}}$  of the SC for all the three media and beyond  $500P_{\text{cr}}$  the  $\rho_{\text{int}}$  remains a minimum indicating that the SC generated for input powers  $> 500P_{\text{cr}}$  for any media is mostly depolarized. A closer look into the plot also gives an indication that for lower input powers SC from BK-7 glass (amorphous) has better  $\rho_{\text{int}}$  when compared to that of the other two crystalline media. This observation is in agreement with that of an earlier work by Midorikawa *et al* [16] which reports a self-induced polarization change of the SC in crystalline media that are optically isotropic and do not show linear birefringence in an ordinary optical field. Though the KDP crystal is an anisotropic media, in this case, we can safely assume it to be isotropic as the SC

is generated along its c-axis that coincides with its optic axis. Thus, at the first look one would get the impression that for lower input powers the SCG in BK-7 glass has least depolarization; though with increase in input power all media generate depolarized continua. As the data presented above is the integrated intensity over the entire continuum, we carried out experiments to see the depolarization at different regions of the spectrum using a spectrometer and the Glan polarizer.



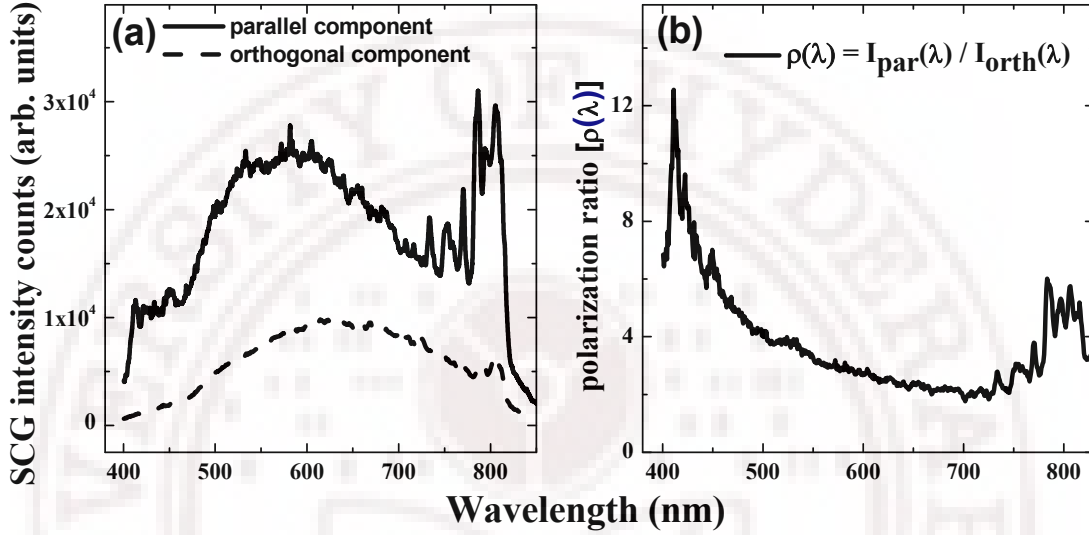
**Fig 5.3:** Plot of integrated polarization ratio of the SC from the different media with increase in the input power in terms of the critical power ( $P_{cr}$ ).

Figure 5.4 illustrates the methodology we followed for obtaining the spectral dependence of polarization. The transmitted SC spectra through the analyzer are first recorded at perpendicular [ $I_{orth}(\lambda)$ ] and at parallel orientations

[ $I_{par}(\lambda)$ ] of the Glan polarizer depicted in figure 5.4(a). The quantity  $\frac{I_{par}(\lambda)}{I_{orth}(\lambda)}$

referred to as the polarization ratio [ $\rho(\lambda)$ ] is then plotted with wavelength as the x-axis as shown in figure 5.4(b). The spectra shown here correspond to SC from a z-cut KDP crystal as shown in figure 5.2. Clearly, if the  $I_{orth}(\lambda)$  component is high or comparable to  $I_{par}(\lambda)$  component of SC then  $\rho(\lambda)$  attains small value

indicating that more depolarization of the SC as one would expect the  $I_{orth}(\lambda)$  component to be minimal if SC is to maintain high degree of input linear polarization. Therefore as per our assertion earlier in this section, the quantity  $\rho(\lambda)$  essentially contains the depolarization information of SC generated.



**Fig. 5.4:** Illustration of the methodology followed to study the depolarization properties of SC. (a) shows the two orthogonal components of SC after analyzer; (b) shows the  $\rho(\lambda)$  with respect to wavelength

Fig. 5.5 shows the polarization ratio  $[\rho(\lambda)]$  of the SC across the spectra under consideration at a very low input power ( $P_{in} \sim 0.6$  GW, corresponding to  $\sim 250P_{cr}$  and  $I_{in} \sim 1.5 \times 10^{12}$  W/cm<sup>2</sup>). Most striking observation to make here and from figure 5.4(b) is that the  $\rho(\lambda)$  for SC of any of the three media is not the same across the continuum spectrum. We find the small peak at 800 nm (residual of fundamental) is surrounded by a pronounced SC depolarization. In contrast, the blue region of the SC (450-750 nm) shows lesser depolarization, and  $\rho$  rises towards the blue edge of the spectrum.

The observed phenomenon can be rationalized by considering that since different spectral components of the SC are generated at different positions along the propagation pathway of the pulse through the medium, the fate of the

polarization of each component is determined by its corresponding nonlinear anisotropic birefringence (NAB) and its interaction length in the SC filament. Because of the input power being several times the critical power of self-focusing, the input pulse effectively undergoes catastrophic collapse resulting in space-time focusing and self-steepening forming an “optical shock” wave inside the medium at a certain distance from the filament starting point [23]. The multiphoton absorption and plasma defocusing weaken the trailing edge of the pulse. Therefore, the effective length of interaction of the SC spectrum components, with the most intense part of the pulse at 800nm, decreases toward the blue part of the spectrum. Thus a more pronounced depolarization is observed for the SC spectrum around the input wavelength, while minor depolarization occurs in the blue wing.

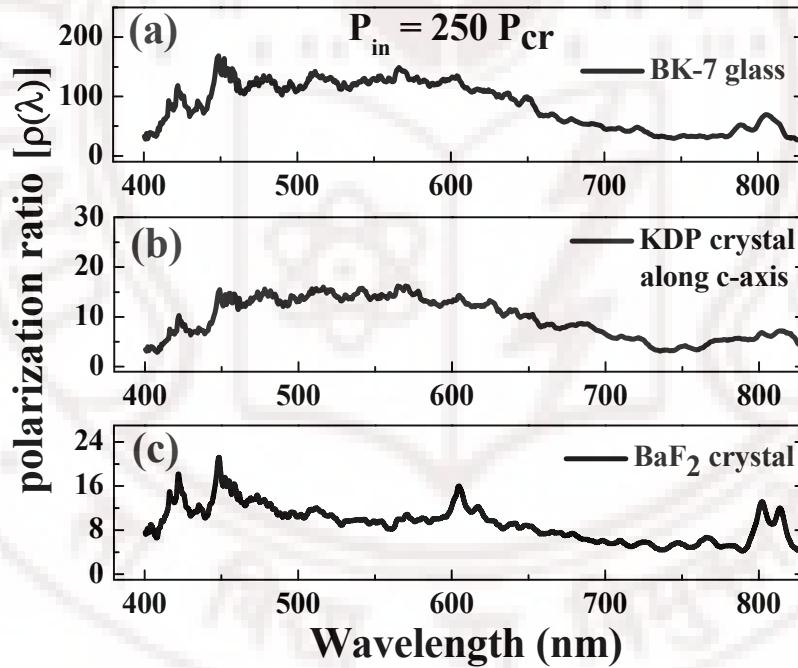


Fig. 5.5: Spectral polarization ratio  $[\rho(\lambda)]$  of the SC at  $P_{in} = 250P_{cr}$

Comparing  $\rho(\lambda)$  in figure 5.5 for the different media we observe that BK-7 glass has a better ratio compared to that of KDP and BaF<sub>2</sub> crystal for lower input powers. In the case of BK-7 glass the value of  $\rho$  in blue region is as high as

~150 when compared to those of KDP and BaF<sub>2</sub> crystal which have values less than 25. The depolarization of SC from BK-7 glass is lower presumably because owing to its amorphous nature the effect of NAB is minimal at lower intensities and the depolarization is mainly because of the interaction of the input pulse with the plasma [13]. However, we find further depolarization in case of the crystalline media like KDP and BaF<sub>2</sub> in addition to the effect of plasma, as there is a substantial contribution of self-induced nonlinear polarization change due to the effect of NAB because of the intrinsic anisotropic  $\chi^{(3)}$  tensor (i.e., it contains some nonzero off-diagonal elements) [14]. Thus, it can be concluded that for lower input powers the material representing amorphous isotropic media has a better polarization ratio compared to the crystalline media. On the other hand, at such lower input powers the blue pedestal in the SC spectra is not intense enough and that could prove a limitation for the applications requiring spectrally bright SC source.

BK-7 glass which shows good  $\rho(\lambda)$  at low input powers nevertheless experiences gradual reduction with the input power. Figure 5.6 shows the variation of the  $\rho(\lambda)$  for input peak powers of 250, 600, 1400 and 2500 P<sub>cr</sub> that corresponds to the input intensities of 1.5, 3.5, 6.3,  $15 \times 10^{12}$  W/cm<sup>2</sup> respectively. For input of 2500P<sub>cr</sub> we observe that the overall  $\rho$  is less than 10 throughout the blue pedestal of the SC indicating maximum depolarization. This is because though BK-7 being an optically isotropic glass, at high input powers it is known to undergo self-induced polarization change because of the transient nonlinear birefringence induced by the incident laser beam itself inside the sample [24]. On the other hand, KDP and BaF<sub>2</sub> crystals show rapid depolarization compared to BK-7 at higher input powers as shown in figure 5.7 and figure 5.8 respectively. For input of 2500P<sub>cr</sub> we observe that the overall  $\rho$  is less than 5 and the depolarization has almost flat response over the entire spectra. Thus, it can be generalized that SC generated in any media at such high input powers has maximum depolarization.



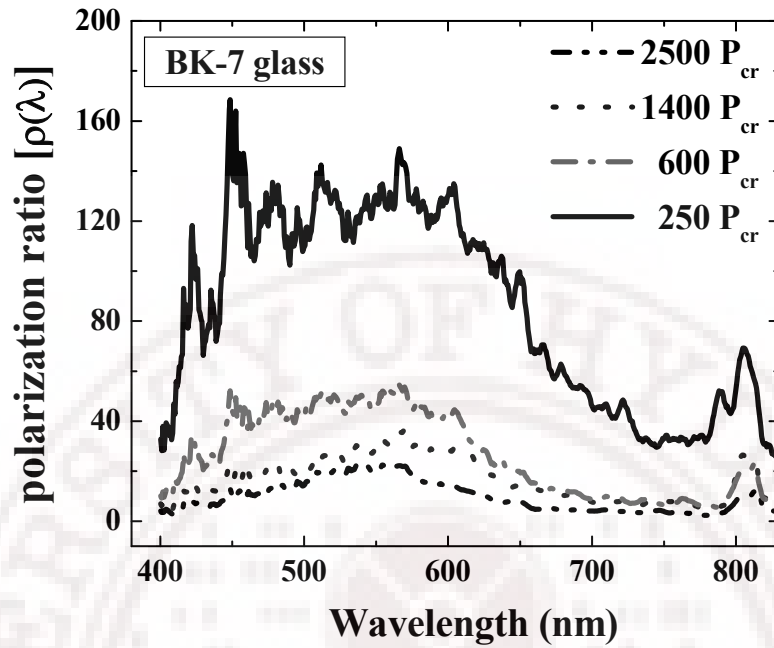


Fig. 5.6: Plot of spectral polarization ratio  $[\rho(\lambda)]$  of the SC from BK-7 glass with increase in the input power in terms of the critical power ( $P_{cr}$ ).

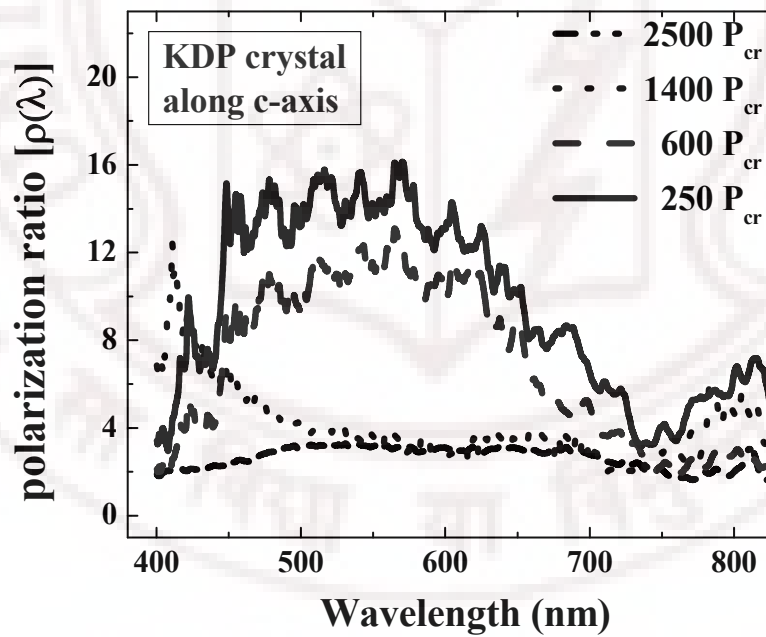
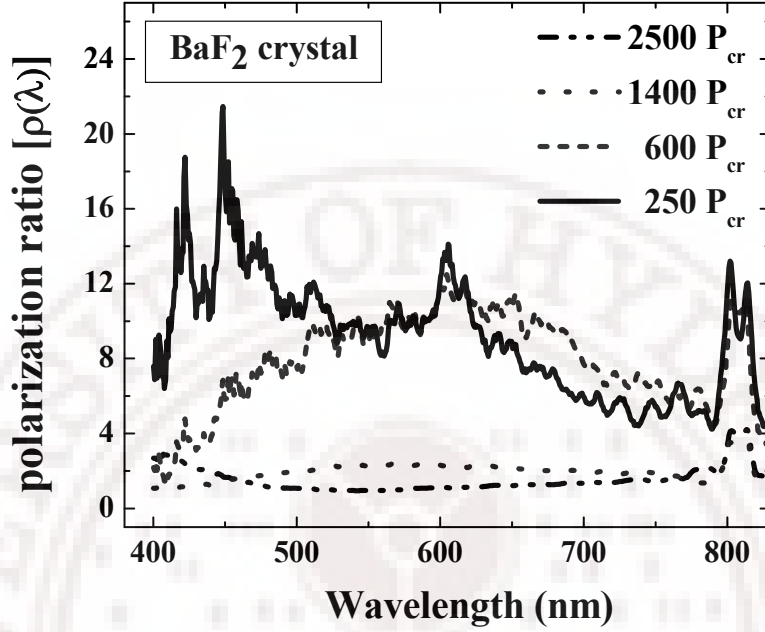


Fig. 5.7: Plot of spectral polarization ratio  $[\rho(\lambda)]$  of the SC from KDP crystal along c-axis with increase in the input power in terms of the critical power ( $P_{cr}$ ).



**Fig. 5.8:** Plot of spectral polarization ratio  $[\rho(\lambda)]$  of the SC from  $\text{BaF}_2$  crystal along c-axis with increase in the input power in terms of the critical power ( $P_{\text{cr}}$ ).

The estimated peak power for the formation of stable single filament is  $\sim 26\text{MW}$  (i.e.,  $\sim 10P_{\text{cr}}$ ) for the media considered here. As we increase the input power, ( $\sim 100P_{\text{cr}}$ ) we start observing multiple filament formation where the number of filaments sharply increases. Each of the individual filaments can generate white light continuum [25]. The supercontinuum that is generated from each of these filaments possesses a high degree of spatial coherence, which has been demonstrated using a simple Young's double slit configuration [3, 26]. We start observing coherent interaction between the filaments leading to the fluctuating interference patterns in the far field image of the output on a screen. At still higher powers ( $>270\text{ MW}$ ,  $\sim 100P_{\text{cr}}$ ), the number of filaments become very large with the effect that the intensity fluctuations within the profile of the beam almost diminishes. When the filaments are more than one but are finite in number, the interference due to the filaments leads to colored fringe-like pattern within the beam profile. With large number of filaments, these patterns merge leading to a uniform white continuum at every position of the beam cross-section.

The polarization of the continuum remained the same as the input polarization until the powers are raised to  $\sim 100P_{cr}$  at which the number of filaments would be much higher than single filament. As mentioned earlier, though these filaments interfere and lead to multiple interference pattern across the beam cross-section, we still observe that the polarization ratio is well maintained. Only at the powers larger than  $100P_{cr}$ , one starts observing drastic reduction in the polarization ratio. At such powers we also expect the onset of plasma. This observation may indicate that the depolarization could be due to scattering by electron density inhomogeneities described by the dielectric tensor of the plasma [27] rather than due to multiple filamentation. Further studies need to be carried out to establish the reasons for the depolarization to quantify the contributions of plasma, multiple filamentation and light scattering.

To conclude our observations till now on the study of  $\rho(\lambda)$  of the different media generating SC, we find the following: (a) the depolarization sets in the SC with increase in input power, (b) different spectral components experience different depolarization with the wavelength band around the input fundamental peak getting maximum depolarization, (c) At higher input powers the polarization is affected because of the combined effect of the interaction of pulse with plasma and the effect of the NAB. Thus, there is always a trade-off between obtaining brighter SC at the cost of linear polarization properties of the SC. Any strategy to overcome this limitation would be of immense relevance to the growing demand of intense femtosecond while light sources with better polarization properties.

### 5.3.2 Reduction of depolarization in KDP crystal

We find that amorphous isotropic media like BK-7 glass which offers better polarization ratio at low powers doesn't hold any advantage at high input powers. Similarly, isotropic cubic media that are centrosymmetric like  $BaF_2$  that has intrinsic anisotropic  $\chi^{(3)}$  tensor cannot do any better at high input powers, though at low input powers there are recent reports on the anisotropic  $\chi^{(3)}$  of cubic media being successfully used to control of the onset of filamentation in a  $BaF_2$

crystal [20] and to some extent getting better polarization ratio in a  $\text{CaF}_2$  crystal at a very low input power of  $\sim 10P_{\text{cr}}$  [18]. However, KDP, being a non-centrosymmetric crystal, has an anisotropic  $\chi^{(3)}$  tensor and hence the anisotropic non-linear refraction ( $n_2$ ) leads to nonlinear anisotropic birefringence (NAB) being different for different orientations of the crystal. Thus the magnitude of NAB depends strongly on the crystal orientation. Taking this cue, we carried out experiments to study the effect of orientation on  $\rho(\lambda)$  in a KDP crystal. It should be noted here that the data shown till now is for the SC generated along the  $c$ -axis of the crystal through which the natural birefringence is not present ( $n_o=n_e$ ) making it behave similar to an isotropic medium. As discussed in chapter 4, since SCG being essentially a third order process, it is intrinsically dependent on the  $\chi^{(3)}$  of the material. The anisotropic property of the crystals results in dependence of  $\chi^{(3)}$  on the rotation angle. The  $\chi^{(3)}(\theta)$  is a function of the independent non-vanishing  $\chi^{(3)}$  components determined by the symmetry. Isotropic cubic crystals like  $\text{BaF}_2$  and  $\text{CaF}_2$  having a space-group symmetry  $43m$  have a well defined expression for effective  $\chi^{(3)}$  [28]. For uniaxial crystals, like sapphire and KDP, the relation for effective  $\chi^{(3)}$  becomes more complicated as there is direction dependence for e- rays but not for o- rays [29]. Moreover, KDP being non-centrosymmetric having a tetragonal structure and  $\bar{4}2m$  symmetry, the expression for effective  $\chi^{(3)}$  is more complex [30]. After ascertaining the intrinsic anisotropic nonlinearity in the previous chapter evidently, we see that the non-centrosymmetric KDP crystal can have orientation dependent  $P_{\text{cr}}$ . We carried out polarization studies to investigate the effect of orientation of plane of polarization on  $\rho(\lambda)$ . Henceforth, in the later part of this article the measurements are presented with respect the input peak intensity rather than in terms of the  $P_{\text{cr}}$ .

Figure 5.9(a) shows the variation of  $\rho(\lambda)$  for the SC generated at an average input power of 350mW that corresponding to a peak intensity of  $\sim 8 \times 10^{12} \text{ W/cm}^2$  along the  $c$ -axis of the crystal with rotation of the plane of input linear polarization. With rotation of the plane of polarization from  $0^\circ$  (horizontal) to  $45^\circ$ , we observed that the  $\rho(\lambda)$  decreases and then increases from  $45^\circ$  to  $90^\circ$ .

Clearly  $\rho(\lambda)$  is at its minimum when the plane of polarization is rotated by  $45^\circ$  incidence indicating that at this position  $I_{orth}(\lambda)$  is almost equal to  $I_{par}(\lambda)$  signifying maximum polarization degradation. However, upon rotation by  $90^\circ$  we have enhancement in the overall  $\rho(\lambda)$  with an increase of polarization ratio in the wavelength region of 450-750 nm when compared to that obtained at  $0^\circ$ .

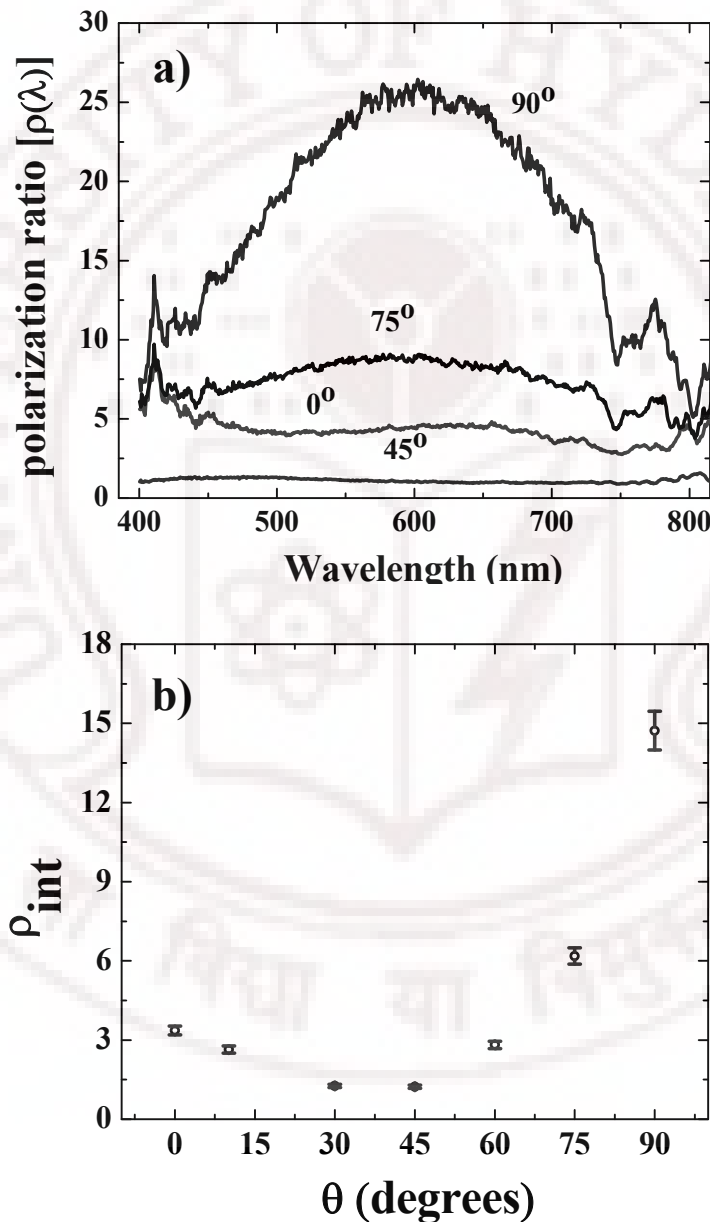
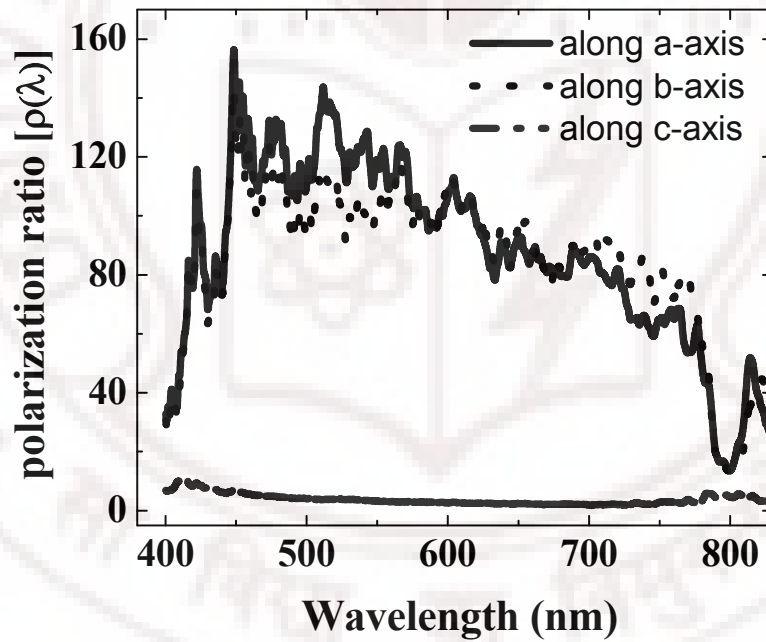


Fig. 5.9 (a) Variation of  $n_2$  with orientation of plane of input polarization relative to the horizontal polarization denoted by  $\theta$ . (b) Variation of  $P_{cr}$  with  $\theta$

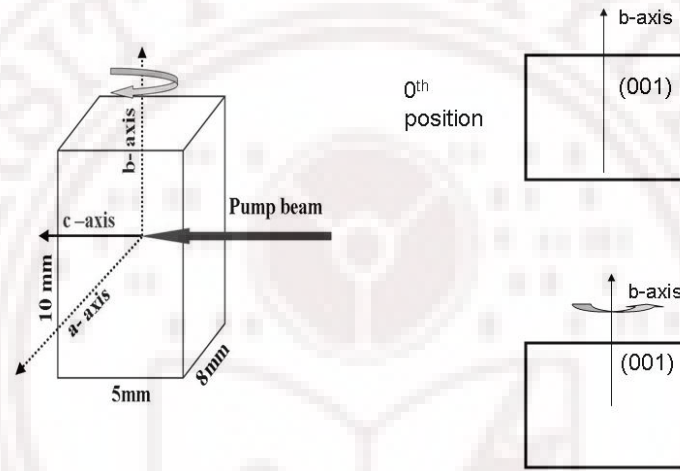
Figure 5.9(b) that shows the plot of variation of  $\rho_{\text{int}}$  as a function of rotation angle ( $\theta$ ) confirming the obtained spectral data. The presented data are the averaged values obtained by repeating the measurements three times with the error bars accounting for a possible 5% experimental error. In other words, with rotation of plane of input polarization a better polarization ratio was obtained. We performed similar studies with BK-7 glass and BaF<sub>2</sub> crystal as well to see any change in the  $\rho(\lambda)$ . As expected we did not see any alteration in the overall  $\rho(\lambda)$  confirming that this is unique to an anisotropic medium like KDP crystal. However, a straightforward explanation to the observed dependence of the  $\rho(\lambda)$  in KDP crystal is not possible with the available literature. Though we expect the  $\rho(\lambda)$  to increase from 0° to 90° following similar trend as the variation of  $P_{\text{cr}}$ , we observed a dip at 45°.



**Fig.5.10:** The polarization ratio  $\rho(\lambda)$  for SCG obtained for three axes of the crystal

The  $\rho(\lambda)$  for SC generated along *a*-, *b*- and *c*-axis of the crystal for the same input power is as shown in figure 5.10. From the figure, it is evident that, the SC along *a*- and *b*- axes have a lower depolarization compared to that along *c*- axis indicating most depolarization of SC along the *c*-axis.  $\rho(\lambda)$  is the lowest

along  $c$ -axis probably because both the polarization components experience same refractive index ( $n_0=n_c$ ). This led us to believe that SC along an axis other than the  $c$ -axis should improve the polarization ratio. To confirm this assertion we carried out our depolarization studies at orientations other than the principal coordinates. We rotated the crystal around the  $b$ -axis with the  $0^{\text{th}}$  position as the direction with the plane of polarization parallel to the  $a$ -axis. Figure 5.11 shows that as we move away from the  $c$ -axis the spectral dependence of  $\rho(\lambda)$  gets better when rotated by  $30^\circ$  relative to the  $0^{\text{th}}$  position.



The crystal is rotated about the  $b$ -axis  $10^\circ$  with respect to the  $0^{\text{th}}$  position, generating continuum with the crystal face (001) plane.

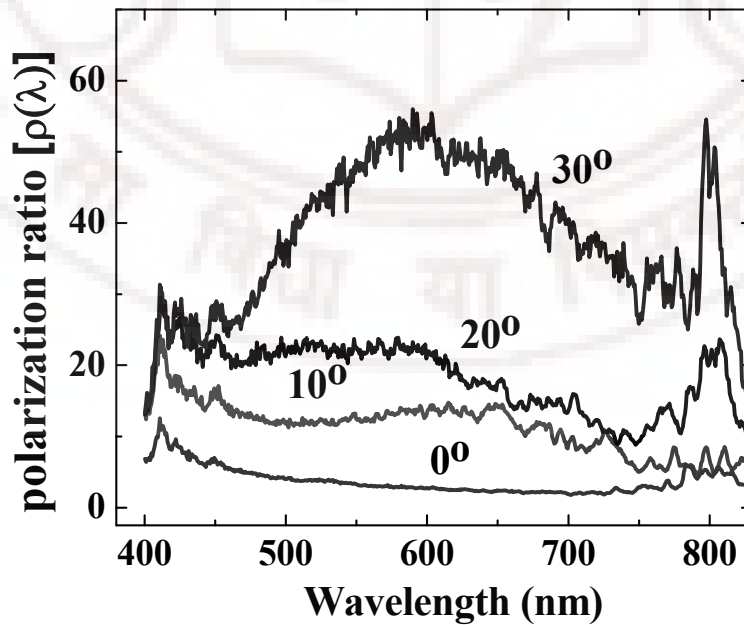
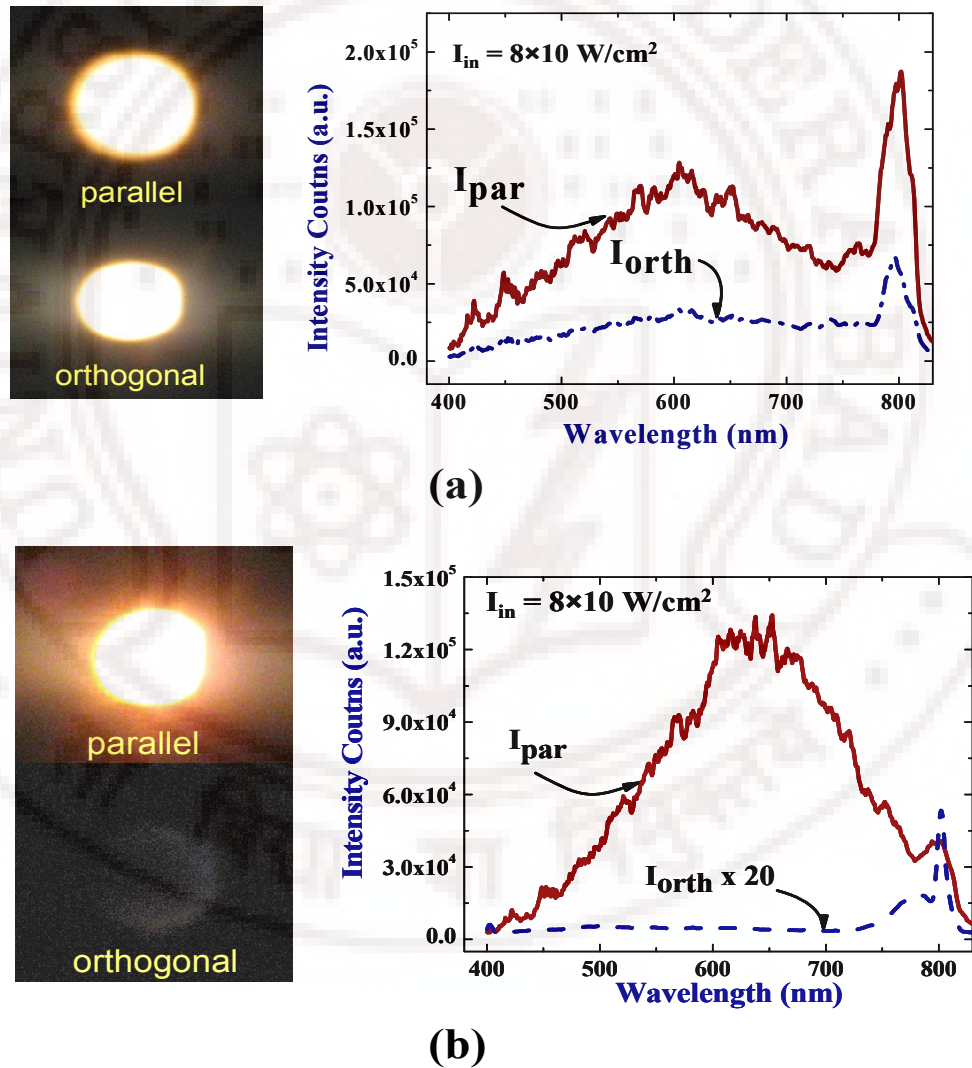


Fig. 5.11:  $\rho(\lambda)$  for SC generated at different crystal orientations



Continuing on this line, we generated SC along several other orientations of the crystal obtaining different  $\rho(\lambda)$ . At one such orientation determined to be along  $\theta = 45^\circ$  and  $\varphi = 3.5^\circ$  (where  $\theta$  is the angle propagation vector relative to  $c$ -axis and  $\varphi$ , the azimuth angle), the generated SC was found to be having the least depolarization. Figure 5.12(a) and (b) shows the SC output in parallel and perpendicular positions of the analyzer respectively for this orientation in comparison to that obtained along the  $c$ -axis at a high input power ( $I_{in} \sim 8 \times 10^{12}$  W/cm<sup>2</sup>).



**Fig. 5.12:** (right) Snapshot of the SCG at the parallel and orthogonal orientation of the analyzer; (left) the spectra recorded for SC at the corresponding analyzer position: (a) SC generated along  $c$ -axis of KDP; (b) SC generated along the preferred orientation of the crystal

On the left side of Fig. 5.12 we present the snapshot of the SC output at the two orthogonal positions of the analyzer. Clearly the contrast between SC outputs generated is large when generated along the preferred orientation when compared to that when generated along the  $c$ -axis. An interesting feature of figure 5.12(b) is that in order to show  $I_{par}(\lambda)$  component in the same figure with  $I_{orth}(\lambda)$  component  $I_{orth}(\lambda)$  is multiplied by 20 numerically giving a direct conformation to the lack of appreciable  $I_{orth}(\lambda)$  component. On the other hand  $I_{orth}(\lambda)$  component in figure 5.12(a) is comparable to  $I_{par}(\lambda)$  indicating major depolarization in all directions.

The integrated intensity measurements of the SC output with rotation of the analyzer is shown in Fig 5.13. The output polarization has a maximum along the direction of the input plane of polarization and we do not observe any rotation in the plane of polarization. The measurements also indicate that the SC is not elliptically polarized but gets partially depolarized.

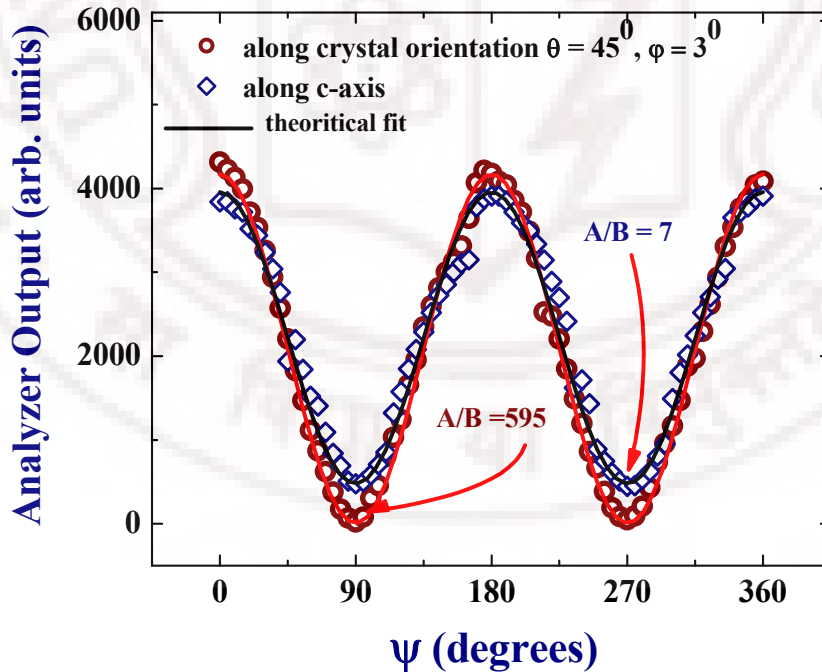


**Fig. 5.13:** Plot of the analyzer output of the SC generated along different orientation of the crystal with respect to the rotation of the analyzer.

The solid curve shown in the figure is a theoretical fit obtained for the relation,  $y = A \cos^2(\psi) + B \cos^2(90 - \psi)$ , where  $\psi$  is the angle of rotation of the analyzer,  $A$  is the intensity parallel to the input plane of polarization and  $B$  represents the depolarized component along the orthogonal direction. For SC generated along the c-axis we obtained  $\frac{A}{B}$  to be  $\sim 7:1$  when compared to a high ratio of  $\sim 595:1$  for SC generated along the preferred orientation of the KDP crystal. Thus, we show that for a non-centrosymmetric crystal the depolarization of the SC is dependant on the direction of propagation of the fundamental and the depolarization can be conveniently reduced by choosing a particular direction of propagation.

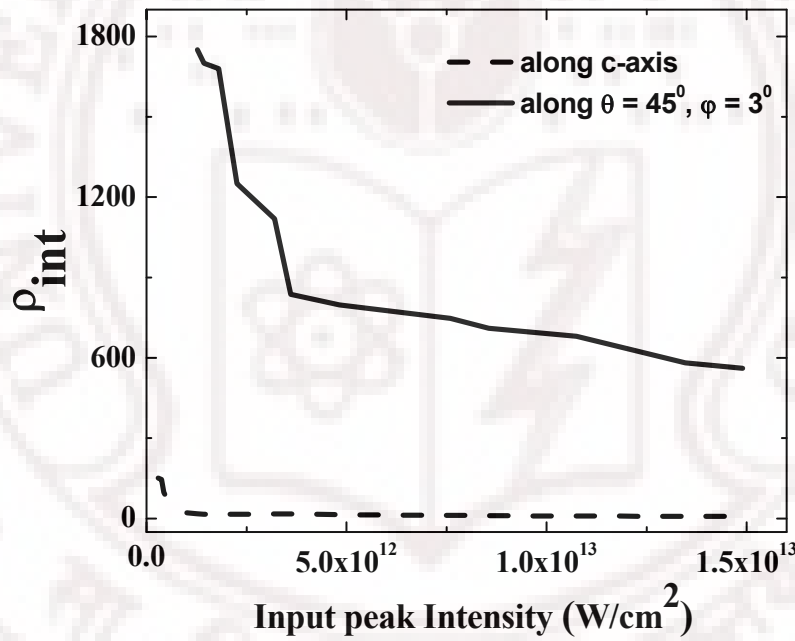


**Fig. 5.14:** Plot of integrated polarization ratio of the KDP SC at different orientation with increase in the input power in terms of the critical power ( $P_{cr}$ ).

Figure 5.14 shows the plot of  $\rho_{int}$  obtained for SC along a particular direction with increase in input power in comparison to what is already obtained for the generated SC along the c-axis of the crystal. There was no observable signal in  $I_{orth}$  position for intensities below  $1.2 \times 10^{12} \text{ W/cm}^2$  in case of the SCG at the specified orientation of the crystal, which tells us that the  $\rho_{int}$  at lower

intensities are much larger than 1800 and that there is no depolarization of SC. We observe that for input intensity beyond  $1.5 \times 10^{12} \text{ W/cm}^2$  (i.e., beyond  $250P_{\text{cr}}$  for other media presented earlier) where other media experience the onset of depolarization, the SC in this case has lesser depolarization. For lower input intensities we see that the ratio is much higher and comparable to what we measure for that of the input pulse.

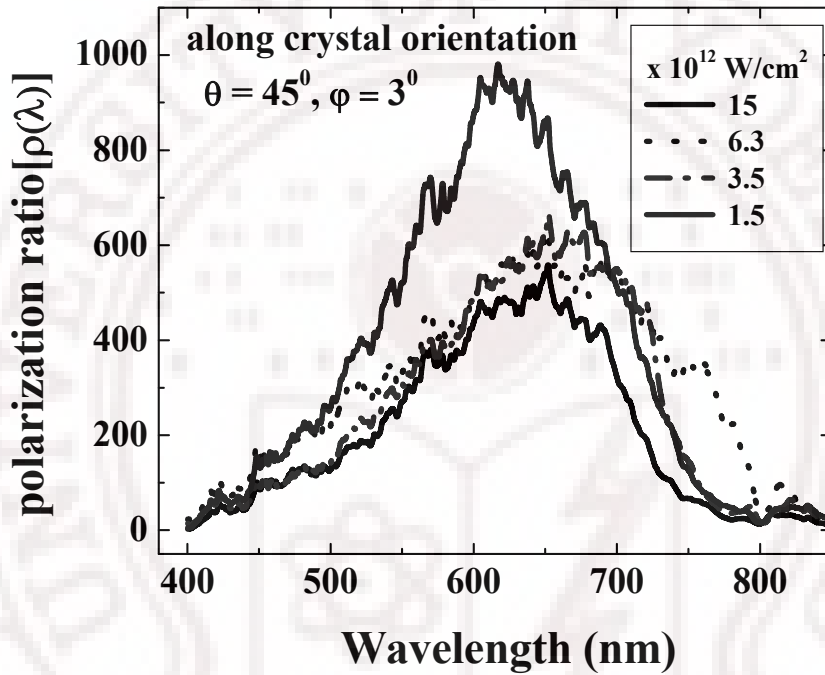


Fig. 5.15:  $\rho(\lambda)$  for SCG along the preferred crystal orientation for various input powers

$\rho(\lambda)$  for SC generated at different input intensities is shown in Figure 5.15. We find that even at high input intensities the spectral response of  $\rho(\lambda)$  remains similar to what is obtained for lower input intensities. Although, we did not attempt to study the polarization properties for input peak intensity more than  $15 \times 10^{12} \text{ W/cm}^2$ , it is expected to have lower depolarization looking at the trend of variation of  $\rho(\lambda)$  at higher input intensities. We also performed experiments to measure the polarization of the output to estimate if there is any rotation of the input polarization or formation of an elliptical polarization using a broadband half-wave and quarter-wave plates at the output by replacing the analyzer. Our

results indicate that the output is still linearly polarized along the input plane of polarization while a part of it gets unpolarized.

In the discussion from our previous chapter the coherence properties were established to be well maintained even at higher input powers. The control over polarization properties of SCG in KDP thus helps with well-defined polarization properties. Till date the best reported  $\rho$  is 2000:1 for SCG in  $\text{CaF}_2$  achieved at low input power  $\sim 10P_{\text{cr}}$  with single filament generation [18]. Thus, the present results hold significance with SC being generated at much higher input peak powers and intensities, allowing intense SC generation with minimum depolarization. Though as shown earlier in this article BK-7 glass had better  $\rho(\lambda)$  compared to  $\text{BaF}_2$  and z-cut KDP crystal it fails to match the ratio obtained for SC generated along the preferred orientation of KDP crystal. Thus, this makes KDP crystal a better choice of media for generating SC for obtaining best polarization properties. With its large bandgap  $\sim 7.12$  eV (174 nm) [31], high damage threshold, and strong nonlinear behavior allowing the enrichment of spectral content in blue region by parametric wave-mixing [4], KDP acts as a versatile candidate for SCG.

#### 5.4 Conclusions:

- In this chapter, we have systematically studied the depolarization properties of the generated SC in different classes of media namely: (a) BK-7 glass representing isotropic amorphous condensed media, (b)  $\text{BaF}_2$  isotropic crystalline condensed media and (c) KDP crystal anisotropic crystalline condensed media.
- We carried out our work by studying the variation of the polarization ratio  $[\rho(\lambda)]$  defined as  $I_{\text{par}}(\lambda) / I_{\text{orth}}(\lambda)$  for SC obtained at different input powers for three media under consideration.
- We find that at low input powers SC generated in BK-7 glass has better  $\rho(\lambda)$  indicating minimum depolarization when compared to that in  $\text{BaF}_2$  and

KDP along its *c*-axis. At high input powers we observe that SC from all three media undergoes maximum depolarization with low  $\rho(\lambda)$ .

- As a strategy to obtain better  $\rho(\lambda)$  the intrinsic non-centrosymmetric property of KDP crystal was used and we observed that  $\rho(\lambda)$  of SCG depends strongly on the following: (i) the plane of polarization of incident light, and (ii) the incident plane of the crystal.
- Though, one would expect the polarization degradation of SCG at high input intensities we observed dramatic reduction in the depolarization with change in orientation of the crystal with respect to *c*-axis of KDP.
- Our results show that the depolarization of SCG is most when generated along the *c*-axis.

### References:

1. R. R. Alfano, *The Supercontinuum laser source*, Springer–Verlag, Berlin (1989).
2. J. M. Dudley, G. Genty, and S. Coen, Rev. Mod. Phys. **78**, 1135 - 1184 (2006); J. K. Ranka, R. S. Windeler, and A. J. Stentz, Opt. Lett. **25**, 25 (2000); T. A. Birks, W. J. Wadsworth, and P. S. J. Russell, Opt. Lett. **25**, 1415 (2000); S. Coen, A. H. L. Chau, R. Leonhardt, J. D. Harvey, J. C. Knight, W. J. Wadsworth, and P. S. J. Russell, J. Opt. Soc. Am. B, **19**, 753 (2002); A. K. Dharamdhikari, F. A. Rajgara, and D. Mathur, App. Phys. B, **80**, 61 (2005); K. Wang, L. Qian, H. Luo, P. Yuan, and H. Zhu, Opt. Express, **14**, 6366 (2006)
3. N. K. M. N. Srinivas, S. S. Harsha, and D. N. Rao, Opt. Express, **13**, 3224 (2005)
4. R. S. S. Kumar, S. S. Harsha, and D. N. Rao, App. Phys. B, **86**, 615 (2007)
5. V. I. Klimov, D. W. McBranch: Opt. Lett, **23**, 277 (1998); R.A. Negres, J.M. Hales: IEEE Journal of Quantum Electronics, **38**, 1205 (2002)
6. R. L. Fork, C. H. Brito Cruz, P. C. Becker, and C. V. Shank, Opt. Lett. **12**, 483 (1987); E. T. J. Nibbering, O. Dühr, and G. Korn, Opt. Lett. **22** 1335 (1997)



7. G Cerullo and Sandro de Silvestri, *Rev. Sci. Instrum.* **74**, 1 (2003); V. V. Yakovlev, B. Kohler, and K. R. Wilson, *Opt. Lett.* **19**, 2000 (1994); M. K. Reed, M. K. Steiner- Shephard, and D. K. Negus, *Opt. Lett.* **19**, 1885 (1994)
8. P. Rairoux, H. Schillinger, S. Neidermeier, M. Rodriguez, F. Ronneberger, R. Sauerbrey, B. Stein, D. Waite, C. Wedekind, H. Wille, L. Wöste, and C. Zeiner, *Appl. Phys. B.* **71**, 573 (2000)
9. G. S. He, T. C. Lin, P. N. Prasad, R. Kannan, Richard A. Vaia, and L. S. Tan, *Opt. Express*, **10**, 566 (2002); L. De Boni, A. A. Andrade, L. Misoguti, C. R. Mendonca, and S. C. Zillo, *Opt. Express*, **12**, 3921 (2004); L. De Boni, L. Gaffo, L. Misoguti, C.R. Mendonca, *Chem. Phys. Lett.* **419**, 417 (2006); M. Balu, J. Hales, D. J. Hagan, and E. W. Van Stryland, *Opt. Express*, **13**, 3594 (2005)
10. T. Udem, R. Holzwarth, and T.W. Hansch, *Nature*, **416**, 233 (2002).
11. J. H. Frank, A. D. Elder, J. Swartling, A. R. Venkitaraman, A. D. Jeyasekharan, and C. F. Kaminski, *J. Microsc.* **227**, 203 (2007).
12. Z. Zhu, and T.G. Brown, *J. Opt. Soc.Am. B.* **21**, 249 (2004); Z. Zhu, and T.G. Brown, *Opt. Express*, **12**, 791 (2004)
13. A. K. Dharmadhikari, F. A. Rajgara, and D. Mathur, *Opt. Lett.* **31**, 2184 (2006)
14. I. Buchvarov, A. Trifonov, and T. Fiebig, *Opt. Lett.* **32**, 1539 (2007)
15. P. Tzankov, I. Buchvarov, and T. Fiebig, *Opt. Commun.* **203**, 107 (2002); M. Ziolk, R. Naskrecki, and J. Karolczak, *Opt. Commun.* **241**, 221(2004).
16. K. Midorikawa, H. Kawano, A. Suda, C. Nagura, and M. Obara: *App. Phys. Lett.* **80**, 923 (2002)
17. A. Srivastava, and D. Goswami, *Phys Lett. A*, **341**, 523 (2005); I. Golub, *Opt. Lett.* **15**, 305 (1990).
18. V. Kartazayev, and R. R. Alfano, *Opt. Commun.* **281**, 463 (2008)
19. D. N. Neshev, A. A. Sukhorukov, A. Dreischuh, R. Fischer, S. Ha, J. Bolger, L. Bui, W. Krolikowski, B. J. Eggleton, A. Mitchell, M. W. Austin, and Y. S. Kivshar, *Phys. Rev. Lett.*, **99**, 123901 (2007)
20. A. K. Dharmadhikari, K. Alti, and J. A. Dharmadhikari, D. Mathur, *Phys. Rev. A*, **76**, 033811 (2007)



21. A. Srivastava, and D. Goswami, Appl. Phys. B., **77**, 325-328 (2003)
22. A. l'Huillier, Ph. Balcou, S. Candel, K. J. Scafer, and K. C. Kulander, Phys. Rev. A, **46**, 2778 (1992).
23. A. L. Gaeta, Phy. Rev. Lett. **84**, 3582 (2000).
24. J. Yang, N. Zhang, and X. Zhu, App. Phys. B **89**, 261 (2007)
25. R. G. Brewer, J. R. Lifszitz, E. Garmire, R. Y. Chiao, and C. H. Townes, Phys. Rev. **166**, 326–331 (1968).
26. K. Cook, A. K. Kar, and R. A. Lamb, Appl. Phys. Lett. **83**, 3861-3863 (2003).
27. R. W. Boyd, *Nonlinear Optics*, 2nd ed. (Elsevier, 2003).
28. R. Adair, L. L. Chase, and S. A. Payne, Phys. Rev. B **39**, 3337 (1989).
29. Q. Guo and S. Chi, and J. Opt. A, Journ. Pure Appl. Opt. A, **2**, 5 (2000)
30. I. A. Kulagin, R. A. Ganeev, R. I. Tugushev, A. I. Ryasnyansky, and T. Usmanov, J. Opt. Soc. Am. B **23**, 75-80 (2006)
31. G. Dimitriev, G. G. Gurzaddyan, D. N. Nikogosyan: *Handbook of Nonlinear Optical Crystals*, 2nd revised ed. (Springer, Berlin, 1977)

The logo of the University of Hyderabad is a circular emblem. The outer ring contains the text "UNIVERSITY OF HYDERABAD" at the top and the Sanskrit motto "सा विद्या या विमुक्तये" at the bottom. The inner circle features a central shield with a book, a flower, and a lightning bolt. Above the shield is a stylized sun or flower motif. The text "CHAPTER 6" is superimposed over the center of the logo.

# CHAPTER 6

### Abstract

*In this chapter we discuss our experimental results on probing the enhanced surface third order nonlinearities at dielectric interfaces. We developed a theoretical formulation of surface  $\chi^{(3)}$  at a phenomenological level and explicitly decomposed the contributions of interface as well as bulk effects on the overall  $\chi^{(3)}$  of the medium. We made use of non collinear four-wave mixing (FWM) at air-dielectric interfaces and generated FWM signal from the two interfaces of a 1mm thick fused silica slide with air using two 800 nm, 100 fs pump pulses in non-collinear pump-probe type geometry to demonstrate our theoretical assertion. We also observed that there is a maximum peak shift of  $\sim 1.5$  nm in FWM signals corresponding to the two interfaces of the same silica slide. Further, we find that the intensity of FWM signal observed at air to silica interface is less than that from silica to air interface. We elaborate on this observation with systematic study of FWM with fused silica glass slide.*

# Femtosecond four wave mixing at air-dielectric interfaces

## 6.1 Introduction

The surface nonlinearity at an interface between two media can be characterized by an effective local surface nonlinear susceptibility that includes both the local and non-local responses of the interface layer to the field. We define the interface layer as follows [1]: In the ideal case where the bulk structures of the media in the two sides of an interface extend all the way to the boundary plane, the overall medium experiences only a sudden structural change at the boundary plane. In real cases, the structure of a medium at a surface interface is always somewhat different from that of the bulk. The changes usually occur in a few atomic layers near the surface or interface. An interface layer often refers to the region where the structural change from the bulk is significant. Around this region, the optical field along the surface normal changes rapidly from its macroscopic values on the other side of the interface. It is generally accepted that the breaking of inversion symmetry at any interface between two media with inversion symmetry causes structural asymmetry and local field variation across the surface layer. This gives rise to discontinuity in the normal component of the electric field and an induced nonlinear polarization containing high-order nonlinear susceptibility tensors [2, 3].

Good literature is available on the second harmonic generation (SHG) at the surfaces of different materials [3-7]. It was found that in a medium with inversion symmetry, the surface contribution to SHG could be comparable with or dominant over the bulk contribution [2-6]. Numerous applications were based on surface enhancement of second order susceptibility  $\chi^{(2)}$  of a medium as a powerful and effective diagnostic tool [7]. On the other hand, though third order nonlinear optical process is allowed in all materials independent of the symmetry

property of the medium, the surface third order susceptibilities  $\chi^{(3)}$  were given lesser consideration, in particular  $\chi^{(3)}$  processes like third harmonic generation (THG). It was concluded from few earlier studies that THG in reflection at metal and semiconductor surfaces is mostly from the bulk, lacking surface characteristics [8]. Moreover, since  $\chi^{(3)}$  processes are much weaker requiring high peak intensities to probe, research groups earlier have overlooked these weak processes resulting in the negligence of this kind of work. Nevertheless, with recent advances in ultrafast laser technology that enable attainment of high peak powers with relatively inexpensive and low-average power lasers, this particular drawback could easily be overcome. Tsang [9] experimentally demonstrated using femtosecond laser pulses that the normally weak but electric dipole allowed THG process can be appreciably strong at an air-dielectric interface and thus may contain useful surface characteristics. Efficiency of the THG at interfaces near the focal point of a tightly focused laser beam has led to numerous applications such as in ultrashort pulse characterizations, microscopy and third order nonlinear characterization of both absorbing and non-absorbing media [10]. However, other than THG phenomenon at interfaces, the manifestation of enhancement of surface third order susceptibilities  $\chi_{surface}^3$  is not observed in any other third order nonlinear processes. In this chapter we demonstrate the effect of enhanced value of  $\chi_{surface}^3$  compared to  $\chi_{bulk}^3$  in one of the most popular third order nonlinear processes, namely Four-wave mixing.

Four-wave mixing (FWM), which is also a consequence of  $\chi^{(3)}$  of the materials, plays a very important role in many applications [11]. Numerous reports in literature deal with the FWM both in degenerate and non-degenerate geometry and usually are generated within the bulk of the sample. Here, we have investigated four wave mixing (FWM) at silica-air interfaces using a femtosecond laser. A systematic study of FWM is reported for the two interfaces of a 1mm fused silica slide. We made the following observations in the course of our study: (i) there is a maximum peak shift of 1.5 nm in the FWM spectra from

air-glass interface; (ii) intensity of the FWM signal at air to silica interface is weaker compared to FWM signal at silica to air interface.

## 6.2 Theoretical formulation of $\chi^{(3)}$ at surfaces

The interface layer of a medium can be defined more generally as the region where the structure and the field change significantly. The thickness of an interface layer is always much smaller than an optical wavelength. As a result, perturbation calculation can be used to deal with the response of an interface layer to an applied field. Boundary conditions require that the electric field components along the interface ( $\hat{x} - \hat{y}$ ) and the displacement current component along the surface normal ( $\hat{z}$ ) are continuous across the interface layer. The electric field component  $E_z$  along  $\hat{z}$ , on the other hand, changes rapidly across the layer. The response of this layer to  $E_z$  is therefore expected to be non-local. Let the field at frequency  $\omega_i$  be  $E(\bar{r}, \omega_i)$ . We can write, in general, the linear and third-order nonlinear polarizations arising from the non-local response of a medium as

$$\begin{aligned} P^{(1)}(\bar{r}, \omega_i) &= \int \tilde{\chi}^{(1)}(r, r', \omega_i) \cdot E(r', \omega_i) d^3 r' \\ P^{(3)}(\bar{r}, 3\omega) &= \iiint \tilde{\chi}^{(3)}(r, r', r'', r''', 3\omega) \cdot E(r', \omega) \cdot E(r'', \omega) \cdot E(r''', \omega) d^3 r' d^3 r'' d^3 r'''. \end{aligned} \quad (6.1)$$

In the bulk, we have  $\tilde{\chi}^{(n)}$  replaced by the bulk value  $\tilde{\chi}_0^n$  which is  $\tilde{\chi}_{01}^n$  in medium 1 on the  $z < 0$  and  $\tilde{\chi}_{02}^n$  in medium 2 on the  $z > 0$ . In the interface layer, we have

$$\begin{aligned} \tilde{\chi}^{(1)} &= \tilde{\chi}_0^{(1)} + \Delta\tilde{\chi}^{(1)} \\ \tilde{\chi}^{(3)} &= \tilde{\chi}_0^{(3)} + \Delta\tilde{\chi}^{(3)} \end{aligned} \quad (6.2)$$

The macroscopic fields are obtained from the averages of corresponding microscopic quantities over a macroscopic volume. In the interface layer, both  $E_z$  and  $P^{(n)}$  can vary rapidly on the atomic scale. Consequently, the definition of a macroscopic quantity depends on the averaging volume. On the other hand,

regardless of the size of the averaging volume,  $E_z$  should change smoothly across the interface layer from its macroscopic value of the medium 1 to its value in medium 2 and the surface optical effects generally depend only on the integrated response of the interface layer to the field that is,  $\int P^{(n)}(z)dz$  integrated across the interface layer. As an example of the manifestation of  $\vec{\chi}_{surface}^{(3)}$ , we consider the case of third-harmonic generation process at interface between two semi-infinite media as shown in figure 6.1.

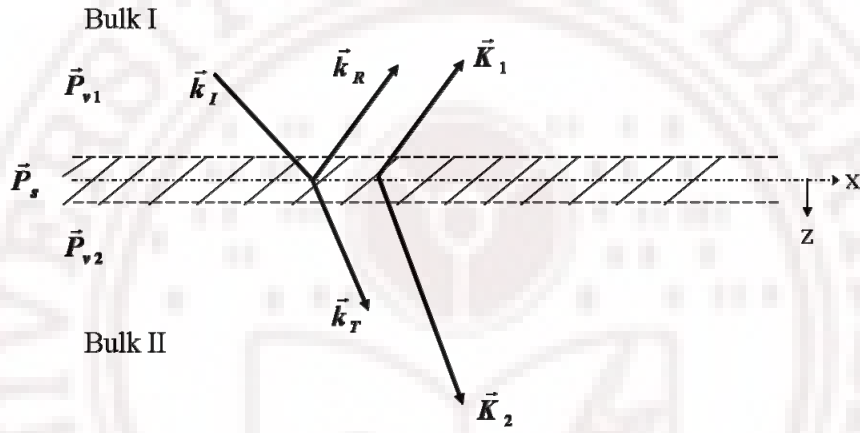


**Fig. 6.1:** Geometry of THG from an interface (shaded region) between the two semi-infinite media.  $\vec{k}_I$ ,  $\vec{k}_R$ , and  $\vec{k}_T$  are the wave vectors for incident, reflected, and transmitted fundamental waves;  $\vec{K}_1$  and  $\vec{K}_2$  are the wave vectors for the waves at  $3\omega$  in media 1 and 2

We write the wave equation for the third harmonic field in the form beginning from the Maxwell's equation as below:

$$\left[ \nabla \times (\nabla \times) - \left[ \frac{3\omega}{c} \right]^2 \vec{\epsilon}_0 \right] \cdot E(3\omega) = -4\pi \left[ \frac{3\omega}{c} \right]^2 \left[ \int \Delta \vec{\chi}^{(1)}(\vec{r}, \vec{r}', 3\omega) \cdot E(\vec{r}', 3\omega) d^3 \vec{r}' \right. \\ \left. + \int \vec{\chi}^{(3)}(\vec{r}, \vec{r}', \vec{r}'', \vec{r}''', 3\omega) : E(\vec{r}', \omega) E(\vec{r}'', \omega) E(\vec{r}''', \omega) d^3 \vec{r}' d^3 \vec{r}'' d^3 \vec{r}''' \right] \quad (6.3)$$

Where we assume

$$\vec{\epsilon}_0 = \vec{1} + 4\pi \int \chi_0^{(1)}(\vec{r}, \vec{r}') d^3 \vec{r}', \text{ that is, } \chi_0^{(1)}(\vec{r}, \vec{r}, \omega_i) = [\vec{\epsilon}_0(\omega_i) - \vec{1}] \delta(\vec{r} - \vec{r}') / 4\pi,$$

with  $\vec{\epsilon}_0 = \vec{\epsilon}_1$  in medium 1 and  $\vec{\epsilon}_0 = \vec{\epsilon}_2$  in medium 2.



Eq. (6.3) is an inhomogeneous second order differential equation and we consider the Green's function approach to solve it. The Green's function  $G(\vec{r}, \vec{r}', \vec{r}'', \vec{r}''', 3\omega)$  for (6.3) is defined to be the solution of the equation

$$\left[ \nabla \times (\nabla \times) - \left[ \frac{3\omega}{c} \right]^2 \vec{\epsilon}_0 \right] \cdot \vec{G} = \delta(\vec{r} - \vec{r}') \vec{1} \quad (6.4)$$

The solution of Eq.(6.3) can be written in terms of  $\vec{G}$ . We consider here a system with translational symmetry in the  $\hat{x} - \hat{y}$  plane such that

$$\begin{aligned} E(\vec{r}, \omega) &= \xi(z, \omega) \exp(ik_x x - i\omega t) \\ E(\vec{r}, 3\omega) &= \xi(z, 3\omega) \exp(3ik_x x - 3i\omega t) \\ P(\vec{r}, \omega) &= P^{(n)}(z, 3\omega) \exp(3ik_x x - 3i\omega t) \end{aligned} \quad (6.5)$$

We then find that

$$\begin{aligned} \xi(z, 3\omega) &= - \int \vec{G}(z, z', 3\omega) \cdot 4\pi \left[ \frac{3\omega}{c} \right]^2 \\ &\quad \times \left[ \Delta\chi^{(1)}(z', z'', 3\omega) \cdot \xi(z'', 3\omega) \times d^3 z'' + P^{(3)}(z', 3\omega) \right] dz' \end{aligned} \quad (6.6)$$

where

$$P^{(3)}(z, 3\omega) = \int \tilde{\chi}^{(3)}(z, z', z'', z''') \cdot \xi(z', \omega) \xi(z'', \omega) \xi(z''', \omega) dz' dz'' dz'''$$

Because of the possible existence of  $\Delta\chi^{(3)}$  (see Eq.(6.2)) and the rapid variation of  $\xi_z$  in the interface layer,  $P^{(3)}$  in the interface layer could be significantly different from that in the bulk. We can decompose  $\xi(z, 3\omega)$  into two parts corresponding to

1.  $P(3\omega)$  in the bulk, and
2.  $P(3\omega)$  in the interface region.

The Green's function  $\vec{G}$  has a property that  $G_{ij}(z, z')$  (for  $j \neq z$ ) or  $\epsilon_0(z')G_{iz}(z, z')$  is continuous in  $z'$ . Therefore, in the interface layer,  $G_{ij}(z, z')$

(for  $j \neq z$ ) and  $\varepsilon_0(z')G_{iz}(z, z')$  should assume essentially their values at  $z' = 0$ . Eq.(6.6) can then be written as (for  $z \neq 0$ )

$$\xi_i(z, 3\omega) = -4\pi(3\omega/c)^2 \left\{ \sum_{j=x,y} G_{ij}(z, 0) [P_{sj}^{(1)}(3\omega) + P_{sj}^{(3)}(3\omega)] + \lim_{z' \rightarrow 0} [\varepsilon_0(z', 3\omega) G_{iz}(z, z')] [P_{sz}^{(1)}(3\omega) + P_{sz}^{(3)}(3\omega)] + \sum_{j=x,y,z} \int G_{ij}(z, z') P_{vj}^{(3)}(z', 3\omega) dz' \right\} \quad (6.7)$$

It is advantageous to consider the continuous displacement current component  $D_z$  related to the  $z$  component of the field  $\xi(z, 3\omega)$  which varies rapidly across the interface layer, through a function  $s(z, 3\omega)$  such that

$$\xi_z(z, 3\omega) = s(z, 3\omega) [D_z(z, 3\omega) - 4\pi P_z^{(3)}(z, 3\omega)]$$

And further in (6.7) we have defined the surface polarization  $P_{sj}^{(n)}$  and the volume polarization  $P_{vj}^{(3)}$  as

$$\begin{aligned} P_{sj}^{(1)}(3\omega) &= \int_I \Delta \chi_{jj}^{(1)}(z, z') \xi_j(z', 3\omega) dz' dz, \quad \text{for } j = x, y \\ &= \int_I \varepsilon_0^{-1}(z, 3\omega) \Delta \chi_{jj}^{(1)}(z, z') s(z', 3\omega) D_z(z', 3\omega) dz' dz, \quad \text{for } j = z, \end{aligned} \quad (6.8)$$

$$\begin{aligned} P_{sj}^{(3)}(3\omega) &= \sum_{k,l,m} \int_I \Delta \chi_{jklm}^{(3)}(z, z', z'', z''') \xi_k(z', \omega) \xi_l(z'', \omega) \xi_m(z''', \omega) dz'' dz' dz, \quad \text{for } j = x, y \\ &= \sum_{k,l,m} \int_I \Delta \chi_{jklm}^{(3)}(z, z', z'', z''') s(z, 3\omega) \xi_k(z', \omega) \xi_l(z'', \omega) \xi_m(z''', \omega) dz'' dz' dz, \quad \text{for } j = z \end{aligned}$$

$$P_{vj}^{(3)}(z, 3\omega) = \int_B \chi_{0,jklm}^{(3)}(z, z', z'', z''') \xi_k(z', \omega) \xi_l(z'', \omega) \xi_m(z''', \omega) dz'' dz' dz'$$

Here  $\int_I$  and  $\int_B$  respectively, denote integrations across the interface layer and in the bulk. Eq.(6.7) with the help of Eq.(6.8), shows explicitly that the interface layer contributes to the output TH field through  $P_{sj}^{(1)}$  and  $P_{sj}^{(2)}$ , both of which are surface polarizations per unit area. Since we are interested only in the field generated by nonlinear wave-mixing we can neglect the  $P_{sj}^{(1)}$  term and write

$$\xi_i(z, 3\omega) = -4\pi(3\omega/c)^2 \left[ \sum_{j=x,y} G_{ij}(z, 0) P_{sj}^{(3)}(3\omega) + \lim_{z' \rightarrow 0} [\epsilon_0(z', 3\omega) G_{iz}(z, z')] P_{sz}^{(3)}(3\omega) + \sum_{j=x,y,z} \int_B G_{ij}(z, z') P_{vj}^3(z', 3\omega) dz' \right] \quad (6.9)$$

The above relation Eq.(6.9) demonstrates explicitly the contribution of the polarization at the interface and in the bulk of the medium to the generation of the nonlinear field at  $3\omega$ . Thus even if the observed nonlinear field in the bulk is found to be negligible, one still has to consider the contribution to the generated field from the nonlinear polarization at the interface, which can be substantial as shall be shown later.

We now focus our discussion on the surface nonlinear polarization  $P_{sj}^{(3)}(3\omega)$ . The surface nonlinear susceptibility  $\tilde{\chi}_s^{(3)}$  can further be expressed in the form

$$P_{sj}^{(3)}(3\omega) = \sum_{j,k,l} \chi_{s,jklm}^{(3)} F_k(0, \omega) F_l(0, \omega) F_m(0, \omega);$$

$$F_i(0, \omega) = \begin{cases} \xi_i(0, \omega), & \text{for } i = x, y \\ D_i(0, \omega), & \text{for } i = z \end{cases}, \quad (6.10)$$

Since both the  $x$  and  $y$  components of the field  $\xi_x$ ,  $\xi_y$  and the displacement current  $D_z$  are continuous and can be regarded as constant across the interface layer. On the other hand, the  $z$  component of the field  $\xi_z(z, 3\omega)$  is rapidly varying across the interface layer. Let us define  $\xi_z(z, 3\omega) = s(z, \omega) D_z(z, \omega)$  with the function  $s(z, \omega)$  incorporating the rapid variation across the interface layer. Using Eq. 6.8, we find, for  $i, j, k = x$  or  $y$ ,

$$\begin{aligned}
\chi_{s,ijkl}^{(3)} &= \int_I \chi_{ijkl}^{(3)}(z, z', z'', z''') dz dz' dz'' dz''' \\
\chi_{s,izkl}^{(3)} &= \int_I \chi_{izkl}^{(3)}(z, z', z'', z''') s(z') dz dz' dz'' dz''' \\
\chi_{s,ijkz}^{(3)} &= \int_I \chi_{ijkz}^{(3)}(z, z', z'', z''') s(z''') dz dz' dz'' dz''' \\
\chi_{s,ijzl}^{(3)} &= \int_I \chi_{izkl}^{(3)}(z, z', z'', z''') s(z'') dz dz' dz'' dz''' \\
\chi_{s,ijzz}^{(3)} &= \int_I \chi_{ijzz}^{(3)}(z, z', z'', z''') s(z'') s(z''') dz dz' dz'' dz''' \\
\chi_{s,izzl}^{(3)} &= \int_I \chi_{izzl}^{(3)}(z, z', z'', z''') s(z') s(z'') dz dz' dz'' dz''' \\
\chi_{s,izkz}^{(3)} &= \int_I \chi_{izkl}^{(3)}(z, z', z'', z''') s(z') s(z''') dz dz' dz'' dz''' \\
\chi_{s,izzz}^{(3)} &= \int_I \chi_{izzz}^{(3)}(z, z', z'', z''') s(z') s(z'') s(z''') dz dz' dz'' dz''' \\
\chi_{s,zzzz}^{(3)} &= \int_I \chi_{zzzz}^{(3)}(z, z', z'', z''') s(z, 3\omega) s(z') s(z'') s(z''') dz dz' dz'' dz'''
\end{aligned} \tag{6.12}$$

This characterizes fully the overall third-order susceptibility of the interface layer. The expression for surface nonlinear susceptibility in Eq.(6.12) contains the usual “local” contribution such as  $\chi_{s,ijkl}^{(3)}$ , which do not depend on the variation of the electric field, and the “non-local” contribution containing the function  $s(z)$ , which depends on the rapid variation of the electric field in the interface layer. We thus observe that in order to obtain the macroscopic susceptibility tensor, one needs to integrate across the interface layer, the overall individual components as shown in the Eq.(6.12). This would entail specification of  $\chi_{ijkl}^{(3)}(z, z', z'', z''')$  at the interface – calculation of which would require the knowledge of the nonlinear optical properties of the region near the interface at a molecular level, which is not possible at the present level of description. The above theoretical results however establish in clear terms the role of surface nonlinearities on the phenomenon of wave mixing at the interface of two isotropic media. We now describe our experimental work on a related problem of general four wave mixing to understand at a phenomenological level the effect of interface contribution to the overall nonlinear third-order susceptibility tensor.

In our present studies we have made an attempt to demonstrate experimentally the interface enhancement effects using the surface four wave

mixing technique. We choose the Four-wave mixing (FWM) arrangement over the conventional third-harmonic generation as from the phase matching considerations we can obtain the FWM signal well separated from the input fundamental fields. In the case of third harmonic generation the generated third harmonic field would be collinear to the fundamental beam making the separation experimentally difficult. As will be shown in the section 6.5 we analyze the observed results based on the contribution to the  $\chi^{(3)}$  term from the interface as well as the bulk.

### 6.3 Experimental details

In the present study we use two pumps in a simple non-collinear pump-probe type of arrangement (discussed in section 2.3) and shown in figure 6.2. The fundamental IR pulses from an amplified Ti: Sapphire laser (Maitai + Spitfire, Spectra Physics) used in the study are centered at 800 nm having a pulse width of 100 fs and a bandwidth of 13 nm. The two fundamental beams of approximately equal average power and beam size of 2 mm are focused onto the 1 mm fused silica slide by a focusing lens of focal length of 100 mm making an angle of  $10^\circ$  on the sample with respect to each other. The Rayleigh range and the beam waist of each beam are calculated to be  $\sim 2$  cm and  $\sim 50$   $\mu\text{m}$  respectively, in the Gaussian approximation. The interaction length  $L$ , of region of overlap of the two beams is  $\sim 300$   $\mu\text{m}$ . The choice of the focal length of the lens is such that (i) there is optimal peak intensity for the generation of FWM signal in the focal volume, (ii) the interaction region of the two beams is such that the two interfaces of the silica slide can be distinguished and (iii) that no continuum is generated. The nomenclature of the two interfaces, followed throughout the report is as shown in figure 6.2(a): aTs refers to the air to silica interface and sTa refers to the second interface i.e., silica to air with respect to the propagation of the fundamental beam. The silica slide is mounted on a translational stage and moved across the focal position of the converging beams in steps of 30  $\mu\text{m}$  from one interface position to the other through the center of the slide. The FWM spectra is recorded at each position and analyzed by coupling the beams directly into the

spectrometer positioned close to the slide. The FWM is detected by coupling the output into spectrometer (Ocean Optics Inc., model SD2000 with spectral range of 200–1000 nm) interfaced to a personal computer. All the data presented in this study are taken with respect to FWM1 beam.

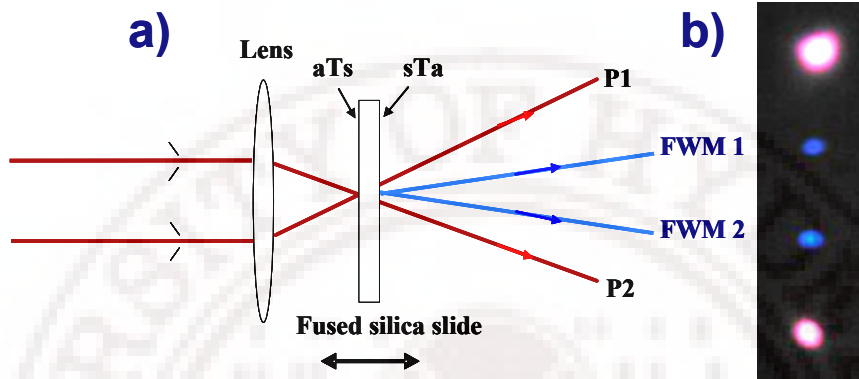


**Fig. 6.2:** (a) Experimental set-up used in the study; (b) Snap-shot of the FWM observed as blue fluorescence on a paper screen.

## 6.4 Studies on FWM at interfaces

### 6.4.1 Preliminary observations

When the two fs pulses overlap temporally and spatially we see the FWM as two blue spots in between the IR spots as shown figure 6.2(b). We observe the FWM at input intensities of fundamental pulses (P1 and P2) in the range of 400 – 800 GW/cm<sup>2</sup> well below the intensities required for the continuum generation (~1000 GW/cm<sup>2</sup>) in the fused silica. Figure 6.3(a) shows the FWM spectra recorded at the two interfaces. Clearly the FWM at aTs has a peak at 267.3 nm and the FWM signal due to sTa appear at 268.8 nm, a peak shift of ~1.5 nm. The observed full width at half maximum ( $\Delta\lambda$ ) of the FWM signal at sTa ( $\Delta\lambda = 3.8$  nm) is found to be broader than the FWM signal at aTs ( $\Delta\lambda = 2.4$  nm). The earlier reports [14, 15] with similar experimental configuration do not discuss the surface effects and refer to this observed signal as THG without recording the spectral content. However we refer to this signal as FWM signal since it represents the interaction between different wave vectors and frequencies. We did not observe any FWM signal in the bulk, i.e., at the center of the silica slide for

the power level used in the study, while we observe FWM only at the two interfaces.

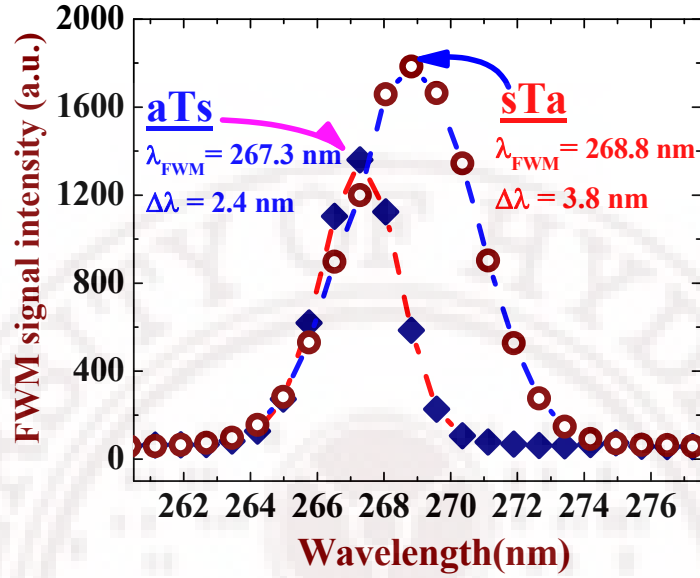


Fig. 6.3: (a) FWM peaks as observed at the two interfaces aTs and sTa. The dashed line is just to guide the eye the scatter of the obtained experimental FWM data showing the symmetry of the FWM signal

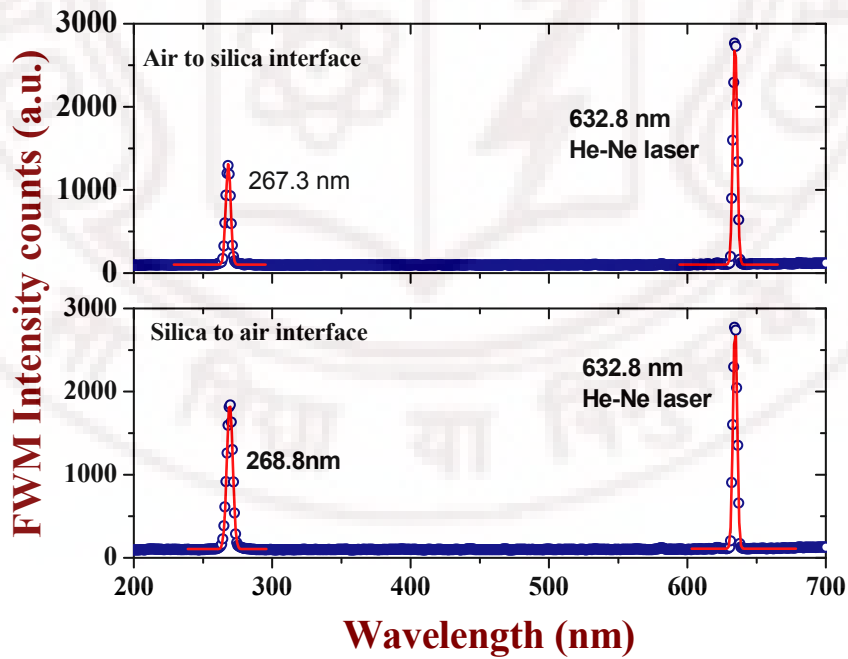
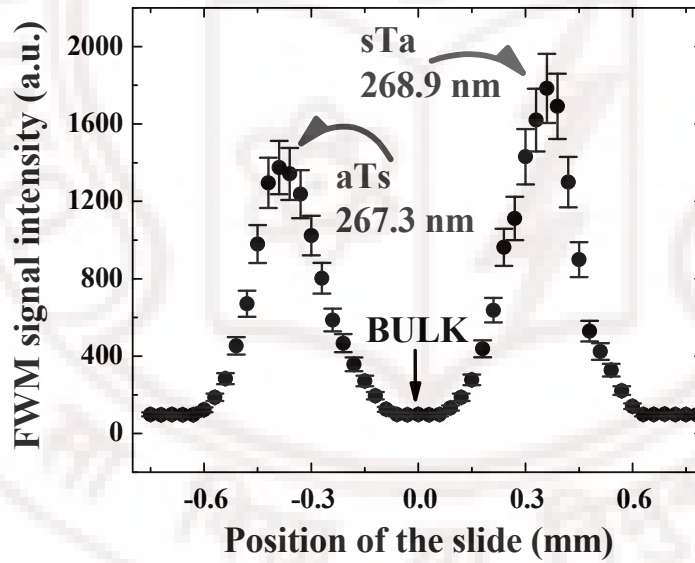


Fig. 6.3: (b) Spectra recorded with He-Ne laser beam as a reference



In order to verify that the peak-shift is not an artifact we sent a He-Ne laser beam as a reference collinear with one of the 800 nm beams and the scattered beam is recorded along with the FWM signal. As seen in figure 6.3(b), the peak corresponding to He-Ne laser beam does not show any shift in its spectrum. Further, in order to avoid the effects of dispersion of fiber, the FWM signal is directly coupled into the slit of the spectrometer rather than coupling it through a fiber. As we translate the fused silica slide across the focal point we observe the following: (i) the FWM signal increases as the aTs approaches the focus and then decreases as it moves away from the focus; (ii) no observable signal in the bulk and (iii) the signal increases gradually till sTa and then decreases as the focal positions moves out of the silica slide. Figure 6.4 shows the signal strength as a function of the position of the silica slide considering the center of the slide as the reference point.



**Fig.6.4:** The variation of the FWM intensity as the fused silica slide is moved across the focal spot of the lens.

Clearly, we see that owing to the interaction length of the two beams, the FWM signal is seen for 300  $\mu\text{m}$  about the two interfaces and no signal for 300  $\mu\text{m}$  about the center. The error bars shown in the figure 6.4 are representatives of the experimental error of 20%, which is reasonable considering the weak signals

involved. This error is estimated by repeating the experiment as many as three times. From the figures (6.3a) and (6.4) we draw an important conclusion that the intensity of the FWM from aTs is weaker compared to FWM from sTa and that both these signals are several orders larger than the bulk value. We rule out the reduction in the FWM signal intensity at aTs owing to the material absorption as fused silica is a high band-gap material and is practically transparent till 190nm.

#### 6.4.2 Spectral studies with position of the slide

Another interesting feature that we observe is the change in spectral content of the FWM at the two interfaces as we change the position of the focal point. This is achieved by translating the silica slide with the help of a micro-positioner, each step being 30  $\mu\text{m}$ . Figure 6.5 is a 3D plot of the intensity of the FWM signal against the slide position. Clearly we find that no signal is generated at the center of the slide.

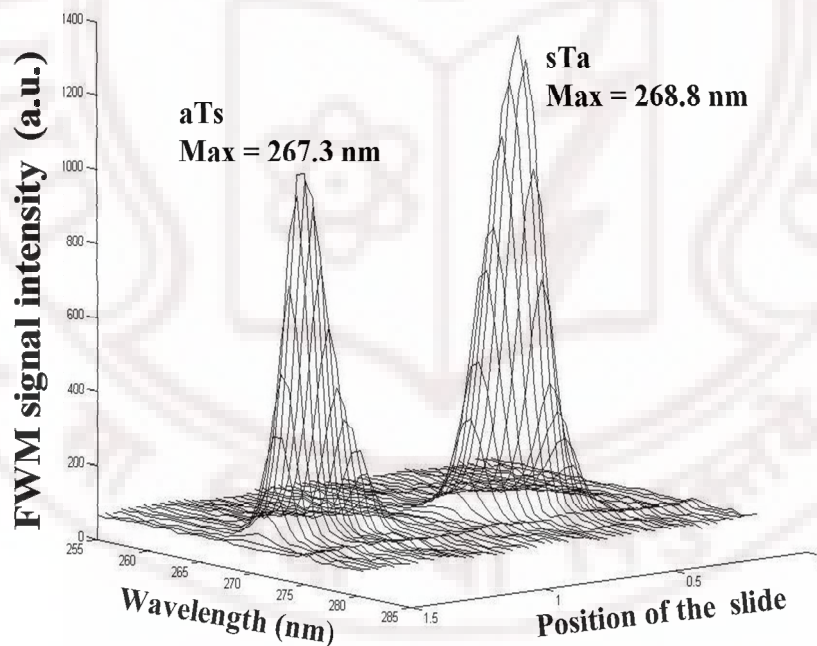


**Fig 6.5(a):** A 3-D plot showing the FWM spectra at various positions in the silica slide

Figure 6.5(b) is a grey scale image plot of the FWM spectra showing the spectra plotted as a function of slide position. From this figure one can observe the peak the overlapping frequencies and the spread of frequencies. At the first

at the interface there is a frequency-shift of  $\sim 1\text{nm}$  as the focal point enters from the air into the silica. This can be seen in the lower group of spectral images of figure, whereas the upper half of the figure shows the spectral content at the sTa interface doesn't show any change i.e., the spectral content is the same when the focal point is (1) in the silica bulk close to sTa interface, (2) on the interface, and (3) in the air close to sTa interface.

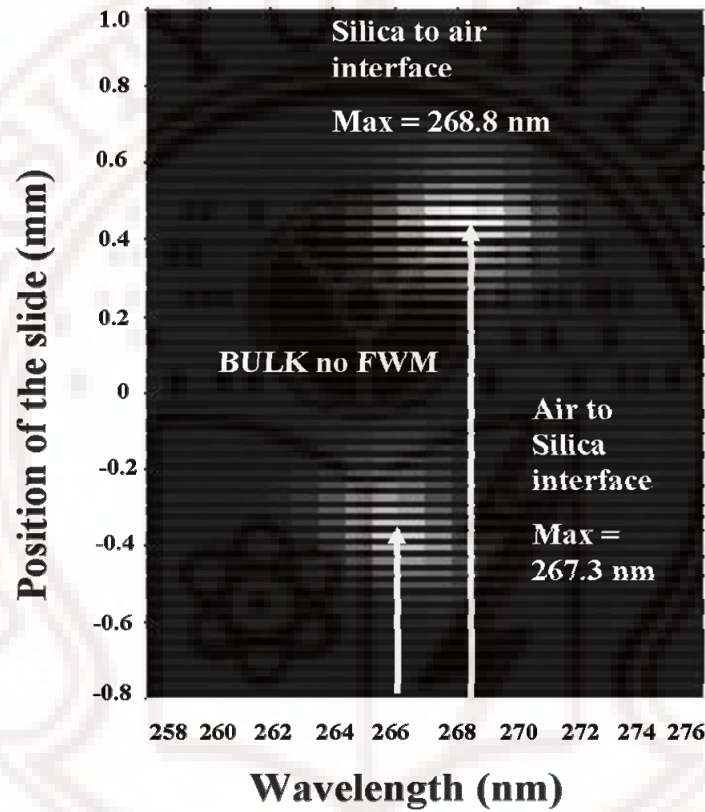


Fig 6.5(b): The spectra plotted as a 2D plot of spectra vs position of the slide.

#### 6.4.3 Intensity studies of the FWM signal

As mentioned earlier we observed the FWM at input intensities of fundamental pulses (P1 and P2) in the range of  $400 - 800 \text{ GW/cm}^2$ . Figure 6.6 shows the FWM signals at aTs and sTa interfaces with increase in fundamental input intensity at the overlap region. Figure 6.7 shows the variation of the peak strength with input intensity. The FWM signal as usual is found to increase cubically with increase in the input beam intensity confirming the third order

nonlinear process [considering the fitting equation:  $y = ax^3$ ]. The error bars shown the figure are representative of the experimental error of 20%, which is reasonable considering the weak signal involved.

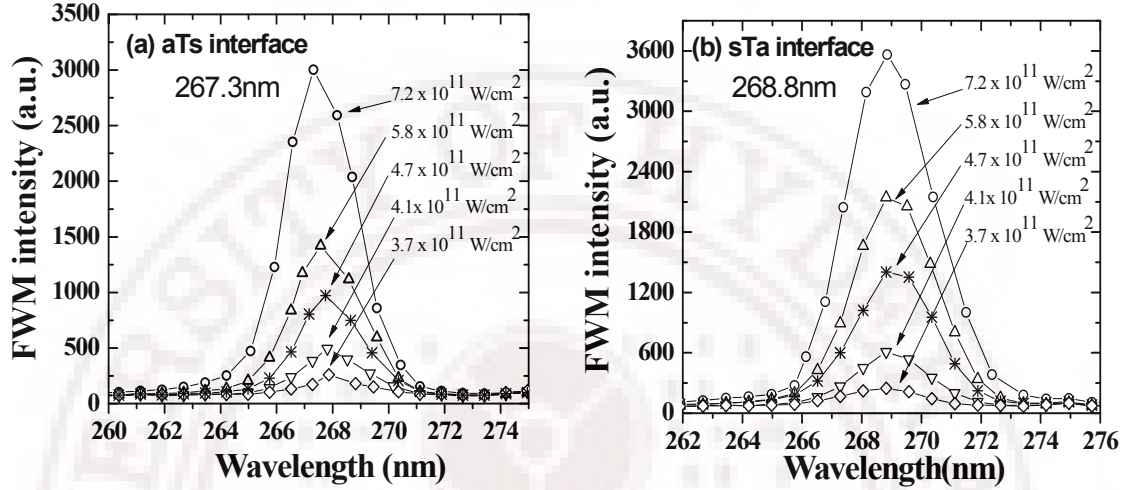


Fig 6.6: Plots of FWM spectra with increase in intensity:  
(a) at aTs interface; (b) at sTa interface

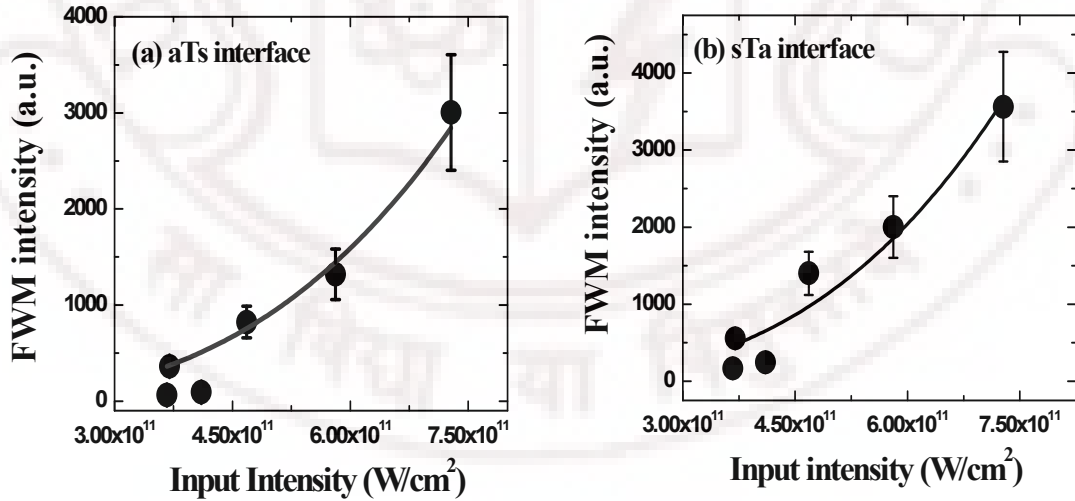


Fig 6.7: Plots of FWM peak as a function of input intensity  
(a) at aTs interface; (b) at sTa interface

#### 6.4.4 Delay studies of the FWM signal

Since the experimental conditions demand perfect temporal overlap of the two input-fundamental beams we observed the reduction of the FWM signal with increase in the delay between the two overlapping pulses. Also no shift in the FWM signal peak was observed within the resolution of the spectrometer used. In the case of FWM signal at aTs interface it is straight forward to visualize but in the case of signal at sTa interface we need to take the dispersion effects into consideration as fs pulses may undergo GVD and get stretched temporarily.

##### Calculation of temporal broadening due to GVD :

From the discussion of GVD calculations in chapter 2 we have the broadening term  $B$  defined as the ratio of the output pulse-width to the input pulse-width i.e.,

$$B = \tau_{out} / \tau_{in} \Rightarrow \tau_{out} = B \times \tau_{in}$$

For a transform-limited gaussian pulse:  $B = \left\{ 1 + \left[ 7.68 \left( k_2 \times \frac{L}{\tau_{in}^2} \right)^2 \right] \right\}^{\frac{1}{2}}$ , where

$k_2$  is the 2<sup>nd</sup> order dispersion coefficient.

In our experimental conditions:

$\tau_{in}$	100 fs
$k_2$ (fused silica at 800nm)	300 fs <sup>2</sup> /cm
L (length of the sample)	0.1cm
$B$	1.01
$\Rightarrow \tau_{out}$	101 fs

From the above calculations, we conclude that after passing through the fused silica slide the temporal broadening due to GVD is negligible and therefore we expect the resultant of the change in FWM signal at the sTa interface due to the delay between the overlapping pulses follow the same trend as observed at aTs interface.

## 6.5 Analysis of the experimental observations

### 6.5.1 Enhancement of $\chi^{(3)}$ at interfaces

The most important conclusion from the discussion in section 6.2, is that there is certain contribution of  $\chi_s^{(3)}$  along with the  $\chi_{bulk}^{(3)}$  on the overall nonlinear polarization field. Thus even if one the overall nonlinear field generated in the bulk is negligible, one should consider substantial contribution from the field generated at the interface. Moreover, although the third-order nonlinear susceptibility  $\chi^{(3)}$  of the bulk of a dielectric material is generally smaller than the second order nonlinear susceptibility  $\chi^{(2)}$ , the use of high-intensity laser beam can give a larger induced third-order polarization  $\mathbf{P}(3\omega)$  than that of corresponding second-order polarization  $\mathbf{P}(2\omega)$ . At an interface, the discontinuity in the normal component of the electric field gives rise to a large gradient in the fundamental electric field normal to the surface, leading to a large nonlinear polarization field. Also at the interface between two non absorbing dielectric media with inversion symmetry, the third-order surface nonlinear susceptibility  $\chi_s^{(3)}$  is always electric dipole allowed while the second order surface nonlinear susceptibility  $\chi_s^{(2)}$  is allowed only because of the degeneracy lifted by the lack of translational symmetry across the interface, which gives  $\chi_s^{(2)}$  and intrinsically smaller value. This qualitative argument indicates that the induced third order polarization field  $\mathbf{P}(3\omega) = \chi^{(3)}\mathbf{E}^3(\omega)$  can easily exceed  $\mathbf{P}(2\omega) = \chi^{(2)}\mathbf{E}^2(\omega)$ , thereby enhancing the efficiency of third order nonlinear processes in transmission from dielectric interfaces even with a moderately intense laser fundamental.

In his experimental work Tsang [9] estimated the value of  $\chi_s^{(3)}$  at air-silica glass interface by direct comparison of THG signal strength obtained at air-glass interface to the THG signal strength obtained in air under identical experimental condition using the amplified fs pulses. The obtained THG yield at

the air-glass interface was larger than that of air by  $\sim 10^{12}$ . The THG intensity depends on the  $\chi^{(3)}$  of the medium as follows [3]:

$$I(3\omega) \propto \left| \hat{e}_{3\omega} \chi^{(3)} : \hat{e}_{\omega} \hat{e}_{\omega} \hat{e}_{\omega} \right|^2 I^3(\omega)$$

Thus the value of  $\chi_s^{(3)}$  at air-silica glass interface is  $\sim 10^6$  larger than the corresponding value of air. Taking the reference  $\chi^{(3)}$  of air to be  $\sim 10^{-17}$  esu [12], the  $\chi_{surface}^{(3)}$  at air-silica glass interface was estimated to be  $\sim 10^{-11}$  esu. The phenomenon of FWM at interfaces agrees well with the above discussion where the third-order nonlinear susceptibility of bulk amorphous fused silica  $\chi_{bulk}^{(3)}$  ( $\sim 1.4 \times 10^{-14}$  esu) [11] is found to be much lower than that at the surface  $\chi_s^{(3)}$  ( $\sim 10^{-11}$  esu ).

### 6.5.2 Analysis for observation of no FWM from bulk:

The coherence length calculated for THG to occur in fused silica from the relation  $l_c = \lambda_0 / |6(n_{\omega} - n_{3\omega})|$  is  $\sim 3\mu\text{m}$ , where  $\lambda_0$  is the wavelength of fundamental at 800 nm and  $n_{3\omega}$  ( $= 1.499$ ) and  $n_{\omega}$  ( $= 1.453$ ) are the refractive indices of fused silica at 267 nm and 800 nm respectively. As  $\chi_{surface}^{(3)}$  is three orders of magnitude larger than  $\chi_{bulk}^{(3)}$  and  $L \gg l_c$ , translation of the slide across the interaction region results in the generation of FWM signal mainly due to significant contribution of  $\chi_{surface}^{(3)}$  throughout the interaction region  $L$ . When the interaction region is entirely inside the bulk we observe no signal due to the effective cancellation of the generated signals as  $L \gg l_c$  and weak signals from the bulk.

We generated the FWM signals using different focal length lenses (6 to 17cm) to alter the interaction length in the bulk and get odd multiples of the  $l_c$



for the interaction region. We still did not observe any signal in the bulk. If there is no enhancement in the nonlinearity at the surface, we should have observed signals while changing the interaction length in the bulk. We therefore conclude that the signals observed at the surfaces are due to the enhanced surface nonlinearities arising from the structural discontinuity and local fields caused by the field discontinuity at the interface.

### 6.5.3: Analysis for observation of peak shift in FWM:

We can explain the observed peak-shift of FWM through the following phase matching considerations. As the Rayleigh range is 2 cm, we can consider the two interacting beams over the interaction region of 300  $\mu\text{m}$  as plane waves. The FWM geometry is shown in figure 6.8, where the pump beams are represented by the wave vectors  $\mathbf{k}_1$  and  $\mathbf{k}_2$ . The generated phase matched FWM signals at  $2\mathbf{k}_1 + \mathbf{k}_2$  and  $\mathbf{k}_1 + 2\mathbf{k}_2$  respectively, appear well separated from the fundamentals  $\mathbf{k}_1$  and  $\mathbf{k}_2$  at an angle  $\theta$ . As can be seen the resultant FWM signals are represented along directions  $d_1$  and  $d_2$  with  $d_1$  pointing radically away from the center of the FWM pattern represented as a blue disk. The reason for this type of representation would be elaborated as we discuss further in this section.

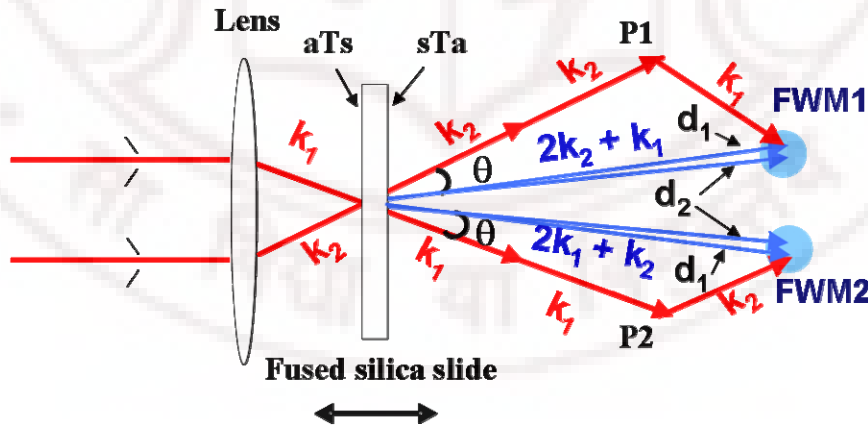
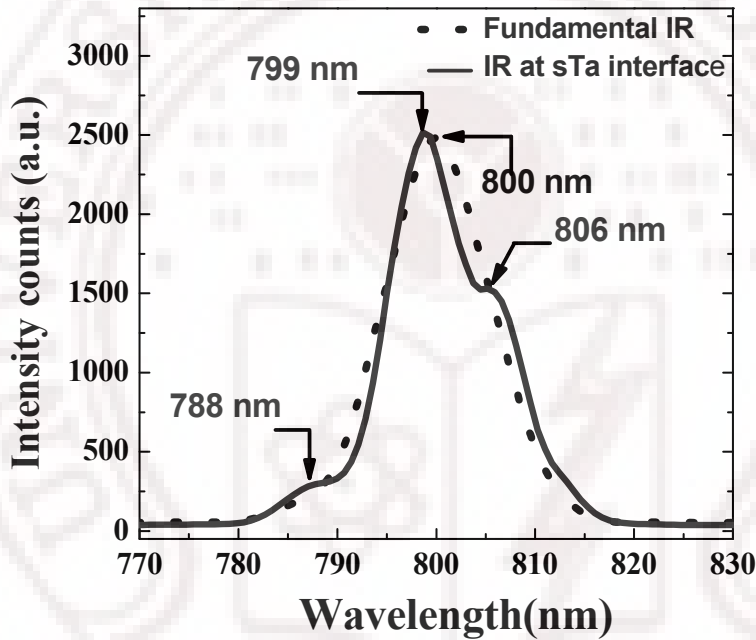


Fig.6.8: Wave-vector representation of the observed FWM.

As seen from the figure, the resultant FWM is calculated by considering the vector addition of the input fundamental  $\mathbf{k}_1$  and  $\mathbf{k}_2$  taking into the angle of interaction of the input beams i.e.,  $10^\circ$ . We performed these calculations

following the cosine law of triangles and obtained the resultant FWM magnitude and direction ( $\theta$ ).

To explain the FWM at aTs interface, we consider the input fundamentals  $\mathbf{k}_1$  and  $\mathbf{k}_2$  to be centered at 800 nm [figure 6.9 dotted curve] the calculated  $\mathbf{k}_1 + 2\mathbf{k}_2$  has a magnitude of 267.5 nm and a calculated value of  $\theta$  to be  $3.3^\circ$ . Thus we find that the calculated FWM signal and  $\theta$  values are in very good agreement with the measured FWM signal of 267.3 nm from aTs interface.



**Fig. 6.9:** The dotted curve showing spectral profile of IR fundamental used for the study before focusing into the slide and solid line is the modified spectral profile of the fundamental while the focus is at sTa interface of the slide

Similarly we recorded the spectrum of the fundamental just when the focus is at sTa interface. The spectra are shown as solid curve in figure 6.9. Clearly the spectral profile of fundamental is changed drastically as the pulse travels through the silica slide with the peak being split into two dominant peaks centered at 799 nm and 806 nm and a small peak centered at 788 nm. In order to explain the observed FWM signal the spectrometer slit ( $25 \mu\text{m}$ ) is scanned across the FWM signal spots. For the direction which is away from the center of the

pattern (direction  $d_1$ ) the spectral peak appears at 268.8 nm and when the slit is moved towards the center of the pattern (direction  $d_2$ ) the peak appears at 268.0 nm indicating wave mixing of different  $\mathbf{k}$ -wave vectors of the spectrally dispersed fundamental beam at the second surface. Figure 6.10 shows the FWM spectra obtained along the two directions. Following discussion pertains to only one position of the slit ( $d_1$ ) where 799 nm ( $\mathbf{k}_1$ ) mixes with 806 nm ( $2\mathbf{k}_2$ ). The data was found to match exactly for the mixing of 806 nm ( $\mathbf{k}_1$ ) and 799 nm ( $2\mathbf{k}_2$ ) leading to 268.0 nm.

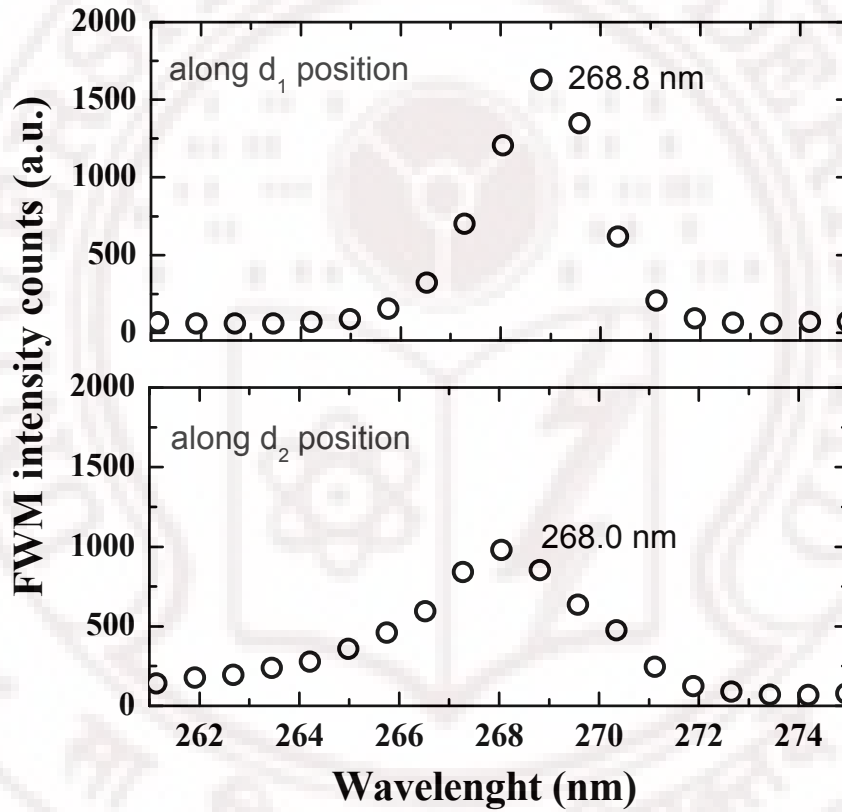


Fig. 6.10: FWM spectra at sTa interface along  $d_1$  and  $d_2$  directions

Having explained the observation of the peak-shift of FWM at the two interfaces we now theoretically simulate the FWM curve obtained at the two interfaces. In order to arrive at the FWM observed at aTs surface, we have assumed mixing of 800 nm ( $\mathbf{k}_1$ ) and 800 nm ( $\mathbf{k}_2$ ) leading to the FWM signal ( $\mathbf{k}_1 + 2\mathbf{k}_2$ ) at 267.3 nm with  $\Delta\lambda \sim 2.6$  nm. Since the fundamental spectra gets modified at

it propagates through the bulk and reaches sTa interface, we deconvoluted the spectra into individual peaks at 788 nm, as shown in Figure 6.11. Since the FWM is essentially an intensity dependent process we neglect the small peak at 788 nm and consider only the peaks at 799 nm and 806 nm.

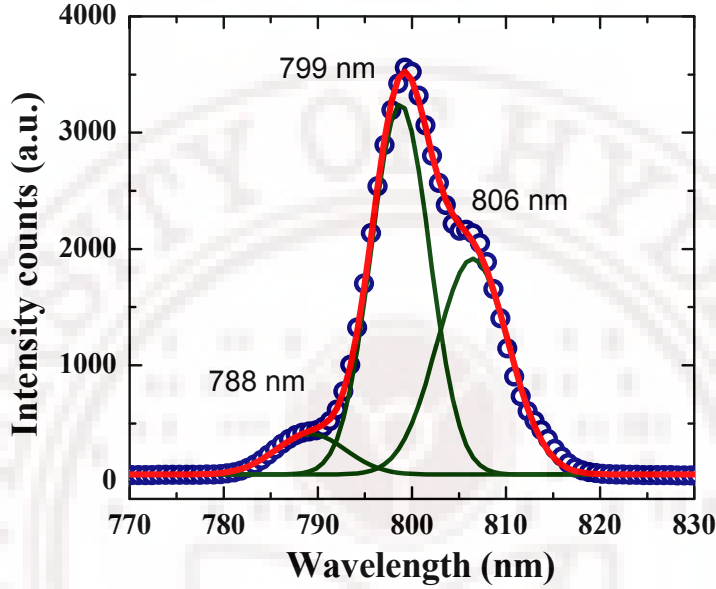


Fig. 6.11: Deconvolution of fundamental spectra at sTa interface

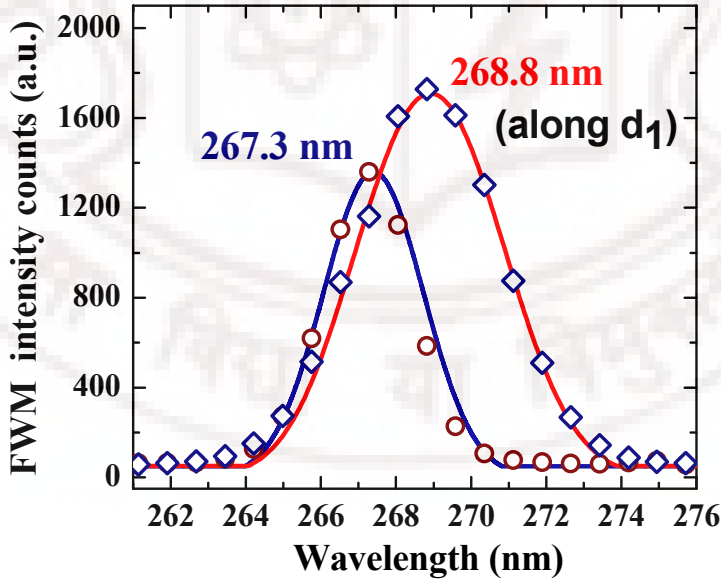


Fig. 6.12: Theoretical simulated FWM spectra at the two interfaces. Open circles and diamonds are the experimental data whereas the solid lines show the simulated curves for wave-mixing at aTs and sTa interfaces respectively taking into account the wave-mixing of all the spectral components present in the fundamental when the spectrometer slit at  $d_1$ .

To obtain the theoretically simulated curve for the FWM signal ( $\mathbf{k}_1 + 2\mathbf{k}_2$ ) at sTa interface, we consider 799 nm (as  $\mathbf{k}_1$ ) and 806 nm (as  $\mathbf{k}_2$ ) assuming suitable efficiencies and obtained the FWM signal at 268.9 nm with  $\Delta\lambda \sim 3.9$  nm for the fundamental beams recorded when the spectrometer slit is in position  $d_1$  at 799 nm and 806 nm. The simulated curves for FWM at aTs and sTa interfaces (along  $d_1$  direction) are shown in figure 6.12. Spectral dispersion in the silica slide gives rise to a distribution of spectrum along with corresponding wave vectors. Thus availability of a wide range of wave vectors due to dispersed spectrum at the second surface is assumed to lead to wave mixing with higher efficiency at the sTa surface. The values of  $\Delta\lambda$  for the simulated curves are also in close agreement with the observed FWM signals. A summary of the experimentally observed and theoretically calculated values of various quantities is presented in Table 6.1, which are in good agreement. The observed differences are mainly due to the resolution of the spectrometer.

**Table 6.1.** Summary of the theoretical predictions for explaining the observed peak shift of FWM signal at the aTs and sTa

	$\mathbf{k}_{\text{FWM}} = \mathbf{k}_1 + 2\mathbf{k}_2$				$\theta$		$\Delta\lambda$	
	$\lambda(\mathbf{k}_1)$ (nm)	$\lambda(\mathbf{k}_2)$ (nm)	$\lambda_{\text{FWM}}$ (nm) Theory	$\lambda_{\text{FWM}}$ (nm) Observed	Theory	Observed	Theory (nm)	Observed (nm)
aTs	800	800	267.5	267.3	$3.3^0$	$3.5^0$	2.6	2.4
sTa slit at $d_1$	806	799	268.9	268.8	$3.4^0$	$3.4^0$	3.9	3.8
sTa slit at $d_2$	799	806	268.2	268.0	$3.5^0$	$3.6^0$	3.0	3.7

At the beginning of the discussion it was pointed out that the observation pertaining to FWM1. Similar observations were also obtained with FWM2. However at sTa the peaks obtained along directions  $d_1$  and  $d_2$  are reverse of that obtained for FWM1. This can be elucidated by considering the following explanation: along the direction  $d_1$ , FWM1 ( $\mathbf{k}_1 + 2\mathbf{k}_2$ ) at 268.8 nm is a resultant of mixing of one photon of 806 nm ( $\mathbf{k}_1$ ) and two photons of 799 nm ( $\mathbf{k}_2$ ), this

implies that in the same experimental conditions in which FWM2 is also generated simultaneously along with FWM1, the FWM2 ( $2\mathbf{k}_1 + \mathbf{k}_2$ ) would be because of mixing of two photons of 806 nm ( $\mathbf{k}_1$ ) and one photons of 799 nm ( $\mathbf{k}_2$ ), resulting in signal at 268.0 nm. Using the same analysis along the directions  $d_2$  we observe FWM2 at 268.8 nm.

#### 6.5.4 Discussion on the nomenclature of usage of FWM and not THG:

We did not use the word third harmonic generation (THG) to describe the observation as used by other researchers [13,14], as our results provides a clear picture of the evolution of frequencies at wave vectors  $2\mathbf{k}_1 + \mathbf{k}_2$  and  $2\mathbf{k}_2 + \mathbf{k}_1$  values which are different from the THG signal. Further we also show in the manuscript how different wave-vectors mix and give rise to different frequencies in the four wave mixing (FWM) signal, which is the main aim of this work. The THG peak of 800 nm should appear at 266.7 nm, whereas the observed peaks are at 267.3 nm and 268.8 to 268.0 nm.

We could have used THG for the case at aTs surface as it involves mixing of 800 nm ( $\mathbf{k}_1$ ) with 800 nm ( $\mathbf{k}_2$ ) following the nomenclature of others. The signal at sTa surface is mainly due to the mixing of 799 nm ( $\mathbf{k}_1$ ) with 806 nm ( $\mathbf{k}_2$ ). Earlier reports call the observed signal as THG and do not show the spectrum of the interacting beams. We recorded the spectrum of the fundamental when the focal point is at the two interfaces of the silica slide. Further the spectrum of the fundamental beams recorded after passing through the surfaces did not show any THG as shown by M. Samoc and others. This clearly tells us that it is the FWM that dominates rather than the THG. Enhancement of the third-order effects at the surface can come from several distinct sources. For a focused beam one has to consider the Gouy shift which may lead to effective cancellation of the third-order effect in the bulk [12] thus, leading to significant THG only at the interfaces. Since the beams are not tightly focused the Gouy-phase is not considered in our case and we attribute the signals observed at the surfaces are due to the enhanced surface nonlinearities arising from the structural

discontinuity and local fields caused by the field discontinuity at the interface. It should also be noted here the observed process is different to a cascaded process involving higher order diffracted fundamental beams, as reported by Liu *et al.* and Crespo *et al.* [15]

## 6.6 Conclusions

- We established that a simple interface between two non absorbing dielectric media has enhanced third order nonlinearities owing to the break of symmetry at the interface in the normal direction resulting in a large field gradient.
- We developed a basic theoretical formulation to demonstrate the there is certain contribution of  $\chi_s^{(3)}$  along with the  $\chi_{bulk}^{(3)}$  on the overall nonlinear polarization field, Thus even if one the overall nonlinear field generated in the bulk is negligible, one should consider substantial contribution from the field generated at the interface.
- Through our studies, the enhancement of  $\chi^{(3)}$  at an air-dielectric interface was demonstrated in this work by employing the four-wave mixing at the interfaces of a fused silica slide with air in a two beam non-collinear geometry using 100 fs, 800 nm amplified pulses.
- By recording the FWM spectra at the two interfaces and the center of the slide we find that there is enhanced FWM at the two interfaces with the FWM at sTa more intense than aTs and no FWM at the center of the slide.
- More interestingly, owing to the spectral modification of a intense fs pulse after propagation through a dispersive medium, we observe that there is maximum peak shift of  $\sim 1.5$  nm in the FWM generated at the two interfaces.



## 6.6 References

1. N. Bloembergen, and P.S. Pershan, Phys. Rev. **128**, 606 (1962); A. Bagchi, R. G. Barrera, and A. K. Rajgopal, Phys. Rev. B **20**, 4824 (1979); W. L. Mochan, R. Fuchs, and R. G. Barrera, Phys. Rev. B **7**, 771 (1983); T.F. Heinz, "Second-order nonlinear optical effects at surfaces and interfaces," in *Nonlinear Surface Electromagnetic Phenomenon*, H.-E. Ponath and G.I. Stegeman, eds. (Elsevier, Amsterdam, 1991), pp. 353-416; J. E. Sipe, J. Opt. Soc. Am. B **4**, 481 (1987);
2. S.S. Jha, Phys. Rev. A **140**, A2020 (1965); S.S. Jha, Phys. Rev. Lett. **15**, 412 (1965); S. S. Jha and C. S. Warke, Phys. Rev. **153**, 751 (1967); S. S. Jha and C. S. Warke, Phys. Rev. **162**, 854 (1967); N. Bloembergen, R. K. Chang, S. S. Jha, and C. H. Lee, Phys. Rev. **174**, 813 (1968);
3. Y. R. Shen, *The Principles of Nonlinear Optics*, (Wiley-Interscience, New York, 1984);
4. H. W. Tom, T. F. Heinz, and Y. R. Shen, Phys. Rev. Lett. **51**, 1983 (1983); P. Guyot-Sionnest, W. Chen, and Y. R. Shen, Phys. Rev. B **33**, 8254-8263 (1986); P. Guyot-Sionnest and Y. R. Shen, Phys. Rev. B **35**, 4420 (1987); P. Guyot-Sionnest and Y. R. Shen, Phys. Rev. B **38**, 7985 (1988).
5. C. H. Lee, R. K. Chang, and N. Bloembergen, Phys. Rev. Lett **18**, 167 (1967); C. C. Wang and A. N. Duminiski, Phys. Rev. Lett. **20**, 668 (1968); C.C Wang, Phys. Rev. **178**, 457 (1969); F. Brown and M. Matsouka, Phys. Rev. **185**, 985 (1969); V. Mizrahi and J. E. Sipe, J. Opt. Soc. Am. B **5**, 660-667 (1988); C. K. Chen, A. R. B. de Castro, and Y. R. Shen, Phys. Rev. Lett. **46**, 145 (1981); J. E. Sipe, V. Mizrahi, and G. I. Stegeman, Phys. Rev. B **35**, 9091 (1987).
6. X. Wei, S. C. Hong, A. I. Lvovsky, H. Held, and Y. R. Shen, J. Phys. Chem. B **104**, 3349 (2000); H. Held, A. I. Lvovsky, X. Wei, and Y. R. Shen, Phys. Rev. B **66**, 205110 (2002), S. Cattaneo, M. Siltanen, F. Wang, and M. Kauranen, Opt. Express **13**, 9714 (2005); S. Cattaneo, and M. Kauranen, Phys. Rev. B **72**, 033412 (2005); P. Figliozzi, L. Sun, Y. Jiang, N. Matlis, B. Mattern, M. C. Downer, S. P. Withrow, C. W. White, W. L. Mochán, and B. S. Mendoza, Phys. Rev. Lett. **94**, 047401 (2005); F. J.

7. Y. R. Shen, *Nature* **337**, 519 (1989) and references there in; Y.R. Shen, *Appl. Phys. B* **68**, 295 (1999) and references there in; G. Lupke, *Surf. Sci. Rep.* **35**, 77(1999);
8. D. J. Moss, H. M. van Driel, and J. E. Sipe, *Appl. Phys. Lett.* **48**, 1150 (1986); J. E. Sipe, D. J. Moss, and H. M. Van Driel, *Phys. Rev. B* **35**, 1129 (1987)
9. T. Y. F. Tsang, *Phys. Rev. A*. **52**, 4116 (1995).
10. D. Meshulach, Y. Barad, Y. Silberberg, *J. Opt. Soc. Am. B* **14**, 2122 (1997); Y. Barad, H. Eisenberg, M. Harowitz, Y. Silberberg, *Appl. Phys. Lett.* **70**, 922 (1997); G. Veres, S. Matsumoto, Y. Nabekawa, K. Midorikawa, *Appl. Phys. Lett.* **81**, 3714 (2002); V. Shcheslavskiy, G. Petrov, V. V. Yakovlev, *Appl. Phys. Lett.* **82**, 3982 (2003).
11. R. L. Sutherland with contributions by D. G. McLean and S. Kirkpatrick, *Handbook of Nonlinear Optics*, Second Edition, Revised and Expanded (New York, NY: Marcel Dekker) (2003).
12. R. W. Boyd, *Nonlinear optics*, 2<sup>nd</sup> Ed., Academic Press, New York (2003).
13. M. Samoc, A. Samoc, and B. L. Davis, *Opt. Express* **11**, 1787 (2003).
14. T. Schneider and J. Reif, *Phys. Rev. A* **65**, 023801 (2002); J. Reif, R.P. Schmid and T. Schneider, *Appl. Phys. B* **74**, 745 (2002); T. Schneider, R. P. Schmid, and J. Reif, *Appl. Phys. B*. **72**, 563 (2001); T. Schneider, D. Wolfframm, J. Reif: *Nucl. Instrum. Methods B* **166**, 809 (2000);
15. J. Liu, and T. Kobayashi, *Opt. Express* **16**, 22119 (2008); H. Crespo, J.T. Mendonca, A. Dos Santos, *Opt. Lett.* **25**, 829 (2000).

The logo of the University of Hyderabad is a circular emblem. The outer ring contains the text "UNIVERSITY OF HYDERABAD" at the top and the Sanskrit motto "सा विद्या या विमुक्तये" at the bottom. The inner circle features a central sun-like symbol with rays, flanked by a stylized atom on the left and a lightning bolt on the right, all set against a background of small dots.

# CHAPTER 7

### Abstract

*In this chapter, we present our results on nonlinear optical properties of 2(3), 9(10), 16(17), 23(24) tetra tert-butyl phthalocyanine and 2(3), 9(10),16(17), 23(24) tetra tert-butyl Zinc phthalocyanine studied using Z-scan technique with 800 nm femtosecond and 532 nm nanosecond pulses. Nonlinear absorption behavior in both femtosecond and nanosecond domains was studied in detail. We observed three-photon absorption with femtosecond laser excitation and strong reverse saturable absorption with nanosecond pulse excitation. We have also evaluated the sign and magnitude of the third-order nonlinearity. Further, we carried out investigation of ultrafast nonlinear optical properties including the time response of studied using degenerate four-wave mixing technique at a wavelength of 800 nm with 100 fs pulses. We recorded large off-resonant second hyperpolarizability ( $\gamma$ ) for these molecules with ultrafast nonlinear optical response in the femtosecond domain. Our studies on their figures of merit indicate these molecules possess enormous potential for photonic switching applications. The performance of these molecules vis-à-vis other molecules, in general, and phthalocyanines, in particular, is discussed.*

# Multiphoton absorption and ultrafast nonlinear optical properties of alkyl phthalocyanines

## 7.1 Introduction

The high intensities associated with fs pulses can induce profound changes in the optical properties of a material leading to a nonlinear response of the real and imaginary parts of polarization. The imaginary part of the nonlinear polarization is associated, for instance, with multiphoton transitions and will exhibit a  $n$ -photon resonance when two level of an atomic or molecular system can be connected by  $n$  optical quanta. Nonlinear absorption refers to the change of transmittance of a material as a function of intensity or fluence. At sufficiently high intensities, the probability of a material absorbing more than one photon before relaxing to the ground state can be greatly enhanced. As early as 1931, Göppert-Mayer derived the two-photon transition probability in a system using the second order quantum perturbation theory [1]. With the availability of high intensities with fs pulses, in addition to numerous investigations into this phenomenon of the simultaneous absorption of two photons, multiphoton ( $>2$ ) absorption has also been widely studied. Multiphoton absorption processes are highly promising for a number of processes including optical limiting [2], 3D microfabrication [3], and optical data storage [4].

Porphyrins and phthalocyanines systems have received particular attention in the context of multiphoton absorption because of their large  $\pi$  electron delocalization, flat structure, and high thermal stability with applications in optical processing devices, practical optical limiters, and biomedical applications [5-8]. In organic materials three-photon absorption (3PA) typically occurs at longer wavelengths in the near infrared region (NIR) introducing advantages including minimization of the scattered light losses and reduction of undesirable linear absorption. The ramifications of such properties in biological

and medical applications include maximization of the radiation penetration depth through tissue, facilitating tumor imaging, and photo-annihilation in the absence of complicated and risky surgery [7]. Such materials will have a broad impact in biology and medicine through three-photon induced photodynamic therapy (PDT) in cancer treatment. Recently novel materials including organic fluorophores like halogenated fluorine molecules, polydiaetylenes, semiconductor nanoparticles have been investigated for their 3PA properties using femtosecond (fs) and picosecond pulses in the NIR spectral regions [9-14]. However, we discovered that there are sporadic reports on organic molecules exhibiting 3PA in the significant wavelength region of 750–850 nm corresponding to the output of commercially available femtosecond Ti:Sapphire source routinely used by the researchers for biological applications. One such report measured two-photon absorption (2PA) spectra of a number of symmetrically substituted polydiaetylenes in the excitation wavelength region from  $\lambda_{\text{ex}} = 800$  to 1600 nm [9]. Phthalocyanines are versatile because they offer enormous structural flexibility with the capacity of hosting ~70 different elements in the central cavity. One of the major drawback with these molecules is majority of them are insoluble in common solvents. However, incorporation of substituents at the peripheral and non-peripheral positions has established to improve the solubility [15]. Recent studies have extracted a large variety of peripheral substituents for improving the poor solubility of unsubstituted phthalocyanines. New molecules with high two-photon (2PA) and three-photon absorption (3PA) cross-sections are interesting for their potential applications in photonics and biomedical applications [16]. Significant studies on application of phthalocyanines in PDT [7] have motivated us further to identify materials, especially phthalocyanine derivatives, with appropriate absorption in the UV region along with a transmission window in the NIR range contributing to multiphoton absorption.

Typically, the presence of nonlinear absorption in molecules like phthalocyanines augments their capability for optical limiting applications while the presence of nonlinear refraction facilitates all-optical switching applications.

Though nonlinear optical properties of variety of phthalocyanines have been investigated till date there are further opportunities and avenues to explore novel structures with superior figures of merit [17]. It is well established that for a third-order nonlinear material to be attractive for optical switching applications the nonlinear response has to be strong (a high value of the effective nonlinear refractive index  $n_2$ ) and instantaneous time response of the induced refractive-index change (typical response is expected in the sub-picosecond range) along with the requirement of minuscule material losses due to one-photon, multi-photon absorption. Furthermore, scattering losses are to be minimal for any signal processing devices application [18]. Accurate determination of the merit factors is imperative for deciding the applicability of third-order NLO materials for optical switching. Unfortunately many reports which dealt with the NLO properties of organic materials in general, with phthalocyanines in particular, furnish fragmentary information about these parameters.

In the light of above mentioned objective to investigate phthalocyanines as a potential candidate with good 3PA cross-section and ultrafast nonlinear optical behavior we concentrated our efforts on the nonlinear optical properties **2(3), 9(10), 16(17), 23(24) tetra tert-butyl phthalocyanine** (referred to as pc1) and **2(3), 9(10), 16(17), 23(24) tetra tert-butyl Zinc phthalocyanine** (referred to as pc2). The multiphoton absorption properties of pc1 and pc2 are obtained using Z-scan with 800 nm, 100 fs and 532 nm, 6 ns laser pulse excitation. From the fs open-aperture (OA) Z-scan data we derived that these molecules exhibit good three-photon absorption (3PA) coefficient/cross-sections even at moderate input intensities. The nanosecond (ns) OA Z-scan studies revealed strong effective nonlinear coefficients for these molecules at an excitation wavelength of 532 nm. We also estimated the sign and magnitude of the third order nonlinearity by means of the closed aperture scans from both ns and fs data.

Further, by utilizing the technique of degenerate four-wave mixing technique (DFWM) near 800 nm with ~100 femtosecond (fs) pulses we investigated the nonlinear optical response of pc1 and pc2. We observed large



third order nonlinear susceptibility [ $\chi^{(3)}$ ] and second order molecular hyperpolarizability [ $\gamma$ ] for these molecules. Time-resolved degenerate four wave mixing (DFWM) measurements in the box-car geometry revealed instantaneous response from these molecules. Our detailed DFWM studies suggest that these molecules are potential candidates for photonic switching applications. We have also tried to establish the competence of these molecules, compared to some of the recently reported molecules [19-27], through their figures of merit evaluation.

## 7.2 Molecular structure and spectroscopic characterization:

Alkyl phthalocyanines were synthesized according to the procedures reported in literature<sup>1</sup> and both pc1 and pc2 were purified before use. Each sample was subjected to a column chromatographic purification process prior to the nonlinear optical measurements. The details of molecular structures are depicted in figure 7.1. The molecular weights of pc1 and pc2 are 748 gm/M and 804 gm/M respectively

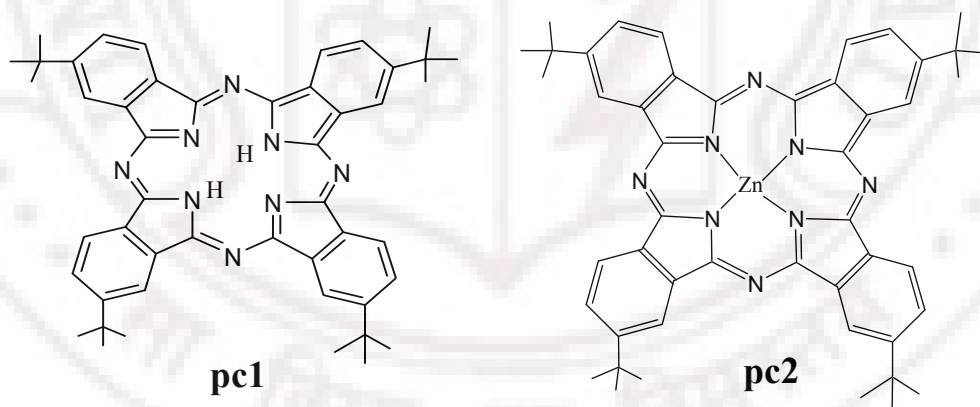


**Fig.7.1:** Structures of the phthalocyanines used (a) tetra *tert*-butyl phthalocyanine (pc1)  
(b) Zinc tetra *tert*-butyl phthalocyanine (pc2)

The absorption spectra were recorded using an UV-visible spectrometer for  $\sim 10^{-4}$  M solutions and are depicted in figure 7.2(a). These molecules show the characteristic linear absorption features typical of other phthalocyanines, the high

energy B (Soret) band and the low energy Q band(s). The compounds remained stable after exposure to laser pulses for a long period of time. Fluorescence spectra of these phthalocyanines, shown in figure 7.3, were recorded using Jobin Yvon Horiba–Fluoromax-3 luminescence spectrometer. pc1 has a sharp peak at 705 nm with excitation at 350 nm, while pc2 has a broad peak surrounding 475 nm along with a sharp peak at 765 nm.

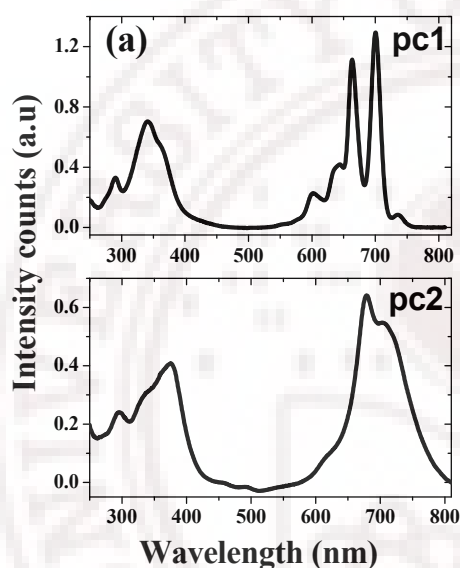


Fig.7.2: Absorption spectra

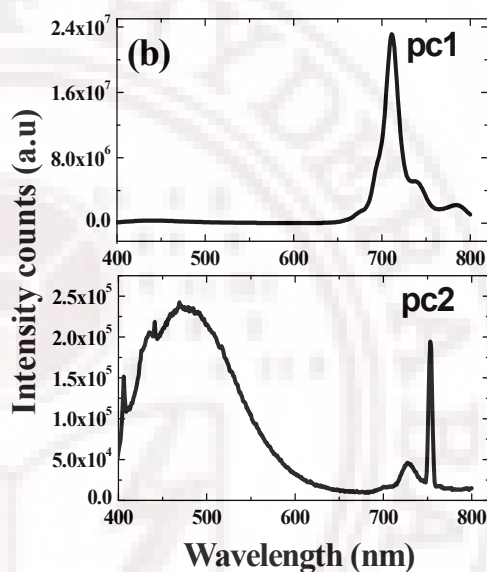


Fig.7.3: Fluorescence spectra of pc1 and pc2

Excited state lifetimes for these molecules were measured using the fluorescence decay measurements and were **6.31** and **3.18 ns** for pc1 and pc2, respectively. Fluorescence decays shown in figure 7.4 were recorded using TCSPC method using the following set up. A diode pumped millennia CW laser (Spectra Physics, 532 nm) was used to pump the Ti–Sapphire rod in Tsunami picosecond mode locked laser system (Spectra Physics). The 750 nm (82 MHz, 2.4 ps FWHM) pulses was taken from the Ti–Sapphire laser and passed through pulse picker (Spectra Physics, 3980 2S) to generate 4 MHz pulses. The second harmonic output (375 nm) was generated by a flexible harmonic generator (Spectra Physics, GWU 23PS). The vertically polarized 375 nm laser was used to excite sample. The incident power at the sample was  $\sim 0.3$  mW. The fluorescence

emission at magic angle ( $54.7^\circ$ ) was dispersed in a monochromator ( $f/3$  aperture), counted by a photomultiplier tube (Hamamatsu R 3809) and processed through multichannel analyzer. The instrument response function for the system was  $\sim 52$  psec. The fluorescence decay was obtained and was analyzed using IBH software (DAS6).

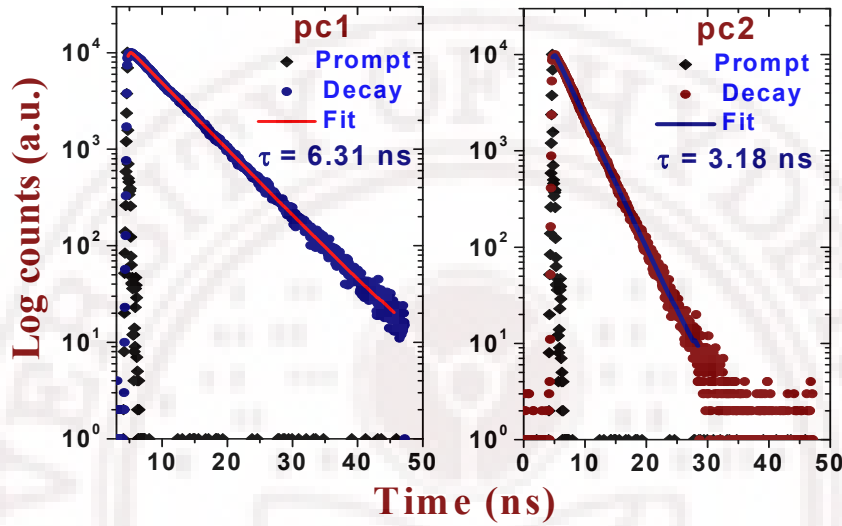


Fig.7.4: Fluorescence decay curves for pc1 and pc2 with TCSPC measurements

### 7.3 Multiphoton absorption studies by Z-scan technique:

#### 7.3.1 Theoretical considerations for multiphoton absorption processes:

Assuming a spatial and temporal Gaussian profile for laser pulses we derive the general equation for open aperture (OA) normalized energy transmittance below:

Two photon absorption (TPA) involves a transition from ground state (1) of a material to a higher-lying state (2) by the simultaneous absorption of two photons via an intermediate virtual state, as schematically shown in figure 7.5(a). In this case, the attenuation of the incident light is described by

$$\frac{dI}{dz} = -\beta I^2$$

where  $\beta$  is the two-photon absorption coefficient.

Three photon or multi photon absorption involves a transition from the ground state to a higher-lying state by the simultaneous absorption of three or more number photons via multiple numbers of virtual states as shown in figure 7.5(b). In this case, the attenuation of the incident light is described by

$$\frac{dI}{dz} = -\alpha_n I^n$$

where  $\alpha_n$  is the n-photon absorption coefficient.

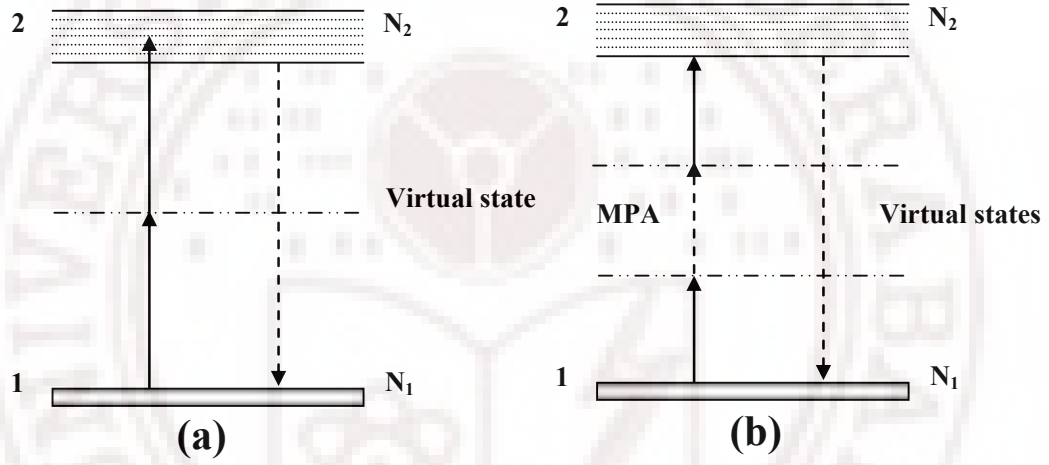


**Fig. 7.5:** Schematic energy level diagram for (a)Two-photon absorption (TPA); (b)Multi-photon absorption (MPA).

$$\frac{dI(z)}{dz} = -\alpha_n I^n(z)$$

$$\int_{I_{in}}^{I_{out}} \frac{1}{I^n(z)} dI(z) = -\alpha_n \int_0^L dz$$

$$-\alpha_n L = \left[ \frac{I^{-n+1}}{-n+1} \right]_{I_{in}}^{I_{out}} \Rightarrow \alpha_n L = \frac{1}{n-1} \left[ \frac{1}{I_{in}^{n-1}} - \frac{1}{I_{out}^{n-1}} \right]$$

$$\alpha_n L = \frac{1}{(n-1)I_{in}^{n-1}} \left[ 1 - \frac{1}{T^{n-1}} \right], \text{ where } T = \frac{I_{out}}{I_{in}} \quad T^{n-1} = \frac{1}{1 + \alpha_n L(n-1)I_{in}^{n-1}}$$

$$T = \frac{1}{\left[1 + \alpha_n L(n-1) I_{in}^{n-1}\right]^{\frac{1}{n-1}}}$$

$$\frac{I_{in}}{\omega_0^2} = \frac{I_{00}}{\omega_z^2}, \text{ where } I_{in} = \frac{I_{00}}{1 + \frac{Z^2}{Z_0^2}} \text{ and } \omega_z^2 = \omega_0^2 \left(1 + \frac{Z^2}{Z_0^2}\right)$$

$$T = \frac{1}{\left[1 + (n-1)\alpha_n L \left(I_{00} / \left(1 + (Z/Z_0)^2\right)\right)^{n-1}\right]^{\frac{1}{n-1}}}$$

$$\Rightarrow T_{OA(nPA)} = \frac{1}{\left[1 + (n-1)\alpha_n L \left(I_{00} / \left(1 + (Z/Z_0)^2\right)\right)^{n-1}\right]^{\frac{1}{n-1}}}$$

where  $\alpha_n$  is the effective MPA coefficient ( $n = 2$  for 2PA;  $n = 3$  for 3PA, and so on),  $I_{00}$  is the peak intensity (at  $Z=0$ ),  $I_{in}$  is intensity at sample position (if  $Z$  is the distance from focal point  $I_{in}$  ( $I_z$ ) is the intensity at that point),  $Z_0 = \pi\omega_0^2/\lambda$  is Rayleigh range,  $\omega_0$  is the beam waist at the focal point ( $Z=0$ ),  $dz$  is small slice of the sample,  $I_{in}$  is input intensity and  $I_{out}$  is output intensity of the sample.

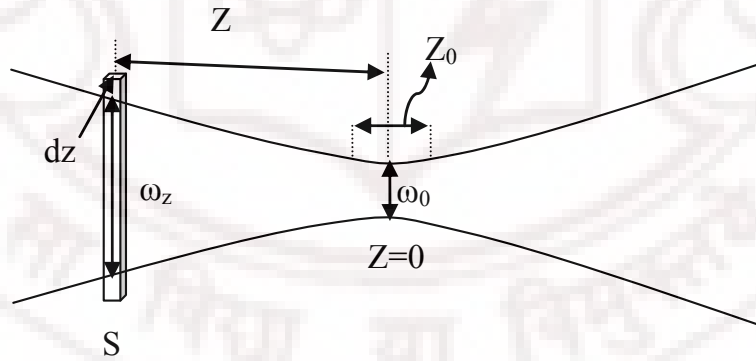


**Fig.7.6:** Schematic diagram of focused laser beam.

If we retain only the 2PA term and ignore all other terms, we have an analytical expression for OA Z-scan for merely two-photon absorbers. Similarly retaining the 3PA term and ignoring the other terms provides us an analytical expression for OA scans for only three-photon absorbers.

$$T_{OA(2PA)} = \frac{1}{1 + \alpha_2 L_{eff} \left( I_{00} / \left( 1 + (z/z_0)^2 \right) \right)} \quad (7.1)$$

$$T_{OA(3PA)} = \frac{1}{1 + 2\alpha_3 L'_{eff} \left( I_{00} / \left( 1 + (z/z_0)^2 \right) \right)^{1/2}} \quad (7.2)$$

The effective path lengths in the sample of length L for 2PA, 3PA is given as

$$L_{eff} = \frac{1 - e^{-\alpha_0 L}}{\alpha_0} \quad L'_{eff} = \frac{1 - e^{-2\alpha_0 L}}{2\alpha_0}$$

### 7.3.2 Experimental Details:

Alkyl phthalocyanines were synthesized according to the procedures reported in literature [28] and were purified before use. All the experiments were performed with samples dissolved in chloroform and placed in 1-mm glass/quartz cuvettes. Amplified fs laser pulses of ~100 fs, 800 nm were used from the laser system as described in chapter-2. To make a complete study for these molecules we also performed z-scan studies with ns pulses. A frequency doubled Nd:YAG laser (Spectra-Physics INDI-40) with 6 ns pulse duration and 10 Hz repetition rate was used for measurements in the ns regime. The Z-scan experimental set up as discussed in chapter 2. Z-scan studies [29] were performed by focusing the input beam using an achromatic doublet ( $f = 120$  mm) for fs excitation and convex lens ( $f = 60$  mm) for ns excitation. The peak intensities used in experiments were in the 200-400 GW/cm<sup>2</sup> and 10-150 MW/cm<sup>2</sup> range for fs and ns pulse excitation respectively. All the studies were performed with solution concentrations of  $5 \times 10^{-4}$  M providing ~75% linear transmission for 532 nm and 85% for 800 nm. We maintained similar intensity levels ensuring identical experimental conditions for both the samples.

### 7.3.3 Three photon absorption with 800 nm, 100 fs pulses:

The open aperture scans for pc1 and pc2 recorded at 800 nm using ~100 fs pulses with an input irradiance of ~387 GW/cm<sup>2</sup> is shown in figure 7.6 and figure 7.7, respectively. We observed strong reverse saturable absorption (RSA) kind of behavior in the intensity range of 200–400 GW/cm<sup>2</sup> beyond which the sample was damaged (seen through the discoloring of solutions). Open aperture Z-scan with nanosecond laser pulses usually has dominant contribution to the observed RSA behavior from excited state absorption. We cannot expect the same for femtosecond laser pulse excitation since the excited state lifetimes and intersystem crossing rates are much slower. Moreover, owing to large peak intensities at the focal point we can expect either 2PA or 3PA as the possible nonlinear absorption mechanism. Further, due to presence of large number of absorption bands in the excited state there is a possibility of resonance enhancement for these processes. In order to distinguish the multi-photon process contributing to the present data we performed intensity dependent absorption studies in the open aperture configuration.

Obtained experimental data was fitted using equations 7.1 and 7.2 and we found the best fit was obtained with the transmission equation for three-photon absorption (3PA). The dashed line in the figures 7.7 represents the theoretical fit with equation 7.1 and the solid line with equation 7.2. It is evident that 3PA is the dominant mechanism for the observed RSA kind of behavior.

To verify the presence of 3PA in the OA data we carried out the least square fitting test and obtained a value of  $\chi^2 \sim 0.0002$  for pc1 and pc2. We obtained values of  $\alpha_2$  and  $\alpha_3$  for both the phthalocyanines with the theoretical fits with equation 7.1 and equation 7.2 for four different intensities in the range of 200–400 GW/cm<sup>2</sup>.



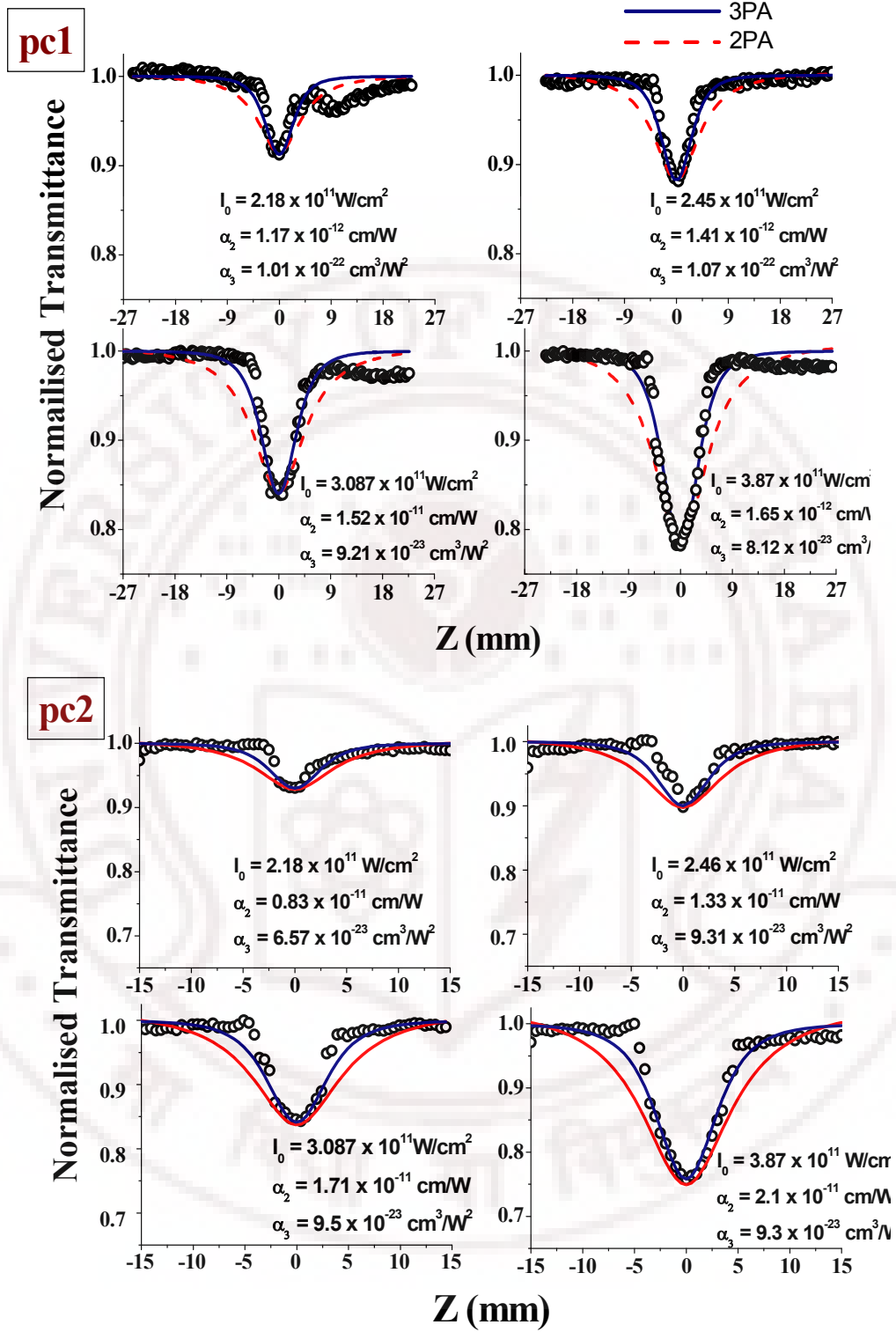


**Fig.7.7:** Open aperture Z-scan curves for pc1 and pc2 obtained with 800 nm, 100 fs pulses. Open circles represents experimental data while the solid line represents theoretical fit with three-photon absorption. Dashed line represents the fit obtained with two-photon absorption.

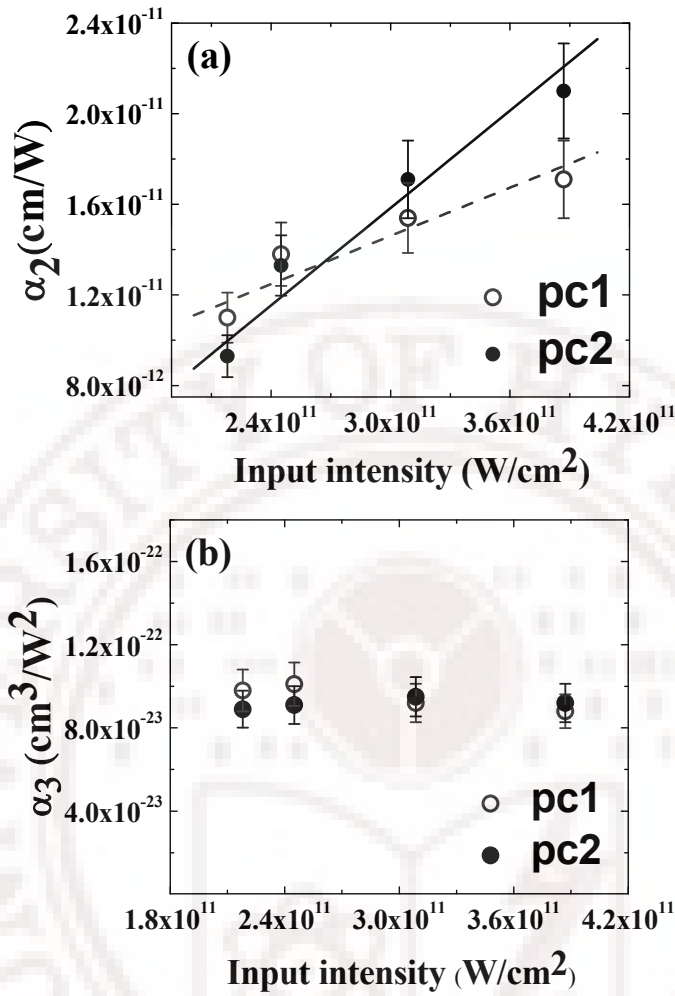


**Fig.7.8:** Plots showing the comparison of intensity dependence of (a)  $\alpha_2$  and (b)  $\alpha_3$  for pc1 (open circles) and pc2 (solid circles) obtained with 800 nm pulses

The intensity dependent behavior of  $\alpha_2$  ( $\alpha_3$ ) is depicted in figure 7.8(a) for both the samples pc1 (open circles) and pc2 (solid circles). The error bars in the figure are indicative of maximum experimental error, which was  $\sim 20\%$  in our case. We observed that for both phthalocyanines  $\alpha_2$  increases linearly with intensity (lines are linear fits). However, as is evident in figure 7.8(b), we find that  $\alpha_3$  remained constant with increasing intensities with average magnitudes to be  $\sim 0.000091 \text{ cm}^3/\text{GW}^2$  and  $\sim 0.000095 \text{ cm}^3/\text{GW}^2$  for pc1 and pc2 respectively. This clearly indicates that the nonlinear absorption process involved is certainly 3PA. Interestingly, within these range of intensities, the samples remained stable

after long exposure to the laser irradiation. However, beyond the intensities of 400 GW/cm<sup>2</sup> we noted that the sample started degrading.

We have evaluated the three-photon absorption cross-section ( $\sigma_3$ ) using the following relation:

$$\sigma_3 = \frac{(\hbar\omega)^2}{N} \alpha_3 \quad (7.3)$$

where  $\omega$  is the frequency of the laser radiation. The values for pc1 and pc2 were  $\sim 1.85 \times 10^{-80}$  cm<sup>6</sup>s<sup>2</sup>/photon<sup>2</sup> and  $\sim 1.93 \times 10^{-80}$  cm<sup>6</sup>s<sup>2</sup>/photon<sup>2</sup> respectively.

For evaluating the strength of nonlinear coefficients obtained with our samples we compare them with those reported in literature, which are presented in table 7.1. We note that our values are one order higher than those reported in organic molecules with fs excitation [10, 11]. However, the values reported by He et al. [12] are three orders of magnitude higher than ours which is quite sensible since the nonlinear properties will, expectedly, be enhanced due to quantum confinement effects.

**Table 7.1:** Comparison of three-photon absorption coefficient ( $\alpha_3$ ) with other reported values in literature

Sample	Wavelength, pulse-width	$\alpha_3$ (cm <sup>3</sup> /GW <sup>2</sup> ) $\times 10^{-5}$	Reference
4,4'-bis(diphenylamino) stilbene (BDPAS) dendrimers	1100 nm, 150 fs	0.51	[10]
Multi-branched chromophore	1300 nm, 160 fs	0.385	[11]
ZnS NC's	800 nm, 120 fs	2400	[12]
<b><i>Tetra tert-butyl phthalocyanine (Free base and Zn)</i></b>	<b><i>800 nm ~100 fs</i></b>	<b><i>9.1 (pc1) 9.5 (pc2)</i></b>	<b><i>This work</i></b>

### 7.3.3 Two photon absorption with 532 nm, 6 ns pulses

The open aperture Z-scans for both pc1 and pc2 illustrated a distinct reverse saturable absorption (RSA) behavior with 532 nm, 6 ns laser pulse excitation. The molecules remained stable for input intensities in the range of 1–500 MW/cm<sup>2</sup>. For intensities above 10<sup>8</sup> W/cm<sup>2</sup> the normalized transmission dropped below 0.3 representing strong nonlinear absorption behavior. It is well established that nonlinear absorption in such materials due to ns pulses has contributions from both excited singlet and/or triplet states apart from two-photon absorption depending on the excitation wavelength. However, for 532 nm excitation we can approximate the nonlinear absorption to an effective process and evaluate the nonlinear coefficient. The role of instantaneous two-photon absorption in the present case is negligible due to the excitation wavelength of 532 nm, which is far from two-photon resonance. The effective coefficient incorporates the contribution of both singlet and triplet excited state absorption. Since the lifetimes of first excited singlet state are few nanoseconds for both the phthalocyanines the intersystem crossing rate will effectively determine the involvement of either higher singlet excited states or higher triplet excited states in the nonlinear absorption mechanism. A comprehensive five-level modeling [6] along with the accurate knowledge of the intersystem crossing times is necessary to pin-point the exact contribution of each of these processes.

Figure 7.9 shows the representative plots of open aperture Z-scans obtained at three different intensities. The data obtained with ns pulses was fitted using equation 2. The best fit produced an effective nonlinear absorption coefficient ( $\alpha_2$ ) of **310 cm/GW** for pc1 and **420 cm/GW** for pc2 measured with a peak intensity of ~6 MW/cm<sup>2</sup>. For higher intensities we expect contribution from higher-order nonlinearities disabling us to judge the exact magnitude of third-order nonlinear coefficient. These values correspond to one of the largest reported till date for any other phthalocyanines. Significantly both pc1 and pc2 possess negligible linear absorption at this wavelength. The values extracted from the fits to the Z-scan data have a maximum error of  $\pm 15\%$  owing to the

calibration errors of the neutral density filters, errors in the estimation of spot size at focus, and fitting errors.

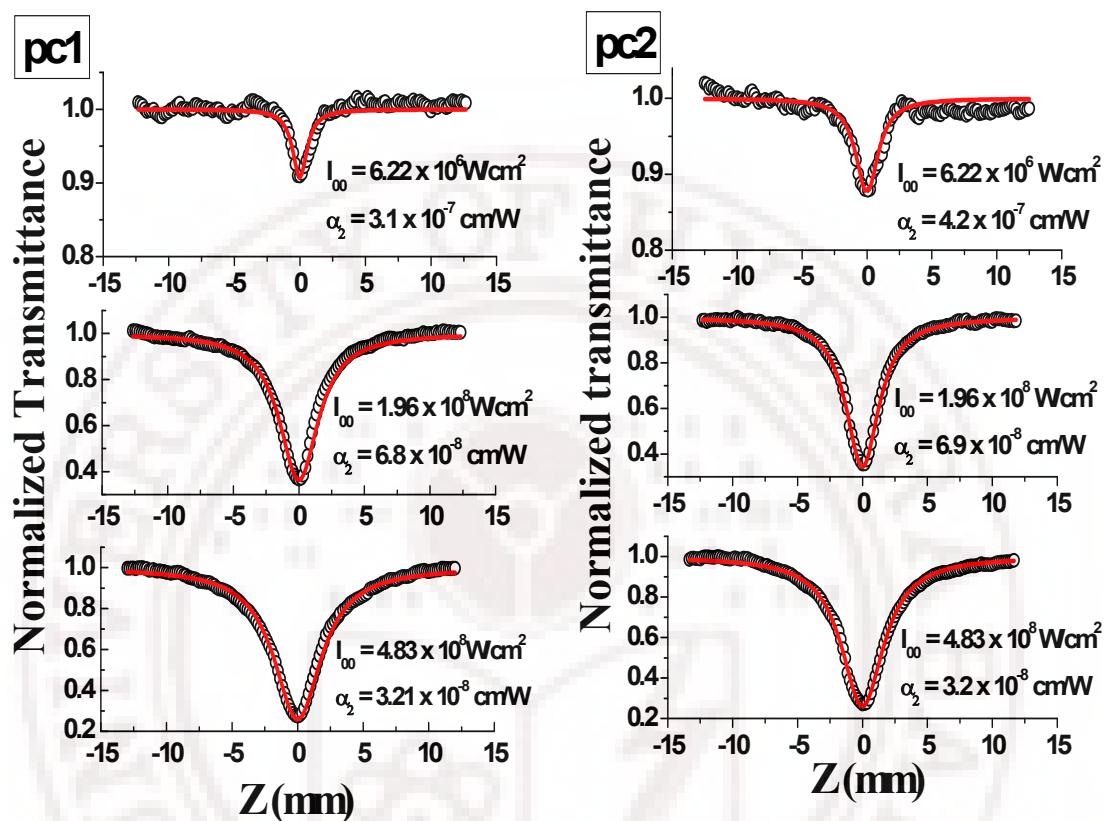


**Fig.7.9:** Open aperture z-scan plots of pc1 and pc2 at various input intensities upon excitation with 532nm, 6 ns laser pulses. The solid line represents the fitting of equation 7.1 for evaluating the nonlinear absorption coefficient.

The metallic phthalocyanine has superior nonlinear absorption coefficient compared to free-base pc1 since the spin-orbit coupling could be significantly more efficient with the metal complex species. Table 7.2 summarizes the recent results reported in literature on the nonlinear absorption properties of different phthalocyanines. Though there are ample results in literature on nonlinear absorption of phthalocyanines obtained with ns pulses, we have chosen these particular values since they were achieved at 532 nm utilizing analysis similar to the one presented here. The peak intensities also were of similar order of magnitude or higher to those used in our case. There is a clear indication that our samples possess superior nonlinear coefficients and these combined with small

linear absorption in the visible range enhances their potential for optical limiting device applications.

The two-photon absorption cross-section ( $\sigma_{TPA}$ ) was calculated from the Eq. (7.4) given below:

$$\sigma_{TPA} = \frac{h\nu}{N} \beta \quad (7.4)$$

$$N = N_A D$$

where N is the number of molecules per unit volume, D is the molar concentration,  $N_A$  is the Avogadro constant, h is the Planck's constant,  $\nu$  is the frequency of laser beam used. The two-photon absorption cross-sections ( $\sigma_{TPA}$ ) were estimated to be  $3.84 \times 10^{-46}$  and  $5.21 \times 10^{-46} \text{ cm}^4 \text{ s photon}^{-1}$  for pc1 and pc2 respectively, which is reasonably high value for organic molecules.

**Table 7.2:** Comparison of two-photon absorption coefficient ( $\alpha_2$ ) with values reported

Sample	Wavelength	$\alpha_2$ (cm/GW)	Intensity (GW/cm <sup>2</sup> )	Reference
Zn Phthalocyanine	532 nm	47.74	-	[30]
Sm(Pc) <sub>2</sub> Eu(Pc) <sub>2</sub>	596 nm 604 nm	31 50	0.143 0.0835	[31]
Alkynyl phthalocyanines	532 nm	12 – 56	0.2 – 2.0	[32]
Nd(Pc) <sub>2</sub>	532 nm	42	0.09	[33]
GaPc dimers	532 nm	32 - 35	0.5	[34]
Octaalkylphthalocyanines and their 15 metallated derivatives	532 nm	15 - 96	0.5	[35]
<b><i>Tetra tert-butyl phthalocyanine (Free base and Zn)</i></b>	<b><i>532 nm</i></b>	<b><i>~310 (pc1) ~420 (pc2)</i></b>	<b><i>0.006</i></b>	<b><i>This work</i></b>

### 7.4 Nonlinear refraction properties with closed aperture Z- scans:

Figures 7.10 (a) and (b) illustrate the typical closed aperture Z-scan curve obtained for pc1 and pc2 with a peak intensity of  $\sim 220 \text{ GW/cm}^2$ . These curves represent normalized data obtained after division of closed aperture data with the open aperture data to eliminate the contribution of nonlinear absorption. The curves were obtained at low peak intensities to avoid contributions to the nonlinearity that are not electronic in origin. It is apparent that both pc1 and pc2 show negative nonlinearity as indicated by the peak-valley structure.

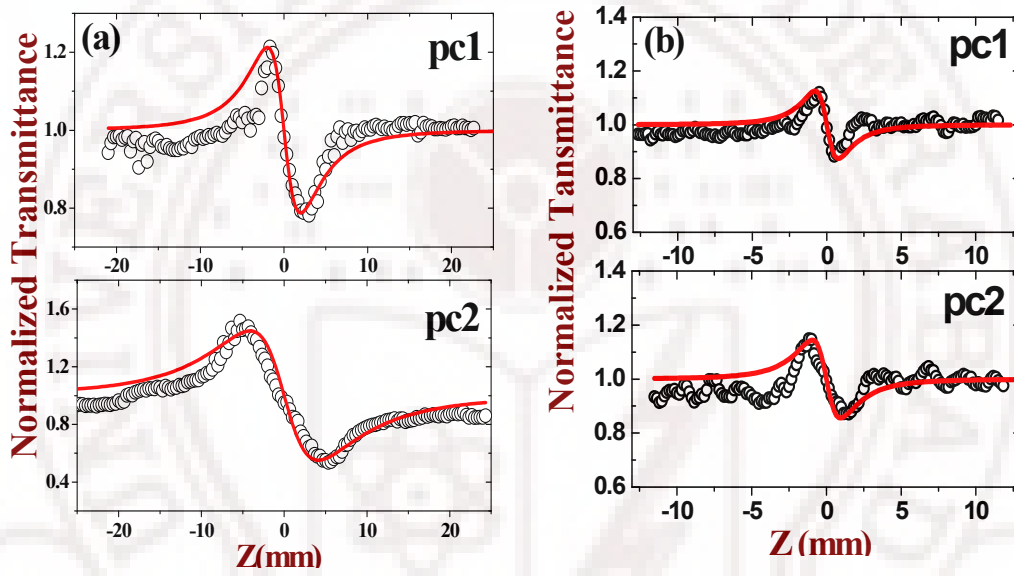


**Fig. 7.10:** Closed aperture Z-scans for (a) fs pulse excitation (b) ns pulse excitation. Solid lines are the theoretical fits

The closed aperture data,  $T_{CA}$ , were fitted to the equation 3. [23].

$$T_{CA} = 1 - \frac{4\Delta\phi_0(z/z_0)}{[1 + (z/z_0)^2][9 + (z/z_0)^2]} \quad (7.5)$$

where  $\Delta\phi_0$  is the phase change. We have evaluated the nonlinear refractive index using:

$$n_2 (\text{cm}^2 \text{W}^{-1}) = \frac{|\Delta\phi_0|\lambda}{2\pi I_{00} L_{eff}} \quad (7.6)$$

The observed phase change ( $\Delta\phi_0$ ) was less than  $\pi$  ( $\Delta\phi_0 = 1.05$  and  $2.65$  for pc1 and pc2 respectively).



The magnitude of the nonlinear refractive index  $n_2$  evaluated was  $\sim 0.56 \times 10^{-15} \text{ cm}^2/\text{W}$  for pc1 and  $\sim 1.14 \times 10^{-15} \text{ cm}^2/\text{W}$  for pc2. With ns excitation the magnitude of nonlinear refractive index  $n_2$  evaluated was  $\sim 1.13 \times 10^{-11} \text{ cm}^2/\text{W}$  for pc1 and  $\sim 0.86 \times 10^{-11} \text{ cm}^2/\text{W}$  for pc2. The trend reversed in the nanosecond domain and the reason for this is being investigated at present. Our immediate analysis on this discrepancy showed that the scattering of the data in the closed aperture Z-scans of pc2 with ns laser pulse excitation was very high, possibly owing to the laser energy fluctuation, leading to larger error in the evaluation of the coefficients.

The nonlinear refractive index  $n_2$  is expressed in terms of the ordinary linear index  $n_0$  and the real part of third-order nonlinear susceptibility  $\chi^{(3)}$  and the imaginary part  $\chi^{(3)}$  in terms of the TPA coefficient ( $\alpha_2$ ) of in Gaussian unit's using the relation<sup>48,49</sup>

$$\text{Re} [\chi^{(3)}] (\text{esu}) = 10^{-4} \frac{\epsilon_0 n_0^2 c^2}{\pi} n_2 (\text{cm}^2/\text{W}) \quad (7.7)$$

$$\text{Im} [\chi^{(3)}] (\text{esu}) = 10^{-2} \frac{\epsilon_0 n_0^2 c^2 \lambda}{4\pi^2} \alpha_2 (\text{cm/W}) \quad (7.8)$$

The real and imaginary parts of third order nonlinearity for pc1 and pc2 were also evaluated.  $\text{Re} [\chi^{(3)}]$  was estimated to be  $\sim 5.93 \times 10^{-10} \text{ esu}$  and  $\sim 4.59 \times 10^{-10} \text{ esu}$  and  $\text{Im} [\chi^{(3)}]$  to be  $\sim 0.97 \times 10^{-10} \text{ esu}$  and  $\sim 0.71 \times 10^{-10} \text{ esu}$  for pc1 and pc2 respectively with ns pulse excitation. The  $\chi^{(3)}$  values measured for pc1 and pc2 in the ns regime were  $6.02 \times 10^{-10} \text{ esu}$  and  $4.64 \times 10^{-10} \text{ esu}$ , respectively.

## 7.5 Optical limiting properties with ns pulses:

An ideal optical limiter, by definition, is a device that exhibits a linear transmittance below a threshold, and clamps the output to a constant above it, thus providing safety to sensors and eye as illustrated in figure 7.11. The limiting

threshold ( $I_{1/2}$ ) of the material is defined as the input intensity/fluence at which the transmittance reduces to half of the linear transmittance.

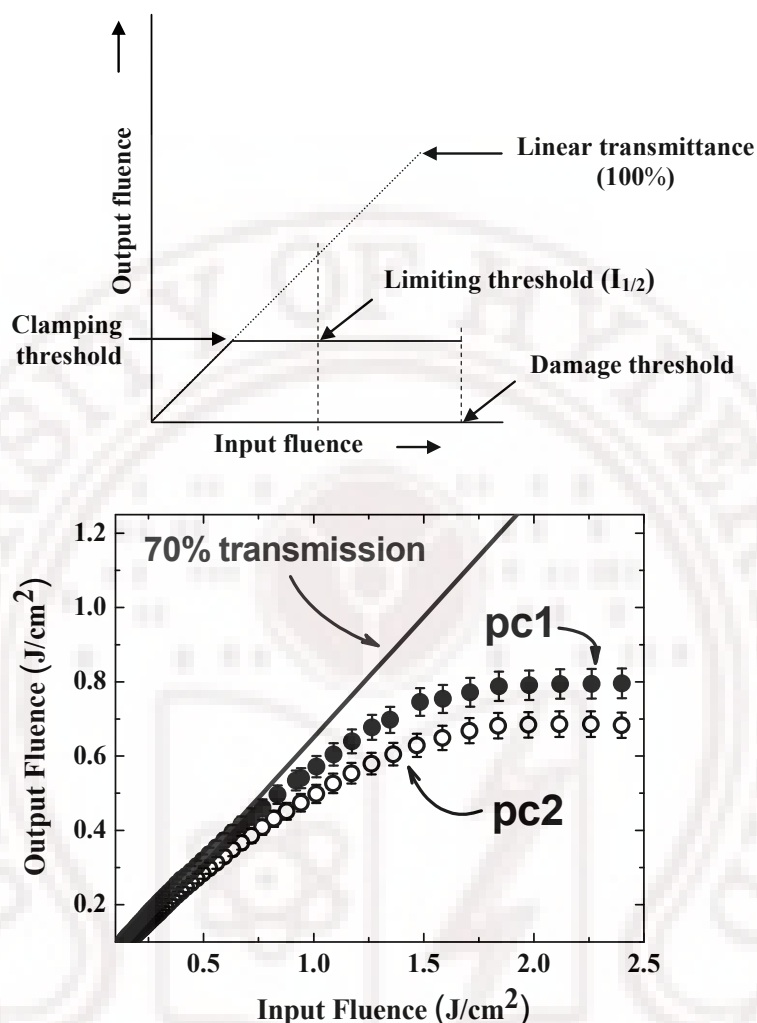


**Fig. 7.11:** Plots showing the optical limiting curves obtained for pc1 and pc2 for ns pumping

The optical limiting data obtained for pc1 and pc2 at 532 nm using 6 ns pulses are shown in figure 7.11 with both the samples exhibiting limiting thresholds ( $I_{1/2}$ ) of  $\sim 0.45 \text{ J}/\text{cm}^2$ . The mechanism for optical limiting could be predominantly excited state absorption since with ns pumping though there is possibility of contribution from two photon absorption (two-step) also. Our studies suggest that the effect of the metal ion on the nonlinear optical properties is not significant for alkyl phthalocyanines. The advantages of these molecules stem from the fact that they have insignificant linear absorption especially in the

450-600 nm spectral range indicating prospective applications in broadband optical limiting.

## 7.6 Investigation of ultrafast nonlinear optical properties by degenerate four-wave mixing studies:

### 7.6.1. Experimental details

The DFWM set up was configured in the standard box-car geometry described in chapter 2 [36, 37]. The fundamental beam was divided into three nearly equal intensity beams (intensity ratio of 1:1.2:0.8) such that they form three corners of a square and are focused into the nonlinear medium (sample) both spatially and temporally. The resultant DFWM signal was detected at the fourth corner of the box which was generated due to the phase-matched interaction  $\mathbf{k}_4 = \mathbf{k}_3 - \mathbf{k}_2 + \mathbf{k}_1$ . All the experiments were performed with samples dissolved in chloroform and placed in 1-mm glass/quartz cuvettes. Sufficient care was observed to reduce the contribution of cuvette signal towards the overall DFWM signal by choosing appropriate focal conditions. The measurement of  $\chi^{(3)}$  values was performed at zero time delay of all the beams. We estimated the magnitude of  $\chi_{1111}^{(3)}$  by maintaining the same polarization for all the three incident beams. A half-wave plate was introduced in the path of beam 2 to control the polarization required for the estimation of  $\chi_{1212}^{(3)}$ .

The transient DFWM profiles were obtained by delaying beam 3 with respect to the other two beams. Through nonlinear transmission measurements the input powers for three mixing pulses were chosen such that the effect of nonlinear absorption was minimal. We believe that the measured  $\chi^{(3)}$  at these intensities is, therefore, purely real in nature without any contribution from the imaginary component arising from multi-photon absorption. Moreover, the choice of low input intensities allowed us to neglect the association of higher order nonlinearities. The intensity measured at the sample due to the three input beams was  $\sim 2.7 \times 10^{10}$  W/cm<sup>2</sup>. Since all the samples had negligible linear

absorption at the working wavelength of 800 nm we expect the measured  $\chi^{(3)}$  and  $\gamma$  values to be off-resonant. All the studies were performed with solutions possessing concentrations of  $\sim 1 \times 10^{-4}$  M/L.

### 7.6.2 Third order nonlinear optical properties by DFWM measurements

The third order NLO susceptibility  $\chi^{(3)}$  was estimated by comparing the measured DFWM signal of the sample with that of neat  $\text{CCl}_4$  as reference [ $\chi^{(3)} = 4.4 \times 10^{-14}$  esu] measured with the same experimental conditions. The relationship used for  $\chi_{sample}^{(3)}$  is [36]:

$$\chi_{sample}^{(3)} = \left( \frac{n_{sample}}{n_{ref}} \right)^2 \left( \frac{I_{sample}}{I_{ref}} \right)^{1/2} \left( \frac{L_{ref}}{L_{sample}} \right) \alpha L_{sample} \left( \frac{e^{\frac{\alpha L_{sample}}{2}}}{1 - e^{-\alpha L_{sample}}} \right) \chi_{ref}^{(3)} \quad (7.9a)$$

where **I** is the DFWM signal intensity,  **$\alpha$**  is the linear absorption coefficient, **L** is sample path length, and **n** is the refractive index. We estimated  $\chi^{(3)}$  values to be  $(4.26 \pm 0.43) \times 10^{-14}$  esu and  $(4.31 \pm 0.43) \times 10^{-14}$  esu for pc1 and pc2 respectively for an input intensity of  $\sim 2.7 \times 10^{10}$  W/cm<sup>2</sup>. One of the main sources of error that arises in experiments is through the intensity fluctuations of laser pulses. This problem is overcome by taking the averaged data of 1000 pulses. The second major source of error could be from the determination of solutions concentration. Considering all the unforced random experimental errors we estimate an overall error of  $\sim 10\%$  in our calculations by repeating the experiment few times. In an isotropic medium  $\chi^{(3)}$  has three independent components, namely,  $\chi_{1111}^{(3)}$ ,  $\chi_{1212}^{(3)}$  and  $\chi_{1122}^{(3)}$ . In the case of non-resonant electronic nonlinearity,  $\chi_{1111}^{(3)} = 3\chi_{1212}^{(3)} = 3\chi_{1122}^{(3)}$  when the three input beams are all vertically polarized and the corresponding  $\chi^{(3)}$  obtained would be  $\chi_{1111}^{(3)}$ . To determine  $\chi_{1212}^{(3)}$ , the probe beam has to be orthogonally polarized with respect to the two pump beams. We measured the values for  $\chi_{1212}^{(3)}$  to be  $(1.47 \pm 0.15) \times 10^{-14}$  esu and  $(1.49 \pm 0.15) \times 10^{-14}$  esu for pc1 and pc2, respectively, and the obtained ratio of

$\chi_{1111}^{(3)}$  to  $\chi_{1212}^{(3)}$  was  $\sim 2.9$  suggesting that there was no significant contribution arising from the coherent coupling effects [19]. We estimated the  $\chi^{(3)}$  value of phthalocyanines in a solid film by assuming a density of  $\sim 1 \text{ g/cm}^3$  using the following relationship [38]

$$\chi_{\text{thin film}}^3 = \frac{N}{N_{\text{solution}}} \chi_{\text{solution}}^3 \quad (7.9b)$$

where  $N$  is the assumed density of the phthalocyanines solid and  $\chi_{\text{solution}}^3$  are the value estimated from Eq.1. The estimated values for the solid films of pc1 and pc2 were  $(5.74 \pm 0.57) \times 10^{-10} \text{ esu}$  and  $(5.37 \pm 0.54) \times 10^{-10} \text{ esu}$ , respectively which are among the largest reported values for these types of molecules. The measured  $\chi^{(3)}$  value of chloroform was insignificant compared to the  $\chi^{(3)}$  value of the samples under similar experimental conditions and thus the contribution from pure solvent was neglected.

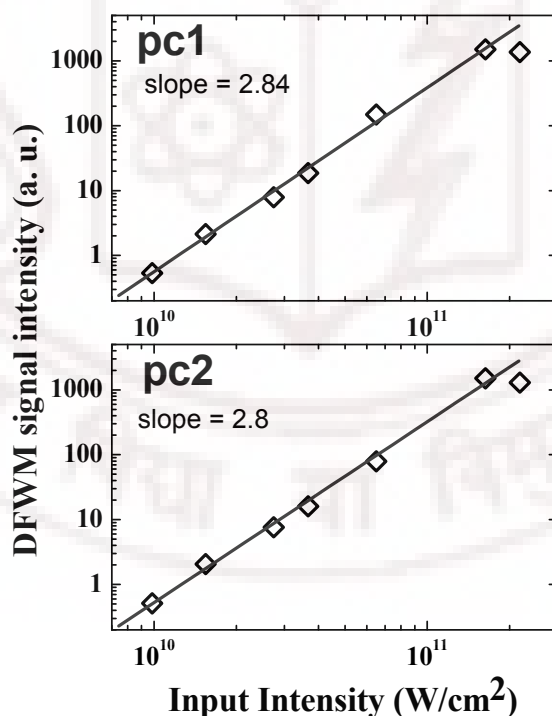


**Fig 7.12:** Plots showing the cubic dependence of DFWM signal for pc1 and pc2 as a function of input intensity

The intensity dependence of the DFWM signal amplitude in both the samples is presented in figure 7.12. At relatively low input intensities ( $<220 \text{ GW/cm}^2$ ) the DFWM signal amplitude followed a dependence that is essentially cubic (with a slope of  $\sim 2.85$ ) clearly indicating that the nonlinearity behaves in a Kerr-like fashion and that origin of DFWM does not have contribution from any multi-photon absorption process in which case the slope of the curve would have been different from 3 [39, 40]. To determine whether our molecules possessed two-photon absorption coefficient  $\beta$ , which corresponds to the imaginary part of  $\chi^{(3)}$ , we performed the nonlinear transmission measurements. For both the molecules we obtained straight lines that intercept the ordinate axis and their values were less than unity, suggesting a one-photon contribution to the absorption. This supports our argument that third-order optical susceptibility of our molecules can be attributed to the nonlinear refractive index at 800 nm. Figure 7.13 shows the linearity in the transmission versus the input intensity for the range of intensities from  $7 \times 10^9$  to  $2.5 \times 10^{11} \text{ W/cm}^2$ . The DFWM signal was measured at an input intensity of  $I_{\text{in}} = 2.7 \times 10^{10} \text{ W/cm}^2$  that was much lower than required for nonlinear absorption which was  $\sim 2.15 \times 10^{11} \text{ W/cm}^2$ .

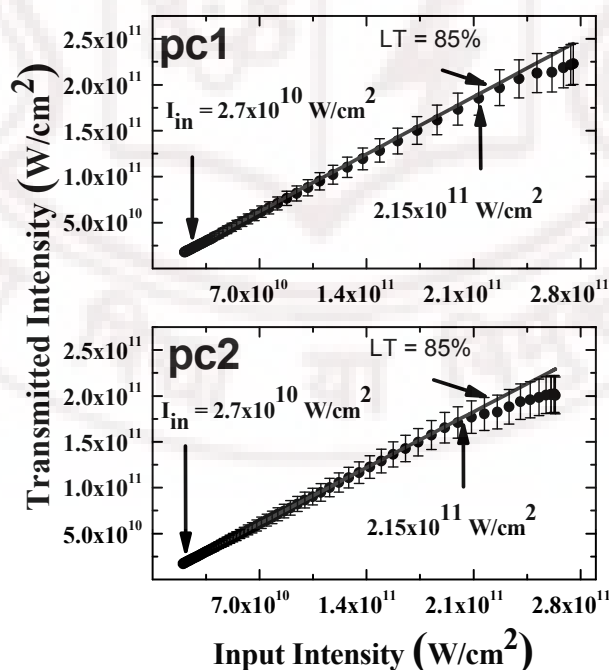


**Fig.7.13:** Plot of output transmittance versus input power, LT represents the linear transmittance at 800 nm.

To estimate the second order hyperpolarizability,  $\gamma$ , at the molecular level we used the following relation [36]:

$$\gamma_{sample} = \chi^{(3)} / T^4 N_0, \quad (7.10)$$

where  $N_0$  is the number density of the molecules per milliliter, and  $T = (n_{sample}^2 + 2)/3$  is the local field factor. We assume that the solvent makes negligible contribution to the signal. We estimated the  $\gamma$  values to be  $(4.27 \pm 0.43) \times 10^{-31}$  esu and  $(4.32 \pm 0.43) \times 10^{-31}$  esu for pc1 and pc2 respectively which are reasonably large in the fs regime compared to some of the phthalocyanines and their analogues reported recently [19-26]. The metallic phthalocyanine had marginally higher nonlinearity and the reason could be attributed to the presence of the metal ion.

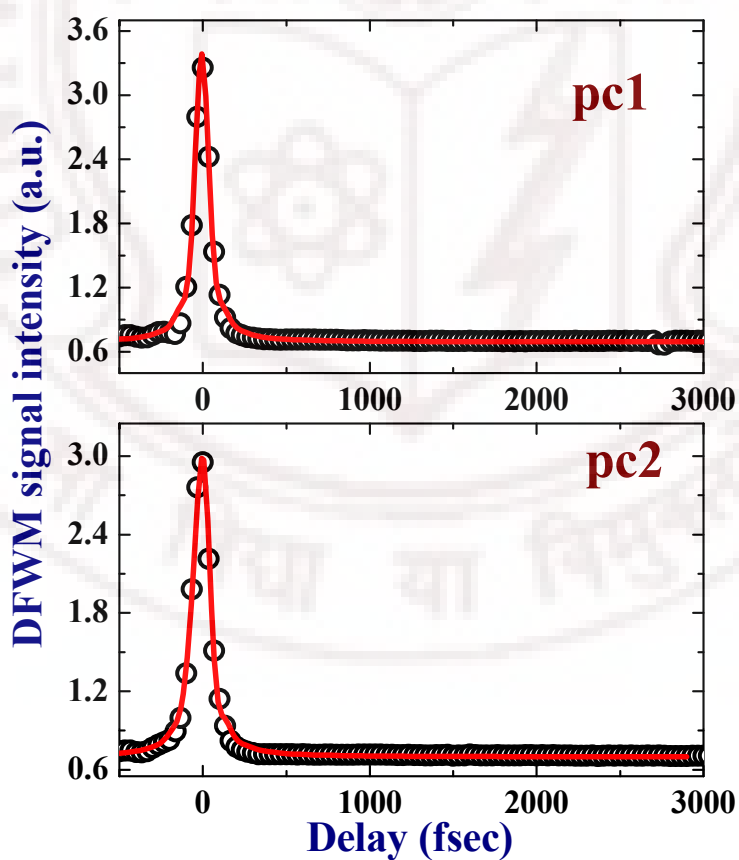


Fig. 7.14: Temporal profiles of DFWM signals of pc1 and pc2



Figure 7.14 shows the temporal response of the DFWM signal recorded as a function of the probe delay. The signal was fitted with a Gaussian function (solid curve) as given by,

$$F(t) = \sqrt{\frac{2}{\pi}} \left( \frac{A}{\omega} \right) \exp \left[ -2 \left( \frac{x - x_c}{\omega} \right)^2 \right] \quad (7.11)$$

where  $A$  is a weight parameter,  $x$  is a variable that corresponds to the delay and  $\omega$  is the obtained FWHM of the fit. The full width half maximum (FWHM) of the fit was similar to the response signal obtained from pure  $\text{CCl}_4$ . The signal profiles were nearly symmetric about the maximum (i.e. zero time delay) illustrating that the response times of the nonlinearities were much shorter than the pulse duration (100 fs). Such an instantaneous response is indicative of the Kerr effect (electronic component) from the distortion of the large  $\pi$ -conjugated electron charge distribution of phthalocyanine molecules. This instant response enhances their potential for photonics switching applications. Interestingly, the trapping levels originating from the multi-conformational and polaronic states situated in the HOMO-LUMO gap also play an important role in the DFWM for measurements in solutions [41].

### 7.6.3 Figures of merit (FOM) for photonic switching applications

A convenient way to quantify the losses is to consider the appropriate merit factors formulated by Stegeman for photonic switching applications [21-24]. These figure of merit (FOM) factors are related to the maximum nonlinear phase shift  $\Delta\phi$  through

$$\Delta\phi = \frac{2\pi}{\lambda} \int_0^L n_2 I(z) dz \quad (7.12)$$

obtained in a given material within a propagation distance  $L$  corresponding to an absorption length.  $\Delta\phi$  change of  $\sim 2\pi$  is essential for switching applications. For one-photon absorption as the dominant loss mechanism, the absorption depth can

be defined as  $\alpha_1^{-1}$ , where  $\alpha_1$  is the absorption coefficient. We have the merit factor  $W$  defined as

$$W = \frac{n_2 I_{sat}}{\alpha_1 \lambda}$$

where  $\lambda$  is the wavelength and  $I_{sat}$  is the light intensity at which the nonlinear refractive-index change saturates. The nonlinear phase shift obtainable on the distance of  $\alpha_1^{-1}$  is equal to  $1.26 W \pi$  rad. Therefore the pre-requisite for superior FOM is:

$$W > 1 \quad (7.13)$$

when the nonlinear losses prevail with materials with strong multi-photon absorption, the nonlinear phase shift will be limited, too. The absorption depth can then be defined as  $(\alpha_2 I_o)^{-1}$  and  $(\alpha_3 I_o^2)^{-1}$  where  $\alpha_2$  and  $\alpha_3$  are the two-photon absorption and three-photon coefficient and  $I_o$  stands for the incident light. As the absorption depth is intensity dependant, it follows that the obtainable phase shift is now intensity independent. The corresponding FOMs can be presented as:

$$T^{-1} = \frac{n_2}{\lambda \alpha_2} \quad (7.14)$$

$$V^{-1} = \frac{3n_2}{\lambda \alpha_3 I_o} \quad (7.15)$$

For a successful operation of a photonics device made of such lossy materials to acquire nominal  $2\pi$  phase shift the following inequalities must be satisfied

$$T < 1, \text{ and } V < 0.68 \quad (7.16)$$

To estimate the values of  $n_2$  we used the data obtained from the calculation of  $\chi^{(3)}$ . We estimated  $n_2$ , which is related to the real part of  $\chi^{(3)}$ , using the relation [34]:

$$n_2(\text{cm}^2/\text{W}) = \frac{0.0395}{n_0^2} \chi^{(3)}(\text{esu}) \quad (7.17)$$

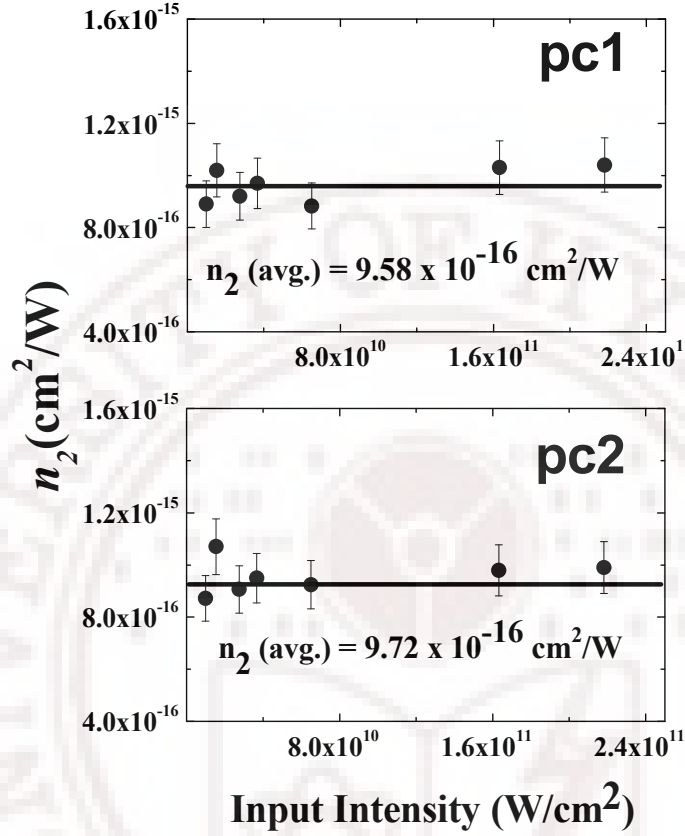


Figure 7.15: Plot of  $n_2$  as a function of input intensity

By performing intensity dependent measurements of  $\chi^{(3)}$  we evaluated the corresponding  $n_2$  and observed that  $n_2$  was independent of the input intensity (see figure 7.15) highlighting the existence of pure nonlinearity. We achieved an average  $n_2$  value of  $9.58 \times 10^{-16} \text{ cm}^2/\text{W}$  and  $9.72 \times 10^{-16} \text{ cm}^2/\text{W}$  for pc1 and pc2, respectively. For an intensity of  $\sim 190 \text{ GW}/\text{cm}^2$ , where nonlinear absorption is negligible, and  $\alpha_1$  for pc1 and pc2 were  $0.06 \text{ cm}^{-1}$  and  $0.09 \text{ cm}^{-1}$ , respectively, we estimated  $W$  to be  $\sim 37.9$  and  $\sim 25.6$  for pc1 and pc2 respectively. Though the nonlinearities are higher in pc2 in contrast to pc1 higher linear absorption resulted in lower figure of merit. These are superior to the required values for photonic switching device with one-photon contribution.

For input intensities  $>215 \text{ GW/cm}^2$  we expect substantial contribution from multi-photon absorption. Our earlier studies demonstrated and confirmed these phthalocyanines possessed strong three-photon absorption coefficient (3PA) with fs pulse excitation near 800 nm. The measured 3PA coefficients ( $\alpha_3$ ) were independent of input intensity and the magnitudes were  $\sim 0.000091 \text{ cm}^3/\text{GW}^2$  and  $\sim 0.000095 \text{ cm}^3/\text{GW}^2$  for pc1 and pc2 respectively. The V parameter calculated from equation 8 and for an input intensity of  $230 \text{ GW/cm}^2$  was **0.57** and **0.59** for pc1 and pc2, respectively. The combination of instantaneous nonlinear response and excellent figures of merit propels pc1 and pc2 as ideal for photonic switching applications. We summarize the evaluated values of nonlinear coefficients and FOM in table 7.3.

**Table-7.3** Summary of the nonlinear optical parameters of pc1 and pc2 studied using DFWM technique with 800 nm excitation and the corresponding one-photon and three-photon figures of merit for photonic switching applications.

Sample	$\chi^{(3)} \text{ esu}^a$	$\gamma \text{ esu}^a$	$n_2 (\text{cm}^2/\text{W})$	$W^b$	$V^c$
pc1	$(4.26 \pm 0.42) \times 10^{-14}$	$(4.27 \pm 0.42) \times 10^{-31}$	$(9.58 \pm 0.95) \times 10^{-16}$	37.8	<b>0.57</b>
pc2	$(4.31 \pm 0.43) \times 10^{-14}$	$(4.32 \pm 0.43) \times 10^{-31}$	$(9.72 \pm 0.97) \times 10^{-16}$	25.6	<b>0.59</b>
<sup>a</sup> $I = 27 \text{ GW/cm}^2$ ; <sup>b</sup> $I = 190 \text{ GW/cm}^2$ ; <sup>c</sup> $I = 230 \text{ GW/cm}^2$					

To put in perspective the merits of our molecules we have tried to compare the coefficients and FOM obtained for our phthalocyanines with some of the other molecules reported recently. Tran *et al.* [19] reported resonantly enhanced nonlinearities of their squaraine dyes near 700 nm with  $\gamma$  values of the order of  $10^{-32} \text{ esu}$ . Fu *et al.* [20] reported large nonlinearities in naphthalocyanine derivatives near 800 nm with value in the range of  $2 \times 10^{-29} \text{ esu}$  to  $7 \times 10^{-29} \text{ esu}$ . However, the large values (two orders of magnitude higher) obtained were again attributed to the resonance enhancement. All the molecules they investigated had strong absorption near 800 nm. Li *et al.* [21] presented their results on centrosymmetric squaraines possessing large nonlinearities studied using fs

DFWM. They achieved  $\gamma$  values of  $\sim 10^{-31}$  esu with fast response times ( $< 100$  fs). Their group [22] also reported similar studies on novel diarylethene–phthalocyanine dyads with largest  $\gamma$  value for one of the compounds being  $10^{-30}$  esu. Kasatani *et al.* [23] also reported large resonant nonlinearities ( $10^{-28}$  esu) for cyanine dyes near 800 nm. Huang *et al.* [24] measured off-resonant nonlinearities of dihydroxy phosphorus (V) tetrabenzotriazacorroles, which are phthalocyanine analogues, in the range of  $10^{-31}$  esu with sub-50 fs response time. Prabhakar *et al.* presented their results of croconate dyes obtained with 100 fs pulses where off-resonant  $\gamma$  values of  $\sim 10^{-32}$  esu were reported [25]. It is apparent that our molecules possess better or similar values obtained for  $\gamma$  and the response times with exception being that reported in reference [28]. We expect further enhancement in the nonlinearities for our sample in the resonant case. In terms of FOM achieved for our molecules, Gu *et al.* [42] presented their measurements for chalcone derivatives with optimum values for W as 26.6, T as 0.13, and V as 0.64 which are comparable to those obtained for our phthalocyanines.

## 7.7 Conclusions

- From the fs open aperture z-scan data we conclude that these molecules exhibit three-photon absorption (3PA) behavior. The measured 3PA coefficients ( $\alpha_3$ ) were independent of input intensity and the magnitudes were  $\sim 0.000091 \text{ cm}^3/\text{GW}^2$  and  $\sim 0.000095 \text{ cm}^3/\text{GW}^2$  for pc1 and pc2 respectively. This is, to best of our knowledge, first report on the 3PA behavior of phthalocyanines.
- The ns data indicated strong reverse saturable absorption and optical limiting. The nanosecond open aperture Z-scan studies revealed strong effective nonlinear absorption coefficient ( $\alpha_2$ ) of  $\sim 310$  and  $420 \text{ cm/GW}$  for pc1 and pc2 respectively. These phthalocyanines exhibited strong optical limiting properties in solutions with ns excitation with recorded limiting thresholds of  $\sim 0.45 \text{ J/cm}^2$ .

- We observed a large overall nonlinearity using ns pulses while the fs pumping indicated a moderate nonlinearity. The sign of nonlinearities for both fs and ns-regimes were negative in nature.
- We measured large off-resonant second hyperpolarizabilities ( $\gamma$ ) for these molecules with ultrafast NLO response. The measured values of  $\gamma$  were  $(4.27 \pm 0.43) \times 10^{-31}$  esu and  $(4.32 \pm 0.43) \times 10^{-31}$  esu for pc1 and pc2, respectively.
- The merit factors for photonic switching applications were estimated. For one-photon absorption as the dominant loss mechanism we estimated W to be  $\sim 37.9$  and  $\sim 25.6$  for pc1 and pc2, respectively. For three-photon absorption as the dominant loss mechanism we estimated V parameter as  $0.57$  and  $0.59$  for pc1 and pc2, respectively, for an input intensity of  $230 \text{ GW/cm}^2$ .

## 7.8 References:

1. M. Göppert-Meyer, Ann. Phys. 9:273 (1931).
2. G. S. He, L-S. Tan, Q. Zheng, and P. N. Prasad, Chem. Rev. **108**, 1245 (2008) and references there in; N. Venkatram L. Giribabu , S. Venugopal Rao and D. N. Rao, Appl. Phys. B, **91**, 149 (2008); P. P. Kiran, D. R. Reddy, B. G. Maiya, A. K. Dharmadhikari, G. R. Kumar, and D. N. Rao Appl. Opt., **41** , 7631 (2002); G. S. He, G. C. Xu, P. N. Prasad, B.A. Reinhardt; J.C. Bhatt, R. McKellar, and A.G. Dillard, Opt. Lett. **20**, 435 (1995), 20, 435; N. Venkatram, R. S. S. Kumar, and D. N. Rao, J. Appl. Phys. **100**, 074309 (2006), N. Venkatram, R. Sathyavathi, and D. N. Rao, Optics express, **15**, 12258 (2007); Y-P. Sun, and J. E. Riggs, Int. Rev. Phys. Chem. **18**, 43 (1999); L. W. Tutt, and T. F. Boggess, Prog. Quant. Electron. **17**, 299 (1993); E.W. Van Stryland, H. Vanherzeele, M.A. Woodall, M. J. Soileau, A. L. Smirl, S. Guha, and T. F. Boggess, Opt. Engg. **24**, 613 (1985); M. P. Joshi, J. Swiatkiewicz, F. Xu, P. N. Prasad, B. A. Reinhardt, and R. Kannan, Opt. Lett. **23**, 1742 (1998); P.P. Kiran, “Optical Limiting



- and Nonlinear Optical Properties of Photo Responsive Materials*,” Ph.D. thesis, University of Hyderabad (2004); N. Venkatram, “*Study of Nonlinear Absorption Properties of II-VI Semiconductor (CdS, CdSe), Metal (Au) and Zinc (II)-Phthalocyanine Nanoparticles with Nanosecond and Femtosecond Laser Excitation*”, Ph.D. thesis, University of Hyderabad (2008).
3. S. Maruo, O. Nakamura, and S. Kawata, Opt. Lett. **22**, 132 (1997); B.H. Cumpston, S.P. Ananthavel, S. Barlow, D.L. Dyer, J.E. Ehrlich, L.L. Erskine, A.A. Heikal, S. M. Kuebler, I.-Y. S. Lee, D. McCord-Maughon, J. Qin, H. Röckel, M. Rumi, X.-L. Wu, S.R. Marder, and J. W. Perry, Nature **398**, 51(1999); S. Kawata, H.-B. Sun, T. Tanaka, K. Takada, Nature **412**, 697 (2001); W. H. Zhou, S. M. Kuebler, K.L. Braun, T.Y. Yu, J.K. Cammack, C.K. Ober, J.W. Perry, and S.R. Marder, Science **296**, 1106 (2002); K. C. Vishnubhatla, “*Optical spectroscopic characterization of rare-earth activated conventional, non-conventional and nanostructured glasses for integrated optics*”, Chapter-4, Ph.D. thesis, University of Hyderabad (2008).
  4. D. A. Parthenopoulos, P.M. Rentzepis, Science **245**, 843 (1989); J. H. Strickler, and W. W. Webb, Opt. Lett. **16**, 1780 (1991); A.S. Dvornikov, and P.M. Rentzepis, Opt. Commun. **119**, 341 (1995); K.D. Belfield, and K.J. Schafer, Chem. Mater. **14**, 3656 (2002).
  5. D. Dini, M. Barthel, T. Schneider, M. Ottmar, S. Verma, M. Hanack, Solid State Ionics **165**, 289 (2003); S. Vagin, M. Barthel, D. Dini, and M. Hanack, Inorg. Chem. **42(8)**, 2683 (2003); M. Hanack, T. Schneider, M. Barthel, J.S. Shirk, S.R. Flom, and R.G.S. Pong, Coord. Chem. Rev. **219**, 235, 2001; M. Calvete, G.Y. Yang, and M. Hanack, Synth. Met. **141** 231(2004); A. Slodek, D. Wöhrle, J.J. Doyle, W. Blau, Macromol. Symp. **235**, 9 (2006); Y. Chen, M. Hanack, Y. Araki, and O. Ito, Chem. Soc. Rev. **34** 517 (2005); C. W. Spangler, J. Mat. Chem. **9** 2013 (1999); S.M. O’Flaherty, S.V. Hold, M.J. Cook, T. Torres, Y. Chen, M. Hanack, and W.J. Blau, Adv. Mater. **15**, 19 (2003); L. De Boni, L. Gaffo, L. Misoguti, C.R. Mendonca, Chem. Phys. Lett. **419**, 417 (2006).



6. D. N. Rao, S. V. Rao, F.J. Aranda, M. Nakashima and J.A. Akkara, J. Opt. Soc. Am. B **14** 2710 (1997); S. V. Rao, N.K.M.N. Srinivas, L. Giribabu, B.G. Maiya, D. N. Rao, R. Philip, and G. R. Kumar, Opt. Commun. **182**, 255 (2000); S. V. Rao, “*Studies of Excited State Dynamics, Third Order Optical Nonlinearity and Nonlinear Absorption in C60, Porphyrins, and Phthalocyanines Using Incoherent Laser Spectroscopy*,” Ph.D. thesis, University of Hyderabad (2000); S.J. Mathews, S. C. Kumar, L. Giribabu, and S. V. Rao, Optics Commun. **280**, 206 (2007).
7. R. Bonnett, Chem. Soc. Rev. **24**, 19 (1995); N. L. Oleinick, A. R. Antunez, M.E. Clay, B. D. Rihter, and M. E. Kenney, Photochem. and Photobio. **57**, 242 (1993); E. A. Lukyanets, J. Porphy. Phthalo. **3**, 424 (1999); P.N. Prasad, *Introduction to Biophotonics*, Chapter-12, Wiley-Interscience, New Jersey (2003); I. Cohanoschi, L. Echeverri, and F. E. Hernández, Chem. Phys. Lett. **419**, 33 (2006); A. Karotki, M. Khurana, J. R. Lepock and B. C. Wilson, Photochem. and Photobio. **82**, 443 (2006); I.G. Meerovich, V. M. Derkacheva, G.A. Meerovich, N.A. Oborotova, Z.S. Smirnova, A.P. Polozkova, I.Y. Kubasova, E.A. Lukyanets, and A.Y. Baryshnikov, Proc. of SPIE, **6427**, 64270X (2007); E. Giorgetti, G. Toci, M.Vannini, and F. Giammanco, Opt. Commun. **217**, 431 (2003) ;
8. A. Remn, U. P. Wild, A.Rebane, J. Phys. Chem. A **106**, 3045 (2002)
9. S. Polyaov, F. Yoshino, M. Liu, G. Stegeman, Phys. Rev. B **69**, 115421 (2004).
10. M. Drobizhev, , A. Rebane, , Z. Suo, C.W. Spangler, J. Lumin. **111**, 291 (2005).
11. T.C. Lin, G.S. He, Q. Zheng, P.N. Prasad, J. Mater. Chem., **16**, 2490 (2006).
12. J. He, W. Ji, J. Mi, Y. Zheng and J. Y. Ying, Appl. Phys. Lett., **88**, 181114 (2006)
13. I. Cohanoschi, M. Garcia, C. Toro, K.D. Belfield, F.E. Hernández, Chem. Phys. Lett. **430**, 133 (2006).
14. E. Giorgetti, G. Toci, M.Vannini, F. Giammanco, Opt. Commun. **217**, 431 (2003).

15. M. Durmu, T. Nyokong, Photochem. Photobiol. Sci. **6**, 659 (2007).
16. D.M. Friedrich, J. Chem. Phys. **75**, 3258(1981); P. Cronstrand, Y. Luo, P. Norman, and H. Agren, Chem. Phys. Lett. **375**, 233 (2003); F.E. Hernandez, K.D. Belfield, and I. Cohanoschi, Chem. Phys. Lett. **391**, 22 (2004); G. Zhou, X. Wang, D. Wang, Z. Shao, and M. Jiang, Appl. Opt. **41**, 1120 (2000); S. Maiti, J.B. Shear, R.M. Williams, W.R. Zipfel, and W.W. Webb, Science. **275** 530 (1997).
17. G. de la Torre, P. Vazquez, F. Agullo-Lopez, T. Torres, Chem. Rev. **104**, 3723 (2004); F.Z. Henari, J. Opt. A.: Pure Appl. Opt. **3**, 188 (2001).
18. G.I. Stegeman, and W. E. Torruellas, Philos. Trans. R. Soc. London Ser. A **1354**, 745 (1996); G. I. Stegeman, in *Contemporary Nonlinear Optics*, G.P. Agrawal and R. W. Boyd, eds. (Academic, San Diego, Calif., 1992), pp 1-40; J. U. Kang, A. Villeneuve, M. Sheik-Bahae, G.I. Stegeman, K. Al-Hemyari, J.S. Aitchison, and C. N. Ironside, Appt. Phys. Lett. **65**, 147 (1994); A. Villeneuve, C. C. Yang, G.I. Stegeman, C-H. Lin and H-H. Lin, Appl. Phys. Lett. **62**, 2465 (1993).
19. K. Tran, G. W. Scott, D. J. Funk, and D. S. Moore, J. Phys. Chem. **100**, 11863 (1996).
20. G. Fu, T. Yoda, K. Kasatani, H. Okamoto, and S. Takenaka, Jpn. J. Appl. Phys. **44**, 3945 (2005); G. Fu, T. Yoda, K. Kasatani, H. Okamoto, S. Takenaka, Synth. Met. **155**, 68 (2005).
21. Z. Li, S. Xu, L. Huang, X. Huang, L. Niu, Z. Chen, Z. Zhang, F. Zhang, K. Kasatani, Chem. Phys. Lett. **441**, 123 (2007).
22. Z. Li, Z. Chen, S. Xu, L. Niu, Z. Zhang, F. Zhang, K. Kasatani, Chem. Phys. Lett., **447**, 110 (2007).
23. K. Kasatani, Opt. Mater. **21**, 93 (2002).
24. L. Huang, Z. Li, F. Zhang, C. H. Tung, K. Kasatani, Opt. Commun. **281**, 1275 (2008).
25. K. Kasatani, Proc. SPIE, **4918**, 286 (2002).
26. R.R. Tykwinski, U. Gubler, R.E. Martin, F. Diederich, C. Bosshard, P. Günter, J. Phys. Chem. B **102**, 4451 (1998).

27. Ch. Prabhakar,, K. Yesudas, K. Bhanuprakash , V. J. Rao, R. S. S. Kumar and D. N. Rao, J. Phys. Chem. C **112**, 13272 (2008).
28. “*Phthalocyanines Properties and Applications*,” Ed.’s C. C. Leznoff, A. B. P. Lever, 1993, Wiley VCH publishers, New York.
29. M. Sheik-Bahae, A. A. Said, T. H. Wei, D. J. Hagan, and E. W. Van Stryland, IEEE J. Quant. Electron. **26**, 760 (1990).
30. Santhi, V.V. Naboodiri, P. Radhakrishnan, V.P.N. Nampoori, J. Appl. Phys. **100**, 053109(2006)
31. K.P. Unnikrishnan, J. Thomas, V.P.N. Nampoori, C.P.G. Vallabhan, Opt. Commun. **217**, 269 (2003).
32. E.M. Garcia-Frutos, .M. O’Flaherty, E.M. Maya, G. de la Torre, W. Blau, P. Vazquez, T. Torres, J. Mater. Chem. **13**, 749 (2003)
33. K.P. Unnikrishnan, J. Thomas, V.P.N. Nampoori, C.P.G. Vallabhan, Appl. Phys. B **75**, 871 (2002)
34. H. Bertagnolli, W.J. Blau, Y. Chen, D. Dini, M.P. Feth, S.M. O’Flaherty, M. Hanack, V. Krishnan, J. Mater. Chem.**15**, 683 (2005)
35. Auger, W.J. Blau, P.M. Burnham, I. Chambrier, M.J. Cook, B. Isare, F. Nekelson, S.M. O’Flaherty, J. Mater. Chem. **13** 1042 (2003)
36. R. L. Sutherland, *Handbook of Nonlinear Optics* (Dekker, New York, 1996).
37. Y. Pang, M. Samoc, P.N. Prasad, J. Chem. Phys. **94**, 5282 (1991).
38. R. Priestley, A.D. Walser, R. Dorsinville, W.K. Zou, D.Y. Zu, N.-L. Yang, Opt. Commun. 131 (1996) 347.
39. M. Samoc, A. Samoc, and B. Luther-Davies, Z. Bao, L. Yu, B. Hsieh, and U. Scherf, J. Opt. Soc. Am. B **15** (1998) 817
40. M. Zhao, Y. Cui, M. Samoc, P. N. Prasad, M. R. Unroe and B. A. Reinhardt, J. Chem. Phys. **95** (1991) 3991
41. I.V. Kityk, A. Fahmi, B. Sahraoui, G. Rivoire, I. Feeks, Opt. Mater. **16** (2001) 417.
42. B. Gu, W. Ji, P.S. Patil, S.M. Dharmaprakash, J. Appl. Phys. **103** (2008) 103511.

The logo of the University of Hyderabad is a circular emblem. The outer ring contains the text "UNIVERSITY OF HYDERABAD" at the top and the Sanskrit motto "सा विद्या या विमुक्तये" at the bottom. The inner circle features a central sun-like symbol with rays, flanked by a stylized atom on the left and a lightning bolt on the right, all set against a background of small dots.

# CHAPTER 8



# Conclusions & Future Perspectives

## 8.1 Conclusions

The high intensities available from fs laser pulses makes the interaction of a fs pulse with the material it propagates through an interesting study, as the pulse itself affects and is affected by the material it propagates through in dramatic ways. Interactions representative of both of these classes form the subject of this thesis. Figure 8.1 shows the pictorial organization of the overview of the studies presented in this thesis.

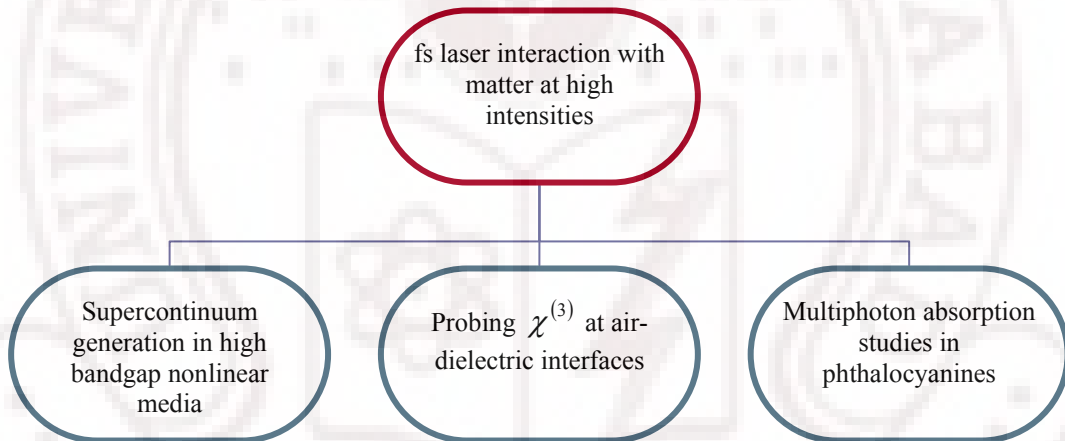


**Fig. 8.1:** Overview of the studies presented in this thesis

### 8.1.1 Supercontinuum generation (SCG) in KDP:

In spite of voluminous literature available on the generation and application of SCG in various media, a more detailed scrutiny in this exciting field of research lead us to investigate in more detail the following aspects of SCG: (a) Several experimental studies revealed that for a particular medium there is a limit to the spectral extent of the attainable SCG with a high-frequency cutoff insensitive to pulse energy; (b) With the general assumption that polarization of the generated SC follows the incident pulse, it has been shown that at high input

powers the SCG gets depolarized due to the formation of low density plasma. However, no report till date has ever dealt with the control of polarization properties of the SCG and hence research in this direction was relevant; and (c) Not much literature is available that discuss the role of media in exercising any control over SCG. Such a control is essential for fundamental understanding and improved SCG source generation.

In the thesis we addressed the above issues by our detailed studies of SCG in quadratic nonlinear media. Potassium Di-hydrogen Phosphate (KDP) crystal is studied as a potential SCG media. The intrinsic  $\chi^{(3)}$  anisotropy of KDP was considered to achieve the desired control over SCG in KDP at different crystal orientations. Initial SCG studies were performed in a z-cut KDP crystal generated along its c-axis and all the general characteristics of SCG were observed. As an effort to study the SCG at other orientations of KDP we tried to generate SCG along the phase matching direction to achieve sum frequency generation and observed an enhancement in the bandwidth of the generated SC. The tunability in the blue region of the spectrum with angle due to wave-mixing between various frequencies present in the SCG and the residual fundamental was demonstrated. An enhanced bandwidth of supercontinuum spanning from 350 nm to 1300 nm was achieved. In addition, by employing arrangement of differently oriented crystals we demonstrated the generation of a spectrally flat SC.

As an effort to achieve desired control over the polarization properties of SCG at high input fundamental peak powers we performed a systematic study of depolarization of SC across its spectral range as a function of the femtosecond laser pump intensity for an anisotropic crystalline condensed medium, KDP crystal, and compare our results with commonly used supercontinuum generation materials namely BK-7 glass and BaF<sub>2</sub>. Our results showed that at higher input power depolarization in the continuum increases for BK-7, BaF<sub>2</sub> and along the direction of the optic axis KDP crystal. However in case of KDP crystal we observe that the depolarization properties are strongly dependent on (i) the plane of polarization of incident light and (ii) the orientation of the crystal with respect



to the incident light. Our studies also confirmed that one can achieve SCG in a KDP crystal that maintains the same state of input polarization even at high input intensities when proper orientation of the crystal is used.

The motivation of pursuing SCG studies in KDP crystal was because the angular dependence of SCG in quadratic nonlinear media could help in one of the toughest challenges SCG experiments demand: To control and generate the continuum with rich content in the spectral region we want with desirable optical properties. The results presented above thus confirm our assertion making nonlinear crystalline media a promising candidate for SCG applications.

### 8.1.2 Enhanced third order nonlinearities at air-dielectric interfaces:

Breaking the inversion symmetry at any interface between two media causes structural asymmetry and local field variations across the interface. This leads to discontinuity in the normal component of the electric field and an induced nonlinear polarization containing high-order nonlinear susceptibility tensors. Several earlier theoretical and experimental studies focused on second harmonic generation (SHG) at the surfaces of different materials. Though third order NLO process are allowed in all materials independent of the symmetry property of the medium surface third order susceptibilities [ $\chi_{surface}^{(3)}$ ] were given lesser consideration because of its weaker magnitude requiring high intensities. This aspect of  $\chi_{surface}^{(3)}$  was rarely addressed both theoretically and experimentally.

In this thesis we addressed this issue with simple experimental demonstration of the effect of interface contribution to the overall nonlinear third-order susceptibility tensor. We chose a typical non collinear four-wave mixing (FWM) geometry and generated FWM signal from the two interfaces of a 1-mm thick fused silica sample with air using two 800 nm, 100 fs pulses. We devised a theoretical formulation that explicitly separates the contribution of  $\chi^{(3)}$  at interface and bulk to the induced nonlinear polarization. Thus even if one the overall nonlinear field generated in the bulk is negligible, one should consider

substantial contribution from the field generated at the interface. By recording the FWM spectra at the two interfaces and the center of the slide we find that there is enhanced FWM at the two interfaces with the FWM at sTa more intense than aTs and no FWM at the center of the slide. More interestingly, owing to the spectral modification of the intense fs pulse after propagation through a dispersive medium, we observe that there is maximum peak shift of  $\sim 1.5$  nm in the FWM generated at the two interfaces.

### 8.1.3 Multi-photon absorption studies in organic molecules:

With high intensities associated with fs pulses multi-photon ( $n > 2$ ) absorption has been widely studied. Phthalocyanines have received particular attention in the context of optical nonlinearities because of their large  $\pi$  electron delocalization, planar structure, and high thermal stability with applications in optical processing devices, practical optical limiters, and biomedical applications. In organic materials, three-photon absorption (3PA) typically occurs at longer wavelengths in the near infrared region (NIR) introducing advantages including minimization of the scattered light losses and reduction of undesirable linear absorption. However, we discovered that there are sporadic reports on organic molecules exhibiting 3PA in the significant wavelength region of 750–850 nm corresponding to the output of commercially available femtosecond Ti:Sapphire source. Though nonlinear optical properties of variety of phthalocyanines have been investigated till date there are further opportunities and avenues to explore novel structures with superior figures of merit.

We addressed these issues by our systematic studies on nonlinear optical properties of a new class of phthalocyanines, 2(3), 9(10), 16(17), 23(24) tetra tert-butyl phthalocyanine and 2(3), 9(10), 16(17), 23(24) tetra tert-butyl Zinc phthalocyanines. From the fs open aperture z-scan data we conclude that these molecules exhibit three-photon absorption (3PA) behavior. The measured 3PA coefficients ( $\alpha_3$ ) were independent of input intensity and the magnitudes were  $\sim 0.000091 \text{ cm}^3/\text{GW}^2$  and  $\sim 0.000095 \text{ cm}^3/\text{GW}^2$  for pc1 and pc2 respectively. This

is, to best of our knowledge, first report on the 3PA behavior of phthalocyanines.

Our study concludes that these alkyl phthalocyanines are prospective candidates for multi-photon applications in the fs regime. A moderate nonlinearity the fs pumping was observed from the closed aperture z-scan data. The sign of nonlinearity for fs pulses were negative in nature. We measured large off-resonant second hyperpolarizabilities ( $\gamma$ ) for these molecules with ultrafast NLO response. The measured values of  $\gamma$  were  $(4.27 \pm 0.43) \times 10^{-31}$  esu and  $(4.32 \pm 0.43) \times 10^{-31}$  esu for pc1 and pc2, respectively. The merit factors for photonic switching applications were estimated. For one-photon absorption as the dominant loss mechanism we estimated W to be  $\sim 37.9$  and  $\sim 25.6$  for pc1 and pc2, respectively. For three-photon absorption as the dominant loss mechanism we estimated V parameter as 0.57 and 0.59 for pc1 and pc2, respectively, for an input intensity of  $230 \text{ GW/cm}^2$ .

## 8.2 Future perspectives

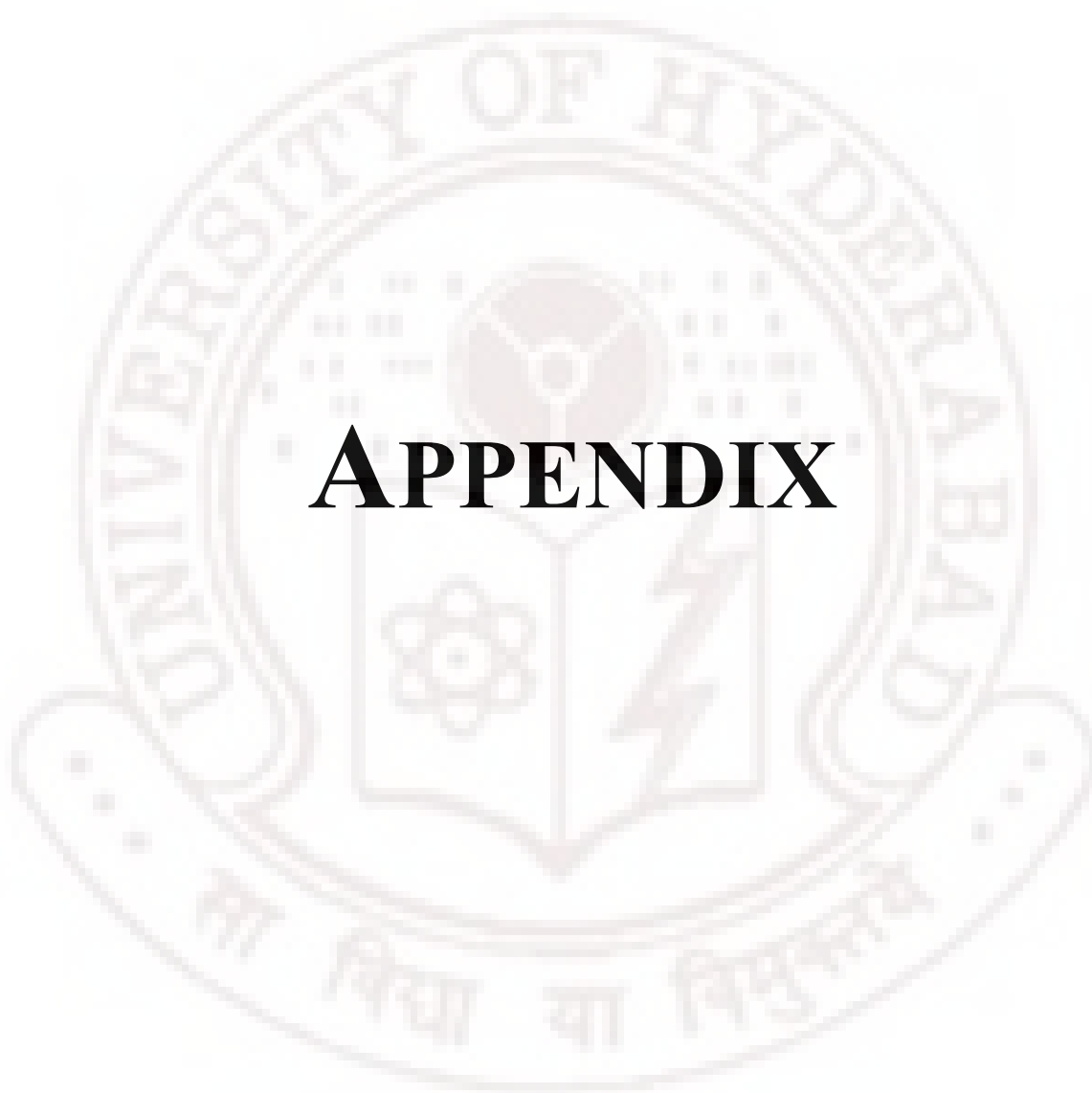
In terms of SCG studies, the availability of various types of fs laser pulse sources means substantial experimental results in various types of material media. However the theoretical explanations of most of the observed phenomenon always lag behind. This is mostly due to the complexity in the number of NLO processes that interplay in different permutations that make the exact quantification of each contribution very difficult. Most of the theoretical results available in literature deal with SCG in isotropic media. The results presented in this thesis deal for the first time with anisotropic crystal with quadratic nonlinearity. The theoretical formalism for these media therefore gets more complicated as one should take into consideration NLO processes that originate due to  $\chi^{(3)}$  as well as  $\chi^{(2)}$  at high intensities. As all the results presented in this thesis are from an experimental point of view a rigorous theoretical formalism of these results would be an extremely challenging task having enormous ramifications in the overall understanding of various aspects of the SCG phenomenon. Further, one can also attempt to study the coherence properties of

the SCG from a nonlinear crystal media, the results of which may lead of wholesome characterization of SCG. The characterization of temporal and spectral phase of SCG pulses is also an important issue one can attempt to address.

Though a rigorous theoretical formalism for  $\chi_s^{(2)}$  (at surface) is available in literature no such mention can be found in case of  $\chi_s^{(2)}$ . This thesis attempted to develop a basic formalism from a heuristic point of view to demonstrate the observed enhanced four-wave mixing signal due to  $\chi_s^{(2)}$  from an air-fused silica interface. However a more rigorous formalism can be derived to bring out the exact nature of  $\chi_s^{(2)}$  tensor and its ratio relative to  $\chi_{bulk}^{(3)}$ . A severe drawback of the experimental arrangement used in this work is its inability to quantify the signal from interfaces and bulk. One can think of various novel ways of such quantification. One proposition in this aspect is to choose suitable media with high  $\chi_{bulk}^{(3)}$  that shows FWM signal from bulk and then determine the ration of signal strength obtained from bulk to interface giving an easy estimate of the enhancement of  $\chi^{(3)}$  at interfaces.

The multiphoton absorption (MPA) in organic molecules is still an area where there is continuous search for new materials with better 3PA cross-sections for various applications. The work presented in the thesis can be easily extending in determining MPA cross-sections in various molecular systems like porphyrins, polydiacetylenes etc.

=====XXX=====



# APPENDIX



## APPENDIX-I

### Propagation of ultrashort pulses through nonlinear media

We begin with the Maxwell's equation, which we write in gaussian units in the form:

$$\begin{aligned}
 \nabla \cdot \tilde{\mathbf{D}} &= 4\pi\tilde{\rho} \\
 \nabla \cdot \tilde{\mathbf{B}} &= 0 \\
 \nabla \times \tilde{\mathbf{E}} &= -\frac{1}{c} \frac{\partial \tilde{\mathbf{B}}}{\partial t} \\
 \nabla \times \tilde{\mathbf{H}} &= -\frac{1}{c} \frac{\partial \tilde{\mathbf{D}}}{\partial t} + \frac{4\pi}{c} \tilde{\mathbf{J}}
 \end{aligned} \tag{1}$$

The use of tilda is to denote a quantity that varies rapidly with time. We are primarily interested in the solution of these equations in regions of space that contains no free charges, no free currents and assume the material is nonmagnetic, so that:

$$\tilde{\rho}=0; \quad \tilde{\mathbf{J}}=0; \quad \tilde{\mathbf{B}}=\tilde{\mathbf{H}}$$

Since the material is nonlinear, the fields  $\tilde{\mathbf{D}}^{(1)}$  and  $\tilde{\mathbf{E}}$  are related to by:  $\tilde{\mathbf{D}}^{(1)} = \tilde{\mathbf{E}} + 4\pi\tilde{\mathbf{P}}$ , where  $\tilde{\mathbf{P}}$  is the polarization vector that depends nonlinearly upon the local value of the electric field  $\tilde{\mathbf{E}}$ .

We take the curl of the curl- $\tilde{\mathbf{E}}$  Maxwell equation in (1), interchange the order of space and time derivatives on the right-hand side of the resulting equations and use equation 2 and 3 and with further simplification we end getting the wave equation in time domain which we express as:

$$\boxed{-\nabla^2 \tilde{E} + \frac{1}{c^2} \frac{\partial^2 \tilde{D}^{(1)}}{\partial t^2} = -\frac{4\pi}{c^2} \frac{\partial^2 \tilde{P}}{\partial t^2}} \tag{2}$$

We express the field quantities in terms of their Fourier transforms as



$$\tilde{E}(\bar{r}, t) = \int E(\bar{r}, \omega) e^{-i\omega t} d\omega / 2\pi \quad (3a)$$

$$\tilde{D}^{(1)}(\bar{r}, t) = \int D^{(1)}(\bar{r}, \omega) e^{-i\omega t} d\omega / 2\pi \quad (3b)$$

$$\tilde{P}(\bar{r}, t) = \int P(\bar{r}, \omega) e^{-i\omega t} d\omega / 2\pi \quad (3c)$$

where all of the integrals are to be performed over the range  $-\infty$  to  $\infty$ . We assume that  $D^{(1)}(\bar{r}, \omega)$  and  $E(\bar{r}, \omega)$  are related by the usual linear dispersion relation as

$$D^{(1)}(\bar{r}, \omega) = \varepsilon^{(1)}(\omega) E(\bar{r}, \omega) \quad (4)$$

By introducing Eqs. (3) and (4) in (2), we obtain a relation that can be regarded as the wave equation in the frequency domain and which is given by

$$\nabla^2 E(\bar{r}, \omega) + \varepsilon^{(1)}(\omega)(\omega^2/c^2) E(\bar{r}, \omega) = -(4\pi\omega^2/c^2) P(\bar{r}, \omega) \quad (5)$$

We derive below the wave equation for the slowly varying field amplitude  $\tilde{A}(\bar{r}, t)$  defined by  $\tilde{E}(\bar{r}, \omega) = \tilde{A}(\bar{r}, t) e^{i(k_0 z - \omega_0 t)} + c.c.$ , where  $\omega_0$  is the carrier frequency and  $k_0$  is the linear part of the wave vector at the carrier frequency. We represent  $\tilde{A}(\bar{r}, t)$  in terms of its spectral content as

$$\tilde{A}(\bar{r}, t) = \int A(\bar{r}, \omega) e^{-i\omega t} d\omega / 2\pi \quad (6)$$

$$\text{and } E(\bar{r}, \omega) = E(\bar{r}, \omega - \omega_0) e^{ik_0 z} \quad (7)$$

Now, in terms of the quantity  $A(\bar{r}, \omega)$  the wave equation (5) becomes

$$\nabla^2_{\perp} A + \frac{\partial^2 A}{\partial z^2} + 2ik_0 \frac{\partial A}{\partial z} + [k^2(\omega) - k_0^2] A = \frac{4\pi\omega^2}{c^2} P(\bar{r}, \omega) e^{ik_0 z} \quad (8)$$

where  $k^2(\omega) = \varepsilon(\omega)(\omega^2/c^2)$

We next approximate  $k(\omega)$  as a power series in the frequency difference  $\omega - \omega_0$  as

$$k(\omega) = k_0 + k_1(\omega - \omega_0) + D \quad \text{where} \quad D = \sum_{n=2}^{\infty} \frac{1}{n!} k_n (\omega - \omega_0)^n \quad (9)$$

so that  $k^2(\omega)$  can be expressed as

$$k^2(\omega) = k_0^2 + 2k_0 k_1 (\omega - \omega_0) + 2k_0 D + 2k_1 D (\omega - \omega_0) + k_1^2 (\omega - \omega_0)^2 + D^2 \quad (10)$$

Here  $D$  represents the high-order dispersion. Introducing (10) in (8) and dropping the invariably small contribution of  $D^2$  term we have:

$$\begin{aligned} \nabla^2_{\perp} A + \frac{\partial^2 A}{\partial z^2} + 2ik_0 \frac{\partial A}{\partial z} + 2k_0 k_1 (\omega - \omega_0) A + 2k_0 D A \\ + 2k_1 D (\omega - \omega_0) A + k_1^2 (\omega - \omega_0)^2 A = -\frac{4\pi\omega^2}{c^2} P(z, \omega) e^{ik_0 z} \end{aligned} \quad (11)$$

By multiplying (11) with  $e^{-i(\omega - \omega_0)t}$  and integrating over all values of  $\omega - \omega_0$ , we convert (14) back to the time domain as

$$\boxed{\begin{aligned} \left[ \nabla^2_{\perp} + \frac{\partial^2}{\partial z^2} + 2ik_0 \left( \frac{\partial}{\partial z} + k_1 \frac{\partial}{\partial t} \right) + 2ik_1 \tilde{D} \frac{\partial}{\partial t} + 2k_0 \tilde{D} - k_1 \frac{\partial^2}{\partial t^2} \right] \tilde{A}(\bar{r}, t) \\ = -\frac{4\pi\omega^2}{c^2} \frac{\partial^2 \tilde{P}}{\partial t^2} e^{-i(k_0 z - \omega_0 t)} \end{aligned}} \quad (12)$$

$$\text{where } \tilde{D} = \sum_{n=2}^{\infty} \frac{1}{n} k_n \left( i \frac{\partial}{\partial t} \right)^n$$

The polarization in terms of its slowly varying amplitude approximation  $\tilde{p}(\bar{r}, t)$  can be represented as:

$$\tilde{P}(\bar{r}, t) = \tilde{p}(\bar{r}, t) e^{i(k_0 z - \omega_0 t)} + c.c., \quad \text{where} \quad \tilde{p}(\bar{r}, t) = 3\chi^{(3)} |\tilde{A}(\bar{r}, t)|^2 \tilde{A}(\bar{r}, t) \quad (13)$$

Therefore, we find that

$$\begin{aligned}\frac{\partial \tilde{P}}{\partial t} &= \left( -i\omega_0 \tilde{P} + \frac{\partial \tilde{P}}{\partial t} \right) e^{i(k_0 z - \omega_0 t)} + c.c. \\ &= -i\omega_0 \left[ \left( 1 + \frac{i}{\omega_0} \frac{\partial}{\partial t} \right) \tilde{P} \right] e^{i(k_0 z - \omega_0 t)} + c.c.\end{aligned}\quad (14a)$$

$$\text{and } \frac{\partial^2 \tilde{P}}{\partial t^2} = -\omega_0^2 \left[ \left( 1 + \frac{i}{\omega_0} \frac{\partial}{\partial t} \right)^2 \tilde{P} \right] e^{i(k_0 z - \omega_0 t)} + c.c. \quad (14b)$$

By introducing (14) in (12) we obtain

$$\begin{aligned}\left[ \nabla^2_{\perp} + \frac{\partial^2}{\partial z^2} + 2ik_0 \left( \frac{\partial}{\partial z} + k_1 \frac{\partial}{\partial t} \right) + 2ik_1 \tilde{D} \frac{\partial}{\partial t} + 2k_0 \tilde{D} - k_1 \frac{\partial^2}{\partial t^2} \right] \tilde{A}(\bar{r}, t) \\ = -\frac{4\pi\omega_0^2}{c^2} \left( 1 + \frac{i}{\omega_0} \frac{\partial}{\partial t} \right)^2 \tilde{P}\end{aligned}\quad (15)$$

We now consider the retarded time frame specified by the coordinates  $z'$  and  $\tau$

defined by  $z' = z$  and  $\tau = t - \frac{1}{v_g} z = t - k_1 z$ , so that

$$\frac{\partial}{\partial z} = \frac{\partial}{\partial z'} - k_1 \frac{\partial}{\partial \tau} \quad \text{and} \quad \frac{\partial}{\partial t} = \frac{\partial}{\partial \tau}$$

Under the transformations the wave equation becomes

$$\begin{aligned}\left[ \nabla^2_{\perp} + \frac{\partial^2}{\partial z'^2} - 2k_1 \frac{\partial}{\partial z'} \frac{\partial}{\partial \tau} + k_1^2 \frac{\partial^2}{\partial \tau^2} + 2ik_0 \left( \frac{\partial}{\partial z'} - k_1 \frac{\partial}{\partial \tau} + k_1 \frac{\partial}{\partial \tau} \right) \right] \tilde{A}(\bar{r}, t) \\ + \left[ 2k_0 \tilde{D} + 2ik_1 \tilde{D} \frac{\partial}{\partial \tau} - k_1^2 \frac{\partial^2}{\partial \tau^2} \right] \tilde{A}(\bar{r}, t) = -\frac{4\pi\omega_0^2}{c^2} \left( 1 + \frac{i}{\omega_0} \frac{\partial}{\partial t} \right)^2 \tilde{P}\end{aligned}\quad (16)$$

Simplifying (19) under the slowly varying amplitude approximation we get

$$\begin{aligned}\left[ \nabla^2_{\perp} - 2k_1 \frac{\partial}{\partial z'} \frac{\partial}{\partial \tau} + 2ik_0 \frac{\partial}{\partial z'} + 2k_0 \tilde{D} + 2ik_1 \tilde{D} \frac{\partial}{\partial \tau} \right] \tilde{A}(\bar{r}, t) \\ = -\frac{4\pi\omega_0^2}{c^2} \left( 1 + \frac{i}{\omega_0} \frac{\partial}{\partial t} \right)^2 \tilde{P}\end{aligned}\quad (17)$$

This equation can be alternatively written as

$$\begin{aligned} & \left[ \nabla^2_{\perp} + 2k_0 \frac{\partial}{\partial z'} \left( 1 + i \frac{k_1}{k_0} \frac{\partial}{\partial \tau} \right) + 2k_0 \tilde{D} \left( 1 + i \frac{k_1}{k_0} \frac{\partial}{\partial \tau} \right) \right] \tilde{A}(\bar{r}, t) \\ & = - \frac{4\pi\omega_0^2}{c^2} \left( 1 + \frac{i}{\omega_0} \frac{\partial}{\partial t} \right)^2 \tilde{p} \end{aligned} \quad (18)$$

We note that several of the terms in this equation depend upon the ratio  $k_1/k_0$ . This ratio can be approximated as follows:

$$\frac{k_1}{k_0} = \frac{v_g^{-1}}{(n\omega_0/c)} = \frac{n_g}{n\omega_0}$$

Ignoring dispersion  $n_g = n$ , so that  $k_1/k_0 = 1/\omega_0$ . In this approximation the wave equation (20) becomes

$$\begin{aligned} & \left[ \nabla^2_{\perp} + 2k_0 \frac{\partial}{\partial z'} \left( 1 + \frac{i}{\omega_0} \frac{\partial}{\partial \tau} \right) + 2k_0 \tilde{D} \left( 1 + \frac{i}{\omega_0} \frac{\partial}{\partial \tau} \right) \right] \tilde{A}(\bar{r}, t) \\ & = - \frac{4\pi\omega_0^2}{c^2} \left( 1 + \frac{i}{\omega_0} \frac{\partial}{\partial t} \right)^2 \tilde{p} \end{aligned} \quad (19)$$

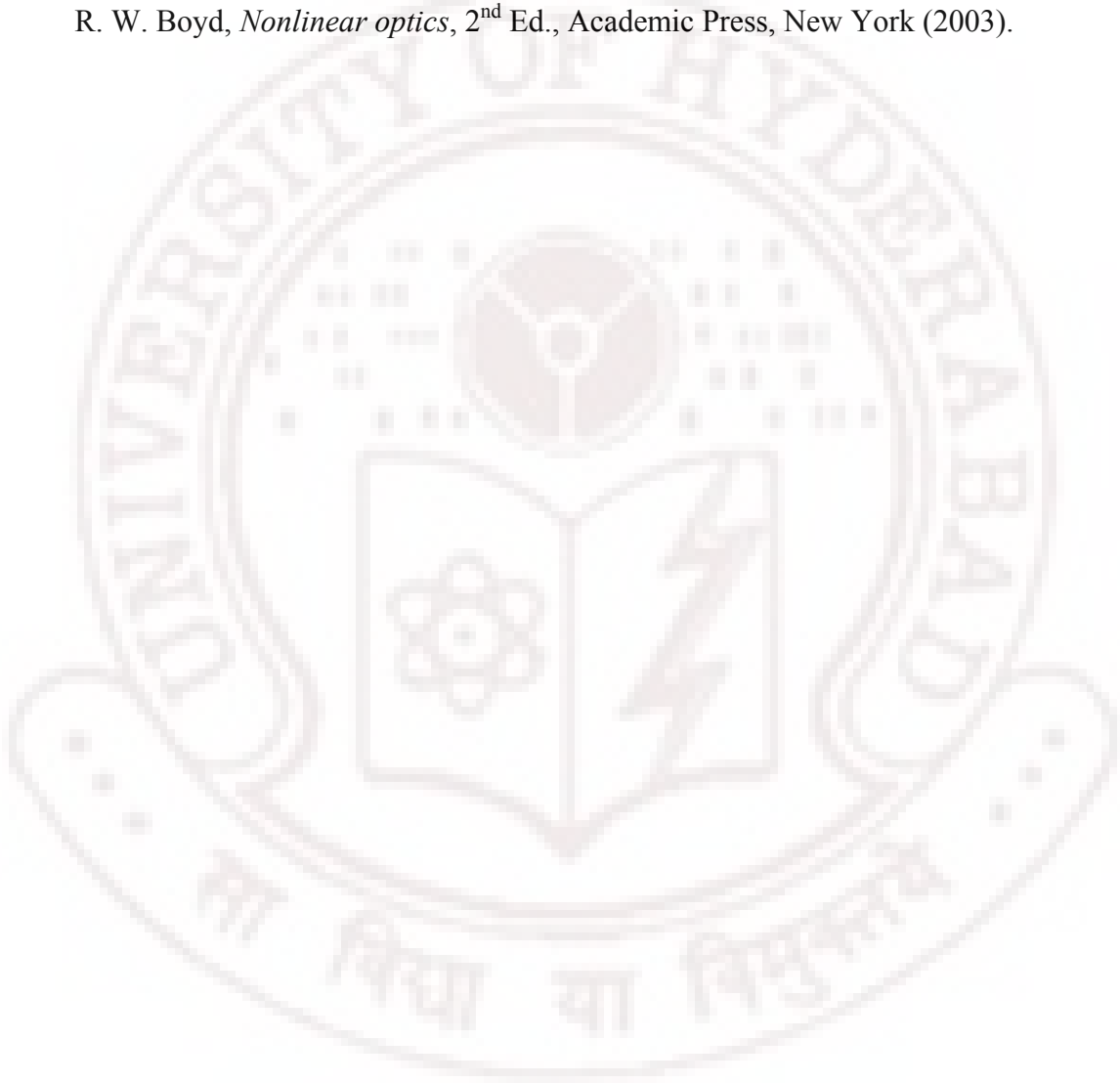
which can also be expressed as

$$\begin{aligned} & \left[ \left( 1 + \frac{i}{\omega_0} \frac{\partial}{\partial \tau} \right)^{-1} \nabla^2_{\perp} + 2ik_0 \frac{\partial}{\partial z'} + 2k_0 \tilde{D} \right] \tilde{A}(\bar{r}, t) \\ & = - \frac{4\pi\omega_0^2}{c^2} \left( 1 + \frac{i}{\omega_0} \frac{\partial}{\partial t} \right)^2 \tilde{p} \end{aligned} \quad (20)$$

This equation is called the *generalized nonlinear Schrödinger equation*. It includes the effects of higher-order dispersion (presence of  $\tilde{D}$ ), space-time coupling and self-steepening.

### References:

1. T. Brabec, and F. Krausz, Phys. Rev. Lett., **78**, 3282 (1997).
- R. W. Boyd, *Nonlinear optics*, 2<sup>nd</sup> Ed., Academic Press, New York (2003).



## Appendix-II

### About the author

R. Sai Santosh Kumar, son of Manohar Murthy and Lakshmi, was born in Srikakulam, of Andhra Pradesh, India, in 1982. He received his primary and secondary school education in Berhampur, Orissa. He then completed his intermediate education from Vignan Vidhyalayas, Guntur, Andhra Pradesh. After the completion of his B.Sc. and M.Sc. (Physics) from Sri Sathya Sai Institute of Higher Learning (Sri Sathya Sai University), he joined the School of Physics, University of Hyderabad to pursue the Ph.D. degree in 2004 under the supervision of Prof. D. Narayana Rao. He qualified for GATE examination in February 2004. He was awarded research fellowship by Counsel of Scientific and Industrial research (JRF and SRF) during 2004-2009. He is the winner of “Young Scientist” award instituted by Dr. K. V. Rao Scientific Society in the year 2008 under the category of Physics.

#### Experimental expertise:

- ◆ Femtosecond Supercontinuum generation in nonlinear crystals and transparent media
- ◆ Probing the enhanced surface nonlinearities with forward two beam non degenerate four-wave mixing.
- ◆ Femtosecond and nanosecond Z-scan technique to measure the nonlinear optical properties of thin films and liquids.
- ◆ Femtosecond time resolved box-car degenerate four-wave mixing to look into the nonlinear optical properties of materials.
- ◆ Pulse width measurement of the fs laser using the intensity autocorrelation correlation techniques.
- ◆ Nanosecond degenerate four-wave mixing in backward geometry
- ◆ Femtosecond laser direct writing in glasses, nonlinear crystals for micro-optical devices and direct writing of channel waveguides.

#### Instruments: Handling Expertise / Operated:

- 100 fs Ti:Sapphire laser system (Mai Tai oscillator + Spitfire regenerative amplifier + OPA)
- High power Nd: YAG Lasers (6 ns, 10Hz)
- Dye Lasers (Rhodamine B in Methanol), He-Ne Lasers

- Raman shifter (H<sub>2</sub> gas)
- Confocal Microscope
- Atomic force microscope (AFM)
- Nano positioner
- UV-Vis-NIR absorption spectrometers (Varian-Cary 5000), Fluoreimeters (Fluoromax-3)
- 200 MHz Digital Oscilloscope (Tektronix)
- Lock-in Amplifiers (SRS 830, Princeton Applied Research)
- Boxcar Averager and Integrator (SRS-250)
- Stepper Motor Controller
- Spectrometers (Jobin Yvon, Ocean Optics USB2000), CCD cameras
- Power Meters (Scientech and Ophir)
- High power optics

#### **Awards:**

1. Winner of **Young scientist Award in Physics for the year 2008**, instituted by Dr. K. V. Rao Scientific society.
2. Recipient of **CSIR/SRF** fellowship, January 2007
3. Recipient of Council of Scientific and Industrial Research (**CSIR**)/**JRF** fellowship, June 2004.
4. Qualified the National Eligibility Test (**NET**) for lectureship under UGC schemes (June 2004).
5. Qualified **GATE-2004** exam with an All India Rank of 256.
6. Recipient of scholarship on merit from the Board of Intermediate Examination, A.P.



## Appendix-III

### List of Publications

#### Journal publications:

1. “Active waveguides fabricated by femtosecond laser direct writing in high quantum efficiency erbium-doped Baccarat glass.” K.C. Vishnubhatla, S. Venugopal Rao, **R. Sai Santosh Kumar**, R.Osellame, S.N.B. Bhaktha, A. Chiappini, A. Chiasera, M. Ferrari, M. Mattarelli, M. Montagna, R. Ramponi, G.C. Righini, and D. Narayana Rao (communicated to Appl. Phys. A)
2. “Ultrafast nonlinear optical properties of alkyl phthalocyanines investigated using degenerate four-wave mixing technique,” **R. Sai Santosh Kumar**, S. Venugopal Rao, L. Giribabu, and D. Narayana Rao (in press, Optical materials, 2009)
3. “Four wave mixing at air-dielectric interfaces with a femtosecond laser excitation” **R. Sai Santosh Kumar**, Suneel Singh, and D. Narayana Rao, Opt. Express **16**, 18034-18039 (2008)
4. “Depolarization properties of the femtosecond supercontinuum generated in condensed media” **R. Sai Santosh Kumar**, K. L. N. Deepak, and D. Narayana Rao, Phys. Rev. A **78**, 043818 (2008) ( Virtual Journal of ultrafast science, Vol. 7, Issue 11, November 2008)
5. “Control of the polarization properties of supercontinuum generation in a noncentrosymmetric crystal”, **R. Sai Santosh Kumar**, K. L. N. Deepak, and D. Narayana Rao, Opt. Lett. **33**, 1198-1200 (2008) (Virtual Journal of ultrafast science, Vol. 7, Issue 8, August 2008)
6. “Linear and Nonlinear Optical Properties of Mesoionic Oxyallyl Derivatives: Enhanced Non-Resonant Third Order Optical Nonlinearity in Croconate Dyes”, Ch. Prabhakar, K. Yesudas, K. Bhanuprakash, V. Jayathirtha Rao, **R. Sai Santosh Kumar**, and D. Narayana Rao, J. Phys Chem. C, **112**, 13272-13280 (2008)
7. “Nonlinear optical properties of alkyl phthalocyanines in the femtosecond, nanosecond, and cw excitation regimes”, **R. Sai Santosh Kumar**, S. Venugopal Rao, L. Giribabu, and D. Narayana Rao Proc. SPIE, **6875**, 68751D (2008)
8. “Inscription and characterization of micro-structures in silicate, FOTURAN and tellurite glasses by femtosecond laser direct writing,” K. C. Vishnubhatla, S.

- Venugopal Rao, **R. Sai Santosh Kumar**, K. Shiva Prasad, P. S. R. Prasad, and D. Narayana Rao, Proc. SPIE **6881**, 688113 (2008)
9. “*Micro-Raman mapping of micro-gratings in BACCARAT glass directly written using femtosecond laser*,” K. C. Vishnubhatla, S. Venugopal Rao, **R. Sai Santosh Kumar**, S. N. B. Bhaktha, A. Chiappini, A. Chiasera, J. Laureyns, M. Ferrari, M. Mattarelli, M. Montagna, R. Osellame, R. Ramponi, G. C. Righini, S. Turrell, and D. Narayana Rao, Proc. SPIE **6881**, 688114 (2008)
  10. “*Femtosecond and nanosecond nonlinear optical properties of alkylphthalocyanines studied using Z-scan*”, **R. Sai Santosh Kumar**, S. Venugopal Rao, L. Giribabu, and D. Narayana Rao, Chem. Phys. Lett. **447**, 274-278 (2007)
  11. “*Broadband supercontinuum generation in a single Potassium Di-hydrogen Phosphate (KDP) crystal achieved in tandem with sum frequency generation*” **R. Sai Santosh Kumar**, S. Sree Harsha, and D. Narayana Rao, Appl. Phys. B. **86**, 615-621 (2007)
  12. “*Second harmonic generation and crystal growth of new chalcone derivatives*”, P.S. Patil; S.M. Dharmaprakash; K. Ramakrishna, H.-K. Hoong-Kun Fun, **R. Sai Santosh Kumar**, and D. Narayana Rao, Journal of Crystal Growth, **303**, 520-524, 2007.
  13. “*Nonlinear absorption and scattering properties of cadmium sulphide nanocrystals with its application as a potential optical limiter*”, N. Venkatram, **R. Sai Santosh Kumar**, and D. Narayana Rao, J. Appl. Phys. **100**, 074309-1–074309-8 (2006). (Virtual journal of nanoscale science & Technology, **V-14**, Issue-17, October 23, 2006), (Virtual journal of ultra fast science, **V-5**, Issue-11, November 2006).
  14. “*Nonlinear optical absorption characterization and optical switching of Au nanoparticle doped SiO<sub>2</sub>-TiO<sub>2</sub> sol-gel films*” N. Venkatram, **R. Sai Santosh Kumar**, S. K. Medda, Sucheta De, Goutam De, and D. Narayana Rao, Journal of Nanoscience and Nanotechnology, **6**, 1990–1994 (2006)

### Conference Papers (International and national):

1. “*Femtosecond third-order nonlinear optical properties of alkyl phthalocyanines studied at 800 nm using degenerate four-wave mixing technique*” **R. Sai Santosh Kumar**, S. Venugopal Rao, L. Giribabu, D. Narayana Rao, National Laser Symposium-08, LASTEC, Vadodara, January 6-10, 2009 [Poster Presentation]
2. “*Femtosecond nonlinear optical properties of an asymmetric phthalocyanine at 800 nm studied using Z-scan and DFWM techniques*”, S. Venugopal Rao, G. Kurumurthy, **R. Sai Santosh Kumar**, and D. Narayana Rao, National Laser Symposium-08, LASTEC, Vadodara, January 6-10, 2009 [Poster Presentation]
3. “*Direct Writing of Microstructures in Bulk Poly (Methyl MethAcrylate) Using Femtosecond Pulses*” K. L. N. Deepak, S. Venugopal Rao, **R. Sai Santosh Kumar**, and D. Narayana Rao, National Laser Symposium-08, LASTEC, Vadodara, January 6-10, 2009 [Poster Presentation]
4. “*Femtosecond laser direct writing of microstructures in poly (methyl methacrylate)*” K. L. N. Deepak, S. Venugopal Rao, **R. Sai Santosh Kumar**, and D. Narayana Rao, Photonics-2008 held at IIT, Delhi [Oral Presentation]
5. “*Nonlinear absorption properties of alkyl phthalocyanines in the femtosecond, nanosecond, and cw excitation regimes,*” **R. Sai Santosh Kumar**, S. Venugopal Rao, L. Giribabu, D. Narayana Rao, Photonics West, LASE-2008, 19-24 January 2008, at San Jose, California. [Poster presentation]
6. “*Micro-Raman mapping of micro-gratings in ‘BACCARAT’ glass directly written using femtosecond laser,*” K.C. Vishnubhatla, **R. Sai Santosh Kumar**, S.N.B. Bhaktha, A. Chiappini, A. Chiasera, J. Laureyns, M. Ferrari, M. Mattarelli, M. Montagna, S. Turrell, D. Narayana Rao, S. Venugopal Rao, Photonics West, LASE-2008, 19-24 January 2008, at San Jose, California. [Oral Presentation]
7. “*Inscription and characterization of micro-structures in silicate, FOTURANTM and tellurite glasses by femtosecond laser direct writing,*” K.C. Vishnubhatla, **R. Sai Santosh Kumar**, K. Shiva Prasad, P.S.R. Prasad, D. Narayana Rao, S. Venugopal Rao, Photonics West, LASE-2008, 19-24 January 2008, [Oral Presentation]
8. “*Supercontinuum Generation in quadratic media with controllable polarization properties*” **R. Sai Santosh Kumar**, K. L. N. Deepak, N. Venkatram, D. Narayana Rao, 5th Asian Conference on Ultrafast Phenomena (ACUP 2008), 6 - 9 January 2008, Singapore. [Invited talk]

9. *“Nonlinear absorption and optical limiting studies of alkyl phthalocyanines studied with nanosecond excitation,”* **R. Sai Santosh Kumar**, S. Venugopal Rao, L. Giribabu, D. Narayana Rao, National Laser Symposium-07, M.S. University of Baroda, Vadodara, December 17 – 20, 2007 [Poster Presentation]
10. *“Polarization properties of femtosecond supercontinuum generated in potassium dihydrogen phosphate crystal,”* **R. Sai Santosh Kumar**, K. L. N. Deepak, D. Narayana Rao, National Laser Symposium-07, M.S. University of Baroda, Vadodara, December 17 – 20, 2007 [Poster Presentation]
11. *“Four wave mixing at air-fused silica interfaces,”* **R. Sai Santosh Kumar**, D. Narayana Rao, National Laser Symposium-07, M.S. University of Baroda, Vadodara, December 17 – 20, 2007. [Poster Presentation]
12. *“Inscription and characterization of micro-structures in silicate, FOTURANTM, and tellurite glasses by femtosecond laser direct writing,”* K.C. Vishnubhatla, S. Venugopal Rao, **R. Sai Santosh Kumar**, K. Shiva Prasad, P.S.R. Prasad, D. Narayana Rao, National Laser Symposium-07, M.S. University of Baroda, Vadodara, December 17 – 20, 2007. [Poster Presentation]
13. *“Micro-structures in ‘BACCARAT’ glass written using femtosecond laser”*, K.C. Vishnubhatla, **R. Sai Santosh Kumar**, S.N.B. Bhaktha, A. Chiappini, A. Chiasera, J. Laureyns, M. Ferrari, M. Mattarelli, M. Montagna, S. Turrell, D. Narayana Rao, S. Venugopal Rao, National Laser Symposium-07, M.S. University of Baroda, Vadodara, December 17 – 20, 2007 [Poster Presentation]
14. *“Supercontinuum Generation in a KDP crystal with excellent polarization behaviour,”* **R. Sai Santosh Kumar** and D. Narayana Rao, Proceedings of International Conference on Fiber-optics, Opto-electronics and Photonics (Photonics - 2006), 12-16 Dec 2006, University of Hyderabad, Hyderabad, India. [Oral Presentation]
15. *“Femtosecond laser direct writing of waveguides and microstructures in silicate and Foturan glasses,”* K.C. Vishnubhatla, **R. Sai Santosh Kumar**, S. Venugopal Rao, D. Narayana Rao, Proceedings of International Conference on Fiber-optics, Opto-electronics and Photonics (Photonics - 2006), 12-16 Dec 2006, University of Hyderabad, Hyderabad, India. [Poster Presentation]
16. *“Synthesis, characterization and nonlinear optical properties of some novel chalcone derivative crystals,”* V. Shettigar, **R. Sai Santosh Kumar**, S. M. Dharmaprakash and D. Narayana Rao, National Laser Symposium-06, CAT, Indore, December-2006.[Poster Presentation]

17. “Tunable white light Generation in Potassium Dihydrogen Phosphate (KDP) crystal,” **R. Sai Santosh Kumar**, D. Narayana Rao, Indo-Japan Student Symposium, January 9, 2006, School of Chemistry, University of Hyderabad. [Oral Presentation.]
18. “Supercontinuum generation and parametric wave mixing in a Potassium Dihydrogen Phosphate (KDP) crystal,” S. Sree Harsha, **R. Sai Santosh Kumar** and D. Narayana Rao, Proceedings of International Conference of Optics and Optoelectronics (ICOL), 12-14 Dec 2005, IRDE, Dehradun, India. [Invited talk]
19. “Generation Of Surface Relief Gratings On Azo Dyedoped Polymer Films Using A Pulsed Laser,” N.V. Reddy, **R. Sai Santosh Kumar** and D. Narayana Rao, National Laser Symposium-05, VIT, Vellore, December-2005 [Poster Presentation]
20. “Tunable white light generation in a Potassium Dihydrogen Phosphate (KDP) crystal,” S. Sree Harsha, **R. Sai Santosh Kumar**, D. Narayana Rao, National Laser Symposium-05, VIT, December-2005. [Poster Presentation]
21. “Two photon absorption and nonlinear scattering studies of CdS nanoparticles” N. Venkatram, **R. Sai Santosh Kumar**, M.A. Akundi, D. Narayana Rao, National Laser Symposium, BARC, Mumbai. January 2005. [Poster Presentation]
22. “The effect of the Local Field on the lifetimes of the  $Tb^{3+}$  doped in a binary glass system”, G. Manoj Kumar, **R. Sai Santosh Kumar**, D. Narayana Rao, XXX Optical Society of India Symposium on Optics and Optoelectronics, SOOP-05, NPL, New Delhi, January 2005. [Poster Presentation]

=====\*\*\*\*\*=====